UNIVERSITY OF CALIFORNIA

Los Angeles

Improving the Safety and Efficacy of CRISPR/Cas9-based Therapies for Duchenne Muscular Dystrophy

A dissertation submitted in partial satisfaction of the requirements for the degree Doctor of Philosophy in Molecular Biology

by

Michael Reza Emami

2022

ABSTRACT OF THE DISSERTATION

Improving the Safety and Efficacy of CRISPR/Cas9-based Therapies for Duchenne Muscular Dystrophy

by

Michael Reza Emami

Doctor of Philosophy in Molecular Biology

University of California, Los Angeles, 2022

Professor Melissa J. Spencer, Chair

Duchenne muscular dystrophy (DMD) is an x-linked recessive lethal muscle wasting disease with no cure. DMD is often caused by out-of-frame mutations that result in a loss of dystrophin protein. However, there is an allelic and milder form of the disease, Becker muscular dystrophy (BMD), which is typically caused by in-frame mutations that result in somewhat functional dystrophin protein. Therefore, a promising strategy to treat DMD is to utilize gene editing tools such as the clustered regularly interspaced short palindromic repeats (CRISPR)-associated protein 9 (CRISPR/Cas9) system to convert a DMD mutation into a BMD mutation resulting in a clinically milder phenotype. However, achieving safe and efficient systemic delivery of the CRISPR/Cas9 system remains a significant challenge for DMD as skeletal muscle comprises ~40% of the total body mass. Here, we develop and optimize non-viral

nanoparticles and adeno-associated viral (AAV) carriers as approaches to achieve safe and efficient systemic CRISPR/Cas9 delivery.

We successfully demonstrate CRISPR/Cas9 delivery *in vitro* using iteratively optimized polymer-based nanoparticles. While these nanocarriers perform well *in vitro*, they inefficiently traffic to skeletal muscle after systemic delivery *in vivo*. In order to improve nanoparticle-mediated delivery to muscle and muscle stem cells, we developed and screened an AAV peptide display library for potential peptide motif ligands that may mediate skeletal muscle and muscle stem cell entry. We identify novel AAV variants highly enriched in skeletal muscle and muscle stem cells. Future work will focus on validating AAV variants and examining whether the muscle-specific peptide motif ligands may improve nanoparticle entry in muscle.

While nanoparticles are promising carriers of CRISPR/Cas9 due to their low immunogenicity, AAV carriers are typically administered at high viral doses and often lead to AAV-induced immunotoxicities that pose life threatening risks. Therefore, we characterize AAV-mediated immune responses that arise in response to double dosing AAV in a dystrophic mouse model, in which the first dose effectively immunizes the mice. We reveal the production of AAV-specific antibodies that leads to subsequent activation of the classical complement pathway and induction of pro-inflammatory cytokines only after the second administration of AAV. Single cell RNA-sequencing (scRNA-seq) similarly confirms pronounced activation primarily after the second dose of AAV. Future work will continue to understand and identify targetable genes, pathways, or immune cell subtypes that may facilitate development of mitigation strategies to improve the safety and efficacy of AAV-based therapies.

The dissertation of Michael Reza Emami is approved.

April Dawn Pyle

Rachelle Hope Watson

Donald Barry Kohn

Stephen Caldwell Cannon

Melissa J. Spencer, Committee Chair

University of California, Los Angeles

2022

Dedication

To my parents, Hamid Emami and Nellie Emami, who go above and beyond their limits to provide my sisters and I with the opportunities they never had.

To my sisters, Michelle and Melissa, for their words of encouragement and unwavering support.

To my partner and anchor, Jessica Nevarez-Mejia, who has made my time at UCLA so much more enjoyable.

Table of Contents

List of Figures

List of Tables

Acknowledgments

I would like to extend my sincerest appreciation to my thesis advisor and mentor, Dr. Melissa J. Spencer for her encouragement, optimism and relentless support of me. I also wish to thank the current and former members of the Spencer lab as well as collaborating labs who have lent me their time and technical expertise. I would also like to extend my gratitude to my thesis committee: Drs. April D. Pyle, Rachelle H. Crosbie, Donald B. Kohn and Stephen C. Cannon for their feedback and insightful comments. I must also thank Dr. Courtney S. Young, who I viewed as my unofficial mentor, for sharing her knowledge, technical expertise, and setting an example of excellence as a researcher, all of which have been invaluable lessons. I must also thank my previous mentors who inspired me to pursue my interests in science and helped shape me into a scientist: Drs. Luis Mota-Bravo, Marlene de la Cruz, Baljinder S. Mankoo, Timothy W. Bredy, Xiang Li, and Maria R. Conte. Lastly, I would like to acknowledge my family, who are a pillar in my life and encourage me in everything I do.

Chapter 2 is adapted from Emami, M.R., Young, C.S., Ji, Y., Liu, X., Mokhonova, E., Pyle, A.D., Meng, H. and Spencer, M.J. (2019), Polyrotaxane Nanocarriers Can Deliver CRISPR/Cas9 Plasmid to Dystrophic Muscle Cells to Successfully Edit the DMD Gene. Adv. Therap., 2: 1900061. https://doi.org/10.1002/adtp.201900061. We would like to thank Jane Wen, Catherine Le, and Rebecca Banh for technical assistance. We extend our greatest thanks to Jinhong Jiang for PRX illustrations. The authors acknowledge the use of instruments at the Nano and Pico Characterization Lab at the California NanoSystems Institute. This material is based upon work supported by the National Science Foundation Graduate Research Fellowship Program under Grant No.

DGE-1650604 (MRE). Any opinions, findings, and conclusions or recommendations expressed in this material are those of the author and do not necessarily reflect the views of the National Science Foundation. Funding was provided by Ruth L. Kirschstein National Research Service Award GM007185 (MRE), and the Ruth L. Kirschstein National Research Service Award T32AR065972 'Muscle Cell Biology, Pathophysiology, and Therapeutics' from the National Institute of Arthritis and Musculoskeletal and Skin Diseases (CSY). Additional funding was provided by the California Institute for Regenerative Medicine (CIRM DISC2-08824), Muscular Dystrophy Association (MDA 578394), pilot and feasibility seed grant from the Center for DMD at UCLA (NIH NIAMS) P30 AR05723, Eli & Edythe Broad Center of Regenerative Medicine and Stem Cell Research at UCLA, and Jesse's Journey. MRE, CSY, and YJ contributed equally to this work. Author contributions were: Conceptualization, Methodology, Visualization, Project Administration, Writing – Review and Editing – MRE, CSY, YJ, XL, HM, ADP, MJS; Investigation, Formal Analysis, Validation – MRE, CSY, YJ, XL; Writing – Original Draft – MRE, CSY; Resources – EM, ADP, MJS; Supervision – HM, ADP, MJS; Funding Acquisition – HM, ADP, MJS.

Chapter 3 is currently unpublished and describes ongoing work. We anticipate the project will be submitted for publication in the next year. I would like to thank everyone who contributed to the work including Giorgia Del Vecchio, Xinjun Zhang, Cloelia Decioccio, Courtney S. Young, April D. Pyle, and Melissa J. Spencer. I would also like to thank Jane Wen, Diana Becerra, and Joyce Lui for technical assistance. We thank and acknowledge the use of instruments from the following cores: Eli and Edythe Broad Center of Regenerative Medicine and Stem Cell Research (BSCRC) Flow

Cytometry Core and Sequencing Core, Johnson Comprehensive Cancer Center (JCCC) Flow Cytometry Core, the Institute for Quantitative and Computational Biosciences (QC Bio), and UPenn Gene Therapy Vector Core for generating the P_0 AAV library. This material is based upon work supported by the National Science Foundation Graduate Research Fellowship Program under Grant No. DGE-1650604 (MRE). Any opinions, findings, and conclusions or recommendations expressed in this material are those of the author and do not necessarily reflect the views of the National Science Foundation. Funding was also provided by Ruth L. Kirschstein National Research Service Award GM007185 (MRE), the CDMD Azrieli Graduate Student Award (MRE), and the Whitcome Predoctoral Fellowship in Molecular Biology (MRE). Additional funding was provided by the California Institute for Regenerative Medicine (CIRM DISC2-10696, ADP) and the Wellstone (U54 AR052646-07, MJS). Author contributions were: Conceptualization, Methodology, Visualization, Project Administration – MRE, CSY, ADP, MJS; Investigation – MRE, CD, CSY, GD; Software, Data Curation – XZ; Formal analysis – MRE; Writing – Original Draft – MRE; Writing – Review and Editing – MRE, MJS; Resources – GD, ADP, MJS; Supervision – CSY, ADP, MJS; Funding Acquisition – ADP, MJS.

Chapter 4 is currently unpublished and describes ongoing work. We anticipate the project will be submitted for publication in the next year. I would like to thank everyone who contributed to the work including Alejandro Espinoza, Feiyang Ma, Philip Farahat, Jeffrey S. Chamberlain, Sergio A. Villalta, Matteo Pellegrini, Courtney S. Young, and Melissa J. Spencer. I would also like to thank Jane Wen and Diana Becerra for technical assistance. We thank and acknowledge the use of services from the following cores: the

Technology Center for Genomics & Bioinformatics (TCGB), the Immune Assessment Core at UCLA, the Institute for Quantitative and Computational Biosciences (QC Bio) at UCLA, and the UCI Vaccine R&D Center. This material is based upon work supported by the National Science Foundation Graduate Research Fellowship Program under Grant No. DGE-1650604 (MRE). Any opinions, findings, and conclusions or recommendations expressed in this material are those of the author and do not necessarily reflect the views of the National Science Foundation. Funding was also provided by Ruth L. Kirschstein National Research Service Award GM007185 (MRE), the CDMD Azrieli Graduate student Award (MRE), and the Whitcome Predoctoral Fellowship in Molecular Biology (MRE). Additional funding was provided by the National Institutes of Health (R01NS117912 MJS and JSC), and the Department of Defense (MD190060 MJS and SAV) and the Muscular Dystrophy Association (CSY-MGB and MJS). Author contributions were: Conceptualization, Methodology, Visualization, Project Administration – MRE MJS; Investigation – MRE, PH, SAV; Software, Data Curation – AE, FM; Formal analysis – MRE, AE, FM; Writing – Original Draft – MRE; Writing – Review and Editing – MRE, MJS; Resources – JSC, MP, PH, SAV; Supervision – MJS; Funding Acquisition – CSY, SAV, MJS.

VITA

Education

- University of California, Los Angeles (UCLA) Sep 2016 – [July 2022]
  [In progress] Ph.D., Molecular Biology (GPA: 3.74)
- University of California, Irvine (UCI) Sep 2012 – June 2016
  B.S., Honors in Biological Sciences (cum laude) (GPA 3.81)

Research Experience

- University of California, Los Angeles (UCLA) Sep 2016 – Present
  Graduate Student Researcher, Dr. Melissa J. Spencer laboratory
  Thesis: Improving the safety and efficacy of CRISPR/Cas9-based therapies for Duchenne muscular dystrophy
- King's College London, United Kingdom June 2016 – Aug 2016
  Summer internship funded by NIH-MHIRT, Dr. Maria R. Conte laboratory
  Examined RNA-protein interactions of the RNA binding protein, LARP4B
- University of California, Irvine (UCI) Sep 2014 – June 2016
  Undergraduate Researched funded by NIH-MARC, Dr. Timothy W. Bredy laboratory
  Thesis: Sex-specific patterns of the epigenome as a putative mechanism in fear-related memory
- King's College London, United Kingdom June 2014 – Aug 2014
  Summer internship funded by NIH-MHIRT, Dr. Baljinder S. Mankoo laboratory
  Investigated the molecular mechanisms involved in regulating limb muscle and limb tendon development in a wildtype mouse model
- University of California, Irvine (UCI) Apr 2013 – June 2014
  Undergraduate Researcher funded by NIH-MBRS, Dr. Luis Mota-Bravo laboratory
  Studied antibiotic resistance genes blaZ and mecA, which confer resistance to beta-lactam antibiotics, present in environmental Staphylococcus spp.

Selected Awards and Fellowships

- Whitcome Pre-doctoral Fellowship in Molecular Biology 2021 – 2022
- National Science Foundation Graduate Research Fellowship Program 2018 – 2021
- First place poster presentation for Rare Diseases category 2021
  LA Bioscience Ecosystem Summit (LA Best) Conference
- Azrieli Graduate Student Award 2021
  Established in honor of Josh Bohbot, a lifelong friend to the Center for Duchenne muscular dystrophy (CDMD)
- UCLA GBP Fellowship Incentive Program 2018 – 2021
- Ruth L. Kirschstein National Research Service Award GM007185 2017 – 2018
- Jayne Unzelman Scholarship, University of California, Irvine 2016
- Phi Beta Kappa (PBK) member inducted on June 9, 2016 2016
- First place poster presentation 2015
  Sigma Xi: The Scientific Research Society Conference under the category of Social and Behavioral Sciences
- Sigma Xi: The Scientific Research Society member 2015

- Carol Becker McGaugh Award 2015
  Center for Neurobiology of Learning and Memory, University of California, Irvine
- First place poster presentation 2015
  American Association for the Advancement of Science (AAAS) Conference under the category of developmental biology

Selected Presentations

1. Emami MR, Espinoza A, Chamberlain JS, Young CS, Villalta SA, Pellegrini M, Spencer MJ. "Characterizing AAV-mediated immune responses in a mouse model of Duchenne muscular dystrophy" 2022 American Society of Gene and Cell Therapy (ASGCT), Hybrid Meeting, May 2022, oral presentation (presented by Dr. Melissa J. Spencer).
2. Emami MR, Young CS, Pyle AD, Spencer MJ. "Identifying New AAV Serotypes with Muscle Stem Cell Tropism" 2021 LA Best – LA Bioscience Ecosystem Summit, Virtual Meeting, May 2021, poster presentation.
3. Emami MR, Young CS, Ying J, Liu X, Pyle AD, Meng H, Spencer MJ. "Polyrotaxane Nanocarriers Can Deliver CRISPR/Cas9 Plasmid to Muscle Cells to Successfully Edit the *DMD* Gene" 2019 American Society of Gene and Cell Therapy (ASGCT), Washington D.C., April 2019, poster presentation.

Publications

1. **Emami, M.R.**, Young, C.S., Ji, Y., Liu, X., Mokhonova, E., Pyle, A.D., Meng, H. and Spencer, M.J. (2019), Polyrotaxane Nanocarriers Can Deliver CRISPR/Cas9 Plasmid to Dystrophic Muscle Cells to Successfully Edit the DMD Gene. Adv. Therap., 2: 1900061. https://doi.org/10.1002/adtp.201900061
2. Li, X., Zhao, Q., Wei, W., Lin, Q., Magnan, C., **Emami, M.R.**, *et al.* The DNA modification N6-methyl-2'-deoxyadenosine (m6dA) drives activity-induced gene expression and is required for fear extinction. *Nat Neurosci* 22, 534–544 (2019). https://doi.org/10.1038/s41593-019-0339-x
3. Ratnu, V.S., **Emami, M.R.** and Bredy, T.W. (2017), Genetic and epigenetic factors underlying sex differences in the regulation of gene expression in the brain. Journal of Neuroscience Research, 95: 301-310. https://doi.org/10.1002/jnr.23886

Intellectual Property

1. Spencer MJ, Emami MR, Pyle AD, Young CS, Kohn DB. 2022. Novel AAV serotypes derived from a library screen. PCT/US2022/027919, filed May 5, 2022.
2. Spencer MJ, Young CS, Pyle AD, Emami MR. 2020. Compositions and methods for modifying dystrophin genes. PCT/US2020/027040, filed July 4, 2020.
3. Meng H, Spencer MJ, Pyle AD, Young CS, Liu X, Ji Y, Emami, MR. 2018. Multi-armed polyrotaxane platform for protected nucleic acid delivery. PCT/US2018/053221, filed September 27, 2018.

Leadership and Volunteering Experience

- Co-President of Bruin Allies for Duchenne (BAD) 2018 – Present
  Organization focused on spreading awareness of Duchenne muscular dystrophy, through fundraising and educational scientific outreach
- Social Chair: Association for Multi-Ethnic Bioscientist's Advancement 2018 – 2019
  Organization geared to creating an equitable environment to promoter the advancement and retention of PhD students by fostering a community

Chapter 1 – Introduction

Duchenne and Becker muscular dystrophy

Duchenne muscular dystrophy (DMD) is a lethal X-linked disorder and one of the most common genetically inherited diseases of children, affecting ~1:5,000 live male births per year[1]. While newborns appear relatively healthy, DMD manifests clinically during childhood and is characterized by severe and progressive muscle wasting resulting in loss of ambulation in adolescence and premature death by the third decade of life. The degeneration of skeletal muscle is slightly delayed in young children as regeneration occurs through endogenous muscle stem (satellite) cells. However, the ability of satellite cells to facilitate repair eventually fails, leading to continued degeneration of skeletal muscle and resulting in fatty and fibrotic tissue replacement of skeletal muscle[2-8]. Eventually patients with DMD develop respiratory complications and/or cardiomyopathy[9]. Improvements in medical care, mobility aids and devices, and the use of corticosteroids have slightly altered disease course, improved standard of living, and lifespan[10-15]. Nevertheless, there is currently no cure for DMD.

Becker muscular dystrophy (BMD) is an allelic form of the disease and manifests a clinically milder phenotype compared to DMD. While DMD patients are wheelchair dependent by 13 years of age, patients with BMD often remain ambulatory until 16 years of age or older[14]. DMD and BMD are caused by mutations in the *DMD* gene encoding dystrophin. Approximately 60% of mutations are deletion mutations that lead to loss of dystrophin protein[16,17]. The discrepancy in clinical phenotype between DMD and BMD is predominantly attributed to the “reading frame” hypothesis[18]. In the context

of deletion mutations, the reading frame hypothesis correlates genetic mutation to a DMD or BMD phenotype. DMD mutations tend to be out-of-frame mutations that disrupt the *DMD* reading frame and prevent expression of dystrophin protein, while BMD mutations are typically in-frame and result in the production of an internally deleted dystrophin that is semi-functional[18].

Dystrophin is a 427kDa cytoskeletal protein that localizes to the sarcolemmal (muscle) plasma membrane. Dystrophin stabilizes the sarcolemmal membrane and serves as a molecular shock absorber by linking the intracellular network of actin to the dystrophin-glycoprotein complex (DGC), which connects to the basal lamina and the extracellular matrix (ECM)[19]. For DMD patients, the absence of dystrophin destabilizes DGC components thereby preventing DGC formation and increasing the susceptibility to contraction-induced damage at the sarcolemma[20,21]. Over time, contraction-induced injury leads to abnormal calcium handling[22,23], production of reactive oxygen species (ROS)[24], muscle necrosis[21], and increased sarcolemmal permeability[25] as myoplasmic proteins leak out of skeletal muscle, namely creatine kinase (CK), which remains a diagnostic biomarker for DMD[26].

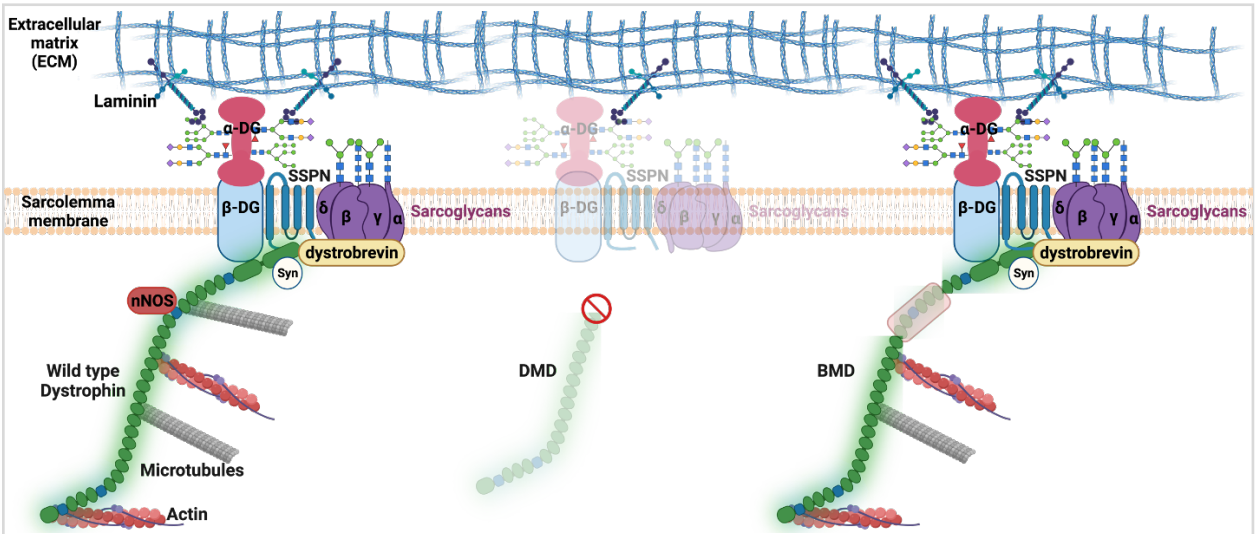

Figure 1-1: Schematic of dystrophin and the dystrophin glycoprotein complex (DGC) in wildtype, DMD, and BMD.
Wildtype dystrophin stabilizes the sarcolemmal membrane by linking the intracellular acting cytoskeleton to the DGC, which connects to the basal lamina and extracellular matrix (ECM). DMD mutations results in lack of dystrophin and loss of DGC assembly at the sarcolemmal membrane. The DGC is composed of α- and β-dystroglycan (DG), α-, β-, γ-, and δ- sarcoglycans, sarcospan (SSPN), dystrobrevin, syntrophins (Syn), and neuronal nitric oxide synthase (nNOS). Depending on the mutation, BMD dystrophin will retain some of the WT dystrophin's function. Created with Biorender.com.

The dystrophin protein consists of an actin-binding domain at the N-terminus, a central rod-domain containing 24 spectrin-like repeats with 4 hinge regions, a cysteine-rich region and a C-terminus (**Figure 1-1**). The central rod domain contains an additional actin binding domain, a microtubule binding motif through spectrin repeats 20-23, and neuronal nitric oxide synthase (nNOS) binding motif with spectrin repeats 16 and 17[27-29]. The cysteine-rich region serves as an anchoring site with β-dystroglycan and the C-terminus binds with dystrobrevin and syntrophins[30,31].

Interestingly, there are portions of the central rod domain in the dystrophin protein that are partially redundant and somewhat dispensable. This is strongly supported by clinical evidence in BMD patients with in-frame deletion mutations encoding the central rod domain[14,16]. One of the clinically mildest BMD mutations

consists of an in-frame deletion of exons 45-55 encoding part of the central rod domain, spectrin repeats 17-22. Clinical phenotyping studies of BMD patients with an exon 45-55 deletion revealed that most of these BMD patients remain ambulatory and asymptomatic into their 50-60s[32-36]. However, this mild phenotype in BMD patients with an exon 45-55 deletion contrasts to the clinical phenotype of BMD patients with exon 45-47 deletion, encoding for part of the spectrin repeats 17-18, which have a more severe phenotype and become wheelchair dependent in their 30s[33,37]. The divergence in clinical phenotype is likely due to improper phasing of the spectrin repeats (**Figure 1-2**). eDystrophin[38] modeling of an exon 45-55 deletion is predicted to maintain phasing whereas an exon 45-47 deletion is out of phase (**Figure 1-2**).

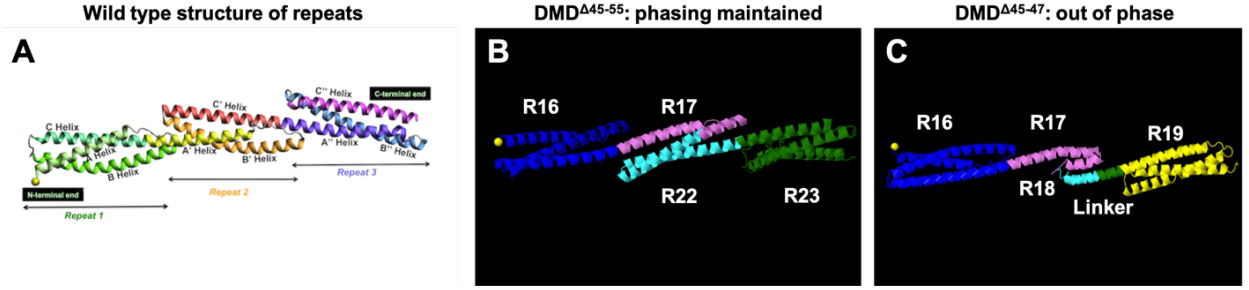

Figure 1-2: Predicted structure of a portion of dystrophin's rod domain modeled using eDystrophin[38].

A) Spectrin-like repeat structure of wildtype dystrophin.
B) Model of an exon 45-55 deletion that is predicted to maintain phasing of spectrin triple helix with repeat 17 (R17) in phase with repeat 22 (R22).
C) Model of an exon 45-47 deletion that is predicted to be out-of-phase with repeat 17 (R17) and repeat (R18), losing the spectrin triple helix.

In addition, a great body of work has empirically determined that ~70% of the *DMD* gene can be deleted and when overexpressed, the truncated dystrophin protein can significantly improve muscle function in mice and canine animal models[39-44]. These highly truncated dystrophin species are referred to as mini- and micro-dystrophins and

are currently being tested in ongoing clinical trials for DMD as a gene replacement therapy (clinicaltrials.gov: NCT03368742, Solid Biosciences; NCT03375164, Nationwide Children's Hospital; NCT03362502, Pfizer).

Existing therapeutic strategies for DMD

To date, there are currently two main classes of FDA approved drugs for DMD: i) Emflaza and ii) antisense oligonucleotides. There is currently one FDA approved corticosteroid, Emflaza (aka deflazacort) is a corticosteroid that reduces inflammation in skeletal muscle tissue[45,46]. Although Emflaza is not a cure for DMD, it delays the loss of ambulation by ~2 years, delays the onset of cardiomyopathy, and improves pulmonary function[45,46]. The benefits of long-term steroid treatment outweigh the tolerable side effects, namely, obesity, cataracts and shorter height[47]. The second class of FDA approved drugs relies on delivering an antisense oligonucleotide to induce skipping of mutant exons during pre-mRNA processing in order to restore the *DMD* reading frame[48]. To date, there are four FDA approved exon skipping drugs targeting exons 51 (Exondys 51), 53 (Vyondys 53 and Viltepso), and 45 (Amondys 45), and with applicability to ~13%, 8% and 9% of all DMD patients, respectively (**Table 1-1**). Exondys 51, Vyondys 53, Viltepso and Amondys 45 successfully demonstrated an increase of ~1%, ~1%, ~4%, and ~1.7% dystrophin by Western blot, respectively[49-55]. Despite the low levels of dystrophin by Western blot, functional improvement in timed function tests have been reported[50-55], with the exception of Amondys 45, which is still ongoing in Phase III and expected to conclude in 2024. In addition, mouse studies have

shown that low levels of dystrophin can improve motor function, suggesting modest levels of dystrophin are needed for functional improvement[56-58].

Table 1-1: FDA approved exons skipping drugs for DMD.

Name	Target Exon	Dystrophin levels (%)	Applicability	Year of approval
Exondys 51	51	~1%	13%	2016
Vyondys 53	53	~1%	8%	2019
Viltepso	53	~4%	8%	2020
Amondys 45	45	~1.7%	9%	2021

Another potential therapeutic therapy for DMD was briefly discussed earlier and relies on using adeno-associated viruses (AAVs) to deliver a highly truncated version of the *DMD* gene, referred to mini- and micro-dystrophin[59]. There are three ongoing clinical trials designed to determine safety and tolerability after systemic delivery to skeletal muscle (clinicaltrials.gov: NCT03368742, Solid Biosciences; NCT03375164, Nationwide Children's Hospital; NCT03362502, Pfizer).

CRISPR/Cas9 as a gene editing therapy for DMD

Many therapeutic strategies for DMD aim to re-frame the *DMD* gene, thereby converting an out-of-frame DMD mutation into an in-frame BMD mutation. Early gene editing systems include Transcription Activator-Like Effector Nucleases (TALENs) and Zinc-Finger Nucleases (ZFNs), which are difficult to design and can be expensive[60-62]. Alternatively, the clustered regularly interspaced short palindromic repeats and CRISPR-associated protein 9 (CRISPR/Cas9) system is inexpensive and user-friendly. In brief, the CRISPR/Cas9 system employs a guide RNA (gRNA) which directs the Cas9 endonuclease to a specific site in the genome, generating a double stranded DNA break (DSB)[63-65]. The cell can repair DSBs through the endogenous DNA repair

machinery via non-homologous end joining (NHEJ) or through homology directed repair (HDR) using donor template DNA in cycling cells[66].

CRISPR/Cas9-mediated reframing of the human *DMD* and murine *Dmd* gene has been validated successfully and abundantly *in vitro* using primary human DMD myoblasts[62,67], DMD-derived induced pluripotent stem cells (iPSCs)[68,69], mouse myoblasts[70], and mouse muscle stem cells[71,72]. Additionally, CRISPR/Cas9-mediated gene editing has been extensively demonstrated *in vivo* in *mdx* and *mdx*^{4cv} dystrophic mouse models[73-76], humanized dystrophic mouse models containing the human *DMD* gene with an out-of-frame exon 45 deletion mutation[77], dystrophic canine models with an exon 50 deletion mutation[78] or exon 51 deletion mutation[79], and dystrophic pigs with an exon 52 deletion mutation[80]. Although these studies highlight the various CRISPR-based strategies that can be employed to treat DMD, strategies centered on achieving safe and efficient delivery of CRISPR/Cas9 *in vivo* remains a considerable challenge (discussed below).

Nanoparticle-mediated delivery of CRISPR/Cas9

In vivo delivery of CRISPR/Cas9 remains a significant hurdle for neuromuscular diseases, such as DMD, in which all muscles are affected, a tissue that comprises ~40% of the total body mass. Efficient delivery and gene editing with the CRISPR/Cas9 system requires co-delivery of the gRNA and the Cas9 endonuclease within the same cell. These components may be co-delivered as a plasmid encoding Cas9 and gRNA, Cas9 mRNA and gRNA, or as a ribonucleoprotein (RNP) in which the Cas9 protein is pre-assembled with the gRNA (**Figure 1-3**). Non-viral carries, namely nanoparticles,

represent a promising vehicle for co-delivery of the CRISPR/Cas9 system in either format to skeletal muscle and muscle stem cells in order to achieve a sustainable therapy for DMD. Nanoparticles are typically nanometers in size and can be designed for colloidal stability, tissue specificity (e.g., to skeletal muscle and muscle stem cells), biodegradability and biocompatibility depending on the materials used for nano synthesis. Moreover, nanoparticles are largely non-immunogenic making them suitable for repeat dosing[81]. Currently, there are over 50 FDA approved nanomedicines with more than 40 in ongoing clinical trials[82-84]. The FDA approved nanomedicines and nanomedicines being tested in clinical trials are mainly for cancer immunotherapy.

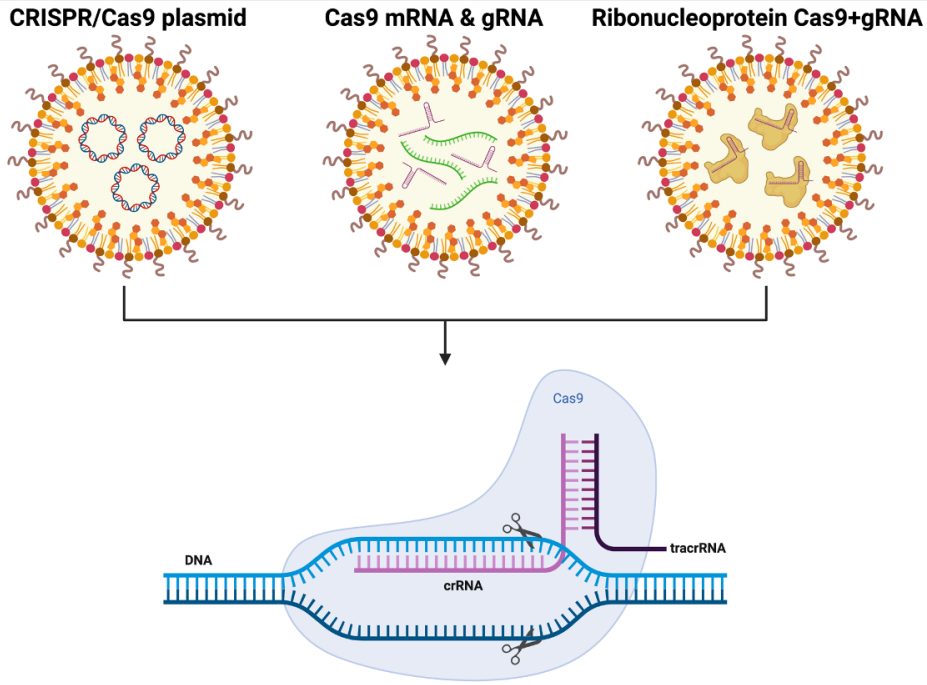

Figure 1-3: Non-viral nanoparticle-mediated delivery of CRISPR/Cas9 can be achieved in three formats.
Efficient delivery and gene editing with the CRISPR/Cas9 system requires co-delivery of the gRNA and the Cas9 endonuclease within the same cell. These components may be co-delivered as a plasmid encoding Cas9 and gRNA (left), Cas9 mRNA and gRNA (center), or as a ribonucleoprotein (RNP, right) in which the Cas9 protein is pre-assembled with the gRNA. Created with Biorender.com.

Nanoparticles composed of lipids[85-94], DNA nanoclews[95], cationic polymers[70,96-98], mesoporous silica[99], gold[100-103], exosomes[104,105], metal-organic frameworks (MOFs)[106] and metal-organic cages (MOCs)[107] have been used to deliver CRISPR/Cas9 *in vitro* and/or *in vivo*. The majority of *in vivo* nano-CRISPR studies rely on local and targeted injection to achieve gene editing, while systemic delivery of nano-CRISPR has been achieved for the lung[89,108], liver[86,87,90,92,93,108], brain[85] and tumors[85,97]. To date, there are three studies that have shown successful nano-CRISPR delivery and gene editing of the murine *Dmd* gene in skeletal muscle using gold[101] or lipid[88,108] nano-formulations. Nevertheless, all the three studies relied on intramuscular injections to reframe the murine *Dmd* gene resulting in ~1% and ~4% dystrophin by Western blot for the gold and lipid nano-formulations, respectively. Current studies have not achieved systemic delivery of nano-CRISPR to skeletal muscle and/or muscle stem cells, yet additional exploration and optimization may position nanocarriers as a favorable vehicle for systemic gene therapies.

AAV-mediated delivery of CRISPR/Cas9 and immunological considerations of AAV and Cas9

An alternative vehicle for CRISPR/Cas9 delivery, and one that is regularly employed, is adeno-associated viruses (AAVs). AAVs are small (~22nm) viruses with a limited packaging size (~4.7kb) and with relatively low immunogenicity when administered at lower doses[109,110]. Importantly, AAVs are naturally occurring viruses with distinct serotypes capable of tissue specific targeting[111,112], making AAVs a promising vehicle for gene therapies, such as DMD in which all muscles are affected.

To date, systemic delivery of AAV-CRISPR to skeletal muscle using serotypes 6, 8, 9, and rh74 have demonstrated efficient CRISPR/Cas9-mediated restoration of dystrophin in dystrophic mice, canine, and pig models[71,73-75,78-80,113-116].

The success of systemic AAV-CRISPR delivery faces additional challenges that will likely delay clinical translation for DMD. First, AAV-CRISPR inefficiently targets muscle stem cells and three studies independently demonstrated MuSC gene editing efficiencies of 1-3% in the *mdx* model[71,117,118]. Additionally, two separate studies demonstrated that a single administration of AAV-CRISPR is unable to sustain dystrophin expression over the life-time of a mouse, and thus, efficient muscle stem cell targeting is likely required in order to achieve a long-lasting therapy[116,119]. Second, pre-existing immunity in the form of humoral and/or cellular responses prevent AAV-CRISPR administration as AAV and Cas9 are both naturally occurring. It is estimated that at least 50% of the general population has pre-existing immunity to AAV and 60% of the population has pre-existing immunity to Cas9[120-123]. One study found that AAV-CRISPR gene editing was compromised in a mouse model with pre-existing immunity to Cas9, leading to cytotoxic CD8 T cells in the liver, liver hepatotoxicity, and a significant reduction of CRISPR-corrected cells[124]. Third, AAV-CRISPR would be limited to a single administration due to antibody formation and activation of antigen reactive T lymphocytes against AAV and/or Cas9, which will prohibit a second dose. Humoral antibody and cellular T cell responses against the AAV capsid has previously been reported following a single administration of AAV for hemophilia A and B gene transfer studies[125,126]. Moreover, one study observed AAV-CRISPR-mediated immunogenicity after a single administration resulting in muscle inflammation, loss of CRISPR/Cas9 viral

genomes, antibody formation against Cas9, activation of Cas9-specific T cells, and production of inflammatory cytokines[79]. Fourth, AAV DNA has been shown to persist for years as an episome in skeletal muscle tissue following AAV gene therapy[127], which will increase the likelihood for Cas9-mediated off-target effects. Long-term expression of Cas9 may exacerbate humoral and cellular immune responses, posing additional safety concerns over AAV-CRISPR-based therapies. One strategy to overcome persistent Cas9-encoded AAV DNA is to co-deliver AAV-CRISPR with an inhibitor of Cas9, termed anti-CRISPRs[128], however, this approach introduces additional foreign proteins that will likely worsen immune responses and anti-CRISPRs only inhibit and do not remove Cas9 *in vivo*. A second and more promising strategy centers on inactivating Cas9-encoded AAV DNA using a gRNA targeted against the Cas9 transgene and driven under a weaker promoter, such as 7sk, which successfully removes Cas9 protein *in vivo* after AAV-CRISPR delivery[129,130]. Fifth, in the absence of pre-existing immunity, the innate immune system has been shown to detect unmethylated cytosine-phosphate-guanine (CpG) AAV DNA via toll-like receptor 9 (TLR9) in human and mouse plasmacytoid dendritic cells (pDCs) eliciting type I interferon responses[131]. Strategies to overcome TLR9 sensing CpGs include depleting AAV DNA of CpGs to evade detection *in vivo* and integrating TLR9 inhibitory sequences in the AAV DNA vector, which similarly evades TLR9 detection[132,133].

Lastly, AAV-CRISPR often requires a dual vector system since AAV has a small payload capacity (~4.7kb), which is too small to carry SpCas9 (~4kb), regulatory sequences and the gRNAs in a single vector (**Figure 1-4**). A dual vector system often requires higher viral doses in order to achieve efficient dystrophin restoration *in vivo*,

however, higher viral doses increase the likelihood of AAV-induced toxicities[79,134]. The need for higher vector doses also poses significant challenges for large scale AAV production and scalability[135]. Many of the aforementioned concerns are being investigated in ongoing studies to improve the safety and efficacy of AAV-CRISPR *in vivo*.

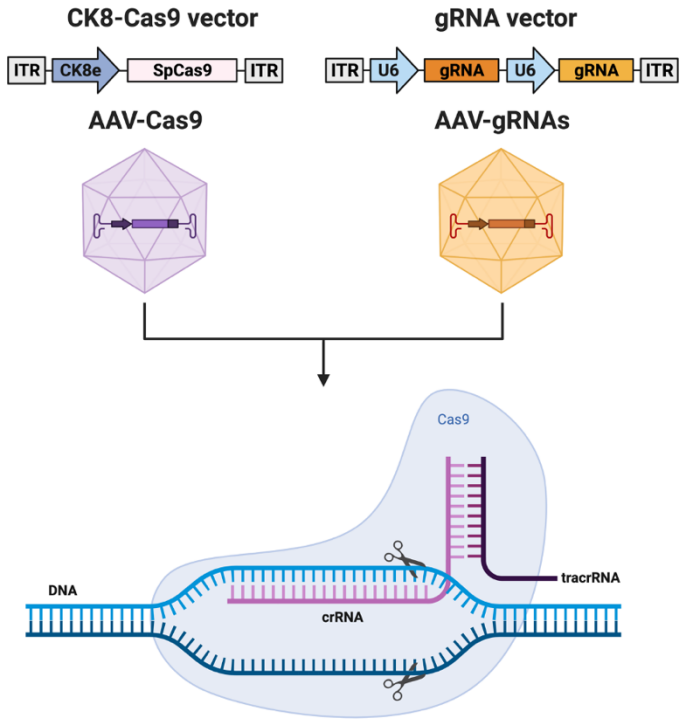

Figure 1-4: AAV-mediated delivery of CRISPR/Cas9 using a dual vector system. Due to the limited packaging size of AAV (~4.7kb), efficient delivery and gene editing with the CRISPR/Cas9 system requires a dual vector approach. One AAV vector encodes the Cas9 endonuclease driven by the muscle-specific promoter, CK8e (left). The second AAV vector encodes the gRNA(s) for directing Cas9-mediated cleavage (right). Successful CRISPR/Cas9 gene editing requires co-delivery of the Cas9 and gRNA AAV vectors within the same cell. Created with Biorender.com.

Significance

Current treatments for Duchenne muscular dystrophy are limited, and have a moderate impact on disease course. Thus, there remains a significant unmet clinical need for innovative and efficacious therapies for DMD. The overarching aim of this research was to develop strategies that would improve the safety and efficacy of CRISPR/Cas9-based therapies for neuromuscular disorders.

Systemic delivery of CRISPR/Cas9-mediated gene therapies remain a substantial challenge for neuromuscular disorders, such as DMD, in which muscles comprise ~40% of the total body mass. While gene-editing strategies are expected to alter disease course, achieving systemic delivery poses additional obstacles. We successfully applied CRISPR/Cas9 delivery *in vitro* using polymer-based nanoparticles. While these nanocarriers performed well *in vitro*, they were not successful after systemic delivery *in vivo*. In order to improve nanoparticle-mediated delivery to muscle and muscle stem cells, we screened an AAV peptide display library for potential peptide motif ligands that may mediate muscle entry. These studies revealed that systemic delivery of CRISPR/Cas9 is significantly more efficient when AAV is used as the carrier compared to nanoparticles. However, AAV-CRISPR inefficiently targets MuSCs, and a single administration of AAV-CRISPR is unable to sustain life-long dystrophin expression. Therefore, we screened an AAV peptide-display library to identify novel AAV variants highly enriched in both muscle stem cells and skeletal muscle. Finally, because AAV-CRISPR is limited to a single administration due to its immunogenicity, we sought to identify immune effectors that arise after a single and double injection of AAV that may enable the development of specific immunosuppressive regimens to achieve AAV redosing. We comprehensively characterized AAV-CRISPR-mediated immune responses, which correlated with immune responses reported in ongoing DMD clinical trials. Ultimately, this work offers the potential to enhance CRISPR/Cas9 delivery to MuSC that may serve as a life-long therapy while simultaneously examining AAV-CRISPR-mediated immune responses to enable the identification of targetable genes,

pathways, or immune cell subtypes that may facilitate the development of mitigation strategies to circumvent adverse AAV-induced immune responses.

Chapter 2 – Polyrotaxane Nanocarriers can Deliver CRISPR/Cas9 Plasmid to Dystrophic Muscle Cells to Successfully Edit the DMD Gene

Abstract

Gene editing with clustered regularly interspaced short palindromic repeats and CRISPR-associated protein 9 (CRISPR/Cas9) has shown promise in models of Duchenne muscular dystrophy (DMD); however, non-viral strategies to deliver CRISPR to muscle have not been widely explored or optimized. Most studies have relied on viral vectors, which are likely limited to single dosing due to their immunogenicity, thus reducing their therapeutic potential. Therefore, there is a need to develop non-viral approaches that allow for delivery and repeat dosing of CRISPR/Cas9 therapies to skeletal muscle. Here, biocompatible multi-arm polyrotaxane (PRX) nanocarriers, are iteratively optimized for packaging large plasmid DNA for delivery to muscle cells. The PRXs are optimized by addition of a disulfide-responsive linker that enhances plasmid release. Furthermore, conjugation of peptides leads to quicker uptake and improved transfection efficiency in humanized dystrophic muscle cells in vitro. Finally, in vitro delivery of PRXs complexed with a CRISPR/Cas9 platform demonstrates effective deletion of DMD exons 45–55, a therapeutic strategy with potential to restore the reading frame for half of DMD patients. This work represents the first PRX platform that is optimized and designed for delivery of large plasmid DNA, such as CRISPR/Cas9, to dystrophic muscle cells.

Introduction

Gene editing has wide-ranging possibilities for improving human life, such as modifying crop and livestock genomes, creating novel model organisms for research, and correcting disease mutations[136]. Early gene editing systems such as Transcription Activator-Like Effector Nucleases (TALEN) and Zinc-Finger Nucleases (ZFN) are effective, but are cumbersome in design and can be expensive to implement[137]. On the other hand, clustered regularly interspaced short palindromic repeats and CRISPR-associated protein 9 (CRISPR/Cas9) is easier to exploit and relatively inexpensive. The CRISPR/Cas9 system utilizes a guide RNA (gRNA) which targets the Cas9 endonuclease to a specific site in the genome which creates a double stranded DNA break (DSB)[63-65]. The cell can repair DSBs through the endogenous DNA repair machinery, non-homologous end joining (NHEJ), or through homology directed repair (HDR) using template DNA in cycling cells[66].

The application of CRISPR/Cas9 offers enormous possibilities for treating monogenic diseases such as the muscular dystrophies, which are a group of inherited muscle disorders. One of the most devastating lethal muscular dystrophies is Duchenne muscular dystrophy (DMD). DMD is caused by out-of-frame mutations in the *DMD* gene resulting in lack of the dystrophin protein, which leads to progressive muscle wasting and premature death[138]. Thus, a promising therapeutic approach for Duchenne is to restore the reading frame by converting an out-of-frame DMD mutation into an in-frame mutation, mimicking the milder, allelic disease, Becker muscular dystrophy[139]. This approach allows production of an internally deleted but functional dystrophin protein. We have developed a CRISPR/Cas9 platform with the intent to permanently restore the

DMD reading frame for mutations within this region[68,77]. The platform (hereafter referred to as CRISPR DMD$^{\Delta 45\text{-}55}$) encompasses a single pair of gRNAs that flank *DMD* exons 45-55, generating an in-frame, internally deleted protein after Cas9 cutting and NHEJ. In Becker patients, an exon 45-55 deletion is associated with one of the mildest clinical phenotypes, with some patients still asymptomatic into their 60s[32-36]. This region also encompasses a hotspot of DMD patient mutations and would be applicable to ~50% of the patient population[32,33]. Proof-of-principle that CRISPR DMD$^{\Delta 45\text{-}55}$ can restore dystrophin protein was demonstrated *in vitro* and after local delivery to skeletal muscle in a humanized dystrophic hDMD del45 mdx mouse model *in vivo*[68,77].

Delivery of CRISPR/Cas9 to muscle has been accomplished *in vitro* and *in vivo* via both viral and non-viral strategies. Viral vectors, such as adeno-associated virus (AAV), have been used to deliver CRISPR/Cas9 to various tissues *in vivo* including muscle[140]. However, since AAV elicits an immune response, it is likely that AAV can only be delivered one time, unless additional procedures are implemented, thus compromising the efficacy of CRISPR-based therapies[141]. Additionally, it has been reported that up to 70% of patients could have pre-existing immunity to AAV, which may limit its efficacy as a therapy[121]. Moreover, the AAV vector genome has been reported to persist as an episome for years in post-mitotic muscle[141,142]. This sustained expression of bacterially-derived Cas9 has the potential to enhance off-target activity or to prompt an immune response against Cas9 and the muscle[127,143]. Lastly, because the AAV payload capacity is limited (~4.7kb), it is challenging to fit SpCas9 (~4kb) and gRNAs in the same vector, thus often necessitating a dual vector system, which effectively cuts the maximum dose in half[144]. Non-viral carriers, such as nanoparticles,

can overcome the challenges associated with AAV delivery and thus represent a promising alternative for CRISPR delivery[145]. Depending on the type of material used, nanocarriers have the ability to carry different types of cargo and can be chemically modified for colloidal stability, biodegradability, biocompatibility, and tissue specificity. In addition, they are largely non-immunogenic and are suitable for repeat dosing[81]. Nanoparticles composed of lipids, DNA (nanoclews), gold, cationic polymers, and metal-organic frameworks (MOFs) have been used to deliver CRISPR *in vitro* and *in vivo*, although reports of nanocarrier mediated delivery of CRISPR to skeletal muscle have been minimal[85-87,89,91-96,98,101-103,106,146]. One study achieved delivery of CRISPR/Cas9 to murine muscle cells *in vitro* using gold nanoparticles. They also carried out local intramuscular injection *in vivo* with an efficiency of less than 1%[101]. However, the translatability of this approach as a DMD therapy is low, as it did not utilize systemic delivery[101].

Additional studies have described nano-mediated approaches to deliver other types cargo to skeletal muscle. Liposomes, polymerosomes, polyethyleneimine (PEI), poly(methyl methacrylate) (PMMA), atelocollagen, perfluorocarbons, and silver nanoparticles have been used to deliver antisense oligonucleotides, rapamycin, siRNA against myostatin, or other genes to muscle[91,147-161]. However, these reports have been fairly limited, mainly showing proof-of-concept without much optimization and it is unclear whether the nanoparticles could be modified to carry a large payload, such as CRISPR/Cas9.

The current work describes the iterative optimization of polyrotaxane (PRX) nanoparticles and demonstrates that PRXs can deliver a large plasmid carrying

CRISPR DMD$^{\Delta 45\text{-}55}$ to dystrophic muscle cells *in vitro*. PRX is characterized as a mechanically interlocked molecule containing a polymer, such as a polyethylene glycol (PEG) backbone, with macrocycles, such as cyclodextrin rings, threaded onto the polymer and stabilized by bulky end groups[162]. The addition of cationic charge on the macrocycles allows for effective complexation of nucleic acid mediated by electrostatic interactions. We custom-designed a 4-arm PRX nanocarrier that was engineered for improved circulation and pharmacokinetics (PK) following intravenous (IV) injection[163]. This report demonstrates iterative improvements on the 4-arm PRX design to enhance plasmid delivery to primary muscle cells derived from a novel humanized dystrophic mouse model, which contains an out-of-frame human *DMD* gene[77]. Engineering the 4-arm PRX with a redox-sensitive disulfide linker improves plasmid release and peptide conjugation enhances the rate and abundance of nanoparticle uptake, which leads to improved gene delivery *in vitro*. The data also demonstrate proof-of-concept that 4-arm PRX nanoparticles can deliver CRISPR/Cas9 to muscle cells and achieve a CRISPR-mediated deletion of *DMD* exons 45-55. This highlights the potential of using 4-arm PRXs for a CRISPR-based therapy for DMD.

Materials and Methods

Mice

All animal care and work were conducted under protocols approved by the UCLA Animal Research Committee in the Office of Animal Research Oversight. hDMD del45 mdx mice were generated and genotyped as described[77].

Cell culture

Primary hDMD del45 mdx myoblasts were obtained from 11 – 13 day old pups by dissociation of muscle tissue using a 1:1 mixture of 1.5mg/mL dispase (neutral protease, Worthington) and 1600U/mL collagenase II (Worthington) in PBS at 200µl per 100mg tissue. Muscles were minced, then incubated at 37°C with slow agitation for 30 mins. Fibroblasts were removed by repeatedly pre-plating. Myoblasts were cultured on entactin-collagenIV-laminin cell attachment matrix (ECL, EMD Millipore) and maintained in F-10 HAM (Sigma) with 20% fetal bovine serum (FBS, Thermo Fisher), 5ng/mL basic fibroblast growth factor (bFGF, Promega) and 1% penicillin/streptomycin (P/S, Thermo Fisher). Myoblasts were differentiated to form myotubes (at >80% confluence) in DMEM (Thermo Fisher) supplemented with 2% horse serum (Thermo Fisher), 1% insulin-transferrin, selenium (ITS, Thermo Fisher) and 1% P/S on Matrigel® basement membrane matrix (Corning). C2C12 murine myoblasts were maintained in DMEM supplemented with 20% FBS and 1% P/S. C2C12 myoblasts were differentiated to form myotubes (at >80% confluence) in DMEM supplemented with 5% horse serum and 1% P/S. B16 murine melanoma cells were maintained in DMEM supplemented with 10% FBS and 1% P/S.

CRISPR plasmid

gRNAs for the exon 45-55 deletion (44C4, 55C3) from[68] were cloned into px333 (Addgene 64073, Andrea Ventura[164]) in tandem using BbsI (New England BioLabs) and BsaI (New England BioLabs). Hereafter, px333 44C4+55C3 refers to the CRISPR plasmid encoding SpCas9 and the two gRNAs.

Chemicals

α-Cyclodextrin (α-CD), triethylamine (TEA), Benzyloxycarbonyl-L-tyrosine (Z-L-Tyr), Benzotriazol-1-yl-oxy-tris(dimethylamino) phosphonium hexafluorophosphate (BOP), 1-hydroxybenzotriazole (HOBt,) N,N-diisopropylethylamine (DIEA), 1,1′-carbonyldiimidazole (CDI), N,N-dimethylethylenediamine (DMAE), 2-aminoethanethiol, 1,4-dithiothreitol (DTT) dimethylformamide (DMF), dimethyl sulfoxide (DMSO) were purchased from Sigma Aldrich. Four-arm PEG tetra-amine hydrochloride salt (10kDa) and linear PEG-diamine hydrochloride salt (3.5kDa) were purchased from Jen Kem Technology. Di-orthopyridyl disulfide PEG (PEG-diOPSS) (3.5kDa) were purchased from Creative PEGworks. NHS-fluorescein and 4-succinimidyloxycaronyl-alpha-methyl-α(2-pyridyldithio)toluene (SMPT) were purchased from Thermo Fisher. 2-(Dimethlamino ethanethiol) hydrochloride was purchased from Santa Cruz Biotechnology. Pyridyldithiol-cysteamine was synthesized as previously described[165]. Amicon Ultra-4 Centrifugal Filter Units (MWCO=10kDa) were purchased from Millipore.

PRX synthesis

For the pristine linear PRX the following steps were completed as previously reported[166]. (i) Linear PEG-diamine was added to aqueous saturated solution of α-CDs to form a polypseudorotaxane inclusion complex. (ii) The polypseudorotaxane ends were blocked with a large blocking group, Z-L-Tyr, by mixing the inclusion complex with Z-L-Tyr, BOP reagent, HOBt and DIEA in DMF. (iii) The α-CDs in the polyrotaxane were

modified with positively charged amine groups by reaction with DMAE and CDI in DMSO.

For the disulfide linear PRX the following steps were completed as previously reported[167]. (i) Linear PEG di(OPSS) was mixed with 2-aminoethanethiol to generate a diamino-PEG with disulfide linkages at both ends (SS-PEG-diamine). (ii) The SS-PEG-diamine was added to aqueous saturated solution of α-CDs to form an SS-polypseudorotaxane inclusion complex. (iii) The polypseudorotaxane ends were blocked with Z-L-Tyr, as done for the pristine linear PRX. (iv) The α-CDs in the SS-polyrotaxane were modified with positively charged amine groups by reaction with DMAE and CDI in DMSO.

For the pristine 4-arm PRX the steps were performed as we described previously[163]. (i) Two arms of a 4-arm PEG tetra-amine were selectively blocked by NHS-Fluorescein. (ii) The 4-arm PEG diamine was then added to aqueous saturated solution of α-CDs to form a 2/4-arm polpypseudorotaxane inclusion complex. (iii) The amino ends of 2/4-arm polypseudorotaxane were blocked with Z-L-Tyr as described above. (iv) The α-CDs in the 2/4-arm polyrotaxane were modified with positively charged amine groups by reaction with DMAE and CDI in DMSO.

For the disulfide 4-arm PRX the following steps were carried out. (i) Two arms of a 4-arm PEG tetra-amine polymer were selectively blocked with NHS-Fluorescein as mentioned above. (ii) The 4-arm PEG diamine was added to aqueous saturated solution of α-CDs to form a 2/4-arm polypseudorotaxane inclusion complex. (iii) The amino ends of 2/4-arm polypseudorotaxane were blocked with Z-L-Tyr as described above. (iv) The α-CDs in the 2/4-arm polyrotaxane were further functionalized with pyriyldithiol groups

by reacting with pyridyldithiol-cysteamine and CDI in DMSO, followed by precipitation in diethyl ether, and washed sequentially in excessive acetone and methanol. (v) The α-CDs with cleavable positively charged amine groups were generated by thiol-exchange reaction between pyridyldithiol-4-arm polyrotaxane and dimethlamino ethanethiol in aqueous solution. The resulting disulfide 4-arm PRX was concentrated with DI water in Amicon centrifugal filter to remove excessive pyridyldithiol-cysteamine.

For peptide conjugation to 4-arm PRX the following steps were carried out. (i) Two arms of a 4-arm PEG tetra-amine polymer were selectively blocked after a reaction with SMPT in DMF at a fixed feed ratio (4-arm PEG:SMPT=1:2, molar ratio). (ii) The 4-arm PEG diamine-SMPT was added to aqueous saturated solution of α-CDs to form a 2/4-arm polypseudorotaxane-SMPT inclusion complex. (iii) The amino ends of 2/4 –arm polypseudorotaxane-SMPT were blocked with Z-L-Tyr as mentioned above. (iv) The α-CDs in the 2/4-arm polyrotaxane were modified with positively charged amine groups by reaction with DMAE and CDI in DMSO as done for pristine 4-arm PRX. (v) Peptides modified with cysteine and glycine spacers were conjugated to the ends of free PEG chains in DMAE-4-arm polyrotaxane-SMPT via thiol exchange chemistry. The peptide sequences are as follows: NCAM ASKKPKRNIKAGGC, PipB RXRRBRRXRRBRXBGGC[168,169]. Thiol groups from cysteine were introduced on the C-terminus of the peptides to facilitate conjugation. An oligo glycine spacer was included at both ends of the functional sequence so that conjugation would not interfere with the binding efficiency. The modified peptides were mixed with DMAE-4-arm polyrotaxane-SMPT at a molar ratio of 5:1 in aqueous solution and reacted for 2 hrs at room temperature. The excessive peptide and pyridine-2-thione was removed via repeated

concentration with DI water in Amicon centrifugal filter. The pyridine-2-thione was collected and quantified by UV-vis spectroscopy to determine the successful peptide conjugation.

The synthesis schemes for PRX formulations (Figures **2-2** and **2-19** and **2-15**)[166,167]. For the list of average CD numbers per polymer and cationic charge density (**Table 2-1**), PRX samples were dissolved in d_6-DMSO or deuterated water and examined on an AV400 spectrometer (Bruker). The integration of C1(H) peak (δa) from α-CD and -CH_2CH_2O- peak (δf) from PEG were used to calculate the total number of α-CD per PRX polymer. The cationic charge density was determined via the integration of -$N(CH_3)_2$ peak (δg) from DMAE and C1(H) peak (δa) from α-CD in ^{1}H-NMR spectra as we reported previously[163]. For peptide conjugated 4-arm PRX, UV-Vis spectroscopy was used to confirm peptide conjugation by the production of pyridine-2-thione (**Figure 2-16**). The enhanced absorbance at 340-380nm demonstrated successful peptide conjugation.

Physiochemical characterization and plasmid loading of PRX formulations

CRISPR plasmid was complexed with different PRXs at various N/P ratios in aqueous solution with an equivalent plasmid concentration of 1μg/mL. The size and ζ-potential of plasmid complexed with different PRXs were measured by ZETAPALS (Brookhaven Instruments Corporation). DNA gel retardation assay was performed with precast agarose gel (Sigma Aldrich). Samples (equivalent to 100ng plasmid) were loaded in gel loading buffer (Sigma Aldrich), ran in TBE buffer at 150V for 30 mins, followed by visualization on gel imager (MultiImage II AlphaImager HP, Alpha Innotech).

To demonstrate the reduction-responsive dissociation of plasmid, CRISPR plasmid laden disulfide 4-arm PRXs were incubated with 5mM DTT solution for 30 mins, before assessing size or DNA gel electrophoresis. The morphology of plasmid laden PRX was visualized by atomic force microscopy (AFM). Plasmid laden PRX was directly added to mica substrate (1cm×1cm), and free plasmid was premixed with 5mM $MgCl_2$-HEPES buffer before addition to mica substrate. The equivalent concentration of plasmid was 0.2μg/mL. The samples were dried with nitrogen gas and imaged on Bruker Dimension FastScan AFM.

PRX delivery in vitro

Myoblasts were seeded at 1.2 x 10^5 cells/cm^2 for growth conditions or 1.7 x 10^5 cells/cm^2 for differentiation where the media was changed to differentiation media the following day. PRX complexed with a pCSCMV:tdTomato reporter plasmid (Addgene 30530, Gerhart Ryffel[170]), or px333 44C4+55C3 CRISPR plasmid (see above) was added to the cells at various PRX to plasmid (N/P) ratios determined empirically and as follows: pristine linear PRX to plasmid: 10:1, disulfide linear PRX to plasmid: 5:1, pristine 4-arm and disulfide 4-arm PRX to plasmid: 3:1, peptide conjugated 4-arm PRX to plasmid: 5:1. For uptake and plasmid dissociation studies, PRXs were conjugated with FITC and plasmid labeled with Cy3 using LabelIT® Tracker kit (Mirus Bio). Imaging for uptake and lysosomal studies was done at time points between 40 mins and 24 hrs using a confocal microscope (SP8-SMD, Leica). Imaging for reporter expression was done at time points between 1 day and 7 days using an Axio Observer Z1 microscope (Zeiss) and 5 random images per well were taken for quantification in ImageJ software

(NIH). For CRISPR delivery, cells were harvested at days 5, 7 or 14 and pelleted for genomic DNA extraction using the Quick-gDNA miniprep kit (Zymo Research) and analyzed with the deletion PCR described below.

PRX delivery in vivo

PRXs were complexed with px333 44C4+55C3 CRISPR plasmid (see above) based on the following (N/P) ratios: 5:1, pristine 4-arm and disulfide 4-arm PRX to plasmid: 3:1, and peptide conjugated 4-arm PRXs to plasmid: 5:1. px333 44C4+55C3 CRISPR plasmid was labeled with Cy3 using LabelIT® Tracker kit (Mirus Bio). hDMD del45 mdx mice were intravenously (i.v.) dosed with 100μg of plasmid complexed with PRX. Muscles and off-target organs were harvested 24 hrs after i.v. delivery to assess biodistribution using the IVIS® Spectrum *in vivo* imaging system (PerkinElmer). After IVIS imaging, muscles were flash frozen in isopentane and cryosectioned at 10μm thickness throughout the majority of the muscle tissue. For immunofluorescent imaging of the Cy3-labeled plasmid, sections were stained for laminin to outline muscle fibers and DAPI. In brief, sections were incubated in TrueBlack (Biotium, 1:20 in 70% ethanol) for 30 sec – 1min, then incubated in blocking buffer (DPBS with 0.25% gelatin, 0.1% tween, and 3% BSA) for at least 1hr. Rabbit-anti-laminin (1:200, Millipore Sigma) was added in TBS and 1% goat serum overnight at 4°C. The next day goat-anti-rabbit IgG AlexaFluor™647 (1:250, Thermo Fisher) were incubated for 1 hr and the slides were mounted with VECTASHIELD containing DAPI (Vector Laboratories) and imaged on the Axio Observer Z1 microscope (Zeiss).

Lipofectamine 2000 transfection

Lipofectamine 2000 (Invitrogen) transfections were carried out in a 96-well plate according to the manufacturer's instructions. In brief, complexes were prepared by mixing 0.2µg tdTomato plasmid DNA with 0.5µl Lipofectamine 2000 (2:5, w/v) per well for myoblasts and myotubes.

CRISPR exon 45-55 deletion PCR

To assay for the exon 45-55 deletion, individual PCR reactions containing primers flanking the deletion (purple arrows in **Figure 2-20A**) or internal to the deletion (red arrows in **Figure 2-20A**) were performed on genomic DNA using AccuPrime Taq High Fidelity (Thermo Fisher) or Herculase II Fusion Polymerase (Agilent Genomics) as described[68]. PCR products were blunt cloned with Zero Bunt TOPO according to the manufacturer's instructions and sequenced by Laragen Inc.

NCAM peptide administration in vitro

A green fluorophore (5-FAM on N-terminus) labeled NCAM peptide (sequence ASKKPKRNIKAGGC[168]) was synthesized by Biomatik. 0.5, 1, 5, 10, 25, and 50µM NCAM peptide was incubated for 6 hrs on C2C12 and B16 cells before imaging.

Intracellular uptake study of Cy-3 labeled CRISPR plasmid

The following working antibody concentrations were used: anti-Lamp-1 antibody (Abcam, ab25245) at 1µg/mL, anti-myosin 4 antibody MF20 at 2µg/mL. Goat anti-rat IgG (H+L) Alexafluor 647 (Thermo Fisher, A21247) and goat anti-mouse IgG (H+L)

Alexafluor 647 (Thermo Fisher, A21235) were used as secondary antibodies, respectively. F-actin was stained with Phalloidin-iFluor 647 Reagent (Abcam, ab176759). The nuclei were counterstained with DAPI. The intracellular distribution of Cy3-labeled plasmid was visualized by confocal microscopy (SP8-SMD, Leica). For the image analysis, Pearson's correlation coefficient was used to determine the level of co-localization between Lamp-1/Cy3-plamid or PRX/Cy3-plasmid[171]. Image Pro Plus (Media Cybernetics) software was used to determine Pearson's correlation coefficient (n=5). To evaluate the intracellular level of Cy3-plasmid, the intracellular fluorescence intensity was analyzed by ImageJ software (NIH) (n=5). The fluorescence intensity per image was normalized to cell number in the case of myoblasts or cell spread area in the case of myotubes for comparison.

MTS colorimetric assay

Cell viability was measured using the CellTiter 96® Aqueous One Solution MTS assay (Promega) according to the manufacturer's instructions. Measurements were taken 24 hrs post administration for myoblasts and 72 hrs post administration for myotubes. In brief, cells were treated with 20uL per well assay reagent and incubated for 2 hrs at 37 °C. Absorbance (OD=490nm) was measured using a microplate reader (M5e, Molecular Device), and normalized to untreated control cells to determine percentage of cell viability (n=6).

Statistical analysis

Results presented in Figures 2-6, 2-7, 2-8, 2-12, 2-13, 2-14, 2-17, 2-18C-D are shown as mean ± standard error of the mean (SEM) and comparison between two conditions was evaluated by the unpaired *t*-test (two-tailed). Results in Figure 2-18E-F are presented as mean ± standard deviation (SD) and comparison between groups was evaluated using one-way analysis of variance (ANOVA) followed by Tukey's post-hoc test. $p < 0.05$ (*), $p < 0.01$ (**), $p = 0.0001$ (***), $p < 0.0001$ (****) were considered significant. Statistical analysis and graphs were generated using GraphPad Prism 6 software.

Results and Discussion

Design and optimization of 4-arm PRX nanoparticles

We have recently demonstrated effective delivery of a plasmid encoding interleukin (IL) in a cancer model using pristine 4-arm PRXs, which had improved gene delivery compared to the classic linear PRX[163]. Enhanced gene delivery of pristine 4-arm PRX was due to the addition of α-cyclodextrin (CD) rings in a spatially and selective fashion onto only 2 out of the 4 PEG arms, which increased PEGylation density, thereby enhancing circulation time after IV administration while maintaining encapsulation of nucleic acid mediated by electrostatic interactions (**Figure 2-1A**). Unlike the pristine 4-arm PRX, the classic linear PRX complexed with nucleic acid results in low PEGylation density, formation of a protein corona, opsonization, and clearance by the reticuloendothelial system (RES)[163].

The pristine 4-arm PRX was synthesized through previously optimized steps, namely 1) bulky end-group protection on 4-arm PEG-tetra-amine, 2) α-CD threading in

saturated sugar aqueous solution, 3) use of an amide coupling reaction to introduce Z-L-tyrosine for PRX stabilization, and 4) amine functionalization (**Figure 2-2**)[163]. Here, we develop iterations of 4-arm PRXs and optimize delivery of large plasmid cargo to primary dystrophic muscle cells. The first approach was to add a redox-responsive disulfide linker between the cationic amine group and the α-CD ring, whereby cleavage leads to dissociation of the positive charge (**Figure 2-1A**, hereafter referred to as disulfide 4-arm PRX). For comparison, pristine linear and disulfide linear PRXs were also made (**Figure 2-3**). In the second approach, two different peptides were conjugated to the nanocarriers to improve targeting and muscle cell uptake (**Figure 2-1A**). One is a cell-penetrating peptide (PipB) that has been shown to improve antisense oligonucleotide uptake to muscle[169]. The second involves coupling a synthetic ligand that interacts with neural cell adhesion molecule (NCAM), which is a receptor expressed on muscle cells, including muscle stem cells[168].

A representative image from atomic force microscopy (AFM) demonstrates self-assembly of a plasmid encoding CRISPR DMD$^{\Delta 45\text{-}55}$ with 4-arm PRX (**Figure 2-1B**). All PRX nanocarriers were extensively characterized for size, zeta-potential, number of CD rings, and optimized for plasmid loading (**Figure 2-4** and **Table 2-1**). The optimal N/P ratio for each formulation was determined from an *in vitro* reporter assay using a tdTomato plasmid (**Figure 2-5**). The size and polydispersity index (PDI) of each 4-arm PRX at the optimized N/P ratio are described (**Figure 2-1C**).

Addition of disulfide-sensitive linker in PRX mediates plasmid release in hDMD del45 mdx murine muscle cells

We tested the ability of pristine and disulfide 4-arm PRXs to enter muscle cells and subsequently escape the lysosome. For this analysis, primary murine myoblasts (MB) and myotubes (MT) were obtained from the hDMD del45 mdx mouse[77]. This model contains a human *DMD* gene with an exon 45 deletion, which is a region of the gene targeted by CRISPR DMD$^{\Delta 45\text{-}55}$ [68]. Pristine and disulfide 4-arm PRXs exhibited efficient plasmid uptake and were able to escape the lysosome in MB and MT (**Figure 2-6**). Pearson's correlation coefficient (PCC) of overlap between a lysosomal marker (LAMP-1) and labeled CRISPR/Cas9 plasmid demonstrated a PCC index of less than 0.7 for all PRXs, suggesting an ability to escape the lysosome at 24 hours (**Figure 2-6**). The pristine linear and disulfide linear PRXs demonstrated similar uptake and lysosomal escape as measured by PCC (**Figure 2-7**). Furthermore, the lack of difference in lysosomal escape between the pristine and disulfide designs was anticipated, as the disulfide linker was designed for a plasmid release mechanism only. Instead, PRXs may be able to escape the lysosomal compartment due to the "proton sponge" effect which has remained a hypothesis and a generally accepted mechanism for cationic polyplexes[172-174].

The disulfide-sensitive linker is expected to enhance plasmid release *in vitro* resulting in a supramolecular dissociation upon exposure to the intracellular reducing environment. The disulfide linker was added to the positively charged α-CD amine groups by thiol-exchange reaction between pyridyldithiol-4-arm polyrotaxane and dimethylamino ethanethiol in aqueous solution (**Figures 2-8A** and **2-9**). The addition of the disulfide linker was confirmed using ^{1}H-NMR for the intermediate precursor and final product (**Figure 2-10**). Abiotic assessment of the redox-responsive linker was tested by

comparing pristine and disulfide 4-arm PRXs before and after incubation with 5mM dithiothreitol (DTT) for 30 minutes. We measured a shift in size suggesting dissociation between disulfide 4-arm PRX and plasmid while no change in size was observed for pristine 4-arm PRX (**Figure 2-8B**). Furthermore, a gel retardation assay of the disulfide 4-arm PRX incubated with 2.5mM and 5mM DTT showed successful plasmid release (**Figure 2-4E**). To validate plasmid release *in vitro*, co-localization of the plasmid cargo (labeled with Cy3) and PRXs (labeled with FITC) was examined in hDMD del45 murine MB and MT. We observed almost complete co-localization (PCC value of 0.9) between the labeled FITC-pristine 4-arm PRX and Cy3-plasmid cargo in MB and MT 24 hours after incubation, which suggests that the nanoparticle did not release the plasmid (**Figure 2-8C** and **2-8D**). As expected, the disulfide 4-arm PRX showed significantly enhanced dissociation in MB and MT 24 hours after incubation (PCC value of 0.63). These data suggest that addition of a disulfide-linker enhances plasmid release in mammalian cells, which are reported to have pools of reducing agents, such as intracellular glutathione (GSH: approximately 5mM)[175-178].

We next assessed whether the released plasmid cargo could traffic to the nucleus by measuring tdTomato reporter protein gene expression in MB and MT (**Figure 2-11**). Pristine and disulfide PRXs were packaged with a tdTomato reporter plasmid and were added to primary MB and MT and the percent of tdTomato positive cells was assessed at time points from 24 hours to 7 days. Disulfide linear and disulfide 4-arm PRXs demonstrated significantly greater tdTomato positive MB at days 1, 2 and 7 (**Figures 2-12A** and **2-13A**). Likewise, there was a significant increase in tdTomato positive MT with the disulfide 4-arm PRX at days 3 and 7 (**Figure 2-12B**). While a slight

trend of increased tdTomato was observed in tdTomato positive MT with the disulfide linear PRX, it was not significantly different (**Figure 2-13B**). This observation suggests the limiting factor of transfection efficiency in MT may not be plasmid release. Instead, the inability of the disulfide linker to significantly increase tdTomato positive MT could be due to a lack of nuclear targeting since myotubes are non-dividing and do not undergo nuclear breakdown[179].

Peptide conjugation to 4-arm PRXs enhance plasmid delivery to muscle cells

In order to improve the specificity and efficacy of PRX delivery to muscle, peptides were conjugated to the nanocarriers. Peptides were modified with cysteine and glycine spacers and were conjugated to the end of free PEG chains in DMAE-4-arm polyrotaxane-SMPT via thiol exchange chemistry on to the pristine 4-arm PRX (**Figures 2-14A** and **2-15**). Peptide modifications were confirmed using UV-vis and ^{1}H-NMR (**Figure 2-16**). We were unable to conjugate peptides onto the disulfide 4-arm PRX since disulfide and peptide conjugation utilize the same thiol exchange reaction and thus the chemistry is technically challenging. However, two peptide-modified versions of pristine 4-arm PRX were generated to aid in muscle targeting. Since targeting muscle stem cells is desirable for long term therapeutic efficacy of CRISPR reframing, a ligand for neural cell adhesion molecule (NCAM) was conjugated to nanoparticles, since NCAM is known to be expressed on muscle cells, including both human muscle stem cells and activated mouse muscle stem cells (referred to as NCAM peptide)[180-182]. Another peptide, PipB, was conjugated to nanocarriers since PipB is a cell penetrating

peptide shown to increase phosphorodiamidate morpholino oligonucleotide (PMO) uptake in muscle[169].

NCAM binding to muscle cells was first validated *in vitro* by incubating a FITC-labeled NCAM peptide with an immortalized mouse muscle cell line, C2C12. C2C12 cells were differentiated to MT, which increase expression of NCAM right after myotube fusion[168,183]. Peptide binding was shown by enhanced FITC signal on C2C12s but not on the negative control cells, NCAM negative, B16 murine cancer cells (**Figure 2-14B**).

Uptake of the peptide-modified nanocarriers was then tested in primary MB and MT compared to pristine 4-arm PRX. We observed that both peptide-conjugated 4-arm PRXs were able to escape the lysosome 24 hours post incubation (**Figure 2-17**). In addition, we observed that PipB 4-arm and NCAM 4-arm PRXs had faster plasmid uptake *in vitro* than the pristine 4-arm PRX (**Figures 2-14C** and **2-14D**). There was significantly more intracellular labeled plasmid cargo observed 40 minutes after administration in cells incubated with peptide-conjugated versions compared to pristine. By 24 hours, this difference was less noticeable, although in MB, PipB 4-arm still had significantly more labeled plasmid cargo and both PipB 4-arm and NCAM 4-arm had more plasmid cargo in MT. Thus, both peptides are able to increase nanoparticle uptake in MB and MT *in vitro* and both do so to a similar extent.

As a more relevant readout of peptide-conjugated 4-arm PRX gene delivery efficiency, we used tdTomato plasmid cargo and examined reporter protein expression in muscle cells 24 hours to 7 days post administration compared to reporter expression after delivery with the lipid-based Lipofectamine 2000 (Lipo 2000) transfection reagent. (**Figures 2-18A-B** and **2-19**). Lipo 2000 yielded up to 16% and 33% tdTomato positive

MB and MT at 1week, respectively (**Figures 2-18C** and **2-18D**). Peptide conjugation resulted in an approximately ninefold improvement of reporter expression when compared to the pristine 4-arm PRX, with up to 11% tdTomato positive MB for PipB and NCAM 4-arm PRXs at 1 week (**Figure 2-18C**). Furthermore, peptide conjugation resulted in up to 27% and 24% tdTomato positive MT for NCAM and PipB 4-arm PRXs, respectively at 1 week, which significantly improved reporter expression by ~85-fold compared to the pristine 4-arm PRX (**Figure 2-18D**). sThe enhanced uptake observed with the peptide-modified 4-arm PRXs support the increased tdTomato transfection results.

Next, the cytotoxicity of all PRX formulations and Lipo 2000 was assessed on primary MB and MT by MTS colorimetric assay. The same concentration of PRXs complexed with the CRISPR plasmid were added to primary murine MB and MT *in vitro* and cell viability was measured 24 hours and 72 hours post-incubation, respectively. There was no observed significant difference in the percent viability for PRX treated MB or MT compared to mock treated control cells (**Figure 2-18E** and **2-18F**). However, there was a significant reduction in cell viability for MB treated with Lipo 2000 (65% cell viability), indicative of cytotoxicity which has previously been reported for Lipofectamine transfections[184,185]. These results suggest that all PRX formulations are not significantly cytotoxic *in vitro*.

PRXs successfully deliver CRISPR/Cas9 to humanized dystrophic myoblasts and myotubes in vitro

PRX efficacy for delivery of a plasmid encoding CRISPR DMD$^{\Delta 45\text{-}55}$ was tested in primary murine MB and MT. CRISPR DMD$^{\Delta 45\text{-}55}$ consists of two gRNAs, one targeted to intron 44 (44C4) and one to intron 55 (55C3), along with SpCas9, that causes deletion of *DMD* exons 45-55 by NHEJ and reframing of the gene (**Figure 2-20A**)[68,77]. Delivery of CRISPR DMD$^{\Delta 45\text{-}55}$ using the disulfide linear PRX demonstrated successful deletion of exons 45-55 as determined by genomic DNA PCR using one primer pair internal to the deletion (undeleted) and one flanking the deletion (deleted allele) after 1 week. However, delivery using the pristine linear PRX did not generate a detectable deletion, even up to 2 weeks after administration (**Figure 2-21A**). CRISPR DMD$^{\Delta 45\text{-}55}$ administration using the disulfide 4-arm PRX also led to efficient CRISPR/Cas9-mediated deletion at 1 week compared to the pristine 4-arm PRX (**Figure 2-21B**). The enhanced DNA editing observed with the disulfide modified PRXs is likely due to the improved redox-responsive release mechanism of the CRISPR plasmid.

Since the highest tdTomato transfection efficiency was observed with the peptide-conjugated 4-arm PRXs (**Figure 2-18**), these formulations were also tested for their ability to deliver CRISPR DMD$^{\Delta 45\text{-}55}$. PipB 4-arm and NCAM 4-arm PRXs carrying CRISPR DMD$^{\Delta 45\text{-}55}$ were added to primary hDMD del45 MB and NCAM 4-arm PRXs to MT. Subsequent assessment of genomic DNA at day 5 demonstrated effective deletion of *DMD* exons 45-55 as analyzed by PCR (**Figures 2-20B** and **2-21C-D**). Sequencing of the rejoining site in the deleted product was performed to demonstrate successful deletion and NHEJ of introns 44 and 55. Representative sequencing traces demonstrate a 1bp insertion or seamless rejoining at the junction site, however since these indels are in the middle of the intron we do not expect them to have any detrimental effects, as

demonstrated in our prior study (**Figure 2-20C**)[68]. Thus, both the peptide-modified 4-arm and disulfide 4-arm PRXs are effective delivery vehicles of DNA to humanized dystrophic muscle cells, including the large CRISPR/Cas9 plasmid.

PRX formulations fail to enter skeletal muscle fibers after intravenous delivery in a mouse model of DMD

We next sought to assess *in vivo* biodistribution of our 4-arm PRX formulations. 4-arm PRXs loaded with Cy3-labeled plasmid were intravenously (i.v.) administered to our humanized dystrophic mouse model and muscles were imaged 24 hrs post-injection. IVIS imaging demonstrated 4-arm PRXs inefficiently trafficked to skeletal muscle, with limited detection observed in the diaphragm and no detection in the heart, which are necessary organs to target in order to alter disease course (**Figure 2-22A**). The 4-arm PRXs were predominantly sequestered in the liver following i.v. delivery. Immunofluorescent analysis revealed the 4-arm PRXs often co-localized with laminin and were confined to the basal lamina and/or interstitial space (**Figure 2-22B**). Unexpectedly, the NCAM 4-arm PRX resulted in poor distribution to skeletal muscle compared to its 4-arm PRX counterparts. Nevertheless, we failed to observe 4-arm PRXs within muscle fibers following systemic or local delivery (data not shown), which strongly suggests that the extracellular matrix and/or basal lamina may pose as an additional barrier for *in vivo* trafficking.

Conclusion

To summarize, 4-arm PRX nanocarriers have been developed and iteratively optimized for efficient delivery of large plasmid cargo such as CRISPR/Cas9, to primary muscle cells. This study highlights the key advantages of PRXs over other nanomaterials, since they are devoid of cytotoxicity, have a large loading capacity, and are chemically tunable to modify their physiochemical properties to enhance gene delivery efficiency. Moreover, we expect PRX nanocarriers could likely be adapted for other nucleic acids such as RNA, which is an approach that offers some advantages for CRISPR delivery compared to DNA, since RNA would not have potential for genomic integration and is short-lived, which could reduce the chance of off-target effects. The innovative aspects of this study include the addition of the disulfide-responsive linker, which enhanced plasmid release following cellular uptake, and conjugation of PipB and NCAM peptides, which augmented gene delivery. Furthermore, this study demonstrated proof-of-concept that 4-arm PRX nanocarriers can deliver a previously validated CRISPR/Cas9 gene editing platform to humanized dystrophic muscle cells and achieve deletion of *DMD* exons 45-55. This work lays a foundation for use of the 4-arm PRX as an efficacious *in vitro* transfection reagent for muscle cells and sets a path to improve systemic delivery for future *in vivo* studies.

Acknowledgments

We would like to thank Jane Wen, Catherine Le, and Rebecca Banh for technical assistance. We extend our greatest thanks to Jinhong Jiang for PRX illustrations. The authors acknowledge the use of instruments at the Nano and Pico Characterization Lab

at the California NanoSystems Institute. This material is based upon work supported by the National Science Foundation Graduate Research Fellowship Program under Grant No. DGE-1650604 (MRE). Any opinions, findings, and conclusions or recommendations expressed in this material are those of the author and do not necessarily reflect the views of the National Science Foundation. Funding was provided by Ruth L. Kirschstein National Research Service Award GM007185 (MRE), and the Ruth L. Kirschstein National Research Service Award T32AR065972 'Muscle Cell Biology, Pathophysiology, and Therapeutics' from the National Institute of Arthritis and Musculoskeletal and Skin Diseases (CSY). Additional funding was provided by the California Institute for Regenerative Medicine (CIRM DISC2-08824), Muscular Dystrophy Association (MDA 578394), pilot and feasibility seed grant from the Center for DMD at UCLA (NIH NIAMS) P30 AR05723, Eli & Edythe Broad Center of Regenerative Medicine and Stem Cell Research at UCLA, and Jesse's Journey. MRE, CSY, and YJ contributed equally to this work.

Author contributions

Conceptualization, Methodology, Visualization, Project Administration, Writing – Review and Editing – MRE, CSY, YJ, XL, HM, ADP, MJS; Investigation, Formal Analysis, Validation – MRE, CSY, YJ, XL; Writing – Original Draft – MRE, CSY; Resources – EM, ADP, MJS; Supervision – HM, ADP, MJS; Funding Acquisition – HM, ADP, MJS.

Figures

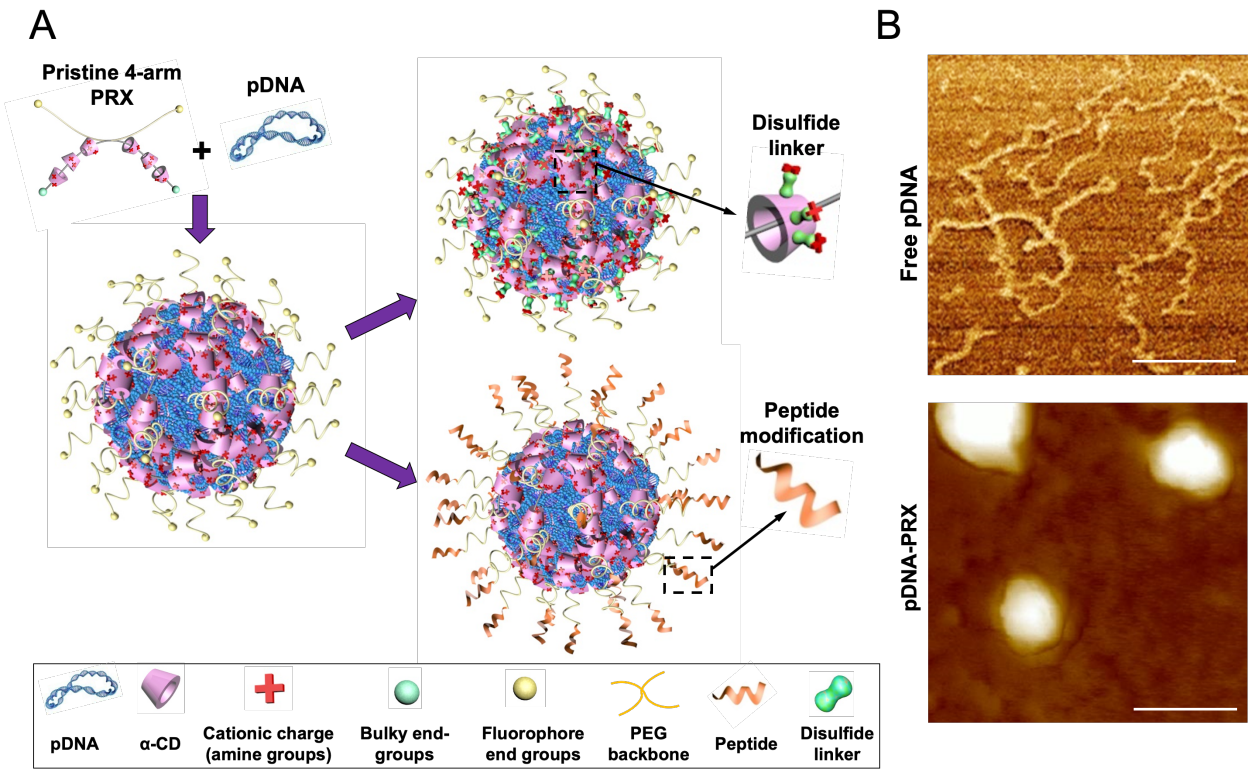

C

PRX	Pristine 4-arm	Disulfide 4-arm	PipB 4-arm	NCAM 4-arm
Size (nm)	187.7 ± 4.6	147.7 ± 5.9	152.8 ± 6.6	131.2 ± 5.1
PDI	0.146	0.188	0.174	0.165

Figure 2-1: Design and optimization of the pristine 4-arm PRX nanoparticle.
A) Cartoon depicting the 4-arm PRX design containing a 4-arm PEG chain (yellow) with positively charged α-CD rings (pink). When plasmid DNA (pDNA) is added (in blue) the positively charged PRX and negatively charged nucleic acids self-assemble. 4-arm PRXs can be modified to include a redox-responsive disulfide linker (in green) or conjugated with peptides (in orange) for cell targeting.
B) Atomic force microscopy images of free plasmid encoding CRISPR DMD$^{\Delta 45\text{-}55}$ before (top) and after nanoparticle formation with 4-arm PRX (bottom). Scale bar represented as 200nm.
C) Summary of physiochemical properties, size, and polydispersity (PDI) of all 4-arm PRX formulations.

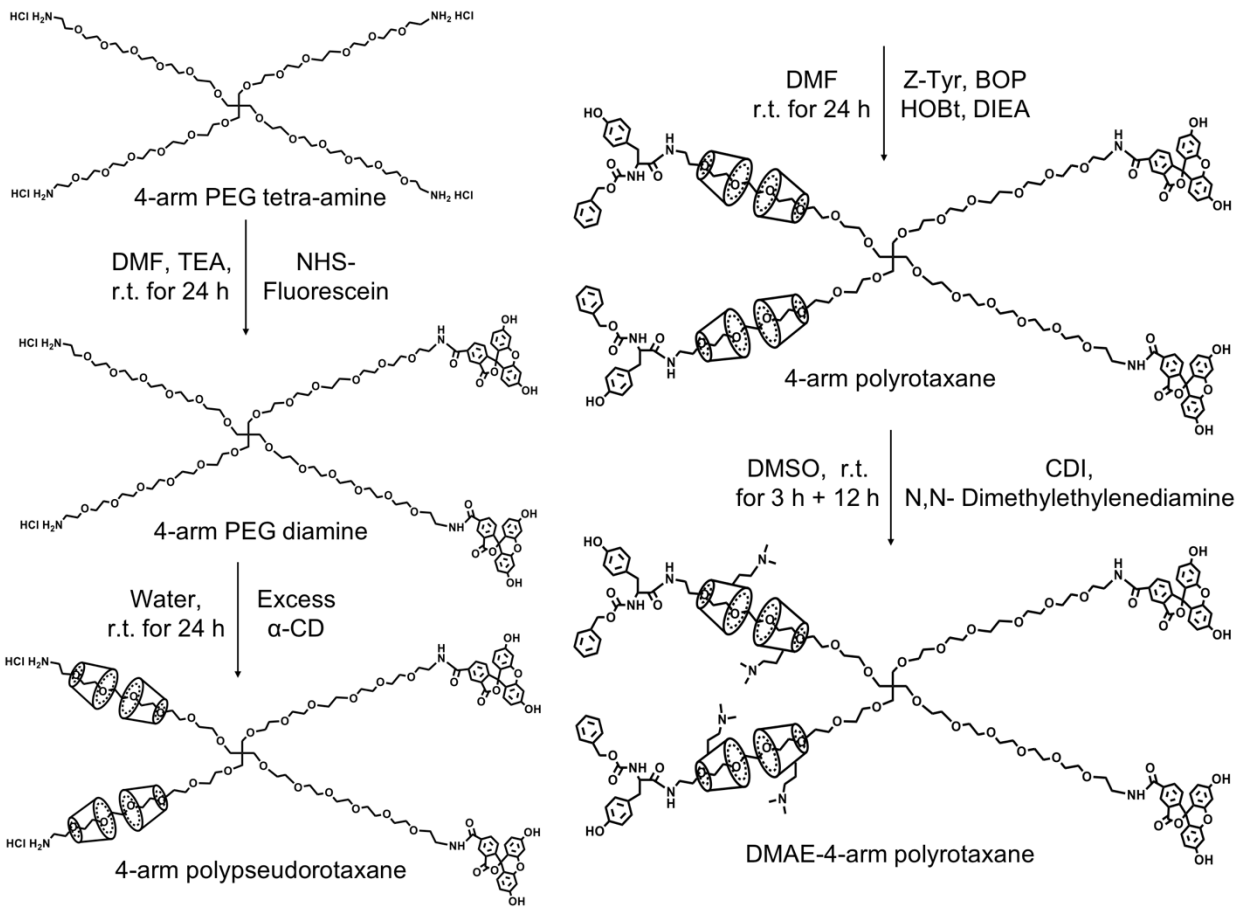

Figure 2-2: Scheme for the synthesis of pristine 4-arm PRX.
Four steps were involved in the synthesis of pristine 4-arm PRX, as we described previously[163]. (i) Two arms of a 4-arm PEG tetra-amine were selectively blocked by NHS-Fluorescein. (ii) The 4-arm PEG diamine was then added to aqueous saturated solution of α-CDs to form a 2/4-arm polypseudorotaxane inclusion complex. (iii) The amino ends of 2/4 arm polypseudorotaxane were blocked with Z-L-Tyr. (iv) The α-CDs in the 2/4-arm polyrotaxane were modified with positively charged amine groups by reaction with DMAE and CDI in DMSO.

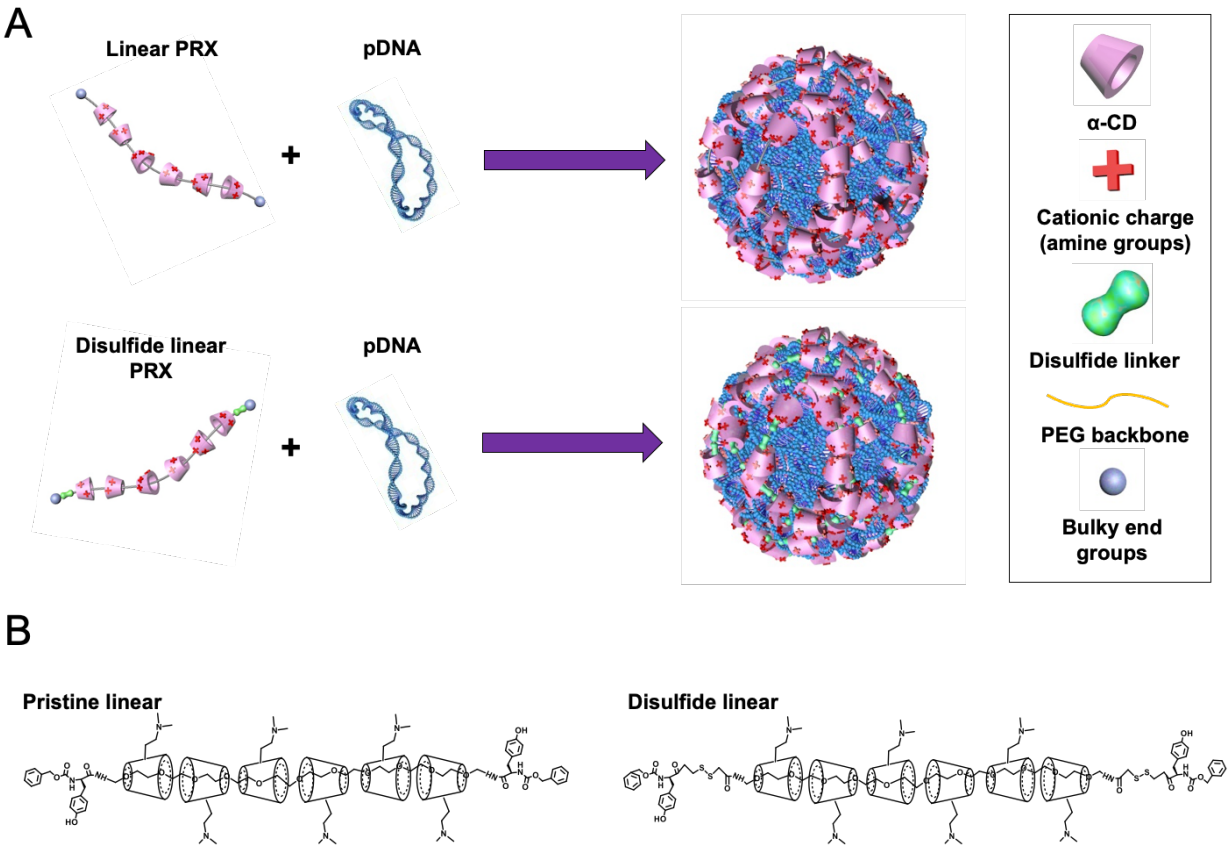

Figure 2-3: Scheme of linear PRXs.
A) Schematic structure of pristine and disulfide linear PRX nanoparticles with α-CD rings threaded along a linear PEG backbone. Positively charged PRX self-assemble and encapsulate plasmid DNA.
B) Chemical structure of pristine and disulfide linear PRXs. The pristine PRX and disulfide linear PRX were synthesized according to previously published protocols[166,167].

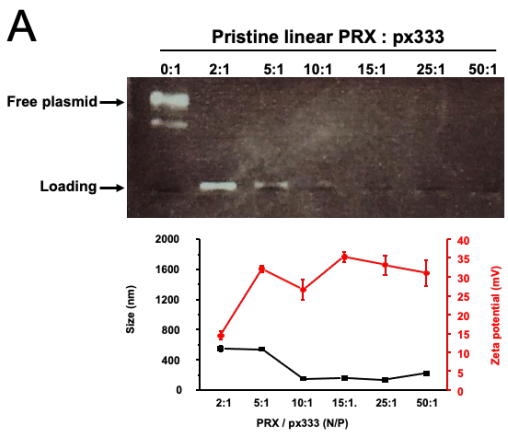
A
Pristine linear PRX : px333
0:1 2:1 5:1 10:1 15:1 25:1 50:1
Free plasmid
Loading
Size (nm)
Zeta potential (mV)
2:1 5:1 10:1 15:1. 25:1 50:1
PRX / px333 (N/P)

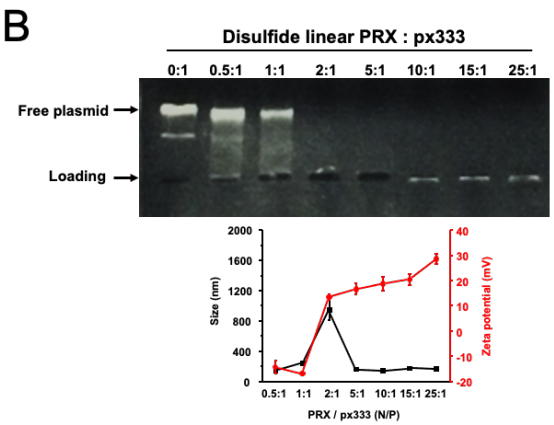
B
Disulfide linear PRX : px333
0:1 0.5:1 1:1 2:1 5:1 10:1 15:1 25:1
Free plasmid
Loading
Size (nm)
Zeta potential (mV)
0.5:1 1:1 2:1 5:1 10:1 15:1 25:1
PRX / px333 (N/P)

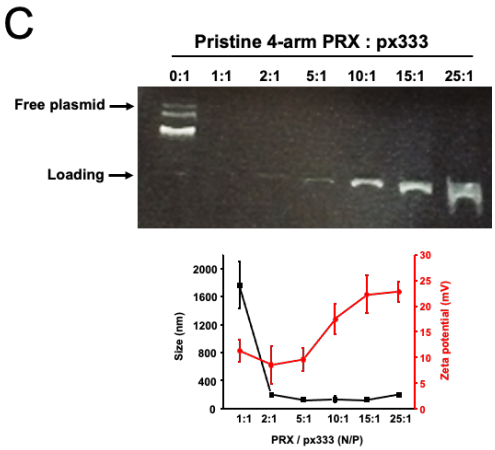
C
Pristine 4-arm PRX : px333
0:1 1:1 2:1 5:1 10:1 15:1 25:1
Free plasmid
Loading
Size (nm)
Zeta potential (mV)
1:1 2:1 5:1 10:1 15:1 25:1
PRX / px333 (N/P)

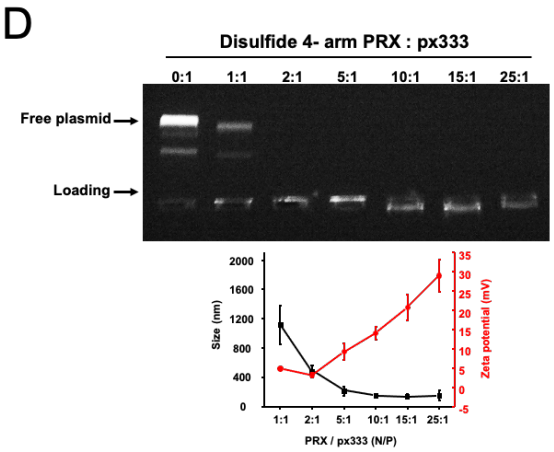
D
Disulfide 4- arm PRX : px333
0:1 1:1 2:1 5:1 10:1 15:1 25:1
Free plasmid
Loading
Size (nm)
Zeta potential (mV)
1:1 2:1 5:1 10:1 15:1 25:1
PRX / px333 (N/P)

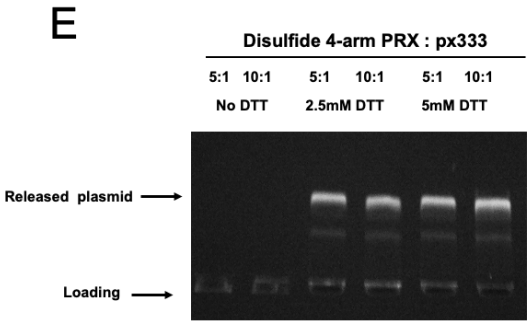
E
Disulfide 4-arm PRX : px333
5:1 10:1 5:1 10:1 5:1 10:1
No DTT 2.5mM DTT 5mM DTT
Released plasmid
Loading

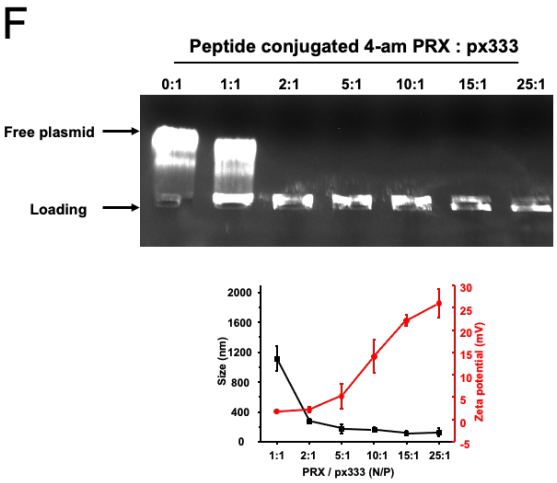
F
Peptide conjugated 4-am PRX : px333
0:1 1:1 2:1 5:1 10:1 15:1 25:1
Free plasmid
Loading
Size (nm)
Zeta potential (mV)
1:1 2:1 5:1 10:1 15:1 25:1
PRX / px333 (N/P)

Figure 2-4: Characterization of all PRXs across different N/P ratios.
Shown are DNA gel retardation assays of size and ζ-potential characterization of CRISPR/Cas9 plasmid (px333) laden PRXs with various N/P ratios in water. All PRX formulations demonstrate an N/P ratio>1:1, suggesting the effective encapsulation of CRISPR plasmid. When incubated with DTT solution, disulfide 4-arm PRX demonstrated redox-responsive release of CRISPR plasmid.
A) Pristine linear PRX.
B) Disulfide linear PRX.
C) Pristine 4-arm PRX.
D) Disulfide 4-arm PRX.
E) Disulfide 4-arm PRX after incubation with DTT.
F) Peptide conjugated 4-arm PRX.

Table 2-1: Summary of physiochemical properties of all PRX formulations used in this study.

	Polymer backbone	CD # per polymer	Cationic charge density	Optimized N/P for CRISPR plasmid	Size (nm)	PDI	Zeta potential (mV)
Pristine linear	Linear PEG (3.5kDa) Completely threaded with CD	26 CDs	6 amines/ CD	10:1	151.8 ± 2.8	0.167	24.6 ± 4.4
Disulfide linear	Linear PEG (3.5 kDa) Completely threaded with CD	22 CDs	6 amines/ CD	5:1	163.1 ± 3.1	0.185	17.8 ± 3.3
Pristine 4-arm	4-arm PEG (10 kDa) 2/4 arm threaded with CD	26 CDs	6 amines/ CD	3:1	187.7 ± 4.6	0.146	11.4 ± 3.0
Disulfide 4-arm	4-arm PEG (10 kDa) 2/4 arm threaded with CD	25 CDs	6 amines/ CD	3:1	147.7 ± 5.9	0.188	12.7 ± 3.6
PipB 4-arm	4-arm PEG (10 kDa) 2/4 arm threaded with CD	24 CDs	6 amines/ CD	5:1	152.8 ± 6.6	0.174	15.7 ± 4.2
NCAM 4-arm	4-arm PEG (10 kDa) 2/4 arm threaded with CD	24 CDs	6 amines/ CD	5:1	131.2 ± 5.1	0.165	16.9 ± 2.7

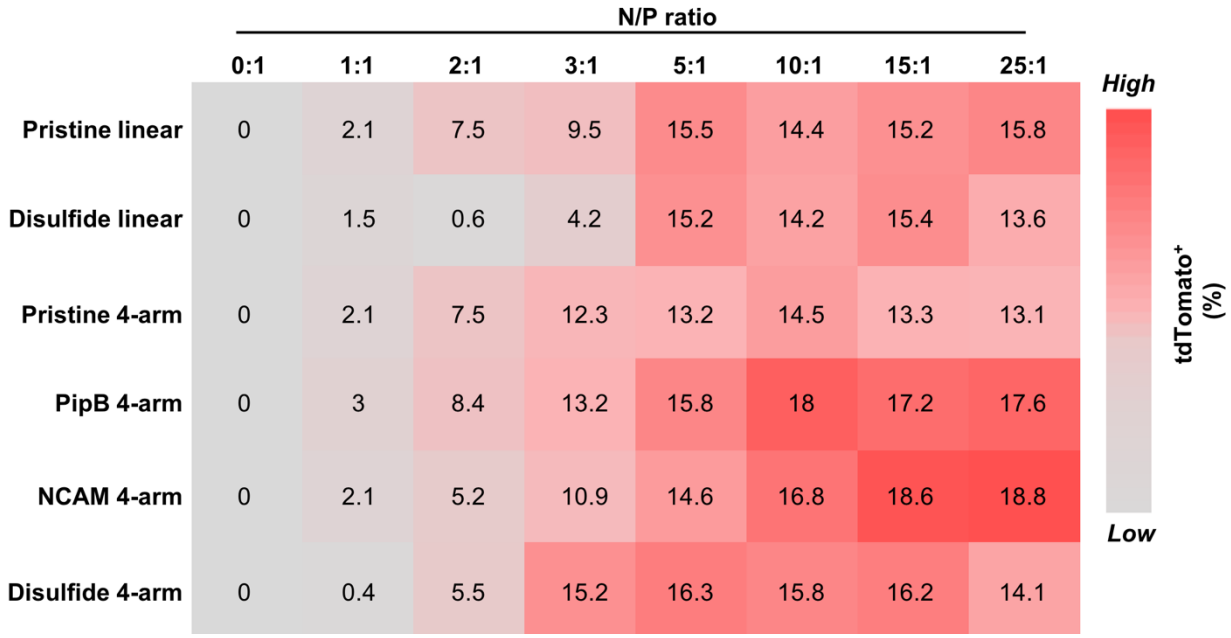

Figure 2-5: Heat map of N/P ratio optimization across all PRX formulations using tdTomato reporter plasmid as cargo in MC38 colon cancer cells.
Shown is the percent tdTomato positive MC38 colon cancer cells 72 hrs after transfection *in vitro* with various PRX formulations across different N/P ratios.

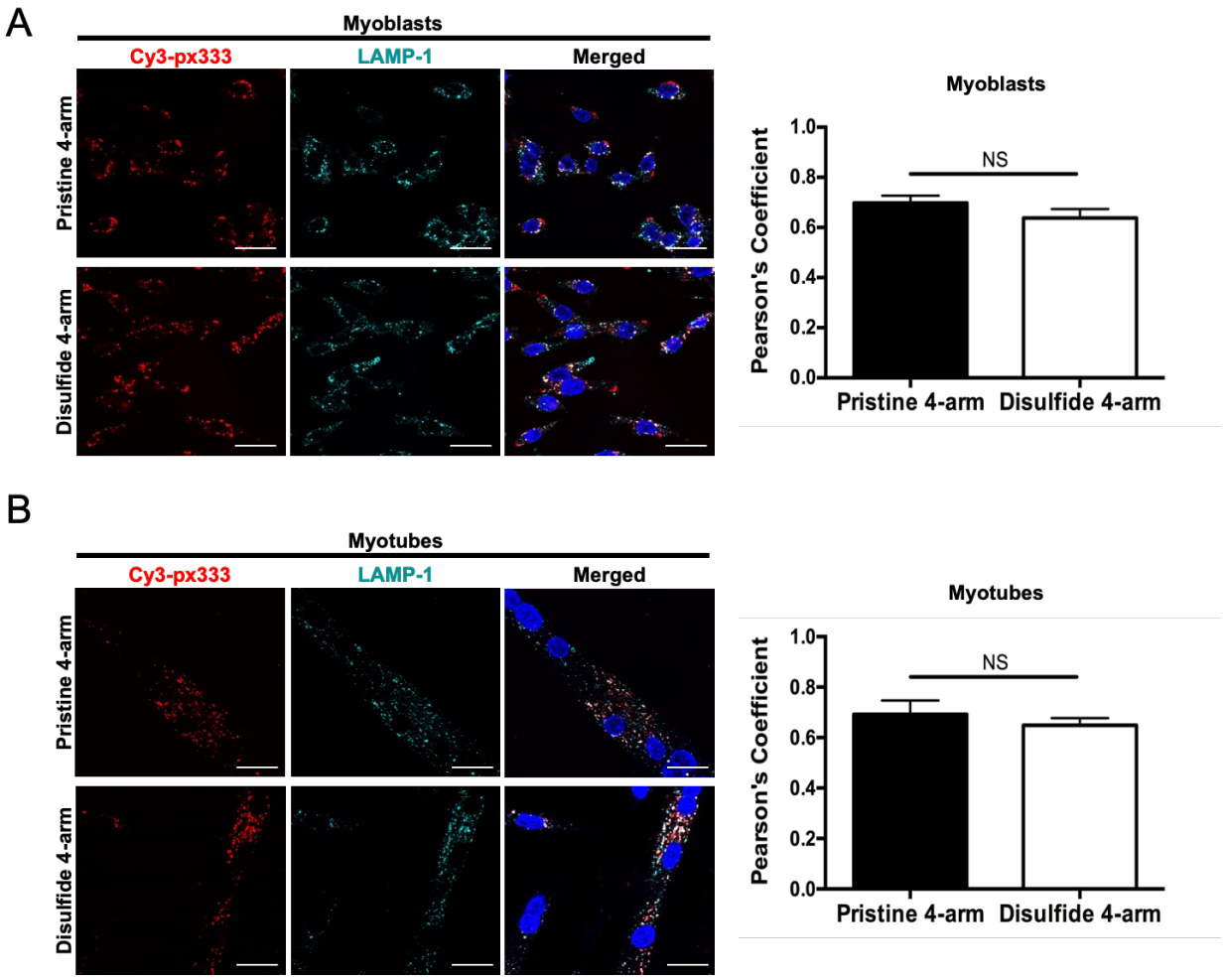

Figure 2-6: Pristine and disulfide 4-arm PRXs are efficiently taken up and can escape the lysosome in muscle cells *in vitro*.
A-B) Confocal microscopy images of intracellular trafficking of pristine 4-arm and disulfide 4-arm PRX nanoparticles carrying Cy3-labeled CRISPR plasmid (red) and stained with lysosomal marker, LAMP-1 (cyan), and DAPI (blue) in hDMD del45 mdx myoblasts (MB) and myotubes (MT) at 24 hrs. Pearson's correlation coefficient (PCC) quantification between plasmid and LAMP-1 co-localization for pristine 4-arm and disulfide 4-arm PRXs in MB and MT. A lower correlation coefficient demonstrates a dissociation between Cy3 plasmid and LAMP-1 signals. Scale bar represented as 25μm. Graphs depict average ± standard error of the mean (SEM). NS: not significant.

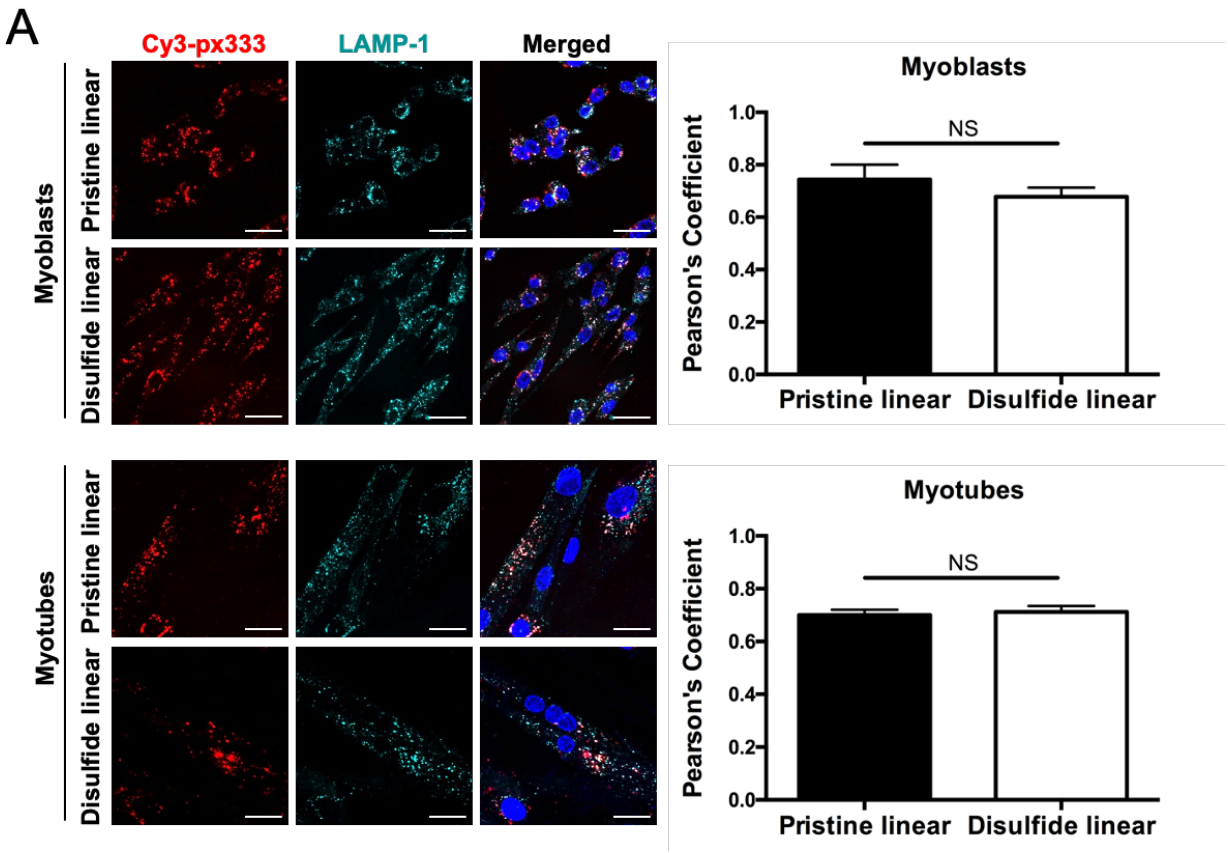

Figure 2-7: Linear PRXs are efficiently taken up and can escape the lysosome in muscle cells *in vitro*.
A) Confocal microscopy images of intracellular trafficking of pristine and disulfide linear PRX nanoparticles carrying Cy3-labeled CRISPR/Cas9 plasmid (red) and stained with lysosomal marker, LAMP-1 (cyan) and DAPI (blue) in hDMD del45 mdx MB and MT at 24 hrs. Pearson's correlation coefficient (PCC) quantification between plasmid and LAMP-1 co-localization for pristine and disulfide linear PRXs in MB and MT. Correlation coefficient demonstrate a dissociation between Cy3 plasmid and LAMP-1 signals. Scale bar represented as 25μm. Graphs depict average ± standard error of the mean (SEM). NS: not significant.

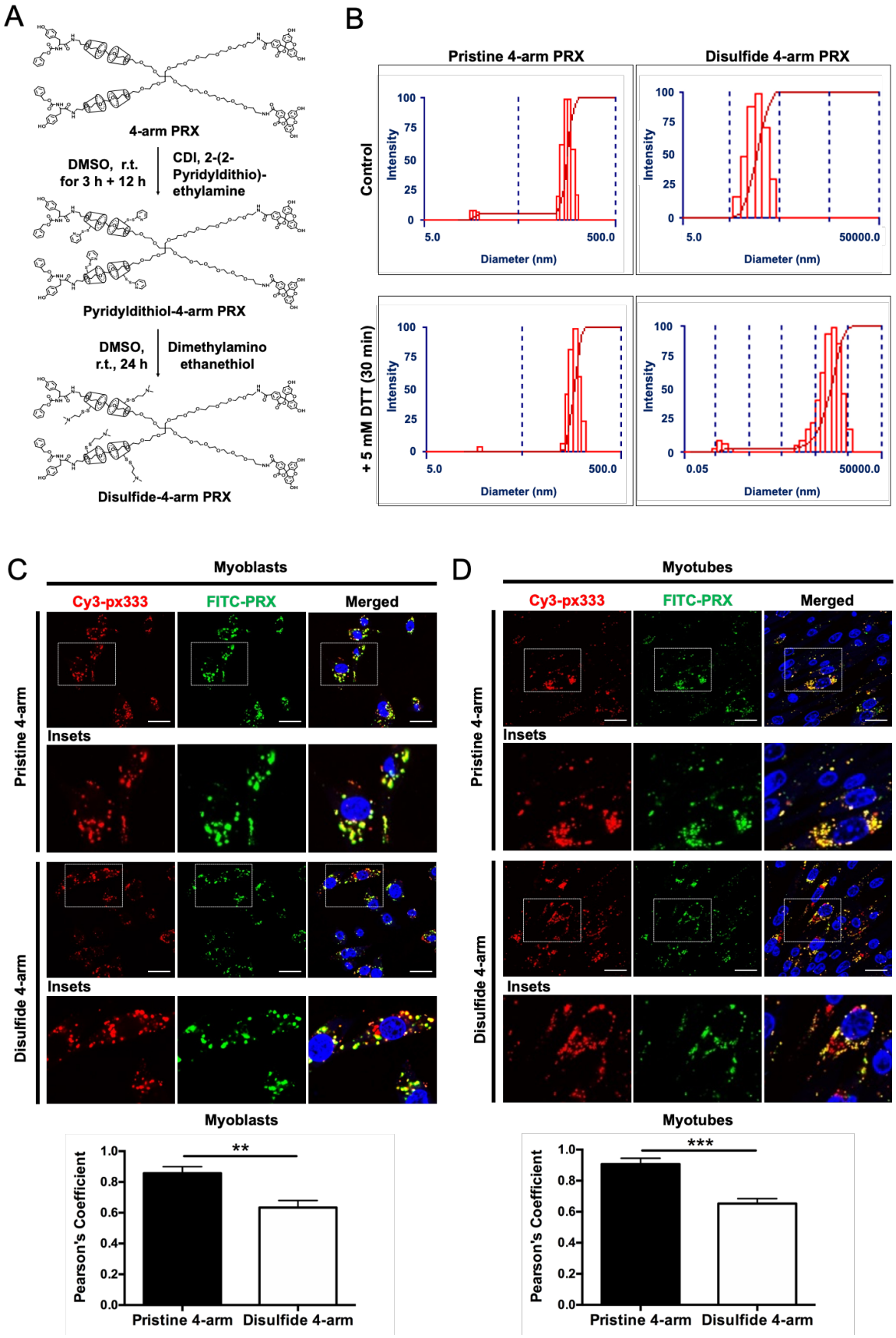
A
4-arm PRX
DMSO, r.t. for 3 h + 12 h
CDI, 2-(2-Pyridyldithio)-ethylamine
Pyridyldithiol-4-arm PRX
DMSO, r.t., 24 h
Dimethylamino ethanethiol
Disulfide-4-arm PRX
B
Pristine 4-arm PRX
Disulfide 4-arm PRX
Control
+ 5 mM DTT (30 min)
Intensity
Diameter (nm)
C
Myoblasts
Cy3-px333
FITC-PRX
Merged
Pristine 4-arm
Disulfide 4-arm
Insets
Myoblasts
Pearson's Coefficient
**
Pristine 4-arm
Disulfide 4-arm
D
Myotubes
Cy3-px333
FITC-PRX
Merged
Pristine 4-arm
Disulfide 4-arm
Insets
Myotubes
Pearson's Coefficient
***
Pristine 4-arm
Disulfide 4-arm

Figure 2-8: Addition of redox-sensitive disulfide linker mediates plasmid release abiotically and *in vitro*.
A) Synthesis scheme for disulfide 4-arm PRX. Two arms of 4-arm PEG were selectively threaded with α-CD rings and further functionalized with pyridyldithioal groups. Tertiary amines were then conjugated via thiol-exchange chemistry with dimethylamino ethanethiol. The disulfide 4-arm PRX was designed to facilitate intracellular plasmid release in response to a redox signal.
B) Size characterization of CRISPR plasmid laden disulfide 4-arm PRX before and after incubation with 5mM DTT (reducing reagent). The significant change in particle size demonstrated the redox-responsive dissociation of CRISPR plasmid with the disulfide 4-arm PRX.
C-D) Confocal microscopy images of pristine 4-arm and disulfide 4-arm PRX nanoparticles labeled with FITC (green) containing Cy3-labeled CRISPR plasmid cargo (red) 24 hr after administration in hDMD del45 MB and MT. PCC quantification of PRX and plasmid co-localization with pristine 4-arm and disulfide 4-arm PRX showing reduced co-localization in disulfide 4-arm PRXs demonstrating increased plasmid release (in red). Scale bar represented as 25μm. Graphs depict average ± standard error of the mean (SEM). NS: not significant; *$p < 0.05$; **$p < 0.01$; ***$p = 0.0001$.

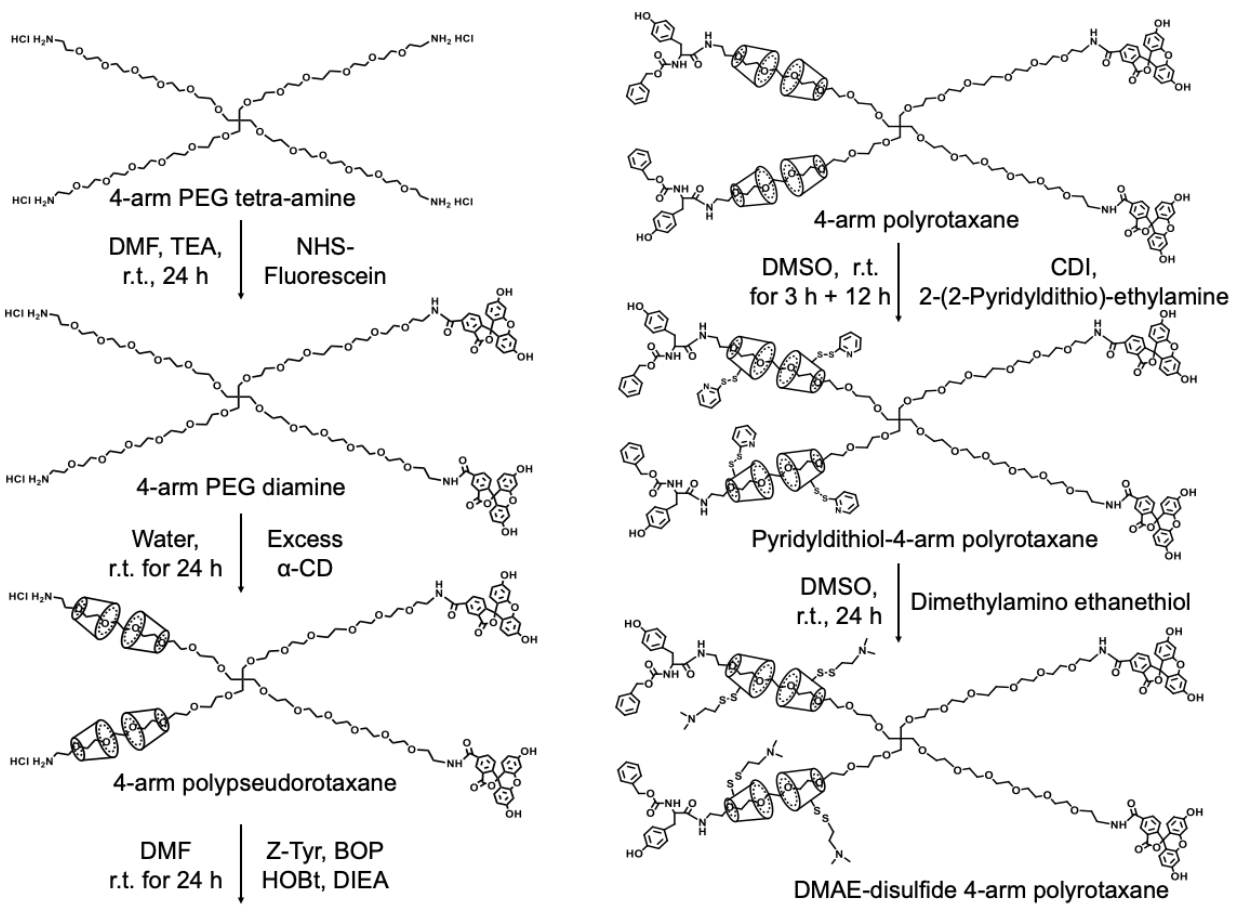

Figure 2-9: Scheme for the synthesis of disulfide 4-arm PRX.
Disulfide linkage between α-CDs on 4-arm polyrotaxane and the cationic charge were introduced via the thiol-exchange reaction between the pendant pyridyldithiol groups on α -CDs and dimethylamino ethanethiol. 4-arm polyrotaxane end-capped with Z-L-Tyr were synthesized as described above for pristine 4-arm PRX. The α -CDs in 2/4-arm polyrotaxane were further functionalized with pyriyldithiol groups. 2/4-arm polyrotaxane (100mg) was first dissolved in DMSO (2mL) together with CDI (211mg) and stirred for 30 mins at room temperature. Pyridyldithiol-cysteamine (322 mg) was then added to the solution and reacted overnight at room temperature. The resulting pyridyldithiol-4-arm polyrotaxane was precipitated in diethyl ether and washed sequentially in acetone and methanol. The α-CDs with cleavable positively charged amine groups were generated by thiol-exchange reaction between pyridyldithiol-4-arm polyrotaxane and dimethylamino ethanethiol. Pyridyldithiol-4-arm polyrotaxane (150mg) reacted with dimethylamino ethanethiol hydrochloride (124mg) under nitrogen protection for 24 hrs. The resulting disulfide 4-arm PRX was precipitated in acetone and repeatedly concentrated with DI water using Amicon centrifugal filters (MWCO=10kDa) to remove excess pyridyldithiol-cysteamine.

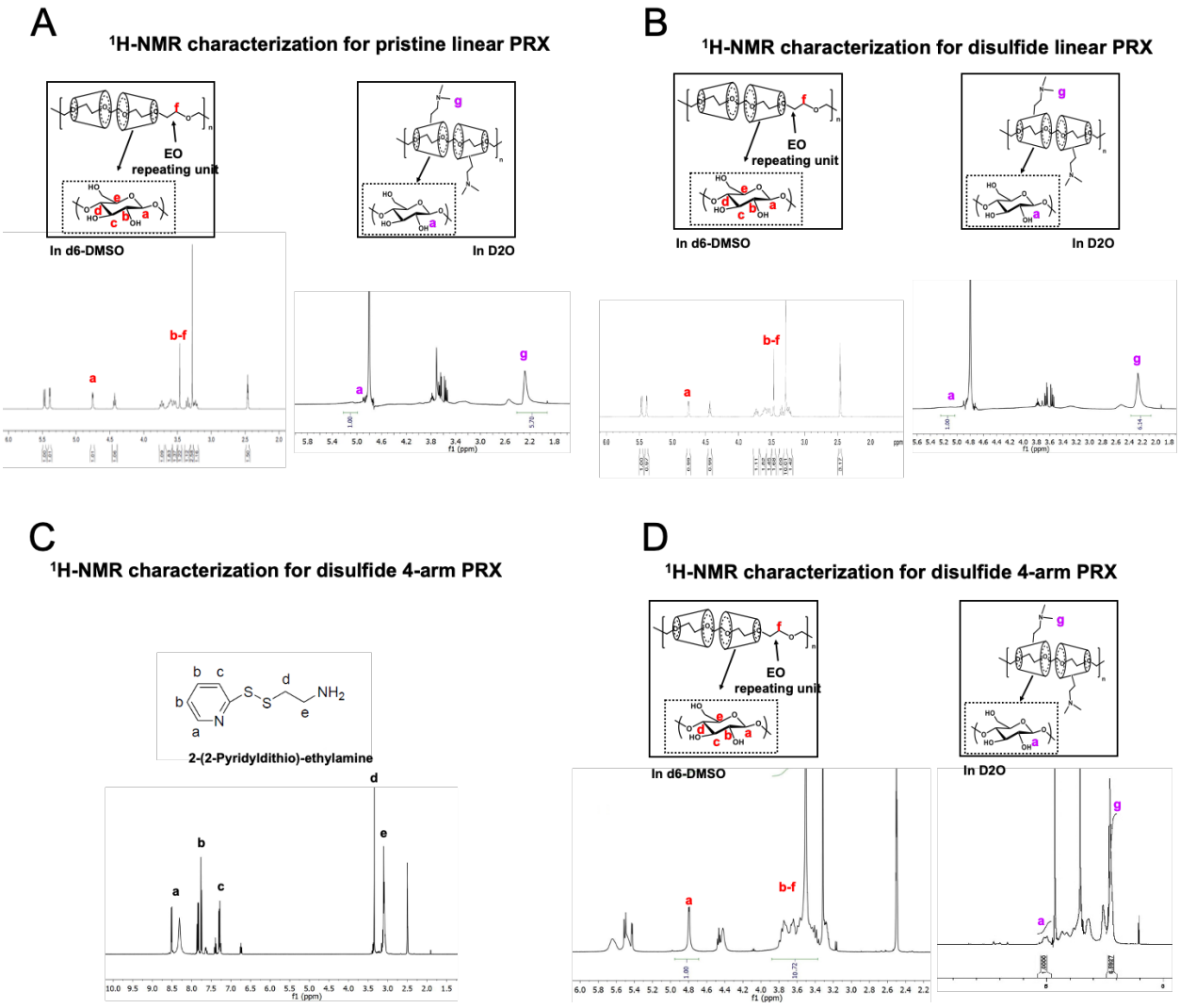

Figure 2-10: ¹H-NMR characterization for disulfide linear and 4-arm PRX.
A) ¹H-NMR characterization of pristine linear PRX in d6-DMSO and pristine linear PRX in deuterated water.
B) ¹H-NMR characterization of disulfide linear PRX d6-DMSO and disulfide linear PRX in deuterated water.
C) ¹H-NMR characterization of pyridyldithiol-cystamine in d6-DMSO. The peaks are consistent with previously published findings[165].
D) ¹H-NMR characterization of disulfide 4-arm PRX in d6-DMSO to characterize the number of α-CDs, and the DMAE-disulfide 4-arm PRX in deuterated water to characterize the density of cationic charge. The integration of C1(H) peak (δa) from α -CD and -CH_2CH_2O- peak (δf) from PEG were used to calculate the total number of α -CD per PRX polymer. The cationic charge density was determined via the integrations of -$N(CH_3)_2$ peak (δg) from DMAE and C1(H) peak (δa) from α -CD in ¹H-NMR spectra as we previously reported[163].

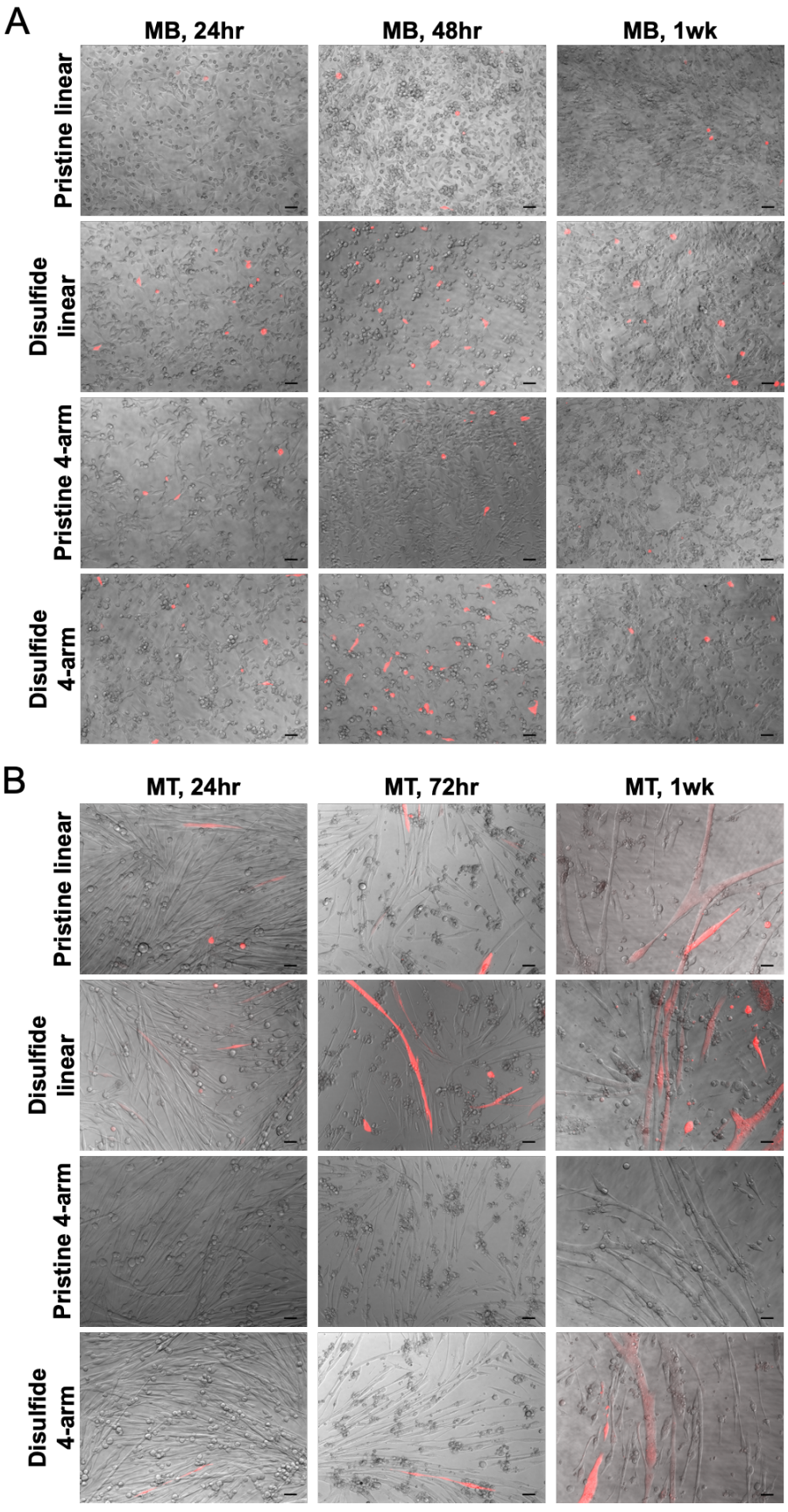
A
MB, 24hr
MB, 48hr
MB, 1wk
Pristine linear
Disulfide linear
Pristine 4-arm
Disulfide 4-arm
B
MT, 24hr
MT, 72hr
MT, 1wk
Pristine linear
Disulfide linear
Pristine 4-arm
Disulfide 4-arm

Figure 2-11: Representative images of tdTomato expression.
Example images of tdTomato (red) and brightfield across pristine linear, disulfide linear, pristine 4-arm, and disulfide 4-arm PRX nanoparticles carrying a tdTomato reporter plasmid.
A) hDMD del45 mdx MB at days 1, 2, and 7. Scale bar represented as 50μm.
B) hDMD del45 mdx MT at days 1, 3, and 7. Scale bar represented as 50μm.

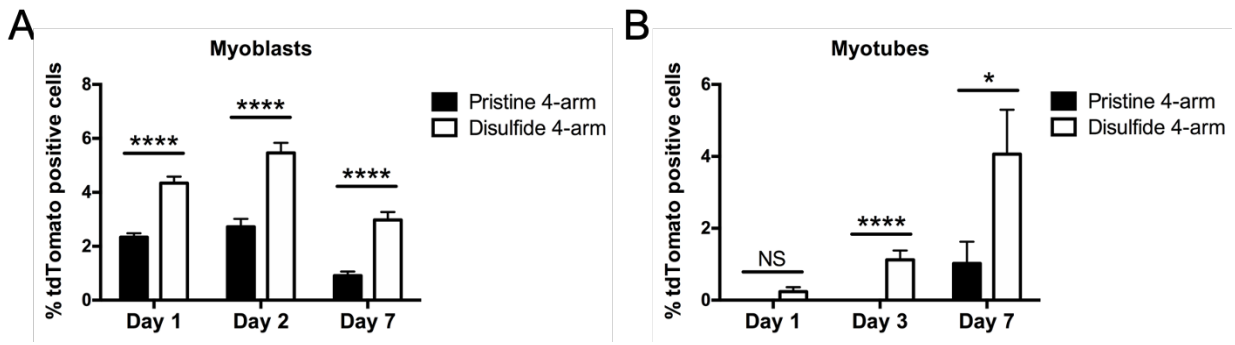

Figure 2-12: Pristine and disulfide 4-arm PRX nanoparticles successfully deliver tdTomato reporter plasmid to muscle cells *in vitro*.
A-B) Transfection efficiencies of pristine and disulfide 4-arm PRX nanoparticles carrying tdTomato reporter plasmid in hDMD del45 mdx MB measured at days 1, 2, and 7 or in hDMD del45 mdx MT measured at days 1, 3, and 7. Transfection efficiency was assessed in triplicate across two independent experiments. Graphs depict average ± standard error of the mean (SEM). NS: not significant; *$p < 0.05$; **$p < 0.01$; ***$p = 0.0001$; ****$p < 0.0001$.

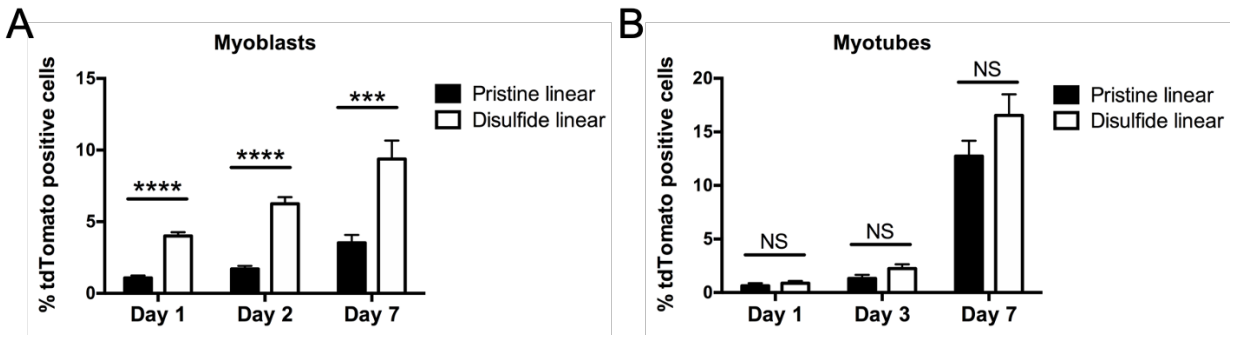

Figure 2-13: Efficiency of tdTomato transfection by pristine linear PRX and disulfide linear PRX.

A-B) Transfection efficiencies of the percent of tdTomato positive cells across pristine and disulfide linear PRX nanoparticles carrying tdTomato reporter plasmid in hDMD del45 mdx MB measured at days 1, 2, and 7 or MT measured at days 1, 3, and 7. Transfection efficiency was assessed in triplicate across two independent experiments for MB and MT. Graphs depict average ± standard error of the mean (SEM). NS: not significant; *$p < 0.05$; **$p < 0.01$; ***$p = 0.0001$; ****$p < 0.0001$.

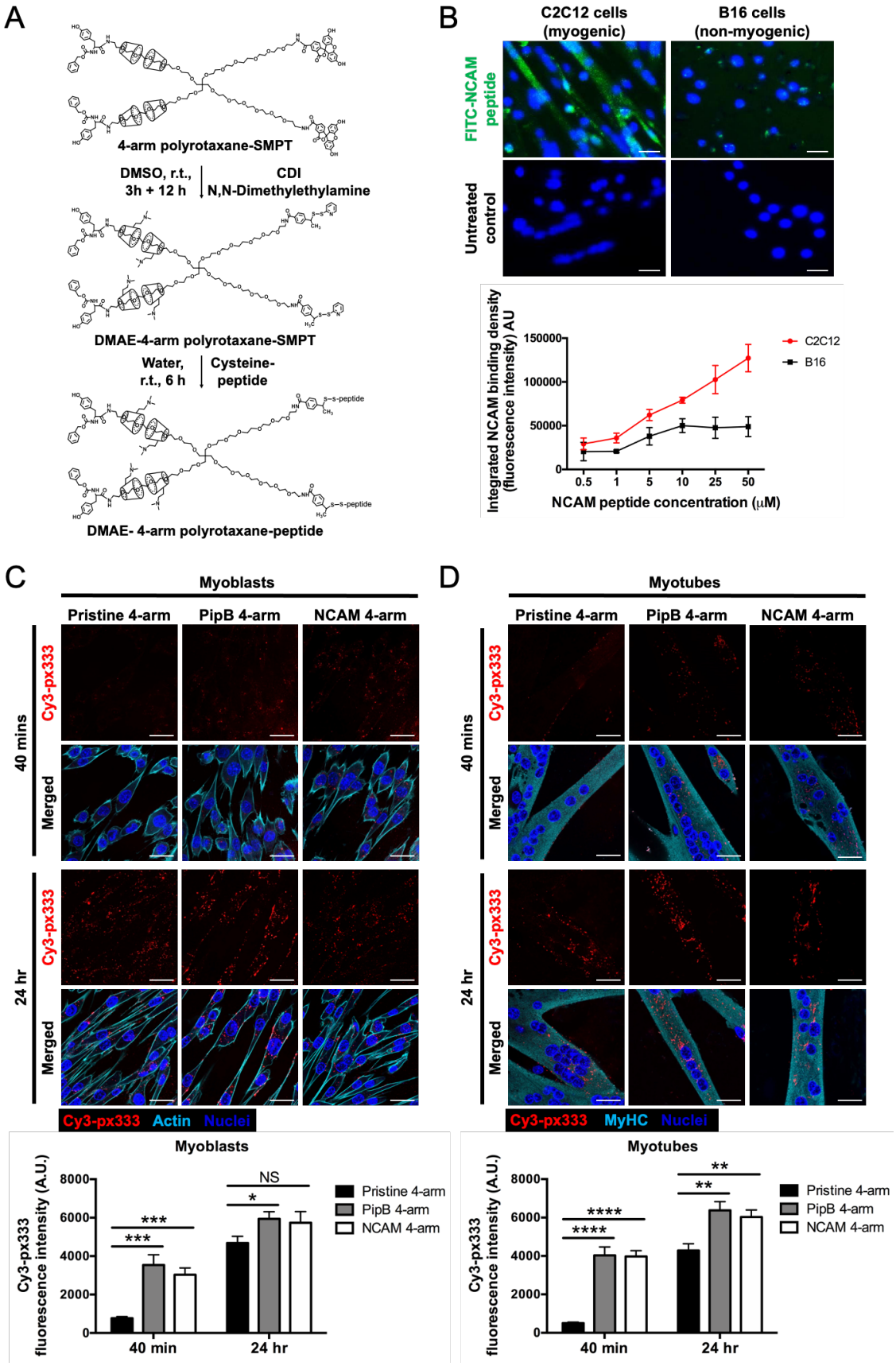
A
4-arm polyrotaxane-SMPT
DMSO, r.t., 3h + 12 h
CDI
N,N-Dimethylethylamine
DMAE-4-arm polyrotaxane-SMPT
Water, r.t., 6 h
Cysteine-peptide
DMAE- 4-arm polyrotaxane-peptide
B
C2C12 cells (myogenic)
B16 cells (non-myogenic)
FITC-NCAM peptide
Untreated control
Integrated NCAM binding density (fluorescence intensity) AU
NCAM peptide concentration (μM)
C2C12
B16
C
Myoblasts
Pristine 4-arm
PipB 4-arm
NCAM 4-arm
40 mins
24 hr
Cy3-px333
Merged
Cy3-px333 Actin Nuclei
Myoblasts
Cy3-px333 fluorescence intensity (A.U.)
40 min
24 hr
NS
Pristine 4-arm
PipB 4-arm
NCAM 4-arm
D
Myotubes
Cy3-px333 MyHC Nuclei
Myotubes

Figure 2-14: Peptide conjugated PRXs enhance the rate and abundance of nanoparticle uptake.
A) Synthesis scheme for PipB and NCAM peptide conjugation on pristine 4-arm PRX. The cysteine modified peptide (NCAM peptide or PipB peptide) was conjugated through a thiol exchange reaction.
B) Imaging of an NCAM peptide labeled with FITC added to C2C12 myotubes or B16 cancer cells (non-muscle cell controls) for 6hrs. Quantification of fluorescence intensity of NCAM peptide on C2C12s is compared to B16 controls across various concentrations of peptide.
C-D) Confocal microscopy images of intracellular trafficking of pristine 4-arm, PipB 4-arm, and NCAM 4-arm PRX nanoparticles carrying Cy3-labeled plasmid (red) in hDMD del45 mdx MB and MT stained with DAPI (blue) and acting (phalloidin, cyan) or myosin heavy chain (MyHC, cyan), respectively. Imaging is shown 40 mins and 24 hrs post-administration. Quantification of Cy3 plasmid intensity in MB and MT at 40 mins and 24 hrs post-administration is shown to demonstrate enhanced uptake with peptide conjugation. Scale bar represented as 25μm. Graphs depict average ± standard error of the mean (SEM). NS: not significant; *$p < 0.05$; **$p < 0.01$; ***$p = 0.0001$; ****$p < 0.0001$.

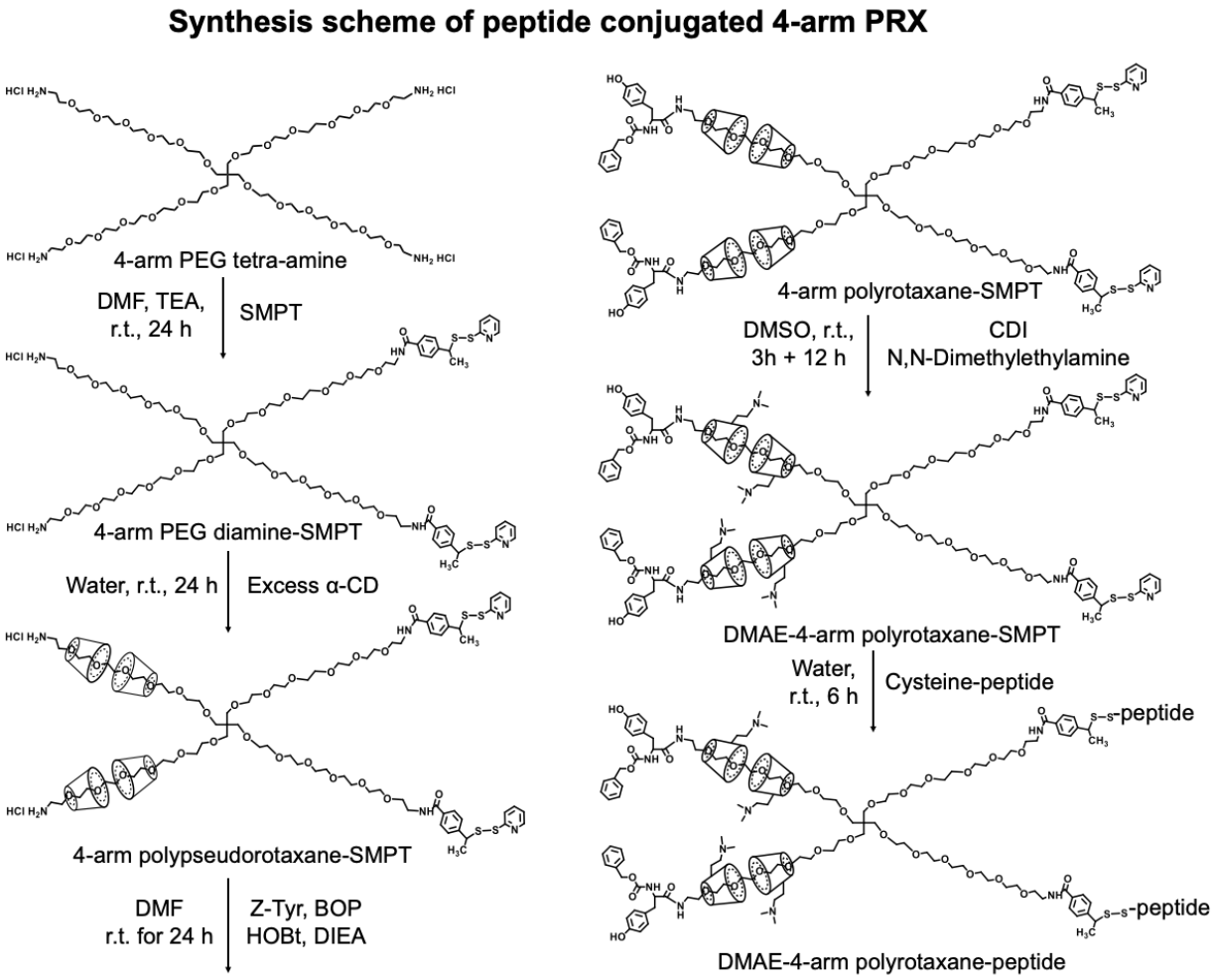

Figure 2-15: Scheme for the synthesis of peptide conjugated 4-arm PRX.
4-arm tetra amine were selectively end-capped with the thiol-reactive functional group SMPT, which provided the conjugation site for cysteine modified peptide. Two arms of a 4-arm PEG tetra-amine polymer were selectively blocked with SMPT in DMF at fixed feed ration (4-arm PEG: SMPT=1:2, molar ratio). Briefly, 4-arm PEG tetra-amine hydrochloride salt 10kDa (103mg) was dissolved in DMF (5mL) with TEA (6mg) before SMPT (7.6mg) was added and stirred at room temperature overnight. The resulting 4-arm PEG diamine-SMPT was precipitated in cold ethyl ether. The formation of 4-arm polypseudorotaxane-SMPT, introducing Z-L-Tyr endcaps and the functionalization of DMAE cationic charge were the same as described for the synthesis of pristine 4-arm PRX[163]. For peptide conjugation, the cysteine modified peptide (NCAM peptide or PipB peptide) were mixed with DMAE-4-arm polyrotaxane-SMPT at a molar ratio of 5:1 in aqueous solution (5mL) and incubated for 2 hrs at room temperature. The pyridine-2-thione generated from the thiol-exchange reaction was collected and quantified by UV-vis spectroscopy to confirm peptide conjugation.

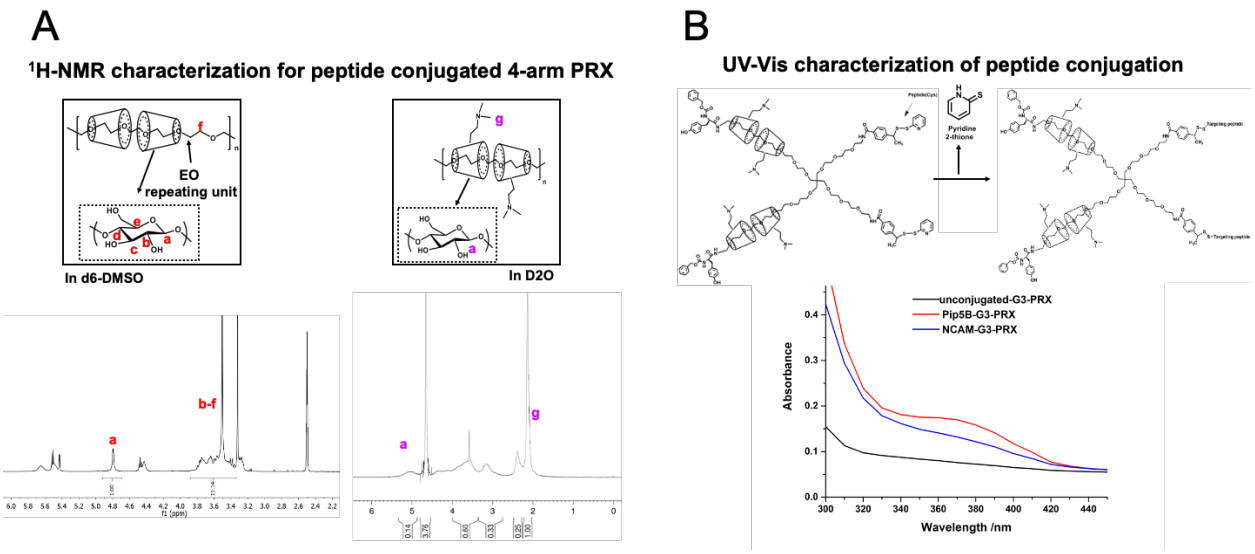

Figure 2-16: Characterization of peptide conjugated 4-arm PRX.
A) ^{1}H-NMR characterization of 4-arm PRX-SMPT in d6-DMSO to characterize the number of α-CDs and DMAE-4-arm PRX-SMPT (the precursor before peptide conjugation) in deuterated water to characterize the cationic charge density.
B) UV-Vis characterization of the pyridine-2-thione molecule which was generated by thiol-exchange reaction between cysteine-modified peptide and DMAE-4-arm PRX-SMPT. The increase in absorbance between 340nm – 380nm confirmed peptide conjugation.

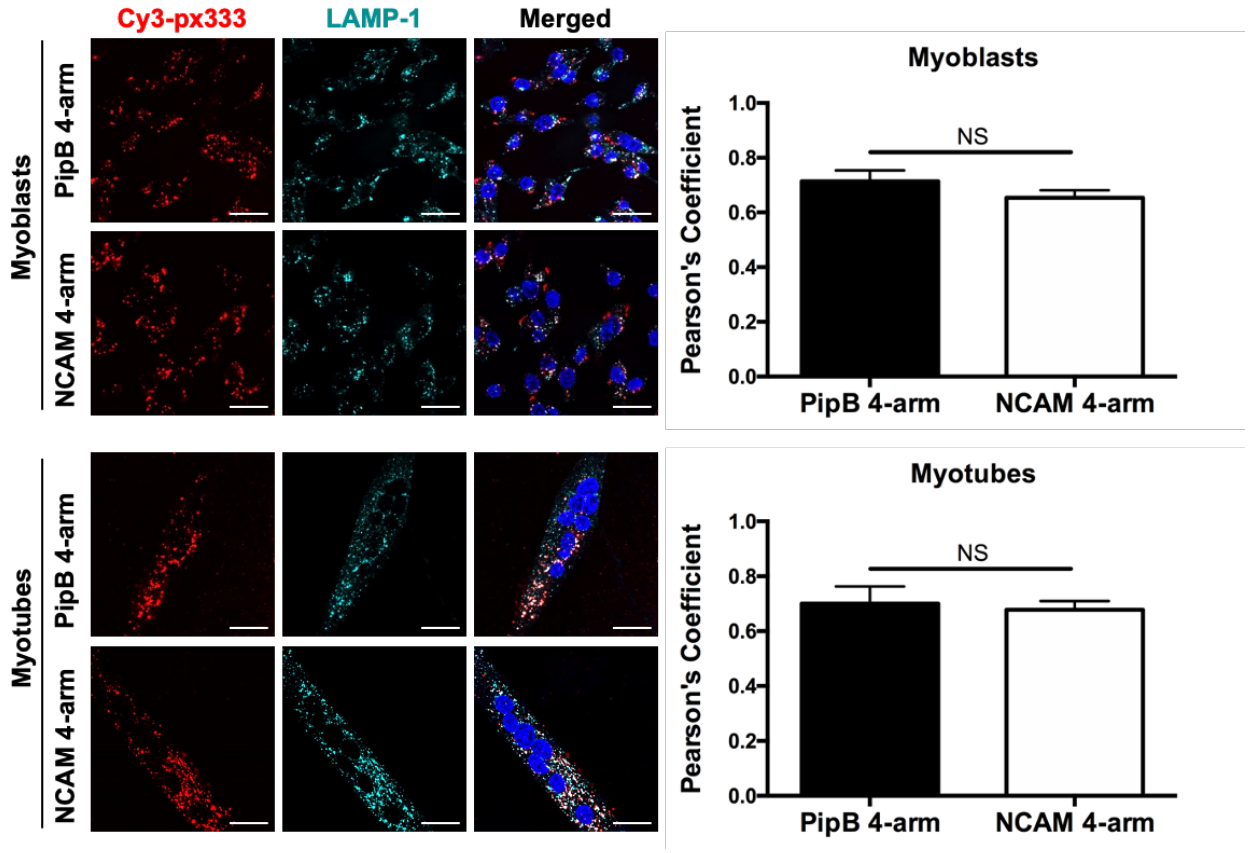

Figure 2-17: Peptide conjugated PRXs are efficiently taken up and can escape the lysosome in muscle cells *in vitro*.
Confocal microscopy images of intracellular trafficking of PipB 4-arm and NCAM 4-arm PRX nanoparticles carrying Cy3-labeled CRISPR/Cas9 plasmid (red) and stained with lysosomal marker, LAMP-1 (cyan) and DAPI (blue) in hDMD del45 mdx MB and MT at 24 hrs. Pearson's correlation coefficient quantification between plasmid and LAMP-1 co-localization for PipB 4-arm and NCAM 4-arm PRXs in MB and MT. Correlation coefficient demonstrate a dissociation between Cy3 plasmid and LAMP-1 signals. Scale bar represented as 25μm. Graphs depict average ± standard error of the mean (SEM). NS: not significant.

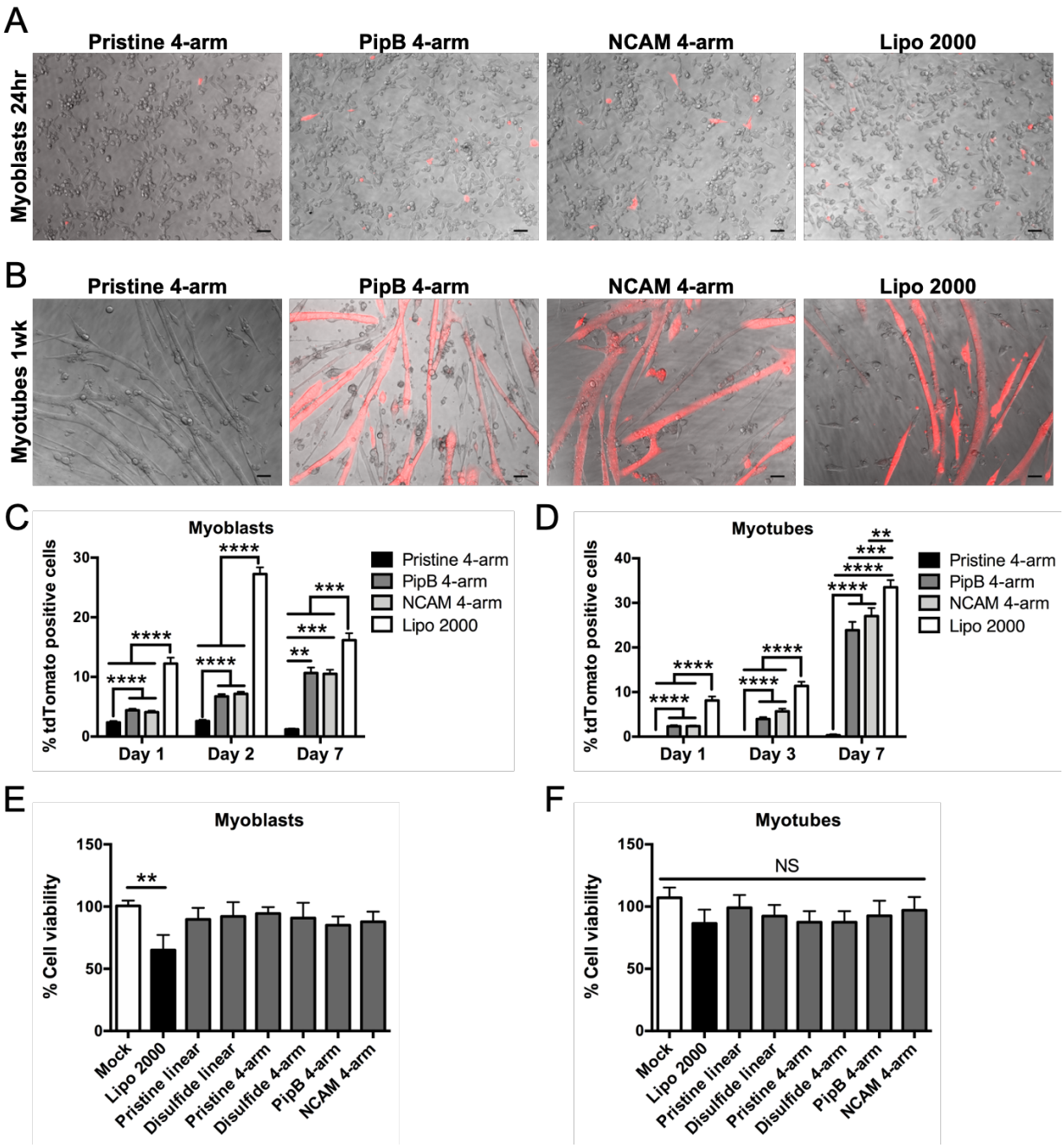
A
Pristine 4-arm
PipB 4-arm
NCAM 4-arm
Lipo 2000
Myoblasts 24hr
B
Pristine 4-arm
PipB 4-arm
NCAM 4-arm
Lipo 2000
Myotubes 1wk
C
Myoblasts
% tdTomato positive cells
Pristine 4-arm
PipB 4-arm
NCAM 4-arm
Lipo 2000
Day 1
Day 2
Day 7
D
Myotubes
% tdTomato positive cells
Pristine 4-arm
PipB 4-arm
NCAM 4-arm
Lipo 2000
Day 1
Day 3
Day 7
E
Myoblasts
% Cell viability
Mock
Lipo 2000
Pristine linear
Disulfide linear
Pristine 4-arm
Disulfide 4-arm
PipB 4-arm
NCAM 4-arm
F
Myotubes
NS
% Cell viability
Mock
Lipo 2000
Pristine linear
Disulfide linear
Pristine 4-arm
Disulfide 4-arm
PipB 4-arm
NCAM 4-arm

Figure 2-18: Peptide conjugated PRXs enhance transfection efficiency *in vitro*.
A-B) Representative images of tdTomato expression (red) merged with brightfield across pristine 4-arm, PipB 4-arm, NCAM 4-arm PRX nanoparticles, and Lipofectamine 2000 carrying tdTomato reporter plasmid in hDMD del45 MB at day 1 and hDMD del45 MT at day 7. Scale bar represented as 50μm.
C-D) Transfection efficiencies of pristine 4-arm, PipB 4-arm, NCAM 4-arm PRXs, and Lipofectamine 2000 measured at days 1, 2, and 7 or days 1, 3, and 7, respectively. Transfection efficiency was assessed in triplicate across two independent experiments. Graphs depict average ± standard error of the mean (SEM).
E-F) Cell viability determined by MTS assay of hDMD del45 MB and MT treated with all PRX formulations and Lipofectamine 2000 24 hrs and 72 hrs post-treatment, respectively. Cell viability was assessed in triplicate. Graphs depict average ± standard deviation (SD). NS: not significant; *$p < 0.05$; **$p < 0.01$; ***$p = 0.0001$; ****$p < 0.0001$.

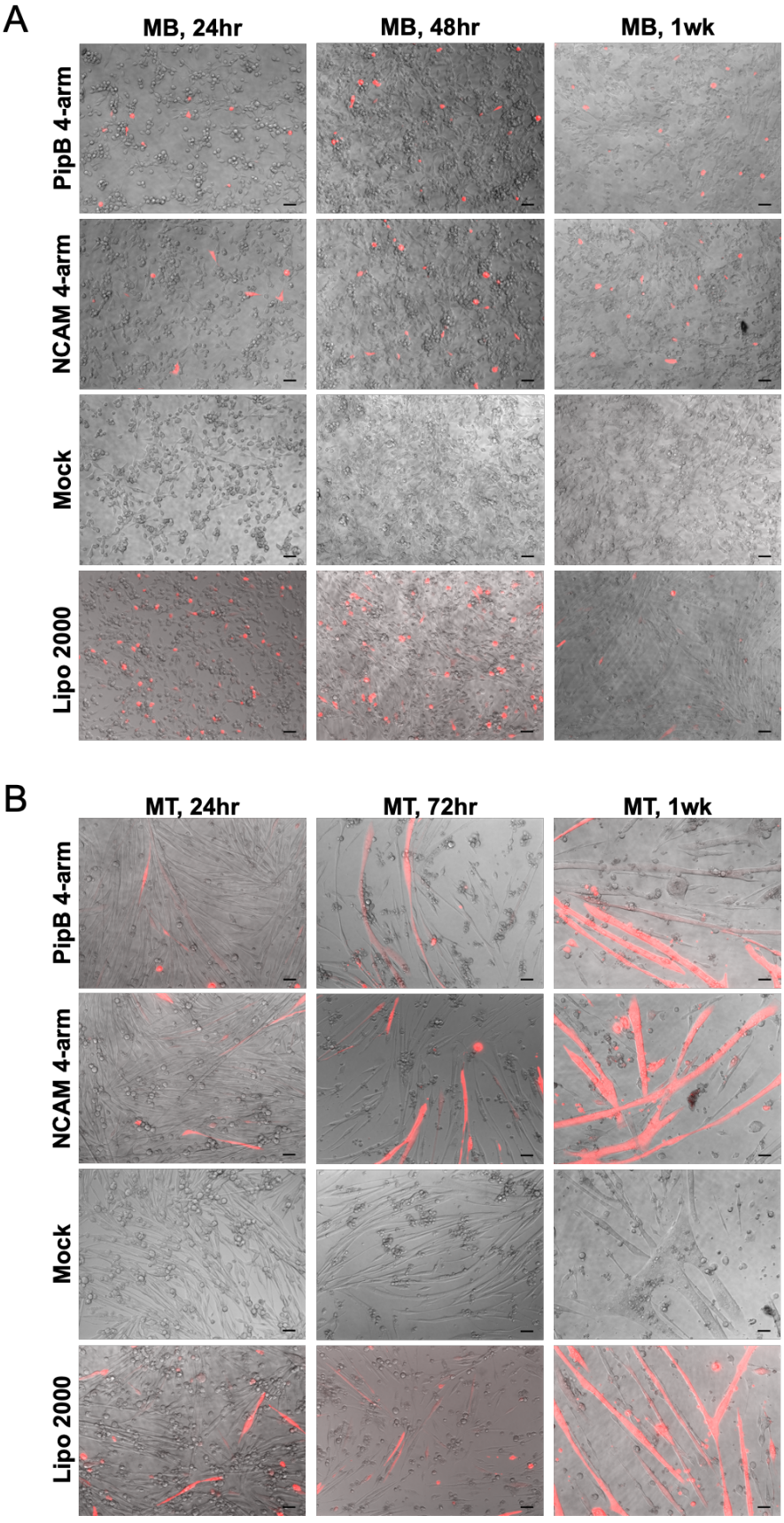
A
MB, 24hr
MB, 48hr
MB, 1wk
PipB 4-arm
NCAM 4-arm
Mock
Lipo 2000
B
MT, 24hr
MT, 72hr
MT, 1wk
PipB 4-arm
NCAM 4-arm
Mock
Lipo 2000

Figure 2-19: Representative images of tdTomato expression.
Example images of tdTomato (red) and brightfield across pristine 4-arm, PipB 4-arm, NCAM 4-arm PRX nanoparticles, and Lipofectamine 2000 carrying a tdTomato reporter plasmid.
A) hDMD del45 mdx MB at days 1, 2, and 7. Scale bar represented as 50μm.
B) hDMD del45 mdx MT at days 1, 3, and 7. Scale bar represented as 50μm.

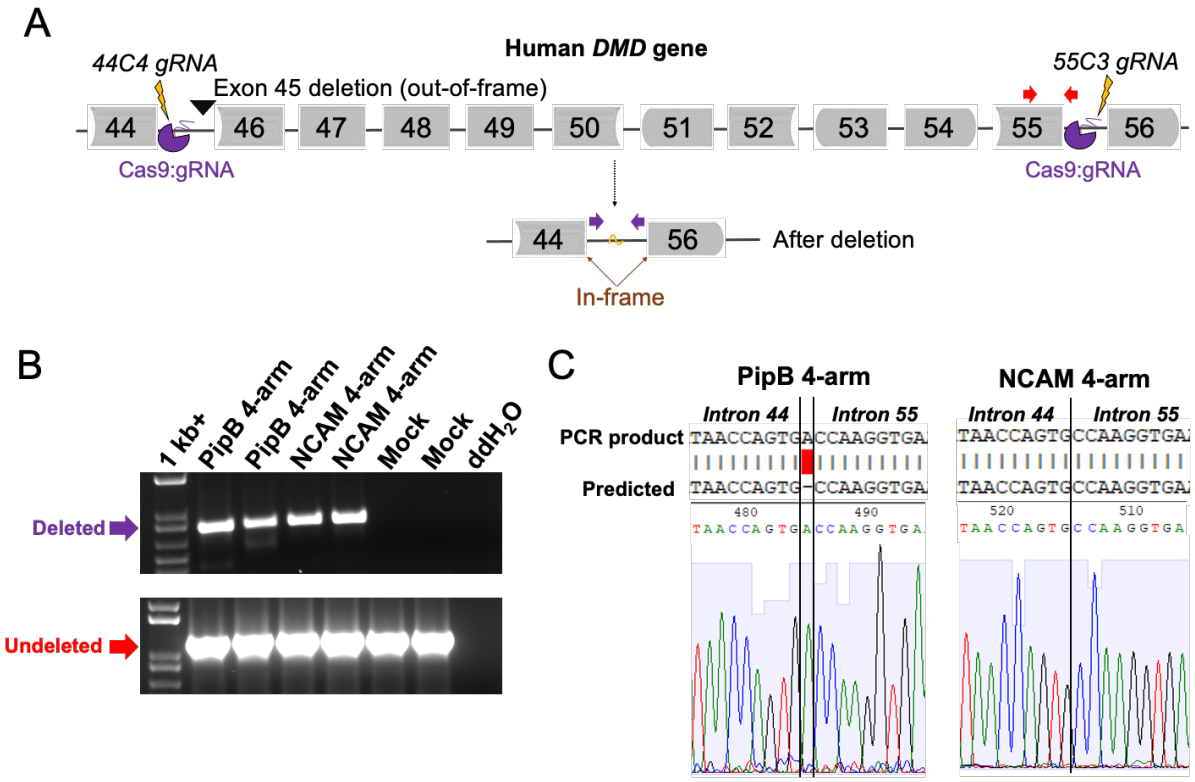

Figure 2-20: Efficient CRISPR/Cas9 editing of DMD exons 45-55 in primary hDMD del45 mdx muscle cells after PipB 4-arm and NCAM 4-arm PRX delivery.
A) Cartoon depicting the region of the human *DMD* gene (not to scale) in hDMD del45 mdx muscle cells targeted for CRISPR/Cas9 deletion. One gRNA to intron 44 and one to intron 55 target the Cas9 nuclease to generate double stranded breaks and result in removal of exons 45-55. This creates an in-frame deletion that restores the reading frame for the out-of-frame exon 45 deletion (black arrow head).
B) PCR on genomic DNA to detect successful deletion of exons 45-55. One primer pair (purple arrows in A) flanks the deletion region in introns 44 and 55 and produces a 788bp band when the deletion has occurred. Another primer pair (red arrows in A) is located internal to the deletion and produces a band at 1,201bp for the undeleted allele as a control. Successful deletion of exons 45-55 was seen in MB after CRISPR delivery by PipB 4-arm and NCAM 4-arm PRXs. Untreated (mock) and water only (ddH_2O) are also shown.
C) Sequencing of the rejoining site revealed successful deletion and rejoining of introns 44 and 55. Example sequences traces are shown demonstrating a 1bp insertion for MB PipB 4-arm and seamless rejoining for MB NCAM 4-arm. These intronic indels are expected to be inconsequential for dystrophin protein production.

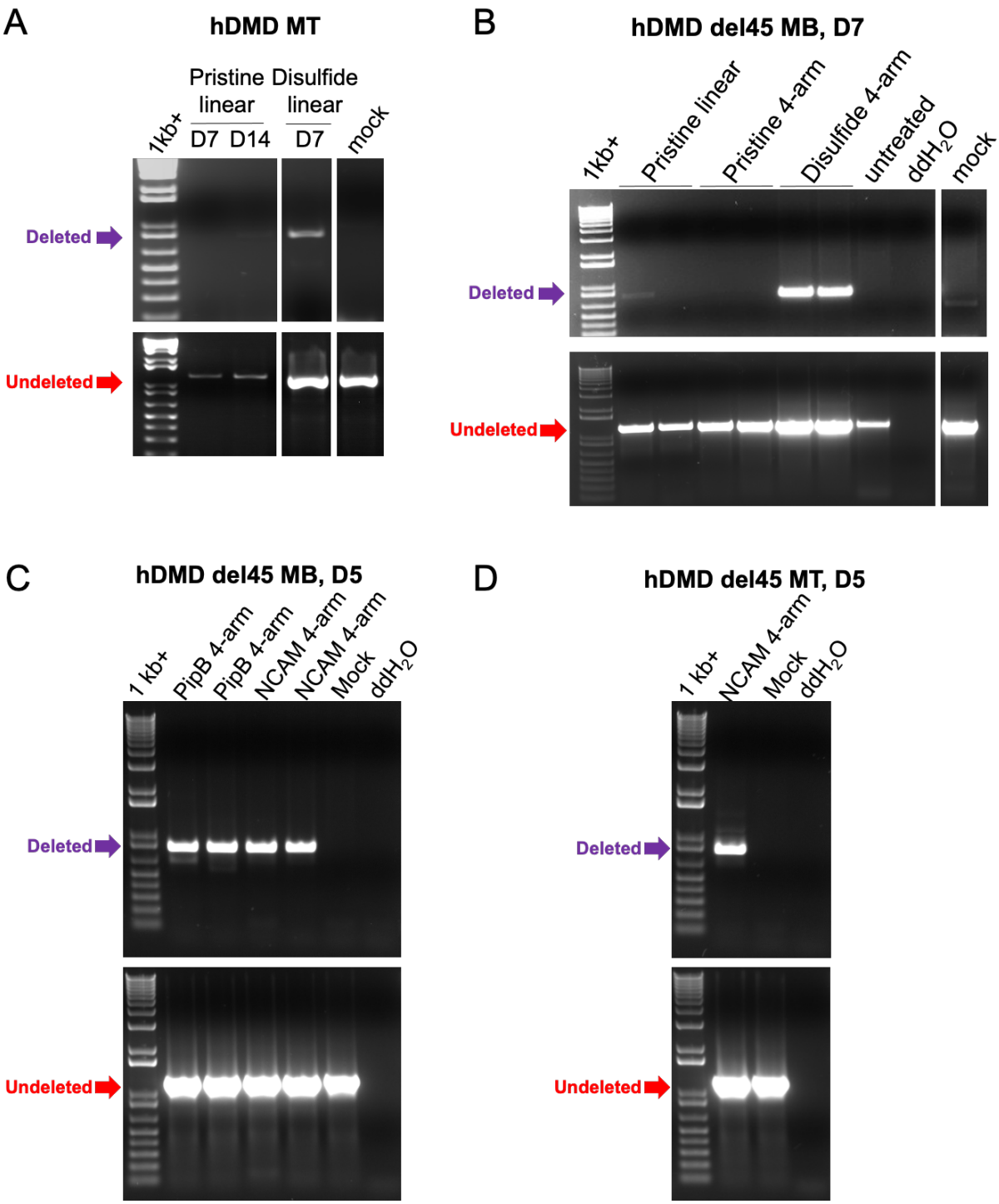
A
hDMD MT
Pristine linear
Disulfide linear
1kb+
D7
D14
D7
mock
Deleted
Undeleted
B
hDMD del45 MB, D7
1kb+
Pristine linear
Pristine 4-arm
Disulfide 4-arm
untreated
ddH2O
mock
Deleted
Undeleted
C
hDMD del45 MB, D5
1 kb+
PipB 4-arm
PipB 4-arm
NCAM 4-arm
NCAM 4-arm
Mock
ddH2O
Deleted
Undeleted
D
hDMD del45 MT, D5
1 kb+
NCAM 4-arm
Mock
ddH2O
Deleted
Undeleted

Figure 2-21: Effective CRISPR/Cas9 editing of DMD exons 45-55 in primary murine muscle cells.
A) PCR on genomic DNA to detect successful deletion of exons 45-55 (purple arrow) or the undeleted allele (red arrow) in wildtype hDMD MT with pristine and disulfide linear PRXs at day 7 (D7) or day 14 (D14). Untreated (mock) is also shown.
B) PCR on genomic DNA to detect successful deletion of exons 45-55 (purple arrow) or the undeleted allele (red arrow) in hDMD del45 MB with pristine linear and pristine and disulfide 4-arm PRXs at day 7 (D7). Untreated (mock) and water only (ddH_2O) are also shown.
C) PCR on genomic DNA to detect successful deletion of exons 45-55 (purple arrow) or the undeleted allele (red arrow) in hDMD del45 MB with peptide conjugated 4-arm PRXs at day 5 (D5). This is a second independent experiment of Figure 2-21B. Untreated (mock) and water only (ddH_2O) are also shown.
D) PCR on genomic DNA to detect successful deletion of exons 45-55 (purple arrow) or the undeleted allele (red arrow) in hDMD del45 MT with NCAM 4-arm PRX at day 5 (D5). Untreated (mock) and water only (ddH_2O) are also shown.

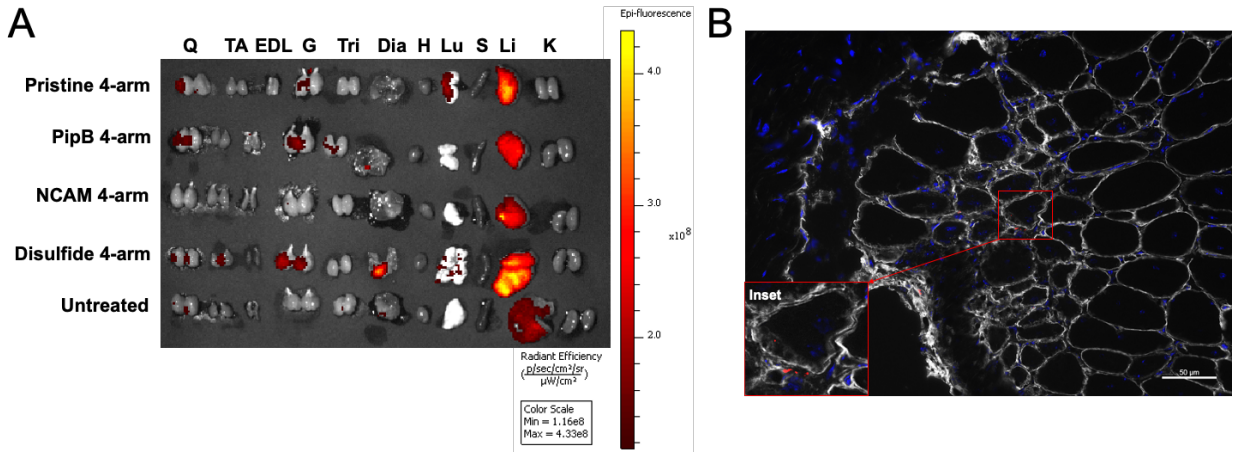

Figure 2-22: Intravenous delivery of PRX nanoparticles inefficiently traffic to muscle and appear confined to the basal lamina and extracellular space.
A) Cy3-labeled plasmid complex with PRX assessed for biodistribution using the IVIS Spectrum *in vivo* imaging system. Muscle tissues and off-target organs were harvested 24 hrs after administration. Q (quadriceps), TA (tibialis anterior), EDL (extensor digitorum longus), G (gastrocnemius), Tri (triceps), Dia (diaphragm), H (heart), Lu (lung), S (spleen), Li (liver), and K (kidney).
B) Imaging of gastrocnemius muscle 24 hr after intravenous delivery of PipB 4-arm PRX containing Cy3-labeled plasmid (red), muscle fibers are stained with laminin (gray), and nuclei are stained with DAPI (blue). PRX formulations are found exclusively outside fibers residing near the basal lamina and/or interstitial space.

Chapter 3 – Identification of Novel AAV Capsid Variants by Screening a Peptide-display Library

Abstract

Duchenne muscular dystrophy (DMD) is a monogenic disease caused by out-of-frame mutations in the *DMD* gene, which results in lack of dystrophin production. Systemic delivery of CRISPR/Cas9 using adeno-associated viruses (AAV) has demonstrated therapeutic success in models of DMD. However, gene correction is not a life-long therapy due to the natural myonuclear turnover of skeletal muscle and inability to efficiently target muscle stem cells (MuSCs), thereby reducing the number of CRISPR-corrected myonuclei and dystrophin expression over time. We hypothesize that skeletal muscle and MuSCs will likely require genomic correction in order to achieve a long-lasting therapy. Here, we develop and screen an AAV peptide-display library, which displays a unique heptameric peptide on the capsid surface that corresponds to the packaged vector genome, in order to select for novel AAV capsid variants with enhanced tropism to skeletal muscle and MuSCs. After two consecutive rounds of selection *in vivo*, we prioritize capsid candidates with high fold enrichment after each step in the screening process and low fold enrichment in off-target organs for secondary validation. As a result, we identify 9 unique and highly enriched skeletal muscle and MuSC-tropic AAV capsid variants with reduced enrichment in the liver. Ongoing validation studies will determine which capsid variants have superior transduction efficiency to skeletal muscle and MuSCs. The identification of skeletal

muscle and MuSC-tropic AAVs offers potential to provide a long-lasting supply of CRISPR-corrected MuSCs and a life-long sustainable therapy for DMD.

Introduction

Duchenne muscular dystrophy (DMD) is a progressive muscle wasting disorder typically caused by frameshifting mutations in the *DMD* gene encoding dystrophin. Due to the nature of these mutations, DMD is amenable to gene editing (e.g., CRISPR/Cas9) and gene replacement strategies (e.g., mini- and micro-dystrophin). Adeno-associated viruses (AAVs) are small, naturally occurring viruses that are capable of infecting a wide range of vertebrates including humans[111,186]. Recombinant AAVs generated using naturally occurring serotypes are the most commonly used vehicles to systemically deliver gene editing and gene replacement strategies in preclinical and clinical studies[187,188]. Yet, systemic delivery of AAV-mediated gene therapies remains a substantial challenge for neuromuscular disorders, such as DMD, in which all muscles are affected and comprise ~40% of the total body mass.

Studies have shown that a single systemic administration of AAV carrying CRISPR/Cas9 in dystrophic mice restores dystrophin expression in a variety of muscle groups, but CRISPR-corrected myonuclei and dystrophin expression is lost over time[116,119]. The loss of dystrophin and CRISPR-corrected myonuclei is likely due to several factors including: i) insufficient levels of dystrophin to protect the weakened sarcolemmal-membrane that exists in dystrophic muscle, ii) inefficient targeting of muscle stem cells (MuSCs) by AAV so any new fibers that arise from regeneration will not be CRISPR-corrected and will continue to dilute the percent of edited myonuclei in

differentiated skeletal muscle, and iii) natural myonuclear turnover in skeletal muscle further reduces number of gene-edited myonuclei[119]. The inability of AAV to target MuSCs is further supported by three independent studies, which confirm that AAV-CRISPR inefficiently transduces MuSCs resulting in gene editing efficiencies of ~1-3% in the *mdx* mouse[71,117,118]. Thus, AAV-mediated gene therapies will likely require MuSCs targeting in order to achieve a self-sustaining long-lasting therapy for DMD.

Therapeutic applications of AAV-mediated gene therapies for neuromuscular diseases are further limited by selective transduction as the most commonly used AAV serotypes are sequestered in non-therapeutic organs, such as the liver[116,119,189]. Several groups have attempted to overcome the aforementioned limitations either by increasing the dose of gRNA to Cas9 AAV vector ratio, which enhances gene-editing efficiency[115,190] or implementing a combinatorial treatment whereby AAV-CRISPR and AAV-micro-dystrophin are co-administered, which maintains long-term dystrophin expression[119]. Although these results are encouraging, these strategies require a large viral dose that may induce immune-related toxicities previously reported in large animal models of DMD[79,134] as well as in ongoing human DMD clinical trials[59,191]. Moreover, the need for a high vector dose creates additional challenges for AAV manufacturing and scalability[135]. Taken together, we hypothesize that a novel AAV capsid variant capable of enhanced skeletal muscle and MuSC transduction along with reduced liver targeting, will result in a more efficacious and longer-lasting gene therapy for DMD.

AAV capsid engineering is an effective strategy to generate novel capsid variants with new properties such as re-directed tissue tropism. AAV capsid engineering technology can be divided into three main categories: i) rational design[192,193], ii)

computational design by machine learning[194,195] and iii) high throughput capsid library screening[196-199]. Novel capsids with re-directed tissue tropism have been successfully generated using site-directed mutagenesis by rational design[200,201]. However, there are major pitfalls with rational design, which requires a mechanistic understanding of AAV transduction, host-receptor interactions as well as capsid structural information[202,203]. As a result, rational design is time consuming and often yields a low diversity of capsid mutants for experimentation[204]. Machine learning is a recently developed method that uses an algorithm trained on experimental data to predict whether capsid variants will generate a viable capsid to successfully package the DNA vector payload[194]. However, machine learning relies on experimental data and is currently unable to predict which variants will have enhanced tissue-specific transduction properties due to the same limitations affecting site-directed rational design[204]. Currently, an advantageous method for identifying capsid variants with re-directed tissue tropism in a high throughput fashion is by screening diverse capsid libraries generated via capsid shuffling[205,206] or peptide-display[197,198]. Peptide-display libraries are capsids containing unique random peptide sequences displayed on the surface of the viral capsid. The use of peptide-display libraries coupled with *in vitro* and/or *in vivo* selection has led to the identification of capsid variants with newly acquired tissue and cell type specificity to the lung[207], endothelial cells[208], neurons[209-212], astrocytes[212], T lymphocytes[213], heart[213-216] and skeletal muscle[215]. However, no study has been conducted to identify AAV capsid variants with specificity to MuSCs.

In this study, we further confirm what others have reported and demonstrate that systemic delivery of AAV9-CRISPR is unable to target MuSCs in adult and inefficiently

targets MuSCs in neonate dystrophic mice. We utilize an AAV9 peptide display library to select and identify novel AAV capsid variants with enhanced targeting to both MuSCs and skeletal muscle. In addition, we refine the identification of lead AAV candidates by selecting for AAV capsids with high skeletal muscle and/or MuSC-specific enrichment along with reduced enrichment in the liver. The use of peptide display libraries allows for the identification of novel AAV capsid variants capable of transducing less permissive cell types such as MuSCs. Additional validation studies are ongoing in order to confirm the efficacy of lead skeletal muscle and MuSC-specific AAV capsid variants.

Materials and Methods

Mice

All animal care and work were conducted under protocols approved by the UCLA Animal Research Committee in the Office of Animal Research Oversight. hDMD del45 mdx mice were generated and genotyped as described[77].

Cell lines

AAV packaging was carried out in the AAVpro293T (HEK293T) cell line, purchased from Takara Bio Inc. HEK293T cells were maintained in Dulbecco's Modified Eagle Medium (Thermo Fisher) supplemented with 10% heat-inactivated fetal bovine serum (Thermo Fisher), 1% MEM Non-Essential Amino Acids (NEAA, Thermo Fisher), 1% GlutaMAX™ supplement (Thermo Fisher), and 1% Penicillin-Streptomycin (P/S, Thermo Fisher). HEK293T cells were passaged using 0.05% Trypsin-EDTA (Thermo Fisher).

Constructs

To test AAV9 transduction and gene editing in skeletal muscle and muscle stem cells the following constructs were used: CK8e-Cas9 (pAAV-CK8e-Cas9), CMV-Cas9 (pAAV-CMV-Cas9) and gRNA vectors (pAAV-Target44C4+55C3). The original Cas9 (pAAV-CK8e-Cas9) and targeting vector plasmids (pAAV-Target) were a gift from Dr. Jeffrey S. Chamberlain and were generated as described[73]. Our gRNAs targeting introns 44 (gRNA 44C4) and 55 (gRNA 55C3) were cloned into the pAAV-Target plasmid in tandem (referred to as pAAVTarget-44C4+55C3). pAAV-CMV-Cas9 plasmid was obtained from Addgene (plasmid #106431).

To generate recombinant AAV libraries, we generated a Cap-depleted Rep plasmid (pRep). pRep-Cap plasmid (Cell Biolabs Inc.) was used to generate Cap-depleted Rep plasmid (pRep). pRep-Cap was digested with ZraI and SrfI to partially remove the rep gene and remove the capsid coding gene. Gibson Assembly (New England BioLabs) was used to clone in the partially removed rep gene encoded by a gBlock (IDT) that contained homology arms against the ZraI and SrfI digested pRep-Cap backbone.

To generate the AAV library plasmid: The ITR-containing Cap(NNK_7) library plasmid (pAAV-library) was generated using NEBuilder HiFi DNA Assembly (New England BioLabs), hereafter referred to as pCapNNK_7. In brief, a 2,221bp gBlock (IDT) encoding the AAV9 capsid gene was synthesized (Cap9-modified) to contain two incompatible SfiI restriction sites as described previously[208]. The Cap9-modified gBlock also contained an insertion of two adenines in between the SfiI loci creating a frameshift

in order to prevent capsid formation from plasmids that had unsuccessful 21 oligonucleotide insertion by cloning[208]. In order to maintain the reading frame of the assembly activating protein (AAP) and the capsid reading frame, which is required for VP oligomerization during capsid assembly[217], a 487bp gBlock (IDT) encoding the p40 promoter was synthesized (p40). The p40 and Cap9-modified gBlocks were cloned in MluI- and AfeI-digested ITR-containing plasmid (Cell Biolabs Inc.) using NEBuilder HiFi DNA Assembly according to the manufacturer's instructions. The newly assembled plasmid was the precursor plasmid (pCap9-precursor) used to clone the randomized 21-oligonucleotide using the incompatible SfiI loci to create pAAV-library. To create pAAV-library, a 79bp single-stranded oligonucleotide (ss-oligoNNK_7) fragment containing the randomized NNK_7 library flanked by homology arms against the incompatible SfiI loci was synthesized (IDT). pAAV-library was assembled by SfiI digestion of the pCap9-precursor plasmid, and assembled with ss-oligoNNK_7 using NEBuilder HiFi DNA Assembly according to the manufacturer's instructions. In theory, the pAAV-library plasmid has 32 possible DNA permutations and 20 possible amino acid permutations, which results in a theoretical diversity of 32^7 (3.4×10^{10}) DNA permutations and 20^7 (1.28×10^9) amino acid permutations or capsid variants.

After the first round of screening we generated tissue-enriched ITR-containing Cap(NNK_7) library plasmid for skeletal muscle, MuSC and Heart. We generated tissue-enriched capsid library plasmids to produce tissue-enriched rAAV libraries to carry out the second and final round of selection. To do so, we isolated AAV DNA after the first round of selection from skeletal muscle, heart and muscle stem cells using the Quick-DNA miniprep plus kit (Zymo Research). Then, we amplified a 1,016bp fragment

containing the tissue-enriched NNK_7 variants using primers 3-NEST-F (5'-CCTTACCAGCACGGTCCAGG-3') and 3-NEST-R (5'-GCTTGTCCTTGTTGAAGGCC-3') and pooled amplicons among the same tissue across mice (i.e., skeletal muscle enriched NNK_7 amplicons were pooled). Finally, we digested the recipient precursor plasmid, pCap9-precursor, with BamHI-HF and BsiWI-HF and inserted the tissue-enriched NNK_7 variants using NEBuilder HiFi DNA Assembly according to the manufacturer's instructions to assemble tissue-enriched library plasmids for skeletal muscle (pSkMu-library), heart (pHeart-library), and muscle stem cells (pMuSC-library).

Recombinant AAV-CRISPR/Cas9 and AAV Library production

AAV9-CRISPR/Cas9: pAAV-CK8e-Cas9, pAAV-AAV-CMV-Cas9, and pAAV-Target44C4+55C3 plasmids were shipped to Virovek Inc. for production and purification of recombinant AAV9-CK8e-Cas9, AAV9-CMV-Cas9, and AAV9-Target. Virovek Inc. purified recombinant AAV9 using the cesium chloride ($CsCl_2$) density ultracentrifugation method and quantified viral titer by qPCR using their ITR primers. Purity of capsid viral proteins was determined by SDS-PAGE (9% polyacrylamide gels).

AAV Library: AAVpro HEK293T cells were seeded in 15-cm dishes at a density of 1.5×10^7 cells/dish. The following day, each plate was transfected with 18μg of Helper plasmid (pHelper; Cell Biolabs Inc.), 18μg of pRep, and 0.5μg of ITR-containing Cap(NNK_7) library plasmid (pCapNNK_7) using TransIT-VirusGEN® (Mirus) according to the manufacturer's instructions. Cells and supernatant were harvest 72 hours post-transfection and provided to Virovek Inc. for purification. Virovek Inc. purified recombinant AAV using the cesium chloride ($CsCl_2$) density ultracentrifugation method,

determined purity by SDS-PAGE and quantified titer by qPCR using their ITR primers. Purity of capsid viral proteins was determined by SDS-PAGE (9% polyacrylamide gels).

Assessing systemic AAV9-CK8e-CRISPR/Cas9 delivery and gene editing in skeletal muscle

hDMD del45 mdx neonates were systemically dosed via intraperitoneal (i.p.) injection with 1.5 x 10^{12} vg/vector at postnatal day 4 (p4). One mouse was injected with Hank's Balanced Salt Solution (HBSS, Thermo Fisher) and used as the vehicle control. Muscles were harvested ~6 weeks post-injection and half of the muscles were taken for mCherry immunostaining and the other half for dystrophin immunostaining.

For dystrophin immunostaining, muscles were harvested and directly flash frozen in isopentane. For mCherry immunostaining, muscles were harvested and fixed in 1% PFA overnight. The following day, muscles were transferred to 5% sucrose for at least 6hr, then transferred to 30% sucrose overnight before being flash frozen in isopentane.

Immunostaining

Harvested muscles were flash frozen or PFA pre-fixed then flash frozen in isopentane and cryosectioned in intervals of 10μm thickness throughout the majority of the muscle tissue. For dystrophin staining, sections were fixed in chilled acetone for 1 – 2 min, then incubated in TrueBlack (Biotium, 1:20 in 70% ethanol) for 30 sec – 1min, then incubated in blocking buffer (DPBS with 5% horse serum and 10% goat serum) for at least 1hr. Primary antibodies consisting of rabbit-anti-dystrophin (1:200, Abcam, ab15277) and rat-anti-laminin (1:20, R&D Systems) were added in TBS and 1% goat

serum overnight at 4°C. The next day secondary antibodies consisting of goat-anti-rabbit IgG fluorescein (1:150, Vector Laboratories) and goat-anti-rat IgG AlexaFluor^{TM}647 (1:250, Thermo Fisher) were incubated for 1hr and the slides were mounted with VECTASHIELD containing DAPI (Vector Laboratories) and imaged on the Axio Observer Z1 microscope (Zeiss).

For mCherry immunofluorescence, TrueBlack (Biotium, 1:20 in 70% ethanol) was used as in dystrophin staining. Blocking buffer consisting of 0.25% gelatin, 0.1% tween, and 3% BSA was added for at least 1hr. Rabbit-anti-laminin (1:200, Millipore Sigma) was added in TBS and 1% goat serum overnight at 4°C. The next day goat-anti-rabbit IgG AlexaFluor^{TM}647 (1:250, Thermo Fisher) were incubated for 1hr and the slides were mounted with VECTASHIELD containing DAPI (Vector Laboratories) and imaged on the Axio Observer Z1 microscope (Zeiss).

Assessing systemic AAV9-CMV-CRISPR/Cas9 delivery and gene editing in muscle stem cells

Two groups of hDMD del45 mdx neonates were used to test AAV9-CMV-CRISPR/Cas9 satellite cell (MuSC) transduction and exon 45-55 editing *in vivo*. The low-dose group (n=3) was dosed intraperitoneally (i.p.) at p4 with 5 x 10^{11} vg/vector (1 x 10^{12} total vg) and the high-dose group (n=3) were dosed i.p. at p5 with 1.5 x 10^{12} vg/vector (3 x 10^{12} total vg). Skeletal muscles from the low-dose and high-dose cohorts were harvested ~7 weeks post-injection and processed for MuSC isolation and cell sorting by FACS (refer to *Isolation and fluorescent activated sorting of muscle stem cells* section for details).

Two groups of hDMD del45 mdx adults were used to test AAV9-CMV-CRISPR/Cas9 satellite cell (MuSC) transduction and exon 45-55 editing *in vivo*. The low-dose group (n=3) was dosed retro-orbitally (r.o) at ~6 weeks with 1.5 x 10^{12} vg/vector (3 x 10^{12} total vg). Skeletal muscles were harvested ~2 weeks post-injection and processed for MuSC isolation and cell sorting by FACS (refer to *Isolation and fluorescent activated sorting of muscle stem cells* section for details).

Isolation and fluorescent activated cell sorting of muscle stem cells:

Muscle stem cell (MuSC) isolation from hDMD del45 mdx mice dosed with AAV9-CMV-CRISPR/Cas9 was performed as previously described[218]. In brief, muscle tissues were isolated, dissociated and minced in 500U/mL collagenase II (Worthington) and incubated at 37°C with slow agitation for 30 mins. Minced tissues were further dissociated using a mixture of 1.5U/mL collagenase D (Roche) and 2.4U/mL dispase (neutral protease, Worthington) and incubated at 37°C with slow agitation for 60 mins. Finally, muscle-associated cells were isolated by centrifugation and filtered using 70µm then 40µm strainers. The cells were then stained with the following primary antibody cocktail: FITC anti-Sca1 (1:5,000, Fischer Scientific), FITC anti-CD31 (1:500, Fisher Scientific), FITC anti-CD11b (1:500, Thermo Fisher), FITC anti-CD45 (1:500, Fisher Scientific), anti-α7 Integrin IgG1 (1:500, MBL), and Biotin anti-CD34 (1:100, Thermo Fisher) for 45 min at 4°C. The cells were then stained with the following secondary antibody cocktail: AlexaFluor^{TM} 647 anti-IgG1 (1:500, Thermo Fisher) and Streptavidin-APC-Cy7 (1:250, BD Biosciences) for 30 min at 4°C. MuSCs (Sca1^{-}, CD31^{-}, CD11b^{-}, CD45^{-}, α7 Integrin^{+}, CD34^{+}) were isolated using a FACSAria sorter (BD) into FACS

buffer. Sorted MuSCs were pelleted for genomic DNA extraction using the Quick-gDNA miniprep kit (Zymo Research) and analyzed with the deletion PCR described in the *CRISPR exon 45-55 deletion PCR* section below.

CRISPR/Cas9-mediated exon 45-55 deletion in MuSCs detected via PCR

Exon 45-55 deletion was assayed via PCR as previously described[70]. PCR products were blunt cloned with Zero Bunt TOPO (Thermo Fisher) according to the manufacturer's instructions and sequenced by Laragen Inc.

AAV library screening in vivo

The first round of library selection was performed using ~7-week-old hDMD del45 mdx mice in two independent groups. The first group (n=3) was dosed with ~3.6 x 10^{11} vg/mouse via retro-orbital (r.o.) injection and tissues were harvested 7 days post-injection. The second group (n=3) was dosed with ~5.5 x 10^{11} vg/mouse via r.o. injection and tissues were harvested 10 days post-injection. Tissue-enriched capsid variants derived from the first screen were then used to produce recombinant AAVs for the second round of selection (refer to the *Constructs* section for details). These tissue-enriched capsid variants were derived from skeletal muscle (referred to as SkMu-Library), heart (referred to as Heart-Library), and muscle stem cells (referred to as MuSC-Library). Each tissue-enriched library was injected in a cohort of ~9-week-old hDMD del45 mdx mice for the second round of selection. The SkMu-Library cohort (n=5 hDMD del45 mdx mice) was dosed with 1.0 x 10^{12} vg/mouse via r.o. injection and tissues were harvested 7 days post-injection. The Heart-Library cohort (n=6 hDMD

del45 mdx mice) was dosed with 1.0 x 10^{12} vg/mouse via r.o. injection and tissues were harvested 7 days post-injection. Finally, the MuSC-Library cohort (n=7 hDMD del45 mdx mice) was dosed with ~1.7 x 10^{12} vg/mouse via r.o. injection and tissues were harvested 7 days post-injection. The tissues harvested in all rounds of selection and discussed here include: heart, diaphragm, triceps, quadriceps, tibialis anterior, gastrocnemius, soleus, psoas, liver, and FACS-sorted muscle stem cells (refer to *Isolation and fluorescent activated sorting of muscle stem cells* section for details).

Next generation sequencing and bioinformatic analysis

Isolated DNA encoding capsid variants from the first and second rounds of selection were amplified with three pairs of primers that flank the NNK_7 insert using AccuPrime Taq DNA Polymerase (Thermo Fisher). The three PCR products were visualized on a 2% agarose gel with ethidium bromide staining to confirm the presence of a single band containing the NNK_7 insert. Amplified PCR products from the three PCR reactions were pooled and purified using DNA Clean & Concentrator-5 (Zymo Research) and then quantified using Qubit dsDNA HS Assay kit (Thermo Fisher). Next generation sequencing (NGS) amplicon libraries were then generated using NEBNext Ultra II DNA Library Prep with Sample Purification (New England BioLabs) and NEBNext Multiplex Oligos for Illumina (Unique Dual Index UMI Adaptors DNA Set 1, New England BioLabs) according to the manufacturer's instructions. The quality of final NGS libraries were assessed using the TapeStation system (Agilent). Samples were pooled and sequenced using one lane of NovaSeqSP (2 x 150bp).

Raw reads for each sample were quality filtered. First, we demultiplexed the Qseq files and retained only those sequences which had precise alignment with the primer sequences used for amplicon amplification. Second, we retained sequences that had precise alignment of the forward and reverse reads, as we performed paired-end sequencing. Finally, we extracted the capsid variants, encoded by the 21bp sequence, flanked by the primer sequences. The isolated 21bp oligonucleotide sequences were then translated into amino acid sequences (7 amino acids in length). In order to rank capsid variants, we computed the abundance of variants by determining the frequency of each unique variant in a given sample and normalizing the abundance of each unique variant by the sequencing read depth for the respective sample. We then calculated an enrichment score (E) for each variant, which is the ratio between the normalized abundance for samples at the end of the second screen (P_2) to the AAV library stocks used for the first (P_0) or the second screen (P_1).

Table 3-1: Primer sequences for amplifying NNK7 insert.

Primer name	Sequence (5' – 3')	Insert size (base pairs)
pRC9 F1 pRC9 R7	CGGACAAAGTCATGATAACC GGTACACATCTCTGTCCTGCC	204
pRC9 F1 pRC9 R10	CGGACAAAGTCATGATAACC GGTTTTGAACCCAGCCGGTG	159
pRC9 F7 pRC9 R7	ACAAGTGGCCACAAACCACCA GGTACACATCTCTGTCCTGCC	134

Results

Systemic delivery of AAV9-CRISPR in a humanized dystrophic mouse model results in inefficient transduction and gene editing in muscle stem cells

We have previously generated a CRISPR/Cas9-based gene-editing strategy designed to restore the *DMD* reading frame[68]. The CRISPR platform utilized a single

pair of guide RNAs (gRNAs) to target introns 44 and 55 to remove 11 exons and reframe the *DMD* gene, termed DMD$^{\Delta 45\text{-}55}$, via non-homologous end joining (NHEJ) DNA repair (**Figure 3-1A**). In order to test the efficacy of systemically administered CRISPR-based therapies, we generated a humanized dystrophic mouse model containing null alleles for both the human *DMD* and murine *Dmd* genes, hereafter referred to as the hDMD del45 mdx mouse (**Figure 3-1B**)[77]. Due to the limited packaging size of AAV, we deliver CRISPR/Cas9 using a dual vector system with the first vector containing SpCas9 downstream the muscle-specific promoter CK8e, and the second vector containing the gRNAs targeting introns 44 and 55 along with an mCherry reporter (**Figure 3-1C**). We and others have shown that AAV-CRISPR efficiently transduces heart and skeletal muscle after systemic delivery to restore dystrophin protein expression (**Figure 3-1D** and **3-1E**).

However, we sought to assess whether AAV9-CRISPR can transduce MuSCs in our hands using neonates and young adult mice. We applied the same dual-vector approach, but swapped the CK8e (muscle-specific promoter) with CMV (ubiquitously expressed promoter) in order to drive SpCas9 expression and detect gene editing in transduced MuSCs (**Figure 3-1F**). We systemically delivered AAV9-CMV-CRISPR in adult hDMD del45 mdx (~6 weeks old) at 1.5 x 10^{12} vg/vector/mouse and sorted for MuSCs 2 weeks post-injection by fluorescence activated cell sorting (FACS) (**Figure 3-1G**). We were unable to detect exon 45-55 deletion by PCR in MuSCs (α7-Integrin^{+}CD34^{+}), MuSC-like (α7-Integrin^{+} only), and non-MuSCs (CD34^{+} only) from dosed adult mice (**Figure 3-1H**). Next, we systemically delivered AAV9-CMV-CRISPR in two cohorts of hDMD del45 mdx neonates (p4) using a middle dose (5.0 x 10^{11}

vg/vector/pup) and a high dose (1.5 x 10^{12} vg/vector/pup). The middle and high dose cohorts were sacrificed 7 weeks post-injection and MuSCs were sorted by FACS. We were unable to detect CRISPR-mediated deletion of exons 45-55 in MuSCs (α7-Integrin^{+}CD34^{+}) from the middle dose cohort. Yet, we were able to detect deletion of exons 45-55 in MuSCs (α7-Integrin^{+}CD34^{+}) from the high dose cohort and sanger sequencing confirmed re-framing of intron 44 with intron 55 via NHEJ (**Figures 3-1H** and **3-1I**). However, genomic editing of exons 45-55 in MuSCs was inefficient when compared to non-MuSC sorted cells (CD34^{+} only) from the high-dose cohort as measured by PCR (**Figure 3-1H**), which was normalized by using equal amounts of input genomic DNA. Our findings correlate with three independent studies that similarly demonstrated inefficient levels of gene editing (~1-3%) after AAV-CRISPR delivery in the *mdx* mouse model[71,117,118].

While AAV9-CRISPR resulted in detectable gene editing in MuSCs from mice dosed as neonates via PCR, we were unable to detect gene editing in MuSCs from mice dosed as young adults. We theorize that the low levels of gene editing detected in MuSCs may not be sufficient for a life-long and self-sustained gene therapy for DMD. Thus, we seek to develop strategies that will enhance AAV specificity and transduction to skeletal muscle and MuSCs.

Generating and screening an AAV9 peptide display library in hDMD del45 mdx mice

We designed the AAV9 peptide display library as previously described[208]. We inserted a randomized 21 oligonucleotide sequence, encoding a heptameric peptide (7-mer), between amino acids 589A and 590Q in the hypervariable surface region VIII

(VR-VIII) of the AAV9 capsid coding sequence in order to expose the 7-mer on the capsid surface[208,219]. The randomized 21 oligonucleotide sequence was engineered to follow an NNK-triplet design, which reduced the combination of ochre (UAA) and opal (UGA) stop codons (2/3) without limiting the variety of amino acids that can be incorporated. The recombinant AAV library was produced using a common triple-transfection approach in HEK293T cells, however we transfected a low amount of pAAV-library DNA in order to minimize cross-packaging and capsid mosaicism[220] (**Figure 3-2A**). SDS-PAGE of the recombinant AAV library confirmed that only the capsid proteins (VP1, VP2 and VP3) were visible and were present in the correct stoichiometric ratio 1:1:10 (**Figure 3-2B**).

For the first round of selection, we systemically administered the AAV library in ~7-week-old hDMD del45 mdx mice (n=6) at ~3.6 x 10^{11} to 5.5 x 10^{11} vg/mouse and were sacrificed ~1-week post-injection. Viral DNA was extracted from heart tissue, skeletal muscle tissues (diaphragm, soleus, triceps), FACS-sorted MuSCs, and liver tissue (**Figure 3-2C**). Isolated viral DNA was PCR-amplified for the NNK_7 capsid locus and re-cloned into the recipient precursor plasmid, pCap9-precursor, to assemble muscle-enriched library plasmids: skeletal muscle (pSkMu-library), heart (pHeart-library), and muscle stem cells (pMuSC-library) plasmids. The muscle-enriched recombinant AAV libraries were produced and purified in order to perform the second and final round of selection *in vivo*. Finally, ~7-8-week old hDMD del45 mdx mice were systemically dosed with the AAV-SkMu-library (n=5) and the AAV-Heart-library (n=3) at 1 x 10^{12} vg/mouse and sacrificed ~1wk post-injection (**Figure 3-2C**). The AAV-MuSC-library was systemically injected in two cohorts of hDMD del45 mdx mice (total n=7) at

1.7 x 10^{12} vg/mouse and sacrificed ~1 week post-injection (**Figure 3-2C**). We harvested and isolated viral DNA from heart tissue, skeletal muscle tissues (diaphragm, soleus, triceps), and liver tissue from all three muscle-enriched AAV libraries. However, we only sorted for MuSCs from the mice injected with the AAV-MuSC-library. We kept the isolated viral DNA from each step of the selection process to generate amplicon-based libraries for next-generation sequencing (**Figures 3-2D** and **3-2E**). The unique 21 oligonucleotide sequence in each capsid variant was used as a barcode to identify capsid variants enriched in skeletal muscle and MuSCs.

NGS analysis identifies capsid variants enriched in MuSCs

NGS analysis was performed for each step of the screening process from the starting AAV library stock (P_0), the tissue-enriched AAV library stocks (P_1) and the isolated DNA from the last round of screening (P_2). For NGS analysis, we analyzed the mice from P_2 individually to select for capsid variants that demonstrated cross-animal reproducibility (**Table 3-2**). In order to quantitatively determine highly enriched capsid variants in MuSCs, we computed enrichment scores. The enrichment scores were calculated by taking the ratio of the relative abundance of each variant in P_2 to the relative abundance of each variant in the starting AAV library stock (P_0) or to the relative abundance of each variant in the tissue-enriched library stock (P_1) (**Figure 3-2C**).

As discussed earlier, the AAV-MuSC-library (P_1) was injected in two separate cohorts of hDMD del45 mdx mice (n=7 total) and FACS-sorted for MuSC (P_2). First, we calculated the enrichment scores between the two MuSC cohorts (P_2) and the starting AAV library stock (P_0) (**Figure 3-3A**). Then, we selected for variants that had

enrichment scores > 2 (P_2:P_0) and we identified a total of 223 and 176 capsid variants enriched in MuSC cohort #1 and MuSC cohort #2, respectively. We found that 90/309 (~29%) capsid variants were shared between MuSC cohorts #1 and #2 (**Figure 3-3B**). We introduced an additional parameter to select for AAV variants that had reduced enrichment scores in off-target organs, such as the liver. We compared the 90 identified MuSC variants to the capsid variants present in the liver and found that 11/90 (~12%) MuSC capsid variants demonstrated liver de-targeting and were MuSC-enriched (**Figure 3-3C**). The remaining 79/90 (~87%) MuSC capsid variants, which had high enrichment scores in MuSC, also had enrichment scores > 2 in the liver and were referred to as MuSC+Liver-enriched capsids. The final parameter we introduced in our NGS analysis, was to compare enrichment scores of the 11 MuSC-enriched and 79 MuSC+Liver-enriched (total=90) capsid variants (P_2) to the AAV-MuSC-library stock (P_1). We anticipated that the MuSC-enriched and MuSC+Liver-enriched variants (n=90) identified from comparing P_2:P_0 would also demonstrate high enrichment scores when comparing P_2:P_1. We confirmed that 8/11 (~73%) MuSC-enriched and 34/79 (~43%) MuSC+Liver-enriched capsid variants demonstrated high P_2:P_1 enrichment scores and thus, were continuously enriched at each step of the screening process from P_0 to P_1 to P_2 (**Table 3-3**).

Finally, we investigated whether the MuSC-enriched (8/11) and MuSC+Liver-enriched (34/79) 7-mer capsid variants revealed a consensus in amino acid chemical properties and amino acid usage (**Figure 3-3D**). We observed that the amino acids overrepresented in the MuSC-enriched 7-mers (VMSVVRP) were distinct from the consensus sequence in MuSC+Liver-enriched 7-mers (GGGGSRV). Moreover,

hydrophobic amino acids were overrepresented in MuSC-enriched 7-mers, whereas polar amino acids were overrepresented in the MuSC+Liver-enriched 7-mers (**Figure 3-3D**). When we combined MuSC-enriched and MuSC+Liver-enriched 7-mers, we obtained a 7-mer consensus plot (GGGGSRP) that was more reminiscent of the MuSC+Liver-enriched 7-mer with similar polar properties (**Figure 3-3E**). However, this perceived similarity was likely due to the overrepresentation of 7-mers from the MuSC+Liver-enriched (n=34) which outnumbered the MuSC-enriched 7-mers (n=8). Our informatic analysis pipeline, which was based on selecting capsid candidates with high enrichment scores, cross-animal reproducibility and reduced enrichment scores in the liver, led us to prioritize 8 MuSC-enriched capsid variants for future validation studies (**Figure 3-3F**).

NGS analysis identifies capsid variants enriched in skeletal muscle

The same informatic analysis pipeline that was applied to MuSC samples was also applied to the skeletal muscle (SkMu) samples (n=5 hDMD del45 mdx). For each mouse, diaphragm, soleus, and triceps SkMu tissues were pooled and used for NGS analysis to detect AAV capsid variants. First, we compared SkMu variants from P_2 to the starting AAV library virus stock P_0 and filtered for variants that had enrichment scores > 2 (P_2:P_0). We identified 81/536 (~15%) capsid variants were shared across all 5 mice and 73/536 (~13%) capsid variants were shared across 4/5 mice (n=154 SkMu capsid variants) (**Figures 3-4A** and **3-4B**). We compared SkMu capsid variants to the capsid variants present in the liver and we identified 22/230 (~10%) SkMu-enriched variants and 132/230 (~57%) SkMu+Liver-enriched capsid variants (**Figure 3-4C**). Lastly, we

compared the enrichment scores of the 22 SkMu-enriched and 132 SkMu+Liver-enriched (total=154) capsid variants (P_2) to the AAV-SkMu-library stock (P_1). We determined that 5/22 (~23%) SkMu-enriched and 32/132 (~24%) SkMu+Liver-enriched capsid variants demonstrated high P_2:P_1 enrichment scores and thus, were continuously enriched throughout the screening process from P_0 to P_1 to P_2 (**Table 3-4**).

Next, we compared the SkMu-enriched (5/22) 7-mer consensus motif to the SkMu+Liver-enriched (32/132) 7-mer consensus motif. We observed that the amino acids overrepresented in the SkMu-enriched 7-mers (GNMEFTS) were distinct from the consensus in SkMu+Liver-enriched 7-mers (GGSSSRP) (**Figures 3-4D** and **3-4E**). A mixture of polar, neutral, and hydrophobic amino acids was detected in SkMu-enriched 7-mers, whereas polar amino acids were disproportionately represented in SkMu+Liver-enriched 7-mers and reminiscent of the MuSC+Liver-enriched 7-mers (**Figures 3-3D** and **3-4E**). When we combined variants from SkMu-enriched and SkMu+Liver-enriched 7-mers, we obtained a 7-mer consensus plot (GGSSSRP) that was more reminiscent of the SkMu+Liver-enriched 7-mer with similar polar properties (**Figure 3-4F**). This observed similarity was likely due to the disproportionate number of 7-mers from the SkMu+Liver-enriched (n=32) which outnumbered the SkMu-enriched 7-mers (n=5) and similar to what we found for MuSC-enriched AAV variants (**Figures 3-3D** and **3-3E**). In summary, we identified a total of 37 SkMu-enriched AAV variants (**Table 3-4**). Lastly, we compared the 37 SkMu-enriched AAV variants with the 42 MuSC-enriched AAV variants and identified 9 overlapping variants highly enriched in both SkMu and MuSCs for future validation experiments (**Figures 3-4G** and **3-4H**).

NGS analysis identifies capsid variants enriched in cardiac muscle

Lastly, we used the same informatic analysis pipeline for the samples dosed with the AAV-Heart-library (n=3 hDMD del45 mdx) to identify variants enriched in cardiac tissue. Again, we compared the Heart variants from P_2 to the starting AAV library virus stock P_0 and selected variants that contained enrichment scores > 2 (P_2:P_0). We identified 166 shared capsid variants between all 3 samples (**Figures 3-5A** and **3-5B**). We compared the Heart capsid variants to the capsid variants present in the liver and we identified 33/239 (~14%) Heart-enriched variants and 133/239 (~55%) were Heart+Liver-enriched capsid variants (**Figure 3-5C**). Lastly, we compared the enrichment scores of the 33 Heart-enriched and 133 Heart+Liver-enriched (total=166) capsid variants (P_2) to the AAV Heart-library stock (P_1). We determined that 22/33 (~67%) Heart-enriched and 101/133 (~76%) Heart+Liver-enriched capsid variants had high P_2:P_1 enrichment scores, suggesting continuous enrichment throughout the screening process from P_0 to P_1 to P_2 (**Table 3-5**).

We found that the amino acids overrepresented in the Heart-enriched 7-mers (GGKGSGS) were fairly similar to the consensus motif observed in the Heart+Liver-enriched 7-mers (GGSGGSP) (**Figures 3-5D** and **3-5E**). Likewise, both 7-mer consensus motifs contained a higher frequency of polar amino acids. When we combined variants from Heart-enriched and Heart+Liver-enriched 7-mers, we obtained a 7-mer consensus plot (GGSGGSP) that was also reminiscent of the Heart+Liver-enriched 7-mer with similar polar properties (**Figure 3-5F**). Interestingly, we noted that the AAV capsid variants highly enriched in MuSC, SkMu and Heart shared similar 7-mer amino acid consensus motifs with polar charged amino acids (**Figures 3-3E** and **3-4F**

and **3-5F**). Despite the similarity in 7-mer consensus motifs, we found that there were AAV capsid variants exclusively enriched in MuSC (~13%), SkMu (~8%) or Heart (~56%) (**Figure 3-5G**). A small fraction (~3.7%) of AAV capsid variants were enriched and shared between MuSC, SkMu and Heart.

Discussion

In this study, we demonstrated that wildtype AAV9 carrying our CRISPR/Cas9 platform is unable to efficiently transduce MuSCs *in vivo* as we were unable to detect gene-editing in MuSCs from young adult mice and faintly detect gene editing in MuSCs from AAV-dosed neonates. One reason that gene editing was detected in neonates is because at this post-natal stage of development, MuSC are actively contributing to muscle growth, dividing, fusing, and therefore facilitating MuSC transduction by AAV[221]. In an effort to enhance adult MuSC targeting by AAV, we generated and screened an AAV9 peptide-display library in order to identify AAV capsid variants enriched in skeletal muscle and MuSCs. Moreover, we devised a comprehensive and methodological analysis pipeline to select for AAV capsid variants with high tissue-specific enrichment, cross-animal reproducibility, and reduced enrichment in off-target organs, such as the liver.

One potential limitation of our high throughput capsid library screen is that we are unable to differentiate between functional and non-functional capsids during selection. Functional capsids are capable of overcoming the multiple steps involved in transduction, which includes cell receptor binding and entry, release of AAV DNA, second-strand synthesis, transcription and translation of the vector transgene[222]. In

order to select for functional AAV capsid variants, CREATE[223], M-CREATE[224], iTRANSDUCE[211], and BRAVE[209] were developed, which all rely on Cre expression, Cre-transgenic animal models and fluorescent reporter expression coupled with FACS sorting cells of interest (e.g., neurons). However, Cre-dependent AAV library screening is not feasible when Cre-transgenic animal models are not readily available and FACS sorting is not a viable strategy for identifying variants enriched in skeletal muscle tissues. Cre-independent strategies, such as TRADE[225], uses a unique vector expressing a fluorescent reporter in the sense strand for FACS sorting cells of interest and the Cap library gene is expressed as an antisense transcript and recovered by reverse transcription PCR (RT-PCR). The antisense RNA recovery provides similar selective pressure for functional AAV capsid variants as the Cre-dependent methods. However, TRADE poses additional screening challenges as the TRADE vector suffers from cryptic splice sites present in the AAV Cap ORF[225,226]. Despite the iterations for high throughput capsid library screening, our AAV9 peptide display library does not require the need for transgenic animal models and thus, can be screened on virtually any *in vivo* model.

Recently, one study executed an AAV library screen based on the recovery of viral Cap DNA and mRNA to select for functional AAV variants specific to skeletal muscle during the screening process[215]. Weinmann et al. 2020 discovered skeletal muscle tropic AAV capsid variants containing a highly conserved RGD peptide motif, which was previously shown to be a recognition sequence for integrins[227]. Although Weinmann et al. 2020 discovered an RGD-containing AAV variant (AAVMYO) with markedly enhanced skeletal muscle transduction, the study was not a traditional AAV

library screen, rather a pre-selected pool of 183 variants from their previous library screening studies was used[213,228]. An independent study conducted by Tabebordbar et al. 2021 performed a traditional AAV library screen using viral Cap mRNA recovery to select for functional AAV variants specific to skeletal muscle, which also led to the identification of an RGD-containing AAV variant referred to as MyoAAV[214]. Both AAVMYO and MyoAAV demonstrated their superiority over wildtype AAV9 with a 10-50-fold increase in fluorescent reporter expression across various skeletal muscle groups. Likewise, AAVMYO and MyoAAV significantly enhanced delivery and transgene expression of micro-dystrophin (μDYS), which is being tested as a gene replacement therapy for DMD in ongoing clinical trials (clinicaltrials.gov: NCT03368742, Solid Biosciences; NCT03375164, Nationwide Children's Hospital; NCT03362502, Pfizer). Unlike Weinmann et al. 2020 and Tabebordbar et al. 2021, we specifically screened our AAV peptide display library for both skeletal muscle and MuSC-specific AAV capsid variants, and while we do not detect RGD-containing AAV capsid variants as being highly enriched in our skeletal muscle or MuSC screens, we do uncover AAV capsid variants that are highly enriched in both skeletal muscle and MuSCs.

Importantly, only Tabebordbar et al. 2021 tested the efficacy of CRISPR delivery and gene-editing using MyoAAV, systemically administering 8-week-old mdx mice with a significantly high dose of MyoAAV-SaCas9 at 4.5×10^{12} vg (~1.5×10^{14} vg/kg) and MyoAAV-gRNA at 9.0×10^{12} vg (~3×10^{14} vg/kg) to reframe the murine *Dmd* gene. Since Tabebordbar et al. utilized a dual vector approach, the cumulative viral dose per mouse was 1.35×10^{13} vg or approximately 4.5×10^{14} vg/kg, which is considerably higher than AAV-μDYS doses used in ongoing clinical trials for Pfizer (3.0×10^{14} vg/kg),

Solid Biosciences (2.0 x 10^{14} vg/kg), and Nationwide Children's Hospital (2.0 x 10^{14} vg/kg). Such a high viral dose and persistent vector genomes of MyoAAV-CRISPR raises concerns over AAV-related immunotoxicities, which has been reported in clinical trials with patient cohorts receiving high doses of AAV gene therapy for DMD and X-linked myotubular myopathy (XLMTM)[59,187,229]. MyoAAV-CRISPR-mediated restoration of dystrophin levels ranged from 10-20% by Western blot for the triceps, tibialis anterior and quadriceps. Yet, MyoAAV-CRISPR yielded underwhelming dystrophin levels in the heart and diaphragm, raising additional concerns regarding the longevity of a single administration of MyoAAV-CRISPR. One study revealed that a single systemic administration of AAV-CRISPR was unable to sustain life-long dystrophin expression in *mdx* mice, due to the fact that AAV inefficiently transduces MuSCs.

While Tabebordbar et al. 2021 did not assess MyoAAV-CRISPR-mediated gene editing efficiencies in MuSCs, they have previously shown a single intraperitoneal administration of AAV9-CRISPR (1.5 x 10^{12} vg per vector) and AAV9-Cre-recombinase (3.0 x 10^{11} vg) in neonate mdx-Ai9 mice, which contain an activatable tdTomato transgene, resulted in ~4% and ~10% tdTomato$^+$ MuSCs (CXCR4$^+$ β1-Integrin$^+$), respectively[71]. Even though AAV9-CRISPR was administered using a 10-fold greater dose, the inefficient CRISPR-mediated induction of tdTomato (~4%) is likely due to the fact that both the Cas9 and gRNA components are packaged in separate AAV vectors and must target the same MuSCs; whereas, Cre-recombinase is encoded in a single AAV vector. Tabebordbar et al. 2021 confirmed MyoAAV modestly improved MuSC targeting after Cre-recombinase delivery in mdx-Ai9 mice compared to AAV9, resulting in ~9.5% tdTomato$^+$ MuSC for MyoAAV and ~3.3% tdTomato$^+$ MuSCs for AAV9.

Nevertheless, these reports suggest that MyoAAV-CRISPR delivery may likely yield low levels of CRISPR-corrected MuSCs *in vivo*. While AAVMYO from Weinmann et al. 2020 was not assessed for CRISPR delivery and gene-editing, it is presumable that AAVMYO would yield similar results to MyoAAV since both AAV capsid variants share the RGD motif mediating skeletal muscle transduction.

Although our AAV9 peptide display library screen cannot distinguish functional from non-functional capsids and relies solely on viral DNA recovery, our screening strategy has proven successful from previous reports which have identified novel capsid variants with re-directed tropisms[207-209,216,228,230-237]. Therefore, our strategy will likely be an effective approach to recover capsids that achieve successful cellular entry and are effective, to a certain extent, in the transduction process. We anticipate that ongoing validation studies will confirm skeletal muscle and MuSC-tropic AAV capsids.

Conclusion

In summary, we report the identification of skeletal muscle and MuSC-enriched AAV capsid variants to be tested in future validation studies. To the best of our knowledge, this is the first report of an AAV library screen selecting for AAV variants enriched in skeletal muscle and MuSCs *in vivo*. In addition, we identify a subset of skeletal muscle and MuSC-enriched AAV variants that are lowly enriched in the liver. We anticipate that an AAV capsid variant capable of liver de-targeting with enhanced skeletal muscle and MuSC specificity will result in a more efficacious and longer-lasting gene therapy for DMD. In addition, such a capsid variant may allow us to achieve therapeutic efficacy at lower doses, thereby reducing AAV-induced toxicities and

improving safety. Ongoing validation studies will identify the capsid variants with superior transduction efficiency, resulting in CRISPR-mediated restoration of dystrophin and long-lasting dystrophin expression after a single AAV administration. We expect that a skeletal muscle and MuSC-tropic AAV may also be translatable to other neuromuscular diseases requiring efficient skeletal muscle and/or MuSC targeting. The advantage of our AAV9 peptide display library is the feasibility of screening in virtually any animal model for virtually any tissue of interest, and thus, has promising implications to discover capsid variants for CRISPR/Cas9 delivery to treat many genetic diseases.

Acknowledgments

We thank Jane Wen, Diana Becerra, and Joyce Lui for technical assistance. The authors thank and acknowledge the use of instruments from the following cores: Eli and Edythe Broad Center of Regenerative Medicine and Stem Cell Research (BSCRC) Flow Cytometry Core and Sequencing Core, Johnson Comprehensive Cancer Center (JCCC) Flow Cytometry Core, the Institute for Quantitative and Computational Biosciences (QC Bio), and UPenn Gene Therapy Vector Core for generating the P_0 AAV library. This material is based upon work supported by the National Science Foundation Graduate Research Fellowship Program under Grant No. DGE-1650604 (MRE). Any opinions, findings, and conclusions or recommendations expressed in this material are those of the author and do not necessarily reflect the views of the National Science Foundation. Funding was also provided by Ruth L. Kirschstein National Research Service Award GM007185 (MRE), the CDMD Azrieli Graduate Student Award (MRE), and the

Whitcome Predoctoral Fellowship in Molecular Biology (MRE). Additional funding was provided by the California Institute for Regenerative Medicine (CIRM DISC2-10696, ADP) and the Wellstone (U54 AR052646-07, MJS).

Author contributions

Conceptualization, Methodology, Visualization, Project Administration – MRE, CSY, ADP, MJS; Investigation – MRE, CD, CSY, GD; Software, Data Curation – XZ; Formal analysis – MRE; Writing – Original Draft – MRE; Writing – Review and Editing – MRE, MJS; Resources – GD, ADP, MJS; Supervision – CSY, ADP, MJS; Funding Acquisition – ADP, MJS.

Figures

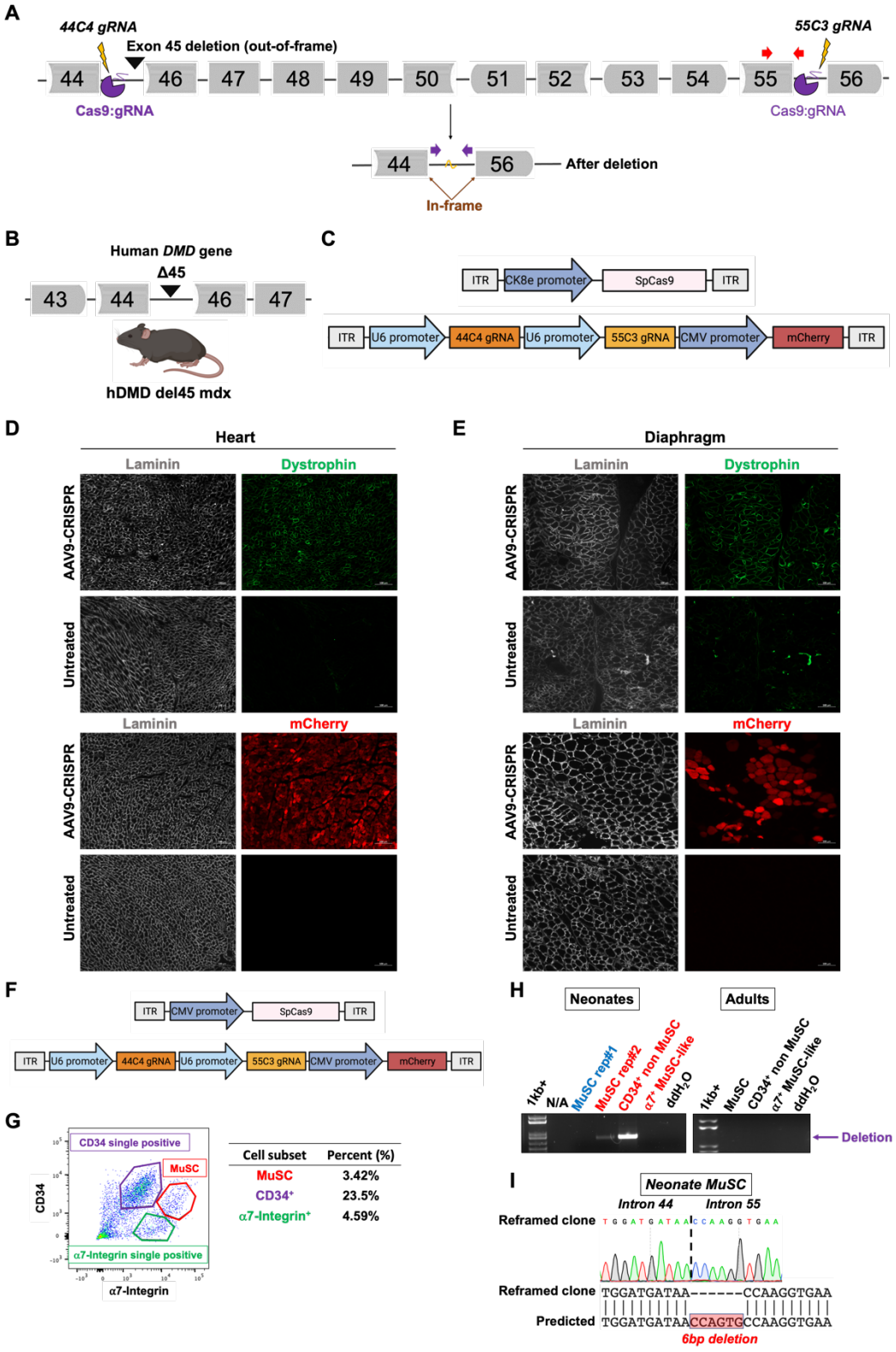
A
44C4 gRNA
Exon 45 deletion (out-of-frame)
55C3 gRNA
44
46
47
48
49
50
51
52
53
54
55
56
Cas9:gRNA
Cas9:gRNA
44
56
After deletion
In-frame
B
Human DMD gene
Δ45
43
44
46
47
hDMD del45 mdx
C
ITR
CK8e promoter
SpCas9
ITR
ITR
U6 promoter
44C4 gRNA
U6 promoter
55C3 gRNA
CMV promoter
mCherry
ITR
D
Heart
Laminin
Dystrophin
AAV9-CRISPR
Untreated
Laminin
mCherry
AAV9-CRISPR
Untreated
E
Diaphragm
Laminin
Dystrophin
AAV9-CRISPR
Untreated
Laminin
mCherry
AAV9-CRISPR
Untreated
F
ITR
CMV promoter
SpCas9
ITR
ITR
U6 promoter
44C4 gRNA
U6 promoter
55C3 gRNA
CMV promoter
mCherry
ITR
G
CD34 single positive
MuSC
α7-Integrin single positive
CD34
α7-Integrin
Cell subset
Percent (%)
MuSC
3.42%
CD34+
23.5%
α7-Integrin+
4.59%
H
Neonates
Adults
1kb+
N/A
MuSC rep#1
MuSC rep#2
CD34+ non MuSC
α7+ MuSC-like
ddH2O
1kb+
MuSC
CD34+ non MuSC
α7+ MuSC-like
ddH2O
Deletion
I
Neonate MuSC
Intron 44
Intron 55
Reframed clone
Reframed clone
TGGATGATAA------CCAAGGTGAA
Predicted
TGGATGATAACCAGTGCCAAGGTGAA
6bp deletion

Figure 3-1: Systemic delivery of AAV9-CRISPR in hDMD del45 mdx mice.
A) Region of the human *DMD* gene targeted with a single pair of gRNAs (lightning bolts) to delete exons 45-55 and reframe the *DMD* gene.
B) Humanized dystrophic mouse model null for both human *DMD* and mouse *Dmd* genes.
C) Schematic of the dual-vector strategy to deliver CRISPR/Cas9 targeting exons 45-55 of the *DMD* gene. Created with BioRender.com.
D-E) Immunofluorescent images of heart and diaphragm sections from hDMDdel45 mdx mice treated with HBSS (vehicle) or AAV9-CRISPR stained with Laminin (white), dystrophin (green) or mCherry (red). Scale bar represents 100μm.
F) Schematic of the dual-vector strategy to deliver CRISPR/Cas9. Created with BioRender.com.
G) Representative FACS plot from neonates intraperitoneally injected with AAV9-CMV-CRISPR to isolate Lin^- α7-$Integrin^+$ $CD34^+$ MuSCs.
H) PCR using primers to detect the exon 45-55 deletion (purple arrows) region of the *DMD* gene (see panel A) isolated from α7-$Integrin^+$ $CD34^+$ MuSCs, single α7-$Integrin^+$ cells (MuSC-like) and single $CD34^+$ (non MuSCs). Neonate MuSCs (blue text) are from the middle-dose cohort and in red text are from the high-dose cohort.
I) Representative sample sequence trace showing rejoining of introns 44 and 55 after CRISPR/Cas9-mediated editing in MuSCs from the high-dose cohort.

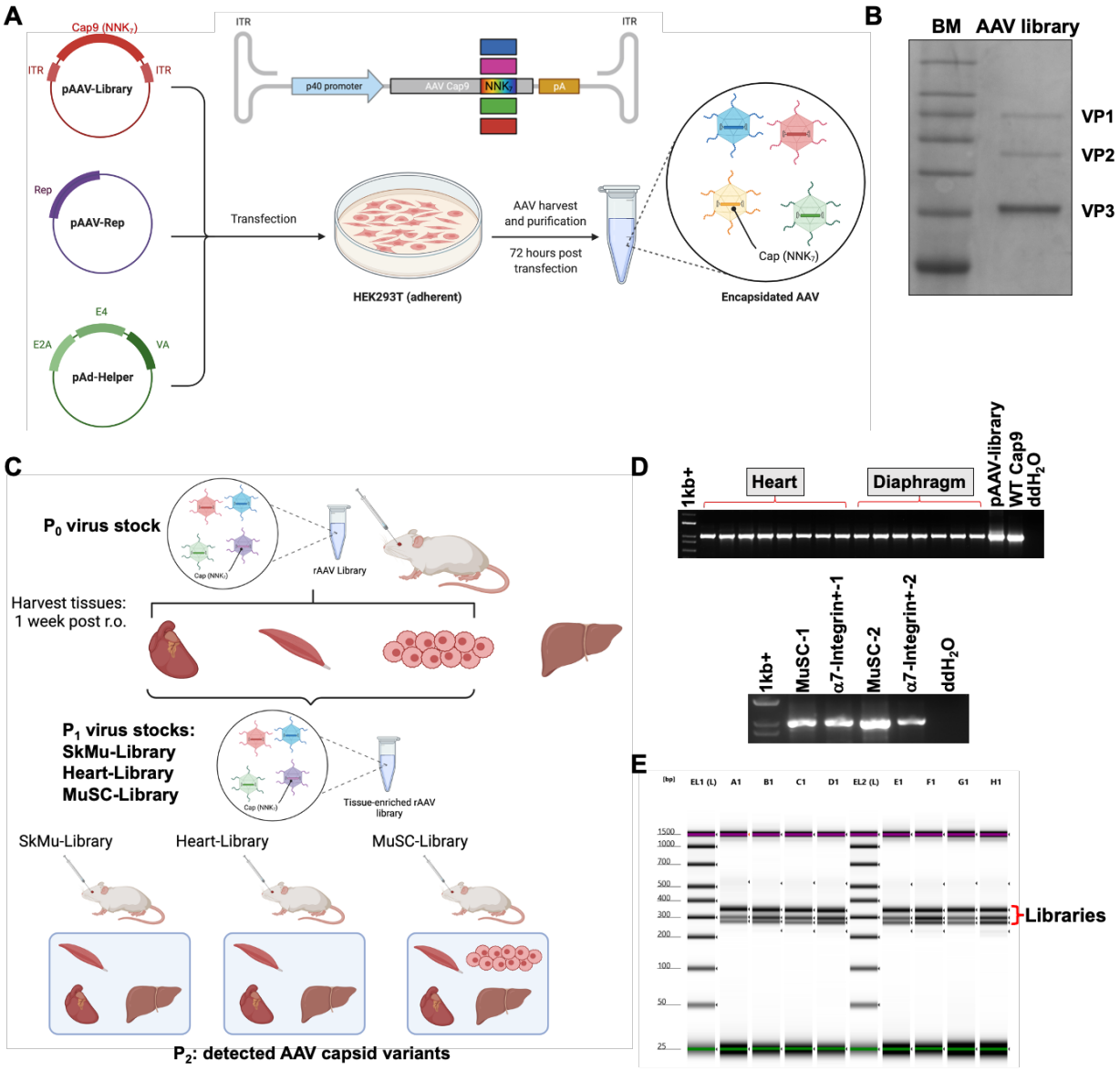

Figure 3-2: Recombinant AAV library production and experimental workflow.
A) Schematic of recombinant AAV library production. Created with BioRender.com.
B) Coomassie stained SDS-PAGE of the recombinant AAV library viral capsid proteins (VP1, VP2 and VP3).
C) Schematic overview of two rounds of AAV selection *in vivo*. Created with BioRender.com.
D) Representative PCR using primers to detect the AAV library DNA from heart, diaphragm, MuSCs (α7-Integrin$^+$ CD34$^+$), and MuSC-like cells (α7-Integrin$^+$ only). The pAAV-library and wildtype (WT) Cap9 were included, which demonstrate the shift in size due to the 21-oligonucleotide insertion in our capsid library.
E) A representative TapeStation gel image used to assess the quality of the final NGS library preparations. Three primer pairs were used to generate the final amplicon-based libraries and the three bands are indicated in the TapeStation gel.

Table 3-2: NGS samples from each step of *in vivo* selection.

Sample#	Mouse ID	Tissue	Screen#
1	RC	Heart	1st screen
2	RC	Dia/Tri/Sol (SkMu)	1st screen
3	RC	Liver	1st screen
4	LC	Heart	1st screen
5	LC	Dia/Tri/Sol (SkMu)	1st screen
6	LC	Liver	1st screen
7	BC	Heart	1st screen
8	BC	Dia/Tri/Sol (SkMu)	1st screen
9	BC	Liver	1st screen
10	7618	Heart	1st screen
11	7618	Dia/Tri/Sol (SkMu)	1st screen
12	7618	Liver	1st screen
13	7619	Heart	1st screen
14	7619	Dia/Tri/Sol (SkMu)	1st screen
15	7619	Liver	1st screen
16	7621	Heart	1st screen
17	7621	Dia/Tri/Sol (SkMu)	1st screen
18	7621	Liver	1st screen
19	Pool	MuSCs	1st screen
20	27	Heart	SkMu-Lib 2nd screen
21	27	Dia/Tri/Sol (SkMu)	SkMu-Lib 2nd screen
22	27	Liver	SkMu-Lib 2nd screen
23	28	Heart	SkMu-Lib 2nd screen
24	28	Dia/Tri/Sol (SkMu)	SkMu-Lib 2nd screen
25	28	Liver	SkMu-Lib 2nd screen
26	29	Heart	SkMu-Lib 2nd screen
27	29	Dia/Tri/Sol (SkMu)	SkMu-Lib 2nd screen
28	29	Liver	SkMu-Lib 2nd screen
29	30	Heart	SkMu-Lib 2nd screen
30	30	Dia/Tri/Sol (SkMu)	SkMu-Lib 2nd screen
31	30	Liver	SkMu-Lib 2nd screen
32	31	Heart	SkMu-Lib 2nd screen
33	31	Dia/Tri/Sol (SkMu)	SkMu-Lib 2nd screen
34	31	Liver	SkMu-Lib 2nd screen
35	45	Heart	MuSC-Lib 2nd screen
36	45	Liver	MuSC-Lib 2nd screen
37	45	Dia only (SkMu)	MuSC-Lib 2nd screen
38	47	Heart	MuSC-Lib 2nd screen
39	47	Liver	MuSC-Lib 2nd screen
40	47	Dia only (SkMu)	MuSC-Lib 2nd screen
41	49	Heart	MuSC-Lib 2nd screen
42	49	Liver	MuSC-Lib 2nd screen
43	49	Dia only (SkMu)	MuSC-Lib 2nd screen
44	50	Heart	MuSC-Lib 2nd screen
45	50	Liver	MuSC-Lib 2nd screen
46	50	Dia only (SkMu)	MuSC-Lib 2nd screen
47	11	Heart	MuSC-Lib 2nd screen
48	11	Liver	MuSC-Lib 2nd screen
49	11	Dia only (SkMu)	MuSC-Lib 2nd screen
50	52	Heart	MuSC-Lib 2nd screen
51	52	Liver	MuSC-Lib 2nd screen
52	52	Dia only (SkMu)	MuSC-Lib 2nd screen
53	53	Heart	MuSC-Lib 2nd screen
54	53	Liver	MuSC-Lib 2nd screen
55	53	Dia only (SkMu)	MuSC-Lib 2nd screen
56	Pool	MuSCs	MuSC-Lib 2nd screen
57	Pool	MuSCs	MuSC-Lib 2nd screen
58	Pool	a7-Integrin+ cells	MuSC-Lib 2nd screen
59	Pool	a7-Integrin+ cells	MuSC-Lib 2nd screen
60	203	Sol (SkMu)	Heart-Lib 2nd screen
61	204	Sol (SkMu)	Heart-Lib 2nd screen
62	205	Sol (SkMu)	Heart-Lib 2nd screen
63	222	Heart	Heart-Lib 2nd screen
64	222	Dia/Tri/Sol (SkMu)	Heart-Lib 2nd screen
65	222	Liver	Heart-Lib 2nd screen
66	223	Heart	Heart-Lib 2nd screen
67	223	Dia/Tri/Sol (SkMu)	Heart-Lib 2nd screen
68	223	Liver	Heart-Lib 2nd screen
69	225	Heart	Heart-Lib 2nd screen
70	225	Dia/Tri/Sol (SkMu)	Heart-Lib 2nd screen
71	225	Liver	Heart-Lib 2nd screen
72	UPenn Prep	AAV DNA, P0	Starting virus stock (P0)
73	Heart Library	AAV DNA, P1	Virus stock for 2nd screen (P1)
74	SkMu Library	AAV DNA, P1	Virus stock for 2nd screen (P1)
75	MuSC Library	AAV DNA, P1	Virus stock for 2nd screen (P1)

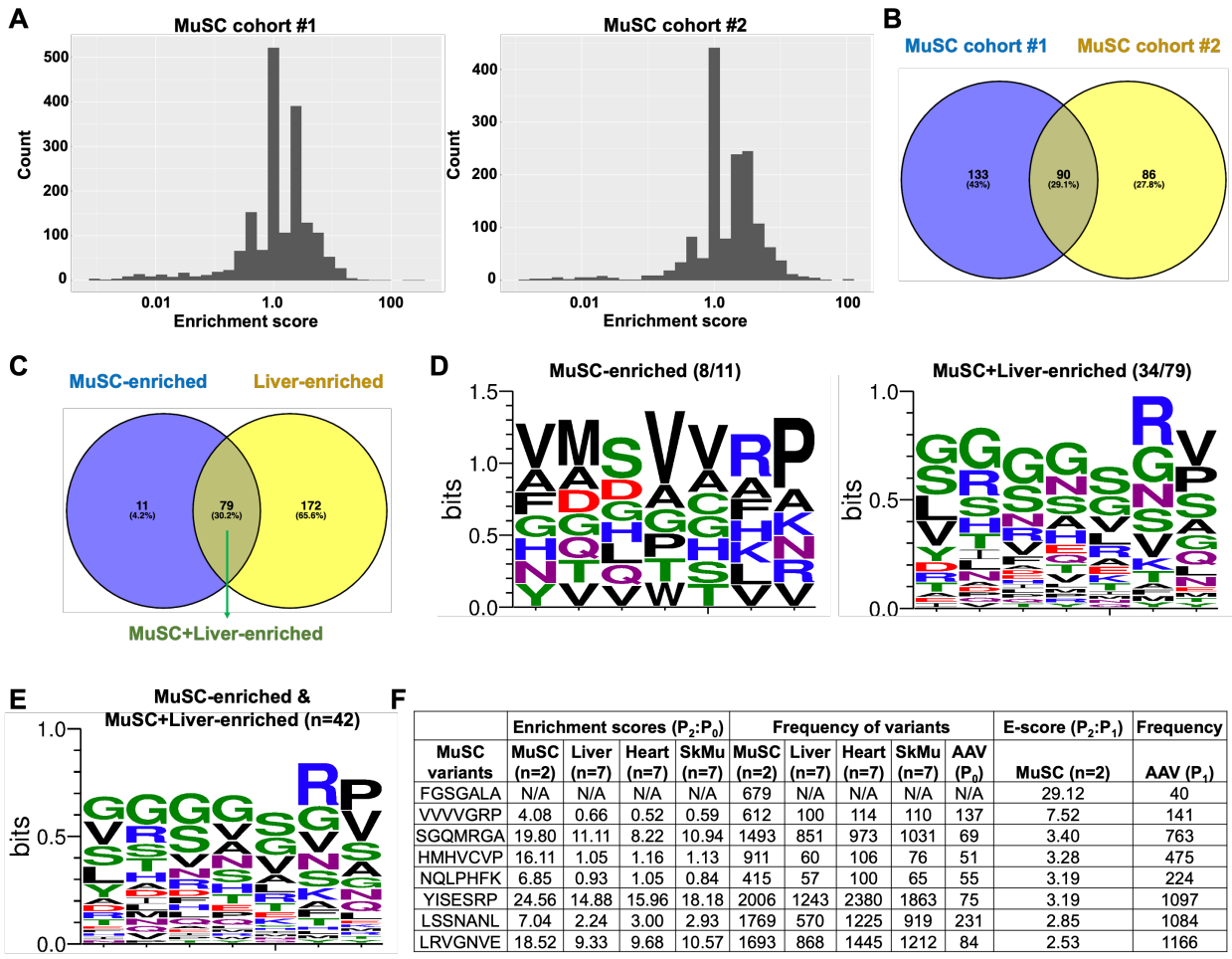

	Enrichment scores (P_2:P_0)				Frequency of variants					E-score (P_2:P_1)	Frequency
MuSC variants	MuSC (n=2)	Liver (n=7)	Heart (n=7)	SkMu (n=7)	MuSC (n=2)	Liver (n=7)	Heart (n=7)	SkMu (n=7)	AAV (P_0)	MuSC (n=2)	AAV (P_1)
FGSGALA	N/A	N/A	N/A	N/A	679	N/A	N/A	N/A	N/A	29.12	40
VVVVGRP	4.08	0.66	0.52	0.59	612	100	114	110	137	7.52	141
SGQMRGA	19.80	11.11	8.22	10.94	1493	851	973	1031	69	3.40	763
HMHVCVP	16.11	1.05	1.16	1.13	911	60	106	76	51	3.28	475
NQLPHFK	6.85	0.93	1.05	0.84	415	57	100	65	55	3.19	224
YISESRP	24.56	14.88	15.96	18.18	2006	1243	2380	1863	75	3.19	1097
LSSNANL	7.04	2.24	3.00	2.93	1769	570	1225	919	231	2.85	1084
LRVGNVE	18.52	9.33	9.68	10.57	1693	868	1445	1212	84	2.53	1166

Figure 3-3: NGS analysis identifies MuSC-enriched AAV capsid variants.
A) Histogram of enrichment score analysis in P_2 MuSC cohorts #1 and #2.
B) Venn diagram of overlapping AAV capsid variants with E-scores > 2 from MuSC cohort #1 and MuSC cohort #2.
C) Venn diagram of MuSC-enriched and Liver-enriched AAV capsid variants.
D) Frequency plots of MuSC-enriched and MuSC+Liver-enriched AAV capsid variants created by WebLogo 3 and using the chemistry color scheme.
E) Frequency plot of MuSC-enriched and MuSC+Liver-enriched AAV capsid variants created by WebLogo 3 and using the chemistry color scheme.
F) The top 8 MuSC-specific AAV candidate variants to be used for future validation studies.

Table 3-3: MuSC-enriched AAV capsid variants.

	Enrichment scores (P2:P0)				Frequency of variants					E-score (P2:P1)	Frequency
MuSC AAV variants	MuSC (n=2)	Liver (n=7)	Heart (n=7)	SkMu (n=7)	MuSC (n=2)	Liver (n=7)	Heart (n=7)	SkMu (n=7)	AAV (P0)	MuSC (n=2)	AAV (P1)
FGSGALA	N/A	N/A	N/A	N/A	679	N/A	N/A	N/A	N/A	29.12	40
VVVVGRP	4.08	0.66	0.52	0.59	612	100	114	110	137	7.52	141
SGQMRGA	19.80	11.11	8.22	10.94	1493	851	973	1031	69	3.40	763
HMHVCVP	16.11	1.05	1.16	1.13	911	60	106	76	51	3.28	475
NQLPHFK	6.85	0.93	1.05	0.84	415	57	100	65	55	3.19	224
YISESRP	24.56	14.88	15.96	18.18	2006	1243	2380	1863	75	3.19	1097
LHGARYS	4.74	3.42	2.33	2.95	72	53	55	57	14	3.15	40
VTSWTKN	5.13	1.71	1.53	1.78	926	321	384	414	170	2.92	566
LSSNANL	7.04	2.24	3.00	2.93	1769	570	1225	919	231	2.85	1084
SGSGSFM	8.43	3.43	5.24	5.01	1767	733	1929	1310	192	2.64	1163
LRVGNVE	18.52	9.33	9.68	10.57	1693	868	1445	1212	84	2.53	1166
GMGTVAR	2.53	1.57	1.31	1.55	715	461	638	559	264	2.53	501
SQNLLSN	7.35	2.10	3.47	2.94	1205	348	942	600	150	2.51	835
STVNGNQ	9.06	2.75	4.16	3.72	471	147	363	244	48	2.38	347
YGNSKVV	4.61	3.95	3.90	4.26	4080	3556	5510	4707	814	2.27	3129
GGDAARY	13.08	4.37	8.64	6.65	795	266	843	504	55	2.26	603
GSFHGTV	5.78	2.79	3.64	4.13	1074	517	1119	951	169	2.24	829
RDGQSRG	5.19	5.20	3.55	4.94	1909	1977	1969	2317	344	2.15	1577
DGTYKGA	6.02	3.31	3.86	4.39	3021	1677	3336	2746	456	2.11	2465
IGSVGKL	3.89	2.50	2.25	2.53	2526	1669	2474	2083	595	2.11	2080
EVGHIRG	8.44	4.85	7.21	7.52	3052	1808	4604	3458	336	2.09	2578
ARSQEVP	9.93	4.69	7.14	7.55	989	481	1259	957	192	2.07	836
LHGARSS	5.46	4.88	3.46	4.47	11073	10119	10936	11489	1872	2.05	9455
TRLNTVQ	7.89	7.00	5.80	7.35	2026	1791	2363	2320	233	2.05	1699
VTNSSRV	7.35	6.78	5.97	7.55	3899	3684	5209	5066	491	2.03	3373
VRFGSNP	4.09	2.79	2.38	2.07	777	541	659	496	176	1.96	697
VSRSGGV	3.47	3.32	3.39	3.75	671	664	1109	927	181	1.96	608
DNRTVNV	36.95	21.32	25.06	27.53	702	425	814	682	18	1.96	644
GTASSRP	9.15	10.42	8.24	10.79	6107	7155	8681	9149	623	1.87	5789
TGVNVKS	3.31	3.37	2.68	3.69	694	733	989	954	196	1.84	671
RGSTMMP	7.97	7.38	6.02	7.41	2211	2079	2721	2601	256	1.83	2119
VSGGQTQ	7.07	3.39	5.31	5.26	1505	732	1891	1409	194	1.78	1459
LNPRSSS	3.63	3.91	3.25	3.78	6573	7343	9514	8744	1691	1.77	6591
YRIGEGT	4.78	2.61	3.57	2.85	2478	1422	2893	1875	488	1.75	2523
AADAVRV	3.17	1.07	2.41	1.68	717	247	835	475	209	1.75	719
VPGEGRV	9.10	4.06	7.10	6.60	1687	804	2278	1570	177	1.73	1763
YDQVSHP	2.63	0.82	1.64	1.53	446	142	435	323	157	1.72	456
GAHPTGG	5.96	3.40	4.09	5.01	2332	1386	2784	2514	369	1.69	2469
SLGGLGN	4.97	2.45	3.76	3.68	327	162	442	302	60	1.65	343
GIGHLAS	5.03	3.35	3.96	4.58	1558	1088	2286	1825	291	1.56	1778
SHEVVRA	8.19	5.76	8.99	9.04	2777	2055	5194	3968	323	1.56	3223
GLRGVSV	3.69	3.98	3.66	3.94	637	701	875	869	163	1.50	762

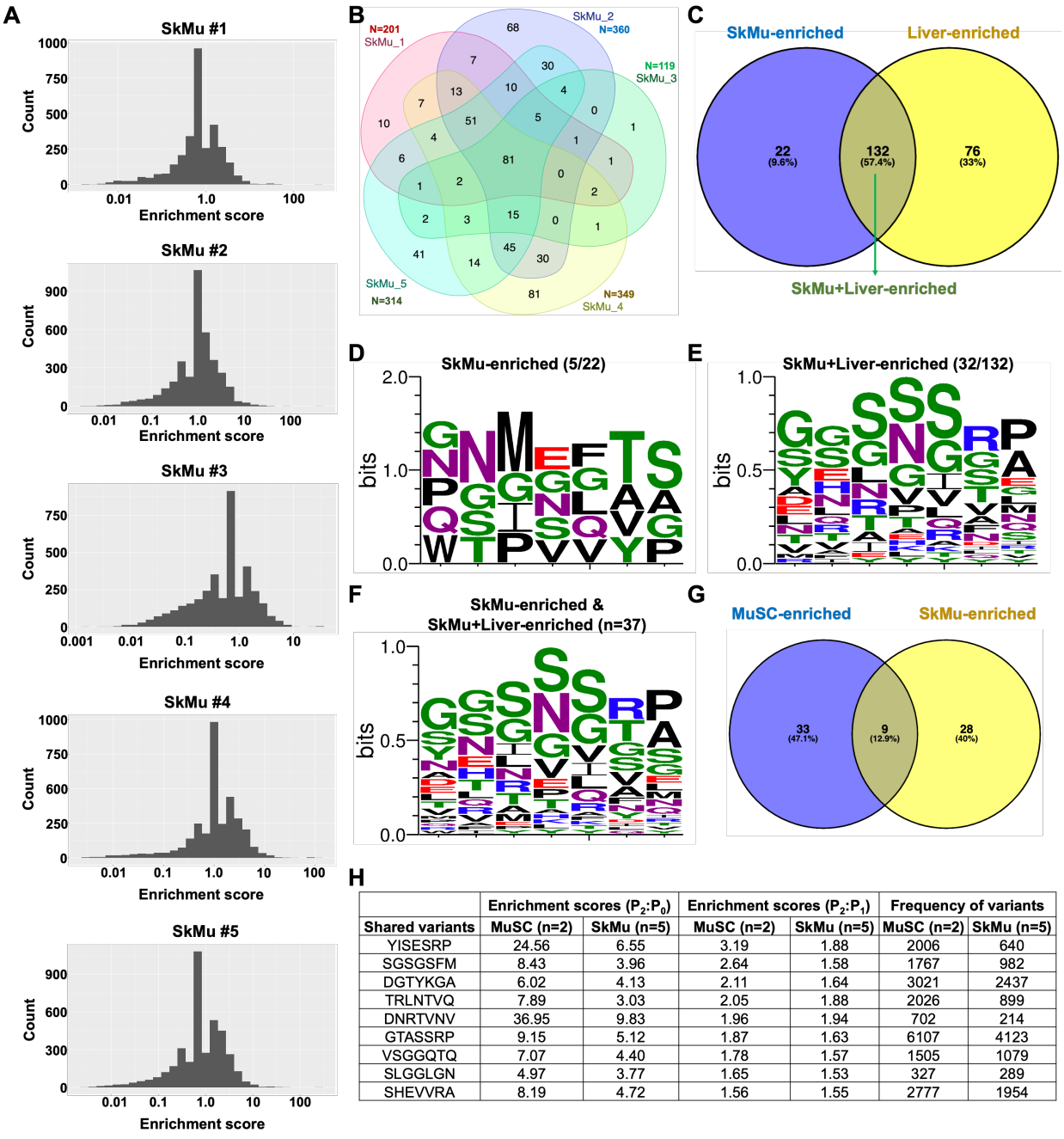

H

	Enrichment scores (P_2:P_0)		Enrichment scores (P_2:P_1)		Frequency of variants	
Shared variants	MuSC (n=2)	SkMu (n=5)	MuSC (n=2)	SkMu (n=5)	MuSC (n=2)	SkMu (n=5)
YISESRP	24.56	6.55	3.19	1.88	2006	640
SGSGSFM	8.43	3.96	2.64	1.58	1767	982
DGTYKGA	6.02	4.13	2.11	1.64	3021	2437
TRLNTVQ	7.89	3.03	2.05	1.88	2026	899
DNRTVNV	36.95	9.83	1.96	1.94	702	214
GTASSRP	9.15	5.12	1.87	1.63	6107	4123
VSGGQTQ	7.07	4.40	1.78	1.57	1505	1079
SLGGLGN	4.97	3.77	1.65	1.53	327	289
SHEVVRA	8.19	4.72	1.56	1.55	2777	1954

Figure 3-4: NGS analysis identifies SkMu-enriched AAV capsid variants.
A) Histogram of enrichment score analysis in P_2 SkMu samples 1-5.
B) Venn diagram of overlapping AAV capsid variants with E-scores > 2 from 5 SkMu samples.
C) Venn diagram of SkMu-enriched and Liver-enriched AAV capsid variants.
D-F) Frequency plots of SkMu-enriched, SkMu+Liver-enriched, and pooled SkMu-enriched and SkMu+Liver-enriched AAV capsid variants created by WebLogo 3 and using the chemistry color scheme.
G) Venn diagram of the 9 overlapping AAV capsid variants with E-scores >2 from SkMu and MuSC samples.
H) List of the 9 shared SkMu-enriched and MuSC-enriched AAV candidate variants with respective E-scores and frequencies.

Table 3-4: SkMu-enriched AAV capsid variants.

	Enrichment scores (P2:P0)			Frequency of variants				E-score (P2:P1)	Frequency
SkMu AAV variants	SkMu (n=5)	Liver (n=5)	Heart (n=5)	SkMu (n=5)	Liver (n=5)	Heart (n=5)	AAV (P0)	SkMu (n=5)	AAV (P1)
WNGELVA	104.04	1.36	36.74	253	47	92	2	325.00	1
AEAPILL	169.49	8.98	288.67	16173	813	25405	70	5.11	3620
GLLNSSP	6.06	2.54	5.30	373	154	302	47	2.22	200
ESGNIRP	6.23	2.34	5.07	351	133	280	45	2.09	209
AHSGGTY	4.11	2.15	3.82	515	274	473	100	1.98	323
DNRTVNV	9.83	5.93	6.09	214	136	136	18	1.94	142
YISESRP	6.55	5.32	5.99	640	512	551	75	1.88	407
TRLNTVQ	3.03	2.25	1.94	899	680	557	233	1.88	585
NSYSVSP	5.05	3.61	3.42	372	266	243	58	1.85	247
NGINGAS	4.52	1.35	4.05	425	133	371	76	1.83	293
EVRVANA	6.57	3.16	5.51	244	116	194	29	1.82	163
MTGLRGT	3.92	4.49	3.84	60	71	57	12	1.71	43
GENAGRA	4.28	2.33	3.99	285	154	249	51	1.67	204
GASPSSI	3.83	2.00	2.84	804	417	577	163	1.66	587
DGTYKGA	4.13	2.89	3.13	2437	1689	1752	456	1.64	1788
GTASSRP	5.12	4.66	3.87	4123	3760	2970	623	1.63	3057
GTPSQYG	2.82	1.55	2.00	1164	645	784	320	1.62	869
TNLNLRE	4.96	3.50	4.11	528	372	415	82	1.61	394
GQSNISR	4.19	3.98	3.27	1082	1029	825	204	1.61	829
YGTVSVP	5.35	4.08	4.45	843	644	668	122	1.61	633
YESSRTA	3.95	2.84	2.55	273	198	172	54	1.58	210
LNSSSYG	3.40	2.62	2.45	3239	2483	2229	738	1.58	2481
SGSGSFM	3.96	2.54	3.68	982	630	877	192	1.58	752
VSGGQTQ	4.40	2.45	4.12	1079	612	982	194	1.57	849
RQTNQIE	3.37	2.72	3.14	246	199	221	58	1.55	196
LGSSGVS	5.34	3.32	5.00	1775	1091	1591	257	1.55	1381
SHEVVRA	4.72	2.69	4.42	1954	1139	1753	323	1.55	1535
PSMGFTP	2.60	1.62	1.91	273	169	192	82	1.53	217
SLGGLGN	3.77	2.74	3.27	289	214	241	60	1.53	231
GSITYTP	2.83	1.87	2.45	500	326	409	136	1.52	394
VSGSSFG	7.42	6.74	5.95	184	164	143	19	1.52	145
SGRNSDL	4.43	2.64	4.63	745	449	753	134	1.51	612
GFNHGAN	4.26	3.50	3.91	3076	2515	2694	558	1.51	2460
QNMVVTS	3.24	1.61	2.47	311	157	228	75	1.50	252
YVNKSQA	3.32	3.06	2.48	976	921	720	236	1.50	813
NHSSGAM	5.63	4.24	4.18	913	668	635	123	1.50	722
GRISGGS	4.43	3.71	3.26	295	254	210	52	1.50	240

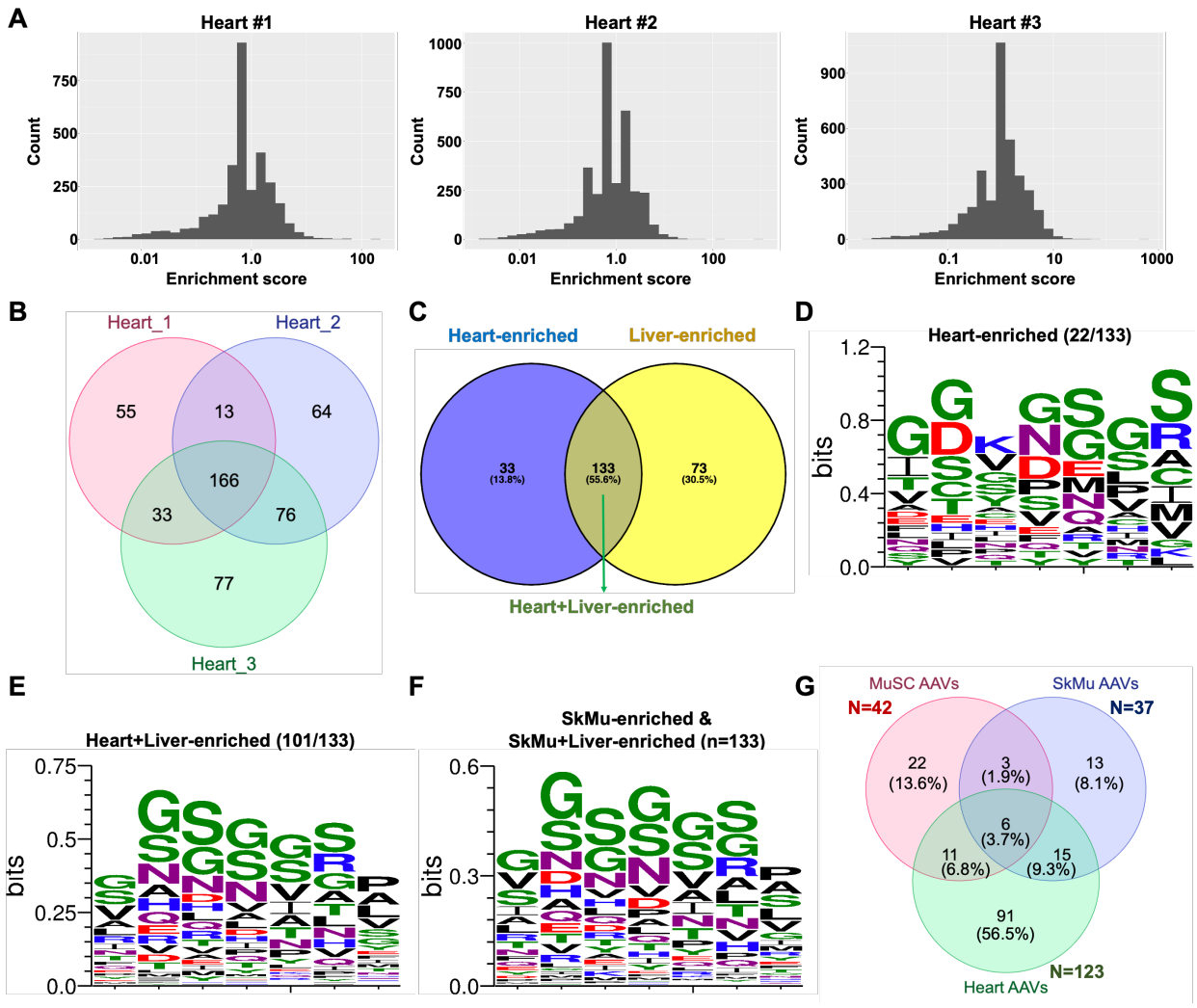

Figure 3-5: NGS analysis identifies Heart-enriched AAV capsid variants.
A) Histogram of enrichment score analysis in P_2 Heart samples 1-3.
B) Venn diagram of overlapping AAV capsid variants with E-scores > 2 from 3 Heart samples.
C) Venn diagram of Heart-enriched and Liver-enriched AAV capsid variants.
D-E) Frequency plots of Heart-enriched and Heart+Liver-enriched AAV capsid variants created by WebLogo 3 and using the chemistry color scheme.
F) Frequency plot of Heart-enriched and Heart+Liver-enriched AAV capsid variants created by WebLogo 3 and using the chemistry color scheme.
G) Venn diagram of overlapping AAV capsid variants highly enriched in MuSC, SkMu and Heart.

Table 3-5: Heart-enriched AAV capsid variants.

	Enrichment scores (P2:P0)			Frequency of variants				E-score (P2:P1)	Frequency
Heart AAV variants	Heart (n=3)	Liver (n=3)	SkMu (n=6)	Heart (n=3)	Liver (n=3)	SkMu (n=6)	AAV (P0)	Heart (n=3)	AAV (P1)
IGCDYPC	2.47	0.87	1.27	99	30	46	29	2.01	45
FDKGAVI	2.97	1.11	1.36	961	318	417	238	1.94	463
LDGVSHM	2.71	0.97	1.50	335	109	166	92	1.82	174
AGIGQAG	3.25	1.68	1.79	184	83	93	40	2.42	68
DVKNGGR	2.71	1.86	2.05	1426	884	1001	386	1.61	825
GDHNTIK	3.33	1.19	2.15	451	148	292	102	1.77	243
FGSVHSP	2.35	2.57	2.44	691	662	687	216	1.77	364
VQMSGYL	3.81	2.52	2.44	379	228	231	74	2.00	179
MNGLRGT	2.59	3.48	2.45	9186	11110	8110	2614	1.53	5605
TTYNSSA	3.14	2.37	2.49	440	291	318	102	1.95	208
DVSLTRM	3.69	2.79	2.50	278	191	172	56	1.87	140
ITSPSVS	3.28	1.97	2.59	334	183	255	76	1.83	173
LHHSPSY	2.66	2.37	2.68	2068	1670	1971	578	1.58	1233
GGYSETS	3.45	1.44	2.82	193	71	143	40	1.64	107
YNGAIHH	4.19	3.66	2.86	723	576	474	129	2.08	330
THGLPIV	3.62	2.40	2.86	841	502	660	171	1.99	394
SMLGGVA	3.34	2.47	2.96	205	133	158	45	1.62	118
NGSTSPV	3.15	1.60	2.96	630	284	581	146	1.83	319
YDQVSHP	4.26	2.58	2.98	901	289	593	157	2.13	399
GQSNISR	3.72	4.46	2.99	1011	1097	204	204	1.90	507
LRDNSAF	3.81	2.41	3.08	647	361	501	123	2.19	271
GEKFMGV	4.20	1.96	3.20	588	244	421	104	1.51	367
GVPKTHD	3.22	3.17	3.20	852	755	817	196	1.94	411
GMGTVAR	3.29	3.96	3.26	1151	1275	1115	264	1.63	673
QLPNNLS	3.24	1.65	3.26	584	269	572	134	1.70	325
GPVVQGA	3.05	1.65	3.37	164	81	165	40	1.89	82
VHGISPL	2.82	2.50	3.42	875	706	1019	234	1.70	492
QNMVVTS	4.14	2.72	3.43	420	247	328	75	1.63	241
ISLPNSI	3.26	1.78	3.44	276	137	269	63	1.66	157
SYIGVAA	2.84	2.60	3.49	1688	1389	2019	442	1.97	805
QVGFPTP	3.11	2.79	3.54	920	752	1009	219	1.61	536
GQGCTQC	4.44	3.05	3.58	429	265	318	72	2.05	198
ITLSGSS	3.06	2.33	3.64	1141	756	1293	267	1.93	537
QRSSNGP	2.96	3.98	3.68	1190	1417	1415	294	1.70	650
LSSMGQL	4.29	2.67	3.69	1457	813	1152	251	1.91	715
FHSSASA	3.32	3.72	3.70	5539	5505	5831	1223	1.83	2818
GASPSSI	3.44	2.25	3.70	775	440	793	163	2.07	344
NARDSGF	5.69	3.72	3.71	364	214	221	47	2.26	150
LRVGNVE	2.76	3.13	3.77	317	320	422	84	2.00	147
NHSSGAM	2.96	3.30	3.81	487	491	606	123	1.75	264
NGQGILK	5.73	3.56	3.82	511	289	332	66	2.66	180
TCNSVGC	5.06	2.00	3.82	592	210	446	87	2.15	260
QDRNYGV	4.31	2.88	3.85	160	94	135	27	1.70	87
IGNGGLI	4.96	2.39	3.87	620	279	478	96	1.98	305
GSEGGSM	3.01	1.21	3.94	399	144	526	99	1.51	250
VSGSSFG	5.11	4.19	3.97	127	96	96	19	2.67	46
RGSNDLP	4.46	3.89	3.98	1194	945	1030	201	1.78	639
AADAVRV	3.73	2.41	3.99	1045	606	1053	209	1.76	561
RQTNQIE	4.13	3.44	4.01	328	242	304	58	2.69	113
EHVEGRR	3.93	1.78	4.02	367	152	359	70	2.42	144
FNISANE	3.23	2.45	4.05	271	181	354	62	1.71	148
NGINGAS	3.51	2.24	4.06	362	205	397	76	2.00	169
SSYSVSL	4.48	3.83	4.19	521	393	451	85	1.86	260
TGQTVLG	4.31	3.00	4.25	353	215	311	59	1.79	180
SNYNVTG	4.39	3.65	4.27	219	156	198	36	2.04	98
SCGDSCR	4.27	2.01	4.34	528	225	521	93	2.25	223
DGTYKGA	3.65	3.86	4.35	2269	2131	2541	456	1.69	1249
GSTYENS	10.91	2.91	4.37	130	33	51	9	2.49	50
VSSQGTS	3.29	2.77	4.38	216	163	285	49	1.84	111
PGSYVSS	2.43	2.99	4.49	271	309	461	83	1.51	169
RDVSSGG	3.70	3.51	4.58	1037	879	1269	207	1.54	632
VDQGRLS	2.77	2.50	4.61	282	229	452	76	1.55	172
GGDAARY	6.71	2.71	4.73	509	181	332	55	2.28	205
VQSGNYV	4.48	3.72	4.73	678	506	667	112	2.00	318
VSEINRG	4.93	2.51	4.75	630	295	578	96	2.11	284
TNRDAQF	4.68	3.58	4.77	1709	1172	1636	272	1.96	823
VSRSGGV	3.35	4.75	4.83	848	1038	1139	181	1.55	497
GFNHGAN	3.25	3.77	4.91	2481	2561	3564	558	1.62	1420
VQVGTGT	4.47	2.89	4.95	1767	1016	1861	292	1.95	848
SGSGSFM	4.08	3.58	4.96	1053	833	1215	192	1.81	550
TNLHVNL	4.09	3.09	5.00	242	164	289	43	1.60	139
SANVFSP	5.08	3.10	5.04	1488	819	1380	212	1.67	815
SGLDKAP	5.56	3.85	5.25	875	546	791	117	1.99	414
GGGSSSA	4.39	3.58	5.30	182	141	216	31	1.71	101
GQDNRAL	6.12	4.37	5.36	376	235	314	45	1.79	195
SSTGTWV	6.03	3.59	5.43	354	196	309	45	2.10	164
YGVDMGL	4.95	1.85	5.48	134	45	147	20	1.99	63
ASNLGTY	4.64	2.95	5.51	1317	759	1593	213	1.91	655
INMQSMA	5.26	3.90	5.51	741	493	757	104	1.94	358
ATAGAII	4.57	2.70	5.56	1142	620	1394	191	1.51	731
LSSNANL	4.05	3.07	5.62	1248	861	1697	231	1.97	600
VASGTVL	6.46	3.63	5.65	1087	550	889	125	2.27	450
GAHPTGG	3.86	3.78	5.67	1939	1684	2674	369	1.68	1078
EGKSSPT	6.14	3.19	5.68	267	122	245	32	2.47	101
MRNTESS	3.76	4.25	5.81	321	322	487	63	1.70	177
VIGHGSA	3.51	3.99	6.03	885	893	1456	185	1.61	511
RSEYNSV	7.54	4.95	6.03	1657	969	1262	162	2.32	667
GTASSRP	3.05	4.74	6.08	2604	3565	4923	623	1.54	1562
LGSGALA	3.93	3.38	6.08	947	727	1388	178	1.74	511
PGNINNN	4.75	4.26	6.18	465	376	588	72	1.77	245
VERGASV	6.68	3.50	6.19	5110	2387	4547	561	1.92	2479
GPSSLRE	4.36	4.72	6.21	215	218	300	38	1.65	127
VSGGQTQ	4.21	3.44	6.24	1095	798	1602	194	1.85	560
IASGNSV	5.56	4.20	6.39	791	540	871	107	1.91	394
AHSGGTY	5.39	4.38	6.41	741	533	822	100	2.02	338
FNNGIHS	5.04	2.89	6.47	1304	679	1685	193	2.59	476
RENPSGM	5.37	4.79	6.73	3595	2873	4183	478	1.55	2098
EVGHIRG	5.57	4.43	6.96	2520	1800	2966	336	1.93	1228
PSSQPLP	5.11	3.70	7.04	951	630	1264	141	1.58	579
VGSLYQP	5.64	4.08	7.05	666	429	822	88	2.32	271
RSQEINL	8.99	6.81	7.08	1339	924	1001	113	1.92	670
SHEVVRA	5.82	4.17	7.32	2558	1617	3158	323	2.18	1095
YGTVSVP	4.78	6.36	7.56	796	955	1230	122	1.53	484
RDSMVNP	6.01	4.31	7.56	2331	1470	2817	283	1.95	1105
NSYSVSP	5.21	5.56	7.71	399	393	585	58	1.99	192
SGDAYRA	8.19	7.52	7.87	315	267	289	29	1.86	162
LGSSGVS	5.52	4.79	7.94	1898	1482	2655	257	1.92	936
HESRPPY	5.94	4.70	8.06	739	516	862	91	1.81	378
SNHDSRV	6.63	3.84	8.10	5472	2848	6548	612	2.32	2211
STVNGNQ	5.09	3.92	8.11	323	225	532	48	1.60	194
TGLNYTT	8.86	6.61	8.15	959	646	847	81	2.12	428
AGNITSF	7.30	4.73	8.27	2627	1509	2848	262	1.71	1416
SLHSPQL	6.22	5.82	8.92	352	286	477	41	1.57	206
INHNSHI	12.89	6.29	9.01	437	187	286	25	3.05	134
ARSQEVP	6.57	4.60	9.02	783	504	1089	92	2.17	353
VIAQGMS	7.45	6.31	9.61	97	75	136	10	2.20	43
IVGSGSA	8.61	5.49	9.64	383	219	399	33	2.52	143
VGQGISL	8.97	6.18	9.96	274	174	285	23	1.83	143
ESGNIRP	11.20	6.41	9.97	686	339	580	45	2.57	248
GENAGRA	7.01	5.40	10.49	470	332	692	51	1.67	272
SLGGLGN	10.05	7.78	12.28	838	570	963	60	2.23	343
GGGTLHH	12.19	8.55	13.31	203	123	207	12	2.35	79
AEAPILL	494.17	9.53	485.92	49343	809	45620	70	22.58	49342

Chapter 4 – Characterizing AAV-mediated Immune Responses in a Mouse Model of Duchenne Muscular Dystrophy

Abstract

Adeno-associated viruses (AAVs) have emerged as one of the leading vectors for gene therapy, and are being evaluated in clinical trials for neuromuscular disorders such as Duchenne muscular dystrophy (DMD). While AAV-based therapies exploit the evolutionary fitness of viruses to transduce cells, the human immune system has co-evolved mechanisms to recognize and neutralize AAV vectors. Thus, innate and adaptive immune responses pose a significant risk to achieving a safe and efficient AAV gene therapy. For DMD, high doses of AAV are needed in order to target the affected muscles of the body; however, such high doses have been associated with a number of serious adverse events (SAEs) involving both innate (e.g., complement activation) and adaptive (e.g., T cell responses) immunity. Here, we show that the mouse immune system neutralizes a second dose of AAV9; we subsequently carry out a comprehensive characterization of immune responses that arise in response to both single and double dosing of AAV9. Mice were systemically dosed and re-dosed with AAV9 at ~1.16 x 10^{14} vg/kg carrying either micro-dystrophin (μDYS), Cas9, or Cas9 with a frameshift mutation (Cas9-FS). Peripheral blood mononuclear cells (PBMCs) and plasma were collected prior to dosing and at various time points after each dose. Plasma was probed for anti-AAV9 antibodies, complement and cytokines. High content protein microarray of the humoral response revealed a significant increase in anti-AAV9 IgGs over the 4-week period between the first and second dose. Complement assays

only revealed significant consumption of C3 and C4 components 5 hours after the second dose. Since anti-AAV9 IgG levels are significantly elevated after the second dose compared to 5 hours after the first dose, these data implicate the classical complement pathway. The potential of each vector to activate toll-like receptor 9 (TLR9) signaling was evaluated and shown to be higher in the Cas9 vectors compared to the μDYS vector. Myeloid-derived pro-inflammatory cytokines were only induced at 5 hours after the second dose of AAV. These cytokines include IP-10 (CXCL10), MIP-1β (CCL4), MCP-1 (CCL2) and TNF-α. We hypothesize that anti-AAV9 activates myeloid cells by Fcγ receptor stimulation via antigen-antibody complexes and/or complement receptor activation via split products arising from anti-AAV9 induced classical complement pathway. Single cell RNA-sequencing (scRNA-seq) of PBMCs support our hypothesis, demonstrating enhanced activation profiles of all main immune types, including monocytes, following the second dose of AAV. These data strongly suggest a role for AAV-capsid antibodies in amplifying AAV-induced immune responses and reveal a model by which mice can mimic some aspects of human AAV-mediated immune responses.

Introduction

Adeno-associated viruses (AAVs) are the leading vectors for delivering gene replacement or gene editing approaches. In neuromuscular disorders, AAV gene-replacement approaches are being evaluated in Phase I/II clinical trials for Duchenne muscular dystrophy (DMD) and X-linked myotubular myopathy (XLMTM). In addition, there is one approved AAV-based gene replacement therapy, marketed as Zolgensma®,

for the treatment of spinal muscular atrophy (SMA). However, serious adverse events (SAEs) attributed to immune responses against the AAV capsid or the transgene protein have been reported in patients receiving high doses of AAV[238-245]. The SAEs in the DMD clinical trial occurred in patients receiving AAV doses greater than 2.0 x 10^{14} vg/kg, which contain a truncated and functional copy of the *DMD* gene termed micro-dystrophin (μDYS). Several patients experienced thrombotic microangiopathy (TMA) and renal failure attributed to complement activation[242,244]. Furthermore, in three DMD clinical trials, five patients developed myositis associated with T cell-mediated cytotoxicity against the μDYS transgene (public disclosure). Lastly, a single patient death occurred due to T cell-mediated cytotoxicity against the AAV9 capsid in the heart (public disclosure). XLMTM clinical trials have also reported four deaths in patients receiving a high-dose of AAV (3.5 x 10^{14} vg/kg) containing a functional copy of myotubularin 1 (*MTM1*). Two of the patients had pre-existing liver disease and one patient succumbed to gastrointestinal bleed, which was also a result of liver failure[238,245]. Similarly, 8 cases of TMA were reported in babies dosed with Zolgensma®, which were resolved with blood and/or platelet transfusions[240,241]. However, one fatal case occurred in a baby dosed with Zolgensma® (1.1 x 10^{14} vg/kg) and the cause of death was attributed to TMA associated with complement activation and the progressive clinical presentation was suggestive of renal failure similar to the SAEs observed in the DMD clinical trials[241]. These observations suggest that AAV is clearly a target of diverse immune responses, and indicate that immune system recognition of AAV is more prominent than previously predicted in pre-clinical animal models. The results of these studies suggest that further investigation of the immune response to AAV may enable

the identification of therapeutic targets and biomarkers for minimizing SAEs and improving the long-term efficacy of AAV-based therapies.

Approximately 30-60% of the general population is estimated to have pre-existing immunity to AAV, as antigen-reactive memory T cells and/or neutralizing antibodies (NAbs) and binding (BAbs) antibodies[121,246]. Screening for NAb and BAb titers has been used to determine trial-eligibility for a variety of AAV-based therapies including DMD, XLMTM, Hemophilia A and Hemophilia B, Spinal muscular atrophy (SMA) among other monogenic diseases[247]. However, standardized assays for determining anti-AAV titers (i.e., neutralization assay or binding assay) are lacking, and there is no universal threshold for exclusion from clinical trials for AAV administration. The durability of naturally acquired AAV-specific antibodies remains unclear, and the presence of NAb titers does not inform on the presence of memory B cells and/or long-lived plasma cells, which reside in the bone marrow. Moreover, pre-trial screening protocols often probe for pre-existing cellular immune responses via the enzyme-linked immunospot (ELISPOT) assay, which detects antigen-reactive IFNγ-secreting effector memory T cells (T_{EM})[248,249]. However, ELISPOT may not have the sensitivity to detect T_{EM} cells, which are present in circulation at low frequencies, as T_{EM} cells survey non-lymphoid tissues. Additionally, the IFNγ-ELISPOT is unable to detect lowly abundant central memory T (T_{CM}) cells, which circulate in the lymphatic system, residing in secondary lymphoid tissues. Despite attempts to screen for humoral and cellular pre-existing immunity, the current assays used in pre-trial screening are clearly not sufficient to exclude patients susceptible to AAV-induced SAEs and are likely not sensitive enough to detect low frequency memory T cells or low NAb/BAb titers. Likewise, the SAEs reported in DMD,

XLMTM and SMA clinical trials strongly implicate additional components of innate and/or adaptive immune responses that are contributing to AAV-induced immunogenicity. Thus, there remains an unmet need to effectively model human AAV-mediated immune responses, which may enable a better understanding of the earliest immunomodulatory effectors, and how they amplify downstream immunity. Targeting the earliest responses will significantly improve the efficacy of mitigation strategies designed to circumvent adverse responses.

Although systemic administration of AAV-based therapies has been well tolerated in small and large animal models, pre-clinical studies did not predict the immune responses that were subsequently observed in clinical trials[116,250,251]. These pre-clinical studies relied on a single systemic administration of AAV and primarily focused on evaluating the efficacy of the therapeutic platform. However, a single AAV dose may not induce an immune response due to the sterile conditions under which the mice are housed, which reduces the risk of natural AAV infections, and thus eliminates pre-existing immunity to AAV. Conversely, natural AAV infections in humans are prevalent, as studies support that up to 60% of the general population contain pre-existing immunity to AAV[121,246]. We hypothesize that implementing a re-dosing strategy, in which the first dose effectively immunizes the mouse, will create a model that better recapitulates human immunity.

In this study, we carry out an AAV double dosing approach and characterize AAV-induced immune responses after the first and second administrations of AAV. Mice were systemically dosed and re-dosed with AAV9 at ~1.16 x 10^{14} vg/kg carrying either micro-dystrophin (μDYS), Cas9, or Cas9 with a frameshift mutation (Cas9-FS),

disrupting expression and protein production. Peripheral blood mononuclear cells (PBMCs) and plasma were harvested at baseline and at various time points after the first and second injections of AAV (five hours, two weeks, four weeks, and six weeks). Our findings demonstrate humoral responses against the AAV capsid are undetectable at baseline and support our hypothesis that mice are at a reduced risk of naturally contracting AAV infections due to sterile housing conditions. In addition, our pre-existing mouse model demonstrates pro-inflammatory cytokine responses and complement activation following the second administration of AAV, which recapitulates immune responses reported in ongoing DMD clinical trials. Finally, we applied single-cell RNA sequencing (scRNA-seq) to unbiasedly characterize immune responses after the first and second dose of AAV. While we observe an activation profile and differentially expressed pro-inflammatory cytokines via scRNA-seq after the second injection of AAV, ongoing validation studies are needed to identify biomarkers for pre-dose screening as well as therapeutic targets to improve the safety and efficacy of AAV-based gene therapies. In summary, our AAV double dosing strategy accurately describes human AAV-immune responses and provides opportunities to model aspects of human immune responses.

Materials and Methods

Mice

All animal care and work were conducted under protocols approved by the UCLA Animal Research Committee in the Office of Animal Research Oversight. hDMD del45 mdx mice were generated and genotyped as described[77].

Constructs

CK8e-Cas9 (pAAV-CK8e-Cas9), gRNA/mCherry (pAAV-Target44C4+55C3/mCherry), and FLAG-CK8e-μDYS (pAAV-FLAG-CK8e-μDYS) vectors: The original Cas9 (pAAV-CK8e-Cas9), targeting vector (pAAV-Target) and FLAG-CK8e-μDYS vectors (pAAV-FLAG-CK8e-μDYS) plasmids were a gift from Dr. Jeffrey Chamberlain and were generated as described[40,73]. Our gRNAs targeting introns 44 (gRNA 44C4) and 55 (gRNA 55C3) were cloned into the pAAV-Target plasmid in tandem (referred to as pAAVTarget-44C4+55C3/mCherry).

CMV-Cas9 (pAAV-CMV-Cas9): pAAV-CMV-Cas9 was obtained from Addgene (plasmid #106431).

FLAG-CK8e-Cas9 (pAAV-FLAG-CK8e-Cas9) and FLAG-CK8e-Cas9-FS (pAAV-FLAG-CK8e-Cas9-FS) vectors: NEBuilder HiFi DNA Assembly (New England BioLabs) was used to generate pAAV-FLAG-CK8e-Cas9 and pAAV-FLAG-CK8e-Cas9-FS. A 386bp gBlock (IDT) containing a FLAG-tag at the N-terminus and part of the Cas9 coding sequence was synthesized (FLAG-Cas9). A 385bp gBlock (IDT) identical to FLAG-Cas9, but with a 1nt-deletion to encode for a frameshifting (FS) mutation in Cas9 was synthesized (FLAG-Cas9-FS). The FLAG-Cas9 and FLAG-Cas9-FS gBlocks were cloned in HincII- and BglII-digested pAAV-CK8e-Cas9 using NEBuilder HiFi DNA Assembly according to the manufacturer's instructions to create pAAV-FLAG-CK8e-Cas9 and pAAV-FLAG-CK8e-Cas9-FS.

Recombinant AAV production

AAV9-CMV-Cas9 and AAV9-Target44C4+55C3/mCherry: pAAV-AAV-CMV-Cas9 and pAAV-Target44C4+55C3/mCherry were shipped to Virovek Inc. for production and purification of recombinant AAV9-CMV-Cas9 and AAV9-Target44C4+55C3/mCherry. Virovek Inc. purified recombinant AAVs using the cesium chloride ($CsCl_2$) density ultracentrifugation method and quantified viral titer by qPCR using their ITR primers.

AAV9-FLAG-CK8e-Cas9, AAV9-FLAG-CK8e-Cas9-FS, and AAV9-FLAG-CK8e-μDYS: pAAV-FLAG-CK8e-Cas9, pAAV-FLAG-CK8e-Cas9-FS, and pAAV-FLAG-CK8e-μDYS were shipped to Vigene Biosciences Inc. for large scale AAV9 production. Vigene Biosciences Inc. purified recombinant AAVs using iodixanol gradient ultracentrifugation and quantified viral titer by qPCR using their ITR primers. Purity of capsid viral proteins was determined by SDS-PAGE (9% polyacrylamide gels).

AAV9 double dosing pilot study in hDMD del45 mdx mice in vivo

A pilot study was conducted in which 7-8-week-old hDMD del45 mdx mice were first dosed with AAV9-CMV-Cas9 at 3.0 x 10^{12} vg via retro-orbital (r.o.) injection. A second dose with AAV9-Target44C4+55C3/mCherry at 3.0 x 10^{12} vg was systemically administered via r.o. injection ~4 weeks after the first dose. The mice were sacrificed ~4 weeks after the second dose. One mouse was used as a second dose only control, receiving an r.o. injection of AAV9-Target44C4+55C3/mCherry. The second dose only control mouse was harvested in the same timeline, ~8 weeks after AAV9-Target44C4+55C3/mCherry.

For mCherry immunofluorescence analysis, muscles from the three mice were harvested and fixed in 1% PFA overnight. The following day, muscles were transferred

to 5% sucrose for at least 6hr, then transferred to 30% sucrose overnight before being flash frozen in isopentane and cryosectioned in intervals of 10μm thickness throughout the majority of the muscle tissue. For mCherry immunofluorescence analysis, sections were washed in TBS for 1 – 2 min, then incubated in TrueBlack (Biotium, 1:20 in 70% ethanol) for 30 sec – 1min, washed with TBS and mounted with VECTASHIELD containing DAPI (Vector Laboratories) and imaged on the Axio Observer Z1 microscope (Zeiss).

For single cell RNA-sequencing (scRNA-seq), peripheral blood mononuclear cells (PBMCs) were only collected from one of the AAV double dosed mouse at baseline (Pre, prior to AAV exposure), ~4 weeks post-injection of the first dose (Post-1), and ~4 weeks post-injection of the second dose (Post-2). Approximately, 0.2mL of whole blood was harvested in EDTA-containing BD Microtainer Capillary Blood Collection Tubes (BD Biosciences). Whole-blood was diluted 1:1 in DPBS and carefully layered over Ficoll-Paque Premium (Fisher Scientific) in a 2:1 ratio of diluted blood to Ficoll. Samples were centrifuged at 800 rcf for 25 mins with the brakes and acceleration turned off. The PBMC layer (buffy coat) was extracted, washed with DPBS, and resuspend in RBC lysis buffer (Qiagen) for 1 – 2 mins. PBMCs were then centrifuged using a low-speed spin (150 rcf for 15 mins) to remove dead RBCs and platelets and cryopreserved in 90% fetal bovine serum (FBS, Thermo Fisher) and 10% dimethyl sulfoxide (DMSO, Millipore Sigma).

AAV9 single and double dosing study in large cohort of hDMD del45 mdx mice in vivo

The larger double dosing study was conducted using ~12-week-old hDMD del45 mdx male and female mice. Three AAV serotype 9 vectors carrying either FLAG-CK8e-Cas9, FLAG-CK8e-Cas9-FS or FLAG-CK8e-μDYS were systemically injected via retro-orbital (r.o.) injection at ~1.16 x 10^{14} vg/kg. Each vector was administered in n=3 males and n=3 females for a total of 9 mice dosed per sex. A second dose (re-dosing) was with the same AAV vector via r.o. injection at ~1.16 x 10^{14} vg/kg ~4 weeks after the first dose. The mice were sacrificed ~6 weeks after the second dose (i.e., ~10 weeks after the first dose) and the heart, skeletal muscle tissues, lung, liver and spleen were harvested and flash frozen in isopentane.

For single cell RNA-sequencing (scRNA-seq), PBMCs were collected, as mentioned above, from all mice at the following time points: prior to AAV exposure (Pre), 2 weeks post-injection of the first dose (Post-1 2wk), 4 weeks post-injection of the first dose (Post-1 4wk), 2 weeks post-injection of the second dose (Post-2 2wk), and 6 weeks post-injection of the second dose (Post-2 6wk). Only two of the three male mice per AAV vector (n=6 male mice total) were submitted for scRNA-seq at the following time points: Pre, Post-1 2wk, and Post-2 2wk.

For Luminex, enzyme-linked immunosorbent assays (ELISAs), and high content protein microarray analysis (HCPM), plasma was collected at the following time points: prior to AAV exposure (Pre), ~5hr post-injection of the first dose (Post-1 5hr), 2 weeks post-injection of the first dose (Post-1 2wk), 4 weeks post-injection of the first dose (Post-1 4wk), ~5hr post-injection of the second dose (Post-2 5hr), 2 weeks post-injection of the second dose (Post-2 2wk), and 6 weeks post-injection of the second

dose (Post-2 6wk). Plasma was isolated during PBMC isolation, discussed earlier, in which plasma is the layer above the PBMC buffy coat.

10x library preparation, sequencing and alignment for the pilot and large cohort studies

scRNA-seq libraries were generated using Chromium Single Cell 3' v.3 (10x Genomics). Libraries from the pilot study were sequenced using NovaSeq 6000 S2 (Illumina) 2 x 50bp paired-end reading strategy. Libraries from the proper large cohort study were sequenced using NovaSeq 6000 S4 (Illumina) 2 x 100bp paired-end reading strategy. Cells were called using Cell Ranger (v.6.1.2, 10x Genomics) with the mouse reference genome (mm10) to generate raw gene expression matrices for each sample.

Single cell RNA-sequencing data analysis and clustering

The raw gene expression matrices were analyzed by R software (v.4.1.2) with the Seurat package[252] v.4.1.0. Low-quality cells were removed when more than 20% of the UMIs were derived from mitochondrial genes, when less than 200 features and more than 1,800 unique features were detected. The data were then normalized using the default NormalizeData function parameters, the FindVariableFeatures function to select 2,000 genes with the highest standardized variance, and the ScaleData function to perform z-score transformation. We then integrated the samples using Harmony (v.0.1.0) and re-analyzed using RunUMAP, FindNeighbors, and FindClusters functions for uniform manifold approximation and projection (UMAP) visualization. The clusters were manually annotated using the top 50 differentially expressed genes produced by the FindAllMarkers function. For subcluster analysis of T cells, B cells, NK cells, and

monocytes, we used the subset function in combination with the same methods discussed to analyze the integrated data.

Detection of complement components with enzyme-linked immunosorbent assays (ELISAs)

Murine plasma samples were used to measure complement C3 (ab157711, Abcam), C4 (NBP2-70040, Novus Biologicals), and C5b9 (OKCD01374, Aviva Systems Biology) levels according to the manufacturer's instructions. Plasma sample were diluted to 1:50,000, 1:20, 1:100, and 1:30 to measure C3, C4, and C5b9, respectively. Each sample and time point were run in triplicate.

Multiplex cytokine analysis using Luminex

A custom ProcartaPlex panel (Thermo Fisher) was designed and consisted of 27 analytes: IFN-α, IFN-β, IFN-γ, IL-1α, IL-1β, IL-2, IL-3, IL-4, IL-5, IL-6, IL-7, IL-9, IL-10, IL-12p70, IL-13, IL-15, IL-17A, IL-18, IP-10, MCP-1, MCP-3, MIG, MIP-1α, MIP-1β, MIP-2a, RANTES, and TNF-α. Analytes were measured on a Luminex 200 instrument (Immune Assessment Core, UCLA) using mouse plasma samples according to the manufacturer's instructions. All male and female plasma samples were assessed at the following time points: Pre, Post-1 (5hr), Post-1 (2wk), Post-2 (5hr), and Post-2 (2wk). The cloud-based ProcartaPlex Analysis application (Thermo Fisher) was used to confirm the raw data were in the working range, in which the observed concentration was between 70% and 130% of the expected concentration from standard controls using either the four-parameter log-logistic (4PL) or five-parameter log-logistic (5PL)

standard curve. Cytokine analytes were expressed in picograms per milliliter (pg/mL). Analytes observed at the lower limits of quantification (LLOQ) were omitted from additional analysis (e.g., IFN-α).

Humoral IgM and IgG responses measured by high content protein microarrays (HCPM)

HCPM chips printed with AAV capsids, Cas9 or µDYS were used to measure humoral IgM and IgG antibody levels. HCPM chips were generated as previously described[253-255]. In brief, proteins of interest (i.e., antigens) were printed directly onto nitrocellulose microarrays at concentrations of 0.1mg/mL, 0.05mg/mL, 0.025mg/mL and 0.0125mg/mL. The antigens of interest included the following: AAV2 (AAV2-EMPTY, Virovek Inc.), AAV8 (AAV8-EMPTY, Virovek Inc.), AAV9 (AAV9-EMPTY, Virovek Inc.), SpCas9 (CAS9PROT-50UG, Millipore Sigma), AAVMYO (a gift from Dr. Xiangmin Xu, Professor of Anatomy and Neurobiology at the University of California, Irvine), and mini-dystrophin protein was provided by Pfizer. Plasma samples were serially diluted for each microarray to determine optimal dilution and ranged from: 1:200, 1:2,000, 1:20,000, and 1:200,000. Finally, antigen-specific humoral responses were assessed for male and female plasma samples at the following time points: prior to AAV exposure (Pre), 2 weeks post-injection of the first dose (Post-1 2wk), 4 weeks post-injection of the first dose (Post-1 4wk), 2 weeks post-injection of the second dose (Post-2 2wk), and 6 weeks post-injection of the second dose (Post-2 6wk). Quantitative analyses were performed by the Vaccine R&D Center at the University of California, Irvine as previously described by their team[253-255].

Statistical analysis

Results presented in Figure 4-3 are shown as mean ± standard deviation (SD) and comparison between time points (groups) was evaluated using one-way analysis of variance (ANOVA) mixed effects model with repeated measures followed by Tukey's post-hoc test. Results presented in Figures 4-4 and 4-5 are shown as mean ± standard deviation (SD) and comparison between time points (groups) was evaluated using one-way analysis of variance (ANOVA) with repeated measures followed by Tukey's post-hoc test. $p < 0.05$ (*), $p < 0.01$ (**), $p < 0.001$ (***), $p < 0.0001$ (****) were considered significant. Statistical analysis and graphs were generated using GraphPad Prism 9 software.

Results

Dual dosing AAV9 leads to enhanced immune responses in hDMD del45 mdx mice

We previously generated a CRISPR/Cas9 gene therapeutic that is designed to restore the *DMD* reading frame by deleting exons 45-55 using a single pair of guide RNAs (gRNAs)[68]. Because we seek to re-dose AAV-CRISPR to develop a long-lasting therapy, we will need to suppress elements of immunity that participate in AAV neutralization. In order to design redosing strategies that evade AAV-host immunity, we comprehensively evaluated immune responses to AAV-CRISPR/Cas9 *in vivo*, utilizing our hDMD del45 mdx mouse model[77], which contains an out-of-frame exon 45 deletion in the human *DMD* gene. A pilot study was conducted in which hDMD del45 mdx mice were dosed with two administrations of AAV9 (4 weeks apart) in which the second dose carried an mCherry reporter (**Figures 4-1A** and **4-1B**). A second dose only control

mouse was used to confirm AAV9-mCherry was functional. As expected, we observed mCherry expression as measured by fluorescence microscopy for the second-dose only control (**Figure 4-1C**). However, mCherry expression was not detected in the heart, diaphragm and tibialis anterior muscles of the re-dosed mice, suggesting that a second exposure to AAV results in neutralization of the vector by the adaptive immune response (**Figure 4-1C**).

Studying the broad immune responses that mediate AAV rejection could reveal novel therapeutic targets for redosing and could improve the safety and efficacy of AAV-based therapies. In order to understand the elements of the mouse immune system that respond to systemically administered AAV vectors, we carried out single-cell RNA sequencing (scRNA-seq) on peripheral blood mononuclear cells (PBMCs) of dosed mice. PBMCs were collected prior to AAV dosing (Pre) and four weeks after the first (Post-1) and second (Post-2) doses for one mouse in the pilot study. scRNA-seq uniform manifold approximation and projection (UMAP) plots demonstrated distinct shifts in transcriptional phenotypes between Pre and Post-1 and Post-2 across all main cell types including B cells, monocytes, natural killer (NK) cells and all T cell subsets (**Figure 4-1D**). The transcriptional differences between Pre, Post-1 and Post-2 time points suggest that mouse immune cells undergo phenotypic changes in response to the first exposure of AAV and even more-so after AAV re-administration to AAV. Yet, despite the transcriptional changes from Pre to Post-1, we only observed clearance of AAV after Post-2, likely due to the time it takes to mount an adaptive immune response. Our pilot study suggests that this approach of doubly dosing AAV may provide an

opportunity to identify critical genes, pathways or immune cell populations that mediate AAV neutralization that could be targeted to improve the efficacy of AAV-based delivery.

Characterizing humoral responses in a large cohort of mice double dosed with AAV9

Next, we carried out a larger study to comprehensively characterize AAV-mediated immune responses *in vivo* using hDMD del45 mdx mice systemically dosed with two administrations (four weeks apart) of AAV9 at 1.16 x 10^{14} vg/kg carrying three different vectors. AAV9 was packaged with either micro-dystrophin (μDYS), Cas9, or Cas9 with a frameshift mutation (Cas9-FS), which disrupts Cas9 protein expression (**Figures 4-2A** and **4-2B**). Cas9 and Cas9-FS vectors offered an opportunity to distinguish between AAV9 capsid-specific and transgene-specific immune responses throughout the assays used in the study. SDS-PAGE of recombinant AAV9-μDYS, AAV9-Cas9, and AAV9-Cas9-FS confirmed that the capsid proteins (VP1, VP2 and VP3) were visible and were present in the correct stoichiometric ratio 1:1:10 (**Figure 4-2C**).

Previous studies have shown that animal models and humans exposed to AAV-based therapies develop anti-AAV antibodies[256-259] and we sought to assess the timing of these responses. Using a high content protein microarray (HCPM) that was printed with AAV9 capsids, we evaluated humoral responses. The HCPM assay revealed a significant increase in anti-AAV9 IgG antibodies post dosing for all three vectors, peaking at the Post-2 (2wk) time point and trending slightly downward by the Post-2 (6wk) time point (**Figure 4-3A**). However, we were unable to detect deviations in anti-AAV9 IgM responses from baseline (Pre) among the three vectors at any time point

(**Figure 4-3A**). In addition, anti-transgene responses were also probed using the HCPM assay; however, we were unable to observe changes in either IgM or IgG levels against Cas9 or μDYS across all time points (**Figure 4-3A**). The absence of detectable anti-transgene responses for the time points assessed is likely due to the fact that we utilized a muscle-specific promoter, CK8e. Thus, non-target tissues transduced by AAV, such as antigen presenting cells, will not express μDYS or Cas9 proteins thereby preventing antigen presentation and humoral immune responses against the transgene[260]. Interestingly, we detected AAV serotype cross-reactivity against other AAV serotypes including AAV2, AAV8, and AAVMYO[215], which is a muscle tropic AAV capsid variant identified via high throughput library screening. Similar to the anti-AAV9 IgG levels, we detected a significant increase in anti-AAV2 IgG, anti-AAV8 IgG, and anti-AAVMYO IgG antibodies post dosing, peaking at the Post-2 (2wk) time point and similarly trending slightly downward by the Post-2 (6wk) time point (**Figure 4-3B**). Additionally, we were unable to detect differences in anti-AAV IgM responses against AAV2, AAV8, and AAVMYO among the three vectors after dosing and re-dosing (**Figure 4-3B**). The production of anti-AAV IgGs are expected to preclude re-dosing due to neutralization, which will block transduction of target cells.

Evaluating complement responses in a mouse model of pre-existing AAV immunity

Complement activation occurs through three different mechanisms: the lectin, the alternative, and the classical pathways. Ongoing clinical trials have recently reported evidence of AAV-mediated complement activation following systemic administration of high dose AAV, and complement activation occurred with a concomitant rise of anti-

AAV antibodies[261,262]. It has been speculated that the pathway being activated was the classical pathway, which is initiated by antigen-antibody complexes (i.e., AAV and anti-AAV IgM or IgG antibodies)[263,264]. Additional support for this hypothesis stems from *ex vivo* studies, in which serum containing anti-AAV IgGs incubated with AAV resulted in detectable complement activation while serum depleted anti-AAV IgGs failed to induce the complement cascade[264]. While complement activation has been reported *ex vivo* and in human clinical trials, there is no published study to support AAV induction of complement activation in animal models.

To test whether our pre-existing mouse model of AAV immunity can activate the classical complement pathway, consistent with humans dosed with AAV, we probed for complement components C3, C4, and C5b9 for the time points in our study (**Figure 4-2A**). We measured significant depletion of complement components C3 and C4 after re-dosing for the Post-2 (5hr) time point (**Figure 4-4A**), which is suggestive of the classical pathway and has been previously reported in DMD clinical trials[261,262]. However, we were unable to detect observable deviations in terminal C5b9 levels (**Figure 4-4A**), which may be attributed to the timing of our assay, since C5b9 was shown to increase three days after the consumption of C3 and C4 in DMD clinical trials[261,262].

Characterizing AAV-induced cytokine responses in dual-dosed mice

Prior studies have attributed AAV-induced innate immune responses to toll-like receptor 9 (TLR9), a pattern recognition receptor (PRR), which senses unmethylated cytosine-phosphate-guanine (CpG) DNA motifs present in AAV genomes[265]. TLR9 signaling can lead to nuclear factor κB (NF-κB) pro-inflammatory cytokine responses

and interferon regulatory factor 7 (IRF7) type I interferons[266]. Several studies have previously confirmed that TLR9 can sense AAV DNA to elicit innate cytokine responses and downstream adaptive CD8 T cell responses[131,265,267]. Given the potential of TLR9 to detect the AAV vector DNAs used in this study, we calculated the risk potential for TLR9 activation (K_{TLR9}) using several equations that consider both stimulatory and inhibitory configurations of CpG DNA motifs as described[268]. As expected, AAV9-Cas9 (K_{TLR9}=20), AAV9-Cas9-FS (K_{TLR9}=20), and AAV9-μDYS (K_{TLR9}=13) were above the speculated threshold (K_{TLR9}>10) to activate TLR9 (**Table 4-1**). Although the μDYS transgene is CpG depleted and contains a lower K_{TLR9} compared to the Cas9 vectors, the packaged μDYS vector is not devoid of CpGs and thus, poses a risk for TLR9 activation.

In order to assess AAV-induced innate immune responses in our pre-existing immunity mouse model, we harvested plasma from dual dosed mice, and performed multiplex cytokine analysis via Luminex. A total of 27 analytes were probed (see methods section); however, 8 analytes were omitted from additional analysis as they were at or below the lower limits of quantification (e.g., IFN-α). We observed significantly elevated levels of myeloid-derived pro-inflammatory cytokines in plasma including IP-10 (CXCL10), MIP-1β (CCL4), MCP-1 (CCL2) and TNF-α, all of which peaked after the second dose for the Post-2 (5hr) time point compared to baseline (Pre) (**Figure 4-5A**). Similarly, previous studies stimulating TLR9 via administration of CpG oligonucleotide (ODN) agonists in mice, non-human primates and humans were also shown to induce IP-10 (CXCL10), MIP-1β (CCL4), MCP-1 (CCL2) and TNF-α[269–273]. However, we noted no statistical difference in IP-10 (CXCL10), MIP-1β (CCL4), MCP-1

(CCL2) and TNF-α between Pre and the Post-1 (5hr) time point (**Figure 4-5B**), which may suggest lack of AAV9 entry in myeloid cells and thus, an inability for TLR9 to sense AAV vector genomes. Unlike CpG ODN stimulation studies, AAV9 ineffectively transduces TLR9-expressing antigen presenting cells, which includes monocytes, dendritic cells, and B cells[186,264].

We posit that AAV capsid antibodies contribute to the increased inflammatory cytokine responses that were only observed in the Post-2 (5hr) time point via two putative mechanisms. First, AAV capsid antibodies present by the second dose bind AAV to activate Fcγ receptor (FcγR) and/or facilitate FcγR-mediated uptake allowing for TLR9 recognition and myeloid activation (**Figure 4-5B**). Second, anti-AAV IgGs create antigen-antibody complexes that subsequently initiate the classical pathway of complement to activate myeloid cells by complement receptor-mediated uptake for TLR9 recognition and/or by complement C3a and C5a split products that bind anaphylatoxin receptors (**Figure 4-5B**). Previous studies have shown FcγR-mediated uptake allows for TLR9 activation in pDCs in response to Coxsackievirus B (CVB) virus and Lupus[274,275]. In addition, one study revealed that AAV-specific BAbs enhanced AAV uptake in HEK293 and Hepa 1-6 cells *in vitro* and introducing an anti-Fc antibody partially blocked AAV uptake[276]. Lastly, support for complement-mediated uptake and myeloid activation was revealed in one study, in which serum containing anti-AAV IgGs and complement C3 incubated with AAV resulted in detectable complement activation, AAV uptake in macrophages, and induction of inflammatory cytokines *in vitro* while C3-depleted serum containing anti-AAV IgGs significantly reduced AAV uptake in macrophages[264]. These studies strongly suggest a need for antibodies to mediate AAV

uptake and/or classical complement activation, resulting in priming of myeloid cells for activation.

Single-cell RNA sequencing (scRNA-seq) confirms monocyte cell activation after the second dose

Next, we applied single-cell RNA sequencing (scRNA-seq) to unbiasedly characterize phenotypic changes in peripheral blood mononuclear cells (PBMCs) collected in the dual dosing experiment. scRNA-seq UMAP plots revealed shifts in transcriptional phenotypes between Pre, Post-1 (2wk), and Post-2 (2wk) time points among all main immune cell types including T cells (29,104 cells), B cells (22,166 cells), natural killer (NK) cells (5,468 cells), and monocytes (5,228 cells) (**Figures 4-6A** and **4-6B**). Considering that myeloid-derived pro-inflammatory cytokine responses were observed 5 hours after the second dose, we examined whether we could detect differences in the proportion of cell types originating from Pre, Post-1 (2wk) and Post-2 (2wk). Importantly, we noted the Post-2 (2wk) time point contributed a greater percentage of NK cells (~40%) and myeloid-derived monocytes (~44%) (**Figure 4-6C**), further implicating monocyte cells in AAV-induced immune responses. In order to support our hypothesis that antibodies are needed to mediate AAV uptake and prime myeloid-derived monocytes, we examined downstream activation markers associated with FcγR and complement receptor engagement that may also mediate TLR9 sensing and activation.

First, we identified three activated clusters of monocytes including classical monocytes ($CD43^{-}Ly6c^{+}$), non-classical monocytes ($CD43^{+}Ly6c^{-}$) and a smaller cluster

of monocytes expressing $CD14^{+}CD68^{+}$ (**Figures 4-6A** and **4-6B**) and assessed expression of complement receptors and FcγRs, which have affinity for IgG immune complexes. Monocytes expressed activating FcγRs including *Fcgr1* (CD64), *Fcgr3* (CD16), and *Fcer1g*, which is a subunit for CD64 and CD16 (**Figure 4-6D**). We also assessed complement receptors including *Cr1l* (CR1 receptor that binds C3b/C4b-deposited antigens), *Cd93* (receptor that binds C1q, which initiates the classical complement pathway), *C5ar1* (receptor that binds anaphylatoxin, C5a) (**Figure 4-6E**). Similarly, activated monocytes differentially expressed pro-inflammatory genes including *Tnf* (TNF-α), *Il1b* (IL-1β), *Ccl3* (MIP-1α), *Ccl4* (MIP-1β), *Ccl5* (RANTES), and *Cxcl2* (MIP-2α), which were significantly upregulated after the second dose in the Post-2 (2wk) time point (**Figure 4-6F**).

Activated monocytes also expressed PRRs including *Tlr9*, *Tlr2*, *Cd14*, and *Myd88*, which is needed for TLR downstream signal transduction (**Figure 4-7A**). While TLR9 senses hypomethylated AAV DNA leading to activation[265], TLR2 has been shown to associate with CD14 and recognize the viral surface of AAV in primary human liver cells leading to activation[277]. Previous studies have revealed that stimulating FcγRs, TLR9 or complement receptors can induce NF-κB-dependent gene expression in plasmacytoid dendritic cells (pDCs) and monocytes[266,278-280], which results in the production of pro-inflammatory cytokines similar to those we observed via Luminex and scRNA-seq. In order to support the hypothesis that NF-κB could be activated, we confirmed elevated expression levels of both canonical NF-κB1 and non-canonical NF-κB2 (**Figure 4-7B**), which is comprised of *Nfkb1*/*Rela* (p50/p65) and *Nfkb2/Relb* (p52/Relb), respectively[281]. The production of NF-κB-dependent cytokines, such as

TNF-α[282], may amplify and prolong inflammatory responses due to positive autocrine feedback loops via TNF receptors (TNFR1/2), which activate non-canonical NF-κB2[283]. We found elevated expression of both *Tnfrsf1a* (TNFR1) and *Tnfrsf1b* (TNFR2) in the classical, non-classical, and $CD14^{+}CD68^{+}$ monocyte clusters (**Figure 4-7C**). In addition, TNFR stimulation can subsequently lead to activation of the transcription factor AP-1 (*Jun*), which is similarly elevated in the activated monocyte clusters (**Figure 4-7C**). These findings strongly suggest that the presence of AAV capsid antibodies and subsequent complement activation can prime myeloid cells by engaging FcγRs, TLRs, and/or complement receptors to induce downstream NF-κB-dependent gene expression (**Figure 4-7D**). Future studies will focus on delineating the mechanisms inducing downstream NF-κB-dependent immune responses, whether canonical or non-canonical NF-κB is induced by AAV, how cytokines amplify immune responses, and how innate responses influence downstream adaptive immunity and AAV neutralization.

Discussion

Innate and adaptive immune responses pose a significant challenge for safe and efficient clinical application of AAV-based gene therapies. Currently, clinical trials rely on pre-trial screening to exclude participants with pre-existing NAbs and/or memory T cell responses who may be susceptible to AAV immunogenicity. However, complement activation and complement related SAEs reported in DMD, XLMTM and SMA clinical trials suggest pre-trial screening in insufficient in detecting additional innate and/or adaptive immune responses that may be contributing to AAV-induced immunotoxicities. These SAEs were unexpected, as AAV administration was well tolerated in small and

large animal models, yet these studies relied on a single administration of AAV to evaluate therapeutic efficacy, with little focus on characterizing immune responses[116,250,251]. In this study, we developed a mouse model of pre-existing immunity that recapitulates some features of the innate and adaptive immune responses similar to those observed in DMD clinical trials.

Firstly, and as anticipated, we demonstrated a humoral anti-AAV9 IgG response after the first dose that persisted 6 weeks after the second dose. In addition, we confirmed anti-AAV9 IgGs cross-reacted with commonly used serotypes including AAV2 and AAV8. In addition, we confirmed cross-reactivity against a newly discovered muscle tropic variant of AAV, termed AAVMYO[215], which suggests that even novel variants may be neutralized by pre-existing capsid antibodies. Our findings correlate with pre-existing anti-AAV studies in which individuals similarly demonstrated cross-reactivity across many serotypes[121]. Therefore, it is unlikely that simply switching AAV serotypes will overcome pre-existing immunity.

Since SAEs in the DMD clinical trials documented SAEs that were associated with complement activation, we also examined whether we could measure consumption of complement components C3 and C4, which would indicate activation. We confirmed that a single administration of AAV did not lead to C3 or C4 consumption; however, significant consumption of C3 and C4 components were measured 5 hours after the second dose in which capsid antibody levels had significantly increased 4 weeks after the first dose. These data are strongly suggestive of classical complement pathway activation, which is initiated by antigen-antibody complexes. Our anti-AAV9 IgG response and subsequent complement activation correlate with the data reported in the

Pfizer DMD clinical trial, in which two participants with rapidly rising anti-AAV9 IgG levels experienced complement related adverse events post dosing[261]. In addition, Solid Biosciences recently reported serious adverse events associated with complement activation[262], and demonstrated using *in vitro* assays that complement activation relies on the presence of pre-existing antibodies. Similarly, both Pfizer and Solid Biosciences observed consumption of complement components C3 and C4 along with an increase in complement component C5b9 post AAV dosing, which peaked at days 4 and 7, respectively[242,244,261,262]. However, we were unable to measure changes in C5b9 levels, which is likely due to the time points assessed in our study, as DMD clinical trial data revealed that C5b9 levels rise 3 days after the consumption of C3 and C4.

In addition to antibody responses and complement activation, the DMD clinical trial sponsored by Pfizer reported AAV-induced cytokine responses, in which one patient with thrombocytopenia had significantly elevated levels of IP-10 (CXCL10), IFN-α2a, and ITAC (CXCL11) with a modest induction of IFN-γ and TNF-α peaking 4 days post AAV dosing[261]. Comparably, we also detected significant plasma levels of pro-inflammatory cytokines including IP-10 (CXCL10) and TNF-α as well as MIP-1β (CCL4) and MCP-1 (CCL2). The induced cytokine responses are strongly suggestive of NF-κB activation, which has been shown to be downstream of TLR9 activation[284-286]. However, we only detected the induction of myeloid-derived IP-10 (CXCL10), MIP-1β (CCL4), MCP-1 (CCL2) and TNF-α after the second dose, which suggests AAV is unable to transduce TLR9-expressing cells including monocytes, dendritic cells and B cells[186,264]. Our data support the model that AAV capsid antibodies present during the second dose consequently initiate the classical complement pathway to mediate AAV uptake and

activate monocytes. Anti-AAV IgGs may prime monocytes through FcγR activation, complement receptor activation, and/or FcγR- and complement receptor-mediated uptake that may allow for TLR9 recognition of AAV DNA.

By using scRNA-seq, we were able to identify monocyte clusters that highly expressed FcγRs, TLRs, and complement receptors. Similarly, the identified monocyte clusters only demonstrated significant upregulation of NF-κB-dependent genes only after the second dose including *Tnf* (TNF-α), *Ccl3* (MIP-1α), *Ccl4* (MIP-1β), *Ccl5* (RANTES), *Cxcl2* (MIP-2α), and *Il1b* (IL-1β). The induction of pro-inflammatory cytokines may also extend myeloid inflammatory responses through positive autocrine feedback loops[283]. We confirmed elevated plasma levels of TNF-α by Luminex and an elevated expression level of TNF-α by scRNA-seq, which was detected and persisted two weeks after the second dose. Importantly, TNF-α expressing monocytes demonstrated elevated expression levels of both TNFR1 and TNFR2, which may indicate the presence of a feed-forward activation loop. Future studies will focus on uncovering how pre-existing anti-AAV antibodies trigger AAV uptake and their role in amplifying downstream innate and adaptive immune responses.

Conclusion

We demonstrated that implementing an AAV double dosing approach in mice successfully emulated some human immune responses reported in clinical trials. Importantly, this was the first study to demonstrate classical complement pathway activation in mice, which was only observed after the second AAV administration. Likewise, we observed the induction of monocyte-derived pro-inflammatory cytokines

only after the second dose, suggesting monocytes are activated through AAV-capsid antibodies and subsequent complement activation. Similarly, scRNA-seq confirmed pronounced activation profiles in monocytes, primarily after the second dose of AAV. Collectively, our AAV double dosing approach more accurately recapitulates human AAV-mediated immune responses compared to prior pre-clinical studies, which relied on a single administration of AAV and thus, offers the potential to model aspects of human AAV-mediated immunity.

Acknowledgments

We would like to thank Jane Wen and Diana Becerra for technical assistance. The authors thank and acknowledge the use of services from the following cores: the Technology Center for Genomics & Bioinformatics (TCGB), the Immune Assessment Core at UCLA, the Institute for Quantitative and Computational Biosciences (QC Bio) at UCLA, and the UCI Vaccine R&D Center. This material is based upon work supported by the National Science Foundation Graduate Research Fellowship Program under Grant No. DGE-1650604 (MRE). Any opinions, findings, and conclusions or recommendations expressed in this material are those of the author and do not necessarily reflect the views of the National Science Foundation. Funding was also provided by Ruth L. Kirschstein National Research Service Award GM007185 (MRE), the Center for DMD at UCLA Azrieli Graduate student Award (MRE), and the Whitcome Predoctoral Fellowship in Molecular Biology (MRE). Additional funding was provided by the National Institutes of Health (R01NS117912 MJS and JSC), and the Department of

Defense (MD190060 MJS and SAV) and the Muscular Dystrophy Association (CSY-MGB and MJS).

Author contributions

Conceptualization, Methodology, Visualization, Project Administration – MRE MJS; Investigation – MRE, PH, SAV; Software, Data Curation – AE, FM; Formal analysis – MRE, AE, FM; Writing – Original Draft – MRE; Writing – Review and Editing – MRE, MJS; Resources – JSC, MP, PH, SAV; Supervision – MJS; Funding Acquisition – CSY, SAV, MJS.

Figures

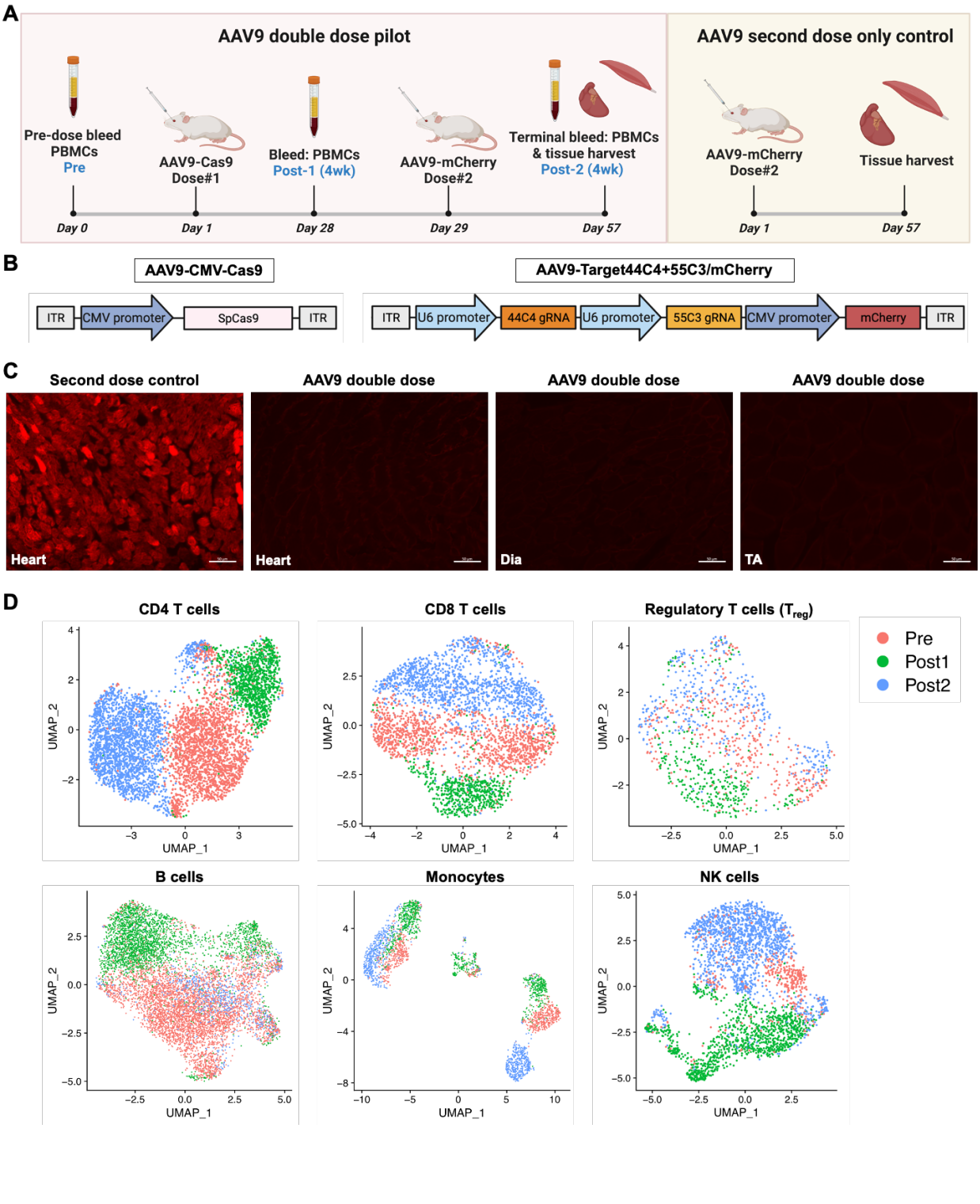
A
AAV9 double dose pilot
Pre-dose bleed PBMCs
Pre
AAV9-Cas9 Dose#1
Bleed: PBMCs
Post-1 (4wk)
AAV9-mCherry Dose#2
Terminal bleed: PBMCs & tissue harvest
Post-2 (4wk)
Day 0
Day 1
Day 28
Day 29
Day 57
AAV9 second dose only control
AAV9-mCherry Dose#2
Tissue harvest
Day 1
Day 57
B
AAV9-CMV-Cas9
ITR
CMV promoter
SpCas9
ITR
AAV9-Target44C4+55C3/mCherry
ITR
U6 promoter
44C4 gRNA
U6 promoter
55C3 gRNA
CMV promoter
mCherry
ITR
C
Second dose control
AAV9 double dose
AAV9 double dose
AAV9 double dose
Heart
Heart
Dia
TA
D
CD4 T cells
CD8 T cells
Regulatory T cells (Treg)
Pre
Post1
Post2
B cells
Monocytes
NK cells
UMAP_1
UMAP_2

Figure 4-1: Profiling AAV9-mediated immune responses in one hDMD del45 mdx mouse.
A) Timeline to study AAV-induced immune responses in one hDMD del45 mdx mouse by scRNA-seq including the timeline of one hDMD del45 mdx mouse used as a second-dose only control. Created with Biorender.com.
B) Schematic of the Cas9 and mCherry vectors used in the pilot double dosing study. Created with Biorender.com.
C) Representative mCherry immunofluorescent imaging of an hDMD del45 mdx mouse first dosed with AAV9-Cas9 then re-dosed with AAV9-mCherry compared to the second-dose only control mouse injected with AAV9-mCherry. Scale bar represents 50μm.
D) Uniform Manifold Approximation and Projection (UMAP) of main immune cell types in single cell sequencing set: CD4 T cells, CD8 T cells, regulatory T cells (T_{reg}), B cells, monocytes, and natural killer (NK) cells. UMAPs are color coded by time point before or after AAV dosing. Pre (pink), Post-1 (green), and Post-2 (blue).

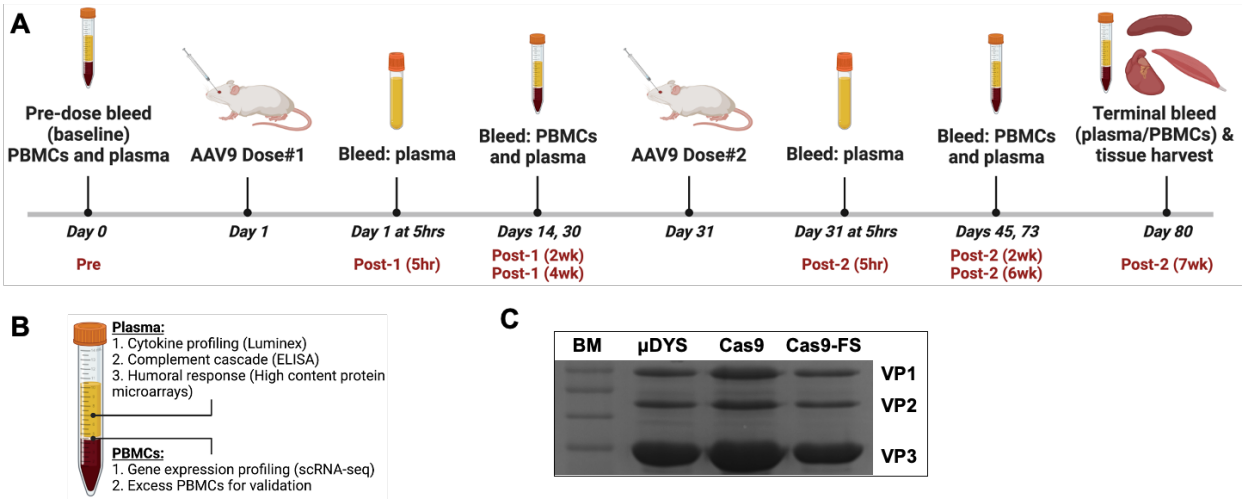

Figure 4-2: Experimental timeline to characterize AAV9-mediated immune responses in a mouse model of pre-existing AAV immunity.
A) Schematic timeline to study AAV9-induced immune responses in hDMD del45 mdx mice. n=9 male and n=9 female mice (3 mice per AAV9 vector) dosed at 1.16 x 10^{14} vg/kg. Created with Biorender.com.
B) Schematic highlighting the assays used in this study. Plasma samples were used to assess cytokine responses (Luminex), complement levels (ELISAs), and humoral antibody responses via high content protein microarrays (HCPM) and PBMCs were characterized by scRNA-seq. Created with Biorender.com.
C) Coomassie stained SDS-PAGE of the recombinant AAV9-µDYS, AAV9-Cas9, and AAV9-Cas9-FS vectors used in the study.

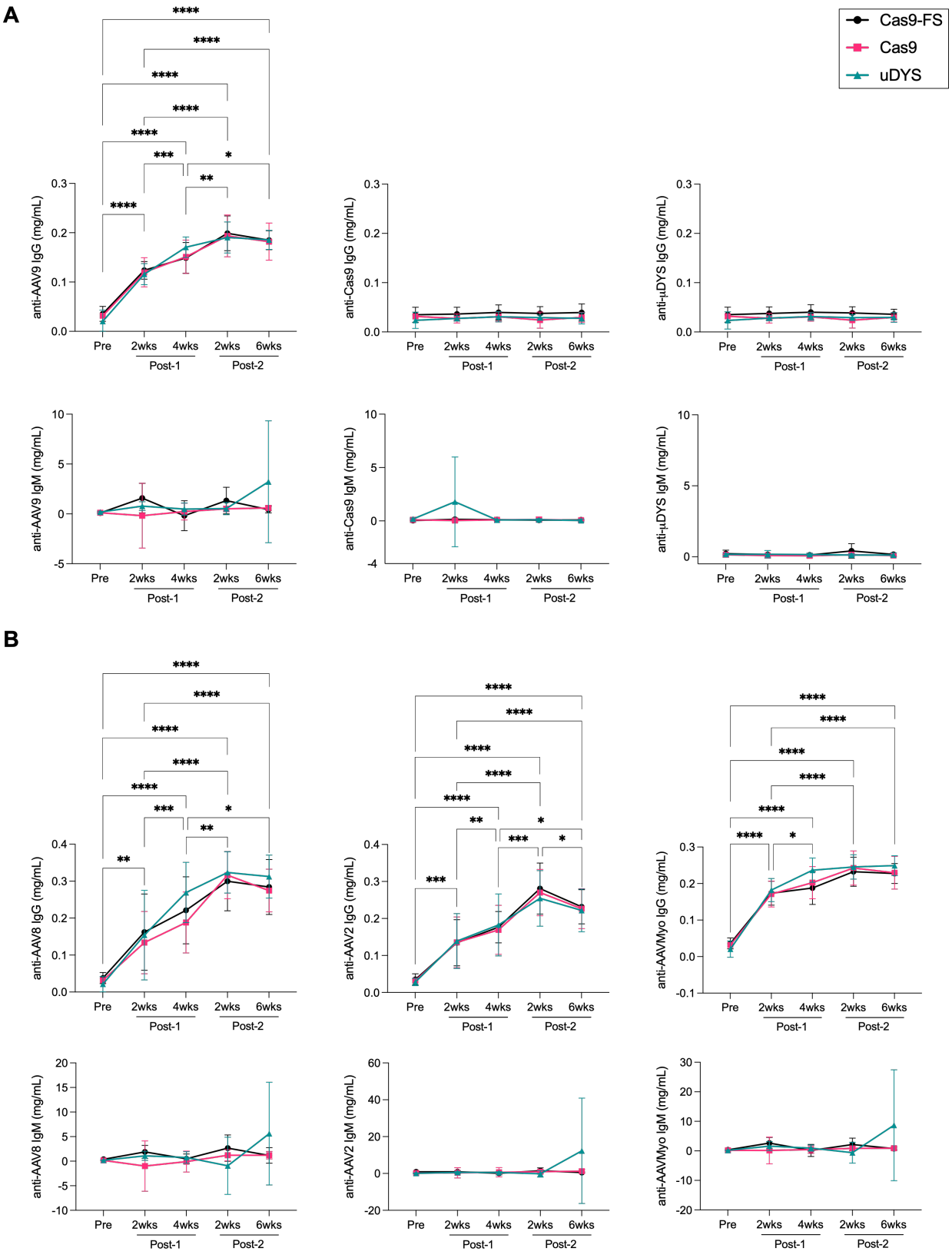
A
B
Cas9-FS
Cas9
uDYS
anti-AAV9 IgG (mg/mL)
anti-Cas9 IgG (mg/mL)
anti-µDYS IgG (mg/mL)
anti-AAV9 IgM (mg/mL)
anti-Cas9 IgM (mg/mL)
anti-µDYS IgM (mg/mL)
anti-AAV8 IgG (mg/mL)
anti-AAV2 IgG (mg/mL)
anti-AAVMyo IgG (mg/mL)
anti-AAV8 IgM (mg/mL)
anti-AAV2 IgM (mg/mL)
anti-AAVMyo IgM (mg/mL)
Pre
2wks
4wks
2wks
6wks
Post-1
Post-2

Figure 4-3: Assessment of anti-AAV9 antibodies using a high content protein microarray (HCPM).
A) anti-AAV9, anti-Cas9, and anti-μDYS IgG and IgM responses were measured via high content protein microarrays (HCPM) from male (n=9) and female (n=8) hDMD del45 mdx mice at the indicated time points. Error bars represent standard deviation. B) Plasma collected from mice double dosed with AAV9 was assessed by HCPM for the ability to bind to other AAV serotypes. Capsids of AAV2, AAV8, and AAVMYO were printed on the chip and plasma from male (n=9) and female (n=8) hDMD del45 mdx mice. Error bars represent standard deviation. $p < 0.05$ (*), $p < 0.01$ (**), $p < 0.001$ (***) and $p < 0.0001$ (****) were considered significant.

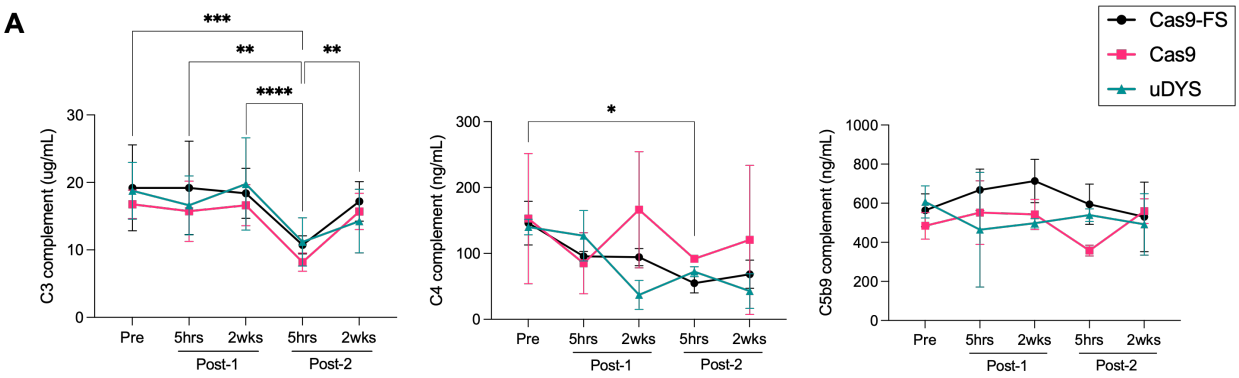

Figure 4-4: Consumption of complement components, C3 and C4, after the second dose of AAV.

A) Plasma from hDMD del45 mdx mice were evaluated by ELISA for levels of complement C3 (n=9 males), C4 (n=9 females), and C5b9 (n=9 females). Error bars represent standard deviation. $p < 0.05$ (*), $p < 0.01$ (**), $p < 0.001$ (***) and $p < 0.0001$ (****) were considered significant.

Table 4-1: Activation potential for toll-like receptor 9 (TLR9).

AAV DNA vector	TLR9 activation potential (K_{TLR9})	Activation (+/-)
CK8e-Cas9-FS	19.7	++
CK8e-Cas9	19.7	++
CK8e-uDYS	12.8	+
AAV2 WT genome	26.0	+++
Human genome	1.0	-

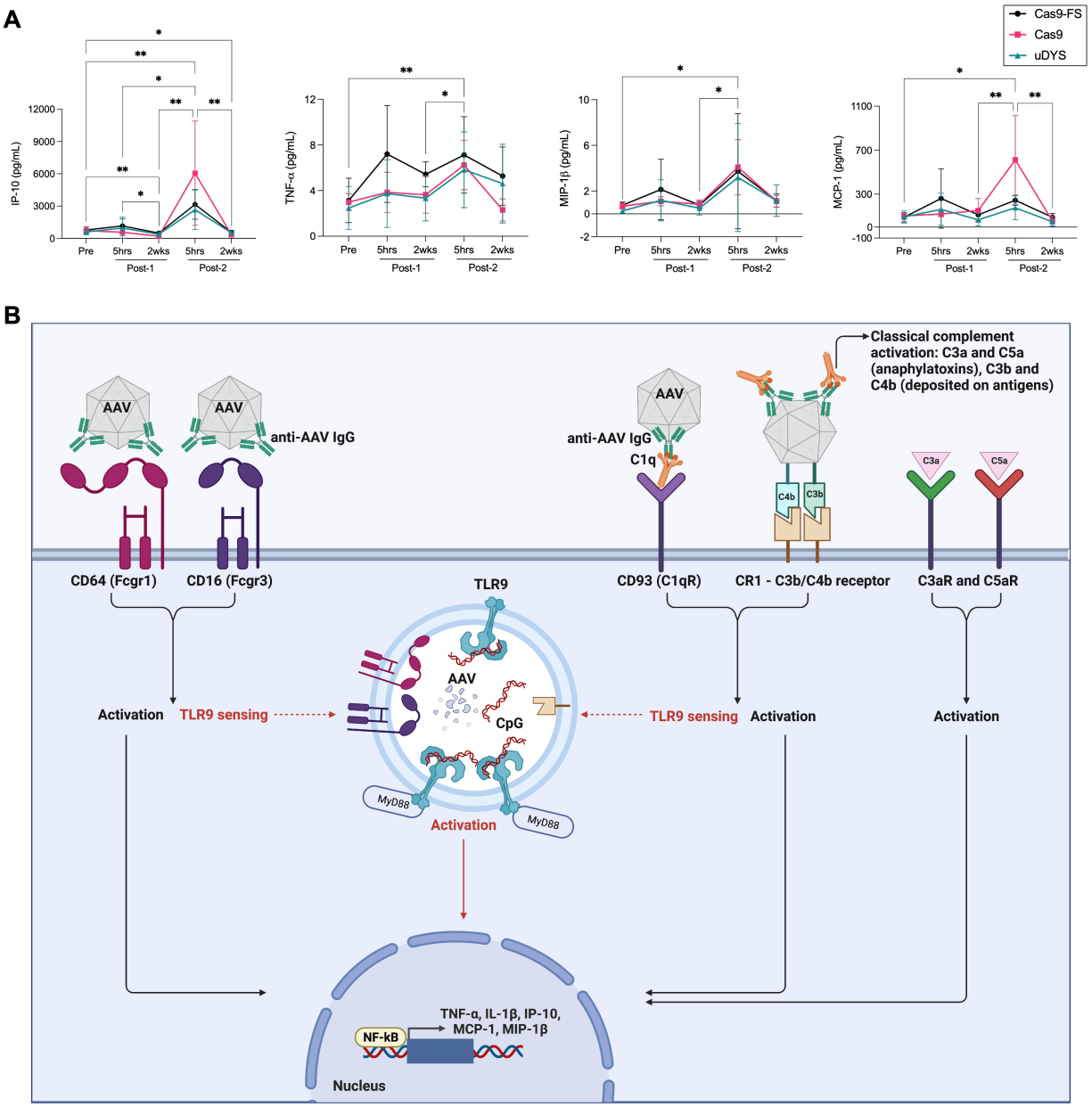

Figure 4-5: Pro-inflammatory cytokine responses after second dose in AAV double-dosed mice.

A) Levels of immunomodulatory analytes: IP-10 (CXCL10), MIP-1β (CCL4), MCP-1 (CCL2), and TNF-α as measured by Luminex ProcartaPlex.

B) Hypothetical pathways that could induce pro-inflammatory cytokine responses after the second dose of AAV9. Our data suggest that antibodies are needed to prime myeloid cells through FcγR and/or complement receptor engagement, leading to subsequent activation.

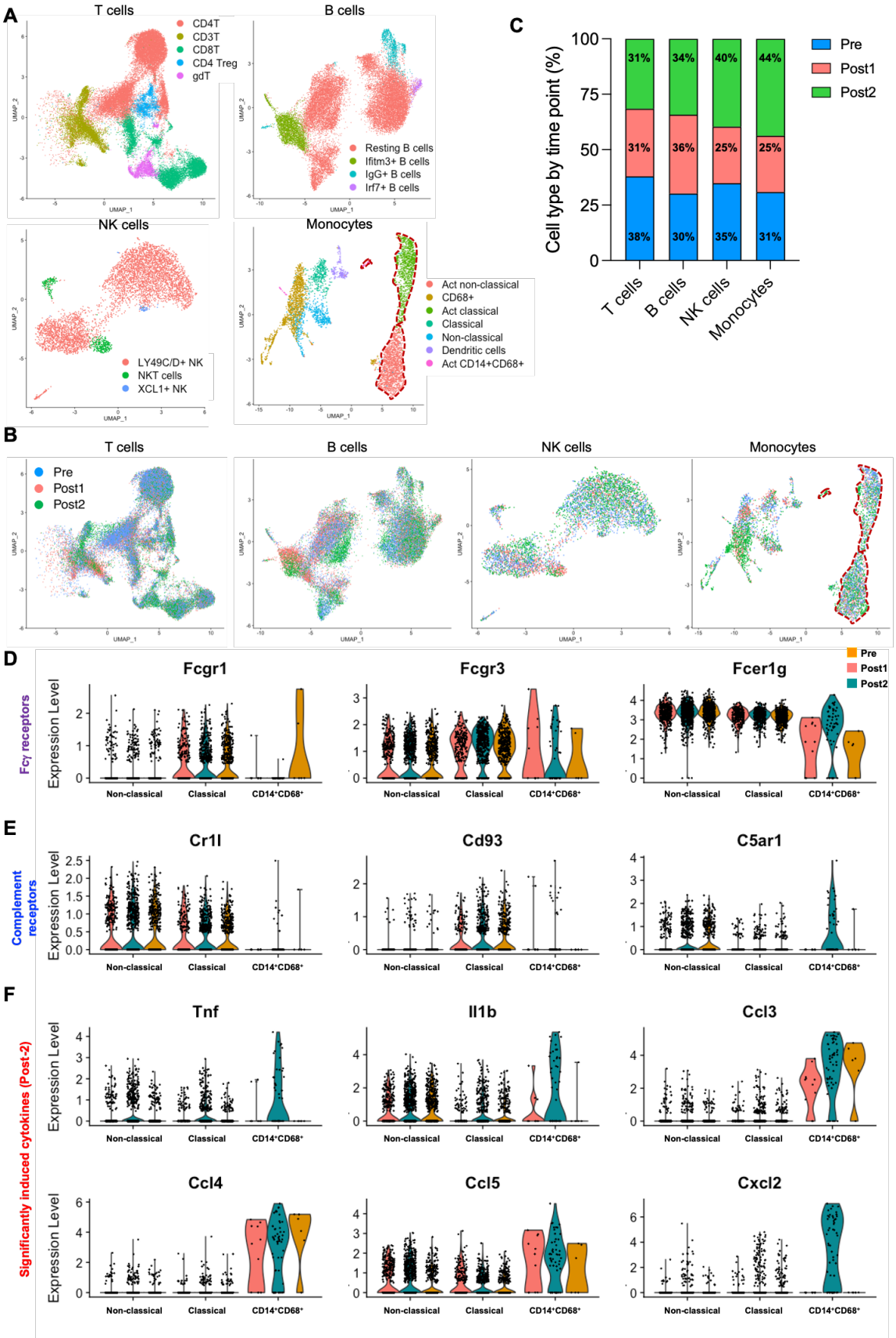
A
T cells
CD4T
CD3T
CD8T
CD4 Treg
gdT
B cells
Resting B cells
Ifitm3+ B cells
IgG+ B cells
Irf7+ B cells
NK cells
LY49C/D+ NK
NKT cells
XCL1+ NK
Monocytes
Act non-classical
CD68+
Act classical
Classical
Non-classical
Dendritic cells
Act CD14+CD68+
UMAP_1
UMAP_2
C
Cell type by time point (%)
Pre
Post1
Post2
31%
34%
40%
44%
31%
36%
25%
25%
38%
30%
35%
31%
T cells
B cells
NK cells
Monocytes
B
T cells
B cells
NK cells
Monocytes
Pre
Post1
Post2
D
Fcγ receptors
Fcgr1
Fcgr3
Fcer1g
Expression Level
Non-classical
Classical
CD14+CD68+
E
Complement receptors
Cr1l
Cd93
C5ar1
F
Significantly induced cytokines (Post-2)
Tnf
Il1b
Ccl3
Ccl4
Ccl5
Cxcl2

Figure 4-6: scRNA-seq analysis demonstrating monocyte activation and induction of NF-κB-dependent target genes after the second systemic administration of AAV9.

A) Uniform Manifold Approximation and Projection (UMAP) of main immune cell types: T cells, B cells, NK cells, and Monocytes. Activated monocyte clusters are indicated in dashed lines.

B) UMAPs are color coded by time point before or after AAV dosing. Pre (blue), Post-1 (pink) and Post-2 (green). Activated monocyte clusters are indicated in dashed lines.

C) Bar graphs shows the percentage of T cells, B cells, NK cells and monocytes by time point. Pre (blue), Post-1 (pink) and Post-2 (green).

D) Violin plots showing the expression of FcγRs upregulated in activated non-classical, classical and $CD14^{+}CD68^{+}$ monocyte clusters.

E) Violin plots showing the expression of complement receptors upregulated in activated non-classical, classical and $CD14^{+}CD68^{+}$ monocyte clusters.

F) Violin plots showing the expression of differentially expressed pro-inflammatory cytokines significantly upregulated Post-2.

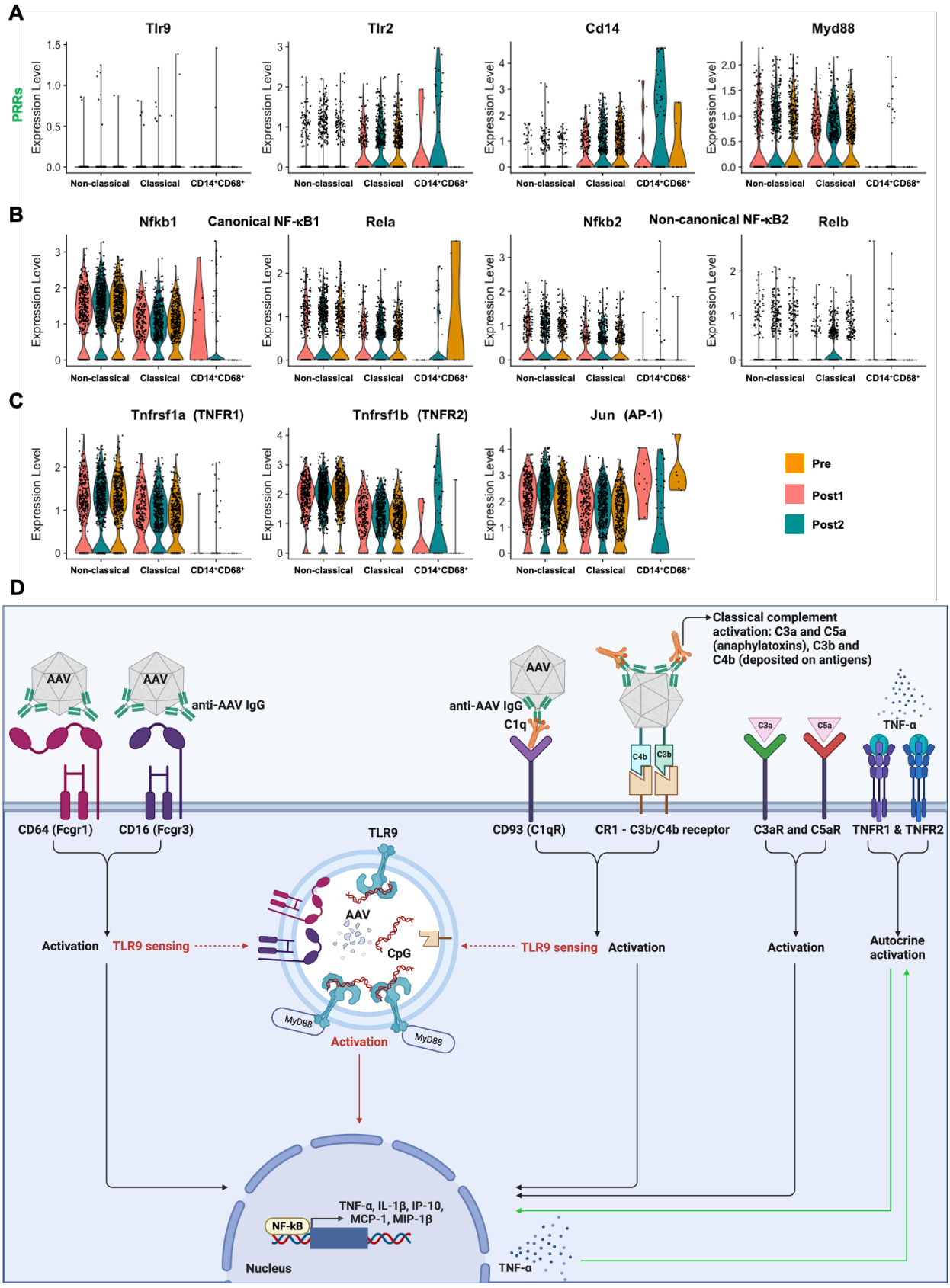
A
PRRs
Tlr9
Tlr2
Cd14
Myd88
Expression Level
Non-classical
Classical
CD14+CD68+
B
Nfkb1
Canonical NF-κB1
Rela
Nfkb2
Non-canonical NF-κB2
Relb
C
Tnfrsf1a (TNFR1)
Tnfrsf1b (TNFR2)
Jun (AP-1)
Pre
Post1
Post2
D
AAV
anti-AAV IgG
CD64 (Fcgr1)
CD16 (Fcgr3)
C1q
CD93 (C1qR)
Classical complement activation: C3a and C5a (anaphylatoxins), C3b and C4b (deposited on antigens)
C4b
C3b
CR1 - C3b/C4b receptor
C3a
C5a
C3aR and C5aR
TNF-α
TNFR1 & TNFR2
TLR9
CpG
MyD88
Activation
TLR9 sensing
Autocrine activation
NF-kB
TNF-α, IL-1β, IP-10, MCP-1, MIP-1β
Nucleus

Figure 4-7: scRNA-seq gene expression of TLRs, canonical and non-canonical NF-κB, and TNF receptors in activated monocyte clusters.
A) Violin plots showing the expression of pattern recognition receptors including *Tlr9*, *Tlr2*, *Cd14*, and downstream adaptor gene, *Myd88*.
B) Violin plots showing the expression of canonical NF-κB1 and non-canonical NF-κB2 genes.
C) Violin plots showing expression of TNF receptors (*Tnfrsf1a* and *Tnfrsf1b*) and one of the downstream transcription factors, *Jun* (AP-1).
D) scRNA-seq supports the hypothesis that FcγRs, complement receptors and TLR9 signaling components are highly expressed in activated monocytes that correspondingly upregulate NF-κB-dependent target genes. Production of TNF-α may amplify NF-κB-dependent gene expression through feed-forward autocrine signaling via TNFR1 and TNFR2.

Chapter 5 – Conclusions

Gene editing provides enormous opportunities to significantly improve human life by means of genetically modifying agricultural crops and livestock, generating novel model organisms for biomedical research, and treating genetic diseases[136,287,288]. The gene editing field has advanced swiftly since the advent of the CRISPR/Cas system, due to its simplicity, high precision, versatility, and a relatively low barrier to entry. While the CRISPR/Cas9 system is widely adopted, there have been additional Cas endonucleases discovered and/or engineered that vary in size, create unique double-stranded breaks, create single-stranded breaks, require unique recognition sequences for cleavage, and are capable of targeting and cleaving RNA[289-291]. Collectively, the CRISPR/Cas system is a revolutionary technology, and although the first two human clinical trials for *in vivo* delivery of CRISPR/Cas9 have shown initial success[292-294], additional follow-up studies are needed to assess therapeutic benefit and long-term effects to maximize safety and efficacy for systemic CRISPR/Cas9 delivery *in vivo*.

While the first two clinical trials testing *in vivo* CRISPR delivery have shown early success for the treatment of Leber congenital amaurosis (LCA) (clinicaltrials.gov: NCT03872479, Editas Medicine Inc.) and the treatment of transthyretin amyloidosis (clinicaltrials.gov: NCT04601051, Intellia Therapeutics and Regeneron Pharmaceuticals), the form and route in which CRISPR was delivered differs between the trials. Editas Medicine Inc. delivered CRISPR/Cas9 in the form of DNA packaged in AAV via subretinal injection while Intellia Therapeutics and Regeneron Pharmaceuticals intravenously delivered CRISPR/Cas9 in the form of Cas9 mRNA and gRNA

encapsulated in lipid nanoparticles effectively targeting the liver[292-294]. Importantly, these two clinical trials underscore the need to identify the suitable CRISPR format (e.g., DNA, RNA, or RNP), the appropriate vehicle to encapsulate CRISPR components, and the route of administration, all of which are paramount to achieving a safe and efficient CRISPR-based therapy.

For neuromuscular disorders, such as Duchenne muscular dystrophy, achieving systemic delivery of CRISPR/Cas9 to all affected muscles of the body remains a significant challenge. Here, we describe two potential approaches to advance translation for systemic CRISPR/Cas9 delivery to muscle *in vivo* via non-viral or viral carriers. While AAV is the most promising viral vector for delivering CRISPR/Cas9, AAV induces an immune response and is likely limited to a single injection unless immunosuppression regimens, plasmapheresis, or anti-AAV IgG-cleaving endopeptidases are used[295-299]. Additionally, AAV-CRISPR inefficiently targets muscle stem cells (MuSCs), which we hypothesize will be required for a sustained life-long therapy for DMD[71,119,300]. Conversely, non-viral nanoparticles are largely non-immunogenic, making them suitable for repeat dosing[81]. In addition, nanoparticles are highly tunable, making them amenable to chemical and peptide targeting modifications which may enable MuSC targeting.

Thus, we first aimed to develop non-viral nanoparticle carriers for CRISPR/Cas9 delivery. We developed and optimized novel polymer-based polyrotaxane (PRX) nanoparticles through successive iterations in primary muscle cells derived from our dystrophic hDMD del45 mdx mouse model[70,77]. We optimized PRXs further by conjugating a synthetic peptide ligand shown to interact with the neural cell adhesion

molecule (NCAM), which is a receptor expressed on muscle cells, including MuSCs[168]. The NCAM-conjugated PRX significantly improved CRISPR/Cas9 delivery and gene editing *in vitro*[70]. While we observed biodistribution of PRXs to skeletal muscle following intravenous delivery *in vivo*, PRXs were unable to target the heart and diaphragm which is necessary to alter disease course for DMD. Although PRXs are capable, to an extent, of trafficking to the limb muscles after intravenous administration, we failed to detect gene editing in skeletal muscle or MuSCs.

In comparison, AAV-CRISPR is capable of restoring dystrophin expression after intravenous delivery. We hypothesize that the PRXs are inefficient due to their inability to traffic across the sarcolemmal membrane, whereas AAV exploits evolutionary fitness to bind receptors, such as laminin receptors, that mediate cell entry. Since AAV is capable of delivering nucleic acids to heart and skeletal muscle; yet, unable to effectively target MuSCs, we aimed to identify novel AAV variants that would efficiently target both skeletal muscle and MuSCs via a peptide-display library screen. Furthermore, we theorize that identifying peptide motifs that allow AAV entry to MuSCs and other tissues, then we could create designer-nanoparticles that may enable improved intravenous delivery of CRISPR/Cas9 to specific tissues *in vivo*. A potential pitfall with conjugating newly identified targeting peptides onto nanoparticles is biodistribution and muscle targeting *in vivo* may not improve PRX-CRISPR delivery, as we have observed with NCAM-conjugated PRXs.

We developed and screened an AAV peptide-display library and identified a total of 9 AAV variants highly enriched in both skeletal muscle and MuSCs. We also identified 8 MuSC- and 5 SkMu-AAV variants with reduced liver enrichment. Also, some

variants demonstrate an improved skeletal muscle to heart enrichment ratio, which is an additional improvement over wildtype AAV9. Future studies include validating the top 9 highly enriched variants that are shared between skeletal muscle and MuSCs. In addition, future work will focus on assessing long-term stability of dystrophin after a single-administration of MuSC-specific AAV-CRISPR in conjunction with functional testing may provide some insight into the percentage of MuSCs that need to be CRISPR-corrected in order to sustain a life-long treatment.

While a novel MuSC-tropic AAV would bode well for immunologically naïve individuals that have not naturally contracted wildtype AAV, there remains relevant concerns regarding AAV immunogenicity that can cause serious adverse events (SAEs), as reported in AAV gene replacement clinical trials[238-245]. However, there are additional safety concerns regarding AAV-CRISPR/Cas9 immunogenicity as Cas9 is bacterially derived with up to 60% of individuals containing pre-existing immunity[120,122,123]. One study demonstrated that a mouse model of pre-existing immunity to Cas9 negated AAV-CRISPR gene editing and resulted in liver hepatotoxicity and an increase in CD8 T cell numbers in the liver[124]. To date, there is one ongoing Phase I/II clinical trial administering AAV-CRISPR to treat LCA via subretinal injection to the eye, which is considered a site of ocular immune privilege and may prove successful[293,301]. Nevertheless, the SAEs observed in AAV-based clinical trials were unexpected because participants were screened for pre-existing immune responses against AAV. The inadequacy of pre-trial screening suggests there may be previously undefined innate and/or adaptive immune components that mediate AAV-induced toxicities.

Consequently, we aimed to unbiasedly characterize AAV-mediated immune responses in our dystrophic mouse model. We generated a mouse model of pre-existing immunity by administering the first dose of AAV, then waiting four weeks to mount an adaptive immune response before re-dosing AAV. Our double dosing approach more accurately modeled characteristics of human AAV immune responses reported in clinical trials. In sum, we observed anti-AAV humoral responses, complement activation, and induction of pro-inflammatory cytokines similar to the immune responses described in DMD clinical trials[261,262]. Preliminary scRNA-seq data suggests activation profiles across the main immune cell types, however future studies require in depth scRNA-seq analysis in order to identify biomarkers for pre-trial screening as well as therapeutic targets to enable safe and efficient delivery of AAV-based gene therapies. Lastly, these data will be compared to human studies being conducted in collaboration with Pfizer, in which we are characterizing AAV-mediated immune responses in patients dosed with AAV-micro-dystrophin via scRNA-seq.

To summarize, we have developed non-viral nanoparticle-mediated carriers capable of delivering CRISPR/Cas9 *in vitro*. We have identified AAV variants demonstrating high enrichment in skeletal muscle and MuSCs, which offers potential as a life-long CRISPR therapy for DMD. Furthermore, we generated a mouse model of pre-existing immunity that effectively models aspects of human immunity, which may enable the development of mitigation strategies to overcome adverse immune responses. Developing a successful CRISPR-based therapy for DMD will require expert contributions in the fields of nano-chemistry, vector biology, immunology, gene-editing, to develop innovative strategies that overcome existing challenges.

Bibliography

1 Mendell, J. R. *et al.* Evidence-based path to newborn screening for Duchenne muscular dystrophy. *Ann Neurol* **71**, 304-313, doi:10.1002/ana.23528 (2012).

2 Batchelor, C. L. & Winder, S. J. Sparks, signals and shock absorbers: how dystrophin loss causes muscular dystrophy. *Trends Cell Biol* **16**, 198-205, doi:10.1016/j.tcb.2006.02.001 (2006).

3 Dumont, N. A. *et al.* Dystrophin expression in muscle stem cells regulates their polarity and asymmetric division. *Nat Med* **21**, 1455-1463, doi:10.1038/nm.3990 (2015).

4 Gumerson, J. D. & Michele, D. E. The dystrophin-glycoprotein complex in the prevention of muscle damage. *J Biomed Biotechnol* **2011**, 210797, doi:10.1155/2011/210797 (2011).

5 Heslop, L., Morgan, J. E. & Partridge, T. A. Evidence for a myogenic stem cell that is exhausted in dystrophic muscle. *J Cell Sci* **113 (Pt 12)**, 2299-2308, doi:10.1242/jcs.113.12.2299 (2000).

6 Jejurikar, S. S. & Kuzon, W. M., Jr. Satellite cell depletion in degenerative skeletal muscle. *Apoptosis* **8**, 573-578, doi:10.1023/a:1026127307457 (2003).

7 Jiang, C. *et al.* Notch signaling deficiency underlies age-dependent depletion of satellite cells in muscular dystrophy. *Dis Model Mech* **7**, 997-1004, doi:10.1242/dmm.015917 (2014).

8 Tichy, E. D. *et al.* Single Stem Cell Imaging and Analysis Reveals Telomere Length Differences in Diseased Human and Mouse Skeletal Muscles. *Stem Cell Reports* **9**, 1328-1341, doi:10.1016/j.stemcr.2017.08.003 (2017).

9 Wahlgren, L., Kroksmark, A. K., Tulinius, M. & Sofou, K. One in five patients with Duchenne muscular dystrophy dies from other causes than cardiac or respiratory failure. *Eur J Epidemiol* **37**, 147-156, doi:10.1007/s10654-021-00819-4 (2022).

10 Gandolla, M., Antonietti, A., Longatelli, V. & Pedrocchi, A. The Effectiveness of Wearable Upper Limb Assistive Devices in Degenerative Neuromuscular Diseases: A Systematic Review and Meta-Analysis. *Front Bioeng Biotechnol* **7**, 450, doi:10.3389/fbioe.2019.00450 (2019).

11 Kourakis, S. *et al.* Standard of care versus new-wave corticosteroids in the treatment of Duchenne muscular dystrophy: Can we do better? *Orphanet J Rare Dis* **16**, 117, doi:10.1186/s13023-021-01758-9 (2021).

12 Matthews, E., Brassington, R., Kuntzer, T., Jichi, F. & Manzur, A. Y. Corticosteroids for the treatment of Duchenne muscular dystrophy. *Cochrane Database Syst Rev* **2016**, Cd003725, doi:10.1002/14651858.CD003725.pub4 (2016).

13 Pedlow, K., McDonough, S., Lennon, S., Kerr, C. & Bradbury, I. Assisted standing for Duchenne muscular dystrophy. *Cochrane Database Syst Rev* **10**, Cd011550, doi:10.1002/14651858.CD011550.pub2 (2019).

14 Tuffery-Giraud, S. *et al.* Genotype-phenotype analysis in 2,405 patients with a dystrophinopathy using the UMD-DMD database: a model of nationwide knowledgebase. *Human mutation* **30**, 934-945, doi:10.1002/humu.20976 (2009).

15 Wang, L. *et al.* Genotypes and Phenotypes of DMD Small Mutations in Chinese Patients With Dystrophinopathies. *Front Genet* **10**, 114, doi:10.3389/fgene.2019.00114 (2019).

16 Flanigan, K. M. *et al.* Mutational spectrum of DMD mutations in dystrophinopathy patients: application of modern diagnostic techniques to a large cohort. *Human mutation* **30**, 1657-1666, doi:10.1002/humu.21114 (2009).

17 Neri, M. *et al.* The Genetic Landscape of Dystrophin Mutations in Italy: A Nationwide Study. *Front Genet* **11**, 131, doi:10.3389/fgene.2020.00131 (2020).

18 Koenig, M. *et al.* The molecular basis for Duchenne versus Becker muscular dystrophy: correlation of severity with type of deletion. *Am J Hum Genet* **45**, 498-506 (1989).

19 Gao, Q. Q. & McNally, E. M. The Dystrophin Complex: Structure, Function, and Implications for Therapy. *Compr Physiol* **5**, 1223-1239, doi:10.1002/cphy.c140048 (2015).

20 Petrof, B. J., Shrager, J. B., Stedman, H. H., Kelly, A. M. & Sweeney, H. L. Dystrophin protects the sarcolemma from stresses developed during muscle contraction. *Proceedings of the National Academy of Sciences of the United States of America* **90**, 3710-3714, doi:10.1073/pnas.90.8.3710 (1993).

21 Weller, B., Karpati, G. & Carpenter, S. Dystrophin-deficient mdx muscle fibers are preferentially vulnerable to necrosis induced by experimental lengthening contractions. *J Neurol Sci* **100**, 9-13, doi:10.1016/0022-510x(90)90005-8 (1990).

22 Hopf, F. W., Turner, P. R., Denetclaw, W. F., Jr., Reddy, P. & Steinhardt, R. A. A critical evaluation of resting intracellular free calcium regulation in dystrophic mdx muscle. *Am J Physiol* **271**, C1325-1339, doi:10.1152/ajpcell.1996.271.4.C1325 (1996).

23 Turner, P. R., Fong, P. Y., Denetclaw, W. F. & Steinhardt, R. A. Increased calcium influx in dystrophic muscle. *The Journal of cell biology* **115**, 1701-1712, doi:10.1083/jcb.115.6.1701 (1991).

24 Whitehead, N. P., Yeung, E. W. & Allen, D. G. Muscle damage in mdx (dystrophic) mice: role of calcium and reactive oxygen species. *Clin Exp Pharmacol Physiol* **33**, 657-662, doi:10.1111/j.1440-1681.2006.04394.x (2006).

25 Allen, D. G., Zhang, B. T. & Whitehead, N. P. Stretch-induced membrane damage in muscle: comparison of wild-type and mdx mice. *Adv Exp Med Biol* **682**, 297-313, doi:10.1007/978-1-4419-6366-6_17 (2010).

26 Okinaka, S. *et al.* Serum creatine phosphokinase. Activity in progressive muscular dystrophy and neuromuscular diseases. *Arch Neurol* **4**, 520-525, doi:10.1001/archneur.1961.00450110050006 (1961).

27 Belanto, J. J. *et al.* Microtubule binding distinguishes dystrophin from utrophin. *Proceedings of the National Academy of Sciences of the United States of America* **111**, 5723-5728, doi:10.1073/pnas.1323842111 (2014).

28 Lai, Y. *et al.* Dystrophins carrying spectrin-like repeats 16 and 17 anchor nNOS to the sarcolemma and enhance exercise performance in a mouse model of muscular dystrophy. *J Clin Invest* **119**, 624-635, doi:10.1172/jci36612 (2009).

29 Prins, K. W. *et al.* Dystrophin is a microtubule-associated protein. *The Journal of cell biology* **186**, 363-369, doi:10.1083/jcb.200905048 (2009).

30 Jung, D., Yang, B., Meyer, J., Chamberlain, J. S. & Campbell, K. P. Identification and characterization of the dystrophin anchoring site on beta-dystroglycan. *J Biol Chem* **270**, 27305-27310, doi:10.1074/jbc.270.45.27305 (1995).

31 Sadoulet-Puccio, H. M., Rajala, M. & Kunkel, L. M. Dystrobrevin and dystrophin: an interaction through coiled-coil motifs. *Proceedings of the National Academy of Sciences of the United States of America* **94**, 12413-12418, doi:10.1073/pnas.94.23.12413 (1997).

32 Beroud, C. *et al.* Multiexon skipping leading to an artificial DMD protein lacking amino acids from exons 45 through 55 could rescue up to 63% of patients with Duchenne muscular dystrophy. *Human mutation* **28**, 196-202, doi:10.1002/humu.20428 (2007).

33 Nakamura, A. *et al.* Comparison of the phenotypes of patients harboring in-frame deletions starting at exon 45 in the Duchenne muscular dystrophy gene indicates potential for the development of exon skipping therapy. *Journal of human genetics* **62**, 459-463, doi:10.1038/jhg.2016.152 (2017).

34 Nakamura, A. *et al.* Follow-up of three patients with a large in-frame deletion of exons 45-55 in the Duchenne muscular dystrophy (DMD) gene. *Journal of clinical neuroscience : official journal of the Neurosurgical Society of Australasia* **15**, 757-763, doi:10.1016/j.jocn.2006.12.012 (2008).

35 Taglia, A. *et al.* Clinical features of patients with dystrophinopathy sharing the 45-55 exon deletion of DMD gene. *Acta myologica : myopathies and cardiomyopathies : official journal of the Mediterranean Society of Myology* **34**, 9-13 (2015).

36 Yazaki, M. *et al.* Clinical characteristics of aged Becker muscular dystrophy patients with onset after 30 years. *European neurology* **42**, 145-149, doi:10.1159/000008089 (1999).

37 Delalande, O. *et al.* Dystrophin's central domain forms a complex filament that becomes disorganized by in-frame deletions. *J Biol Chem* **293**, 6637-6646, doi:10.1074/jbc.M117.809798 (2018).

38 Nicolas, A. *et al.* Assessment of the structural and functional impact of in-frame mutations of the DMD gene, using the tools included in the eDystrophin online database. *Orphanet J Rare Dis* **7**, 45, doi:10.1186/1750-1172-7-45 (2012).

39 Phelps, S. F. *et al.* Expression of full-length and truncated dystrophin mini-genes in transgenic mdx mice. *Hum Mol Genet* **4**, 1251-1258, doi:10.1093/hmg/4.8.1251 (1995).

40 Ramos, J. N. *et al.* Development of Novel Micro-dystrophins with Enhanced Functionality. *Molecular therapy : the journal of the American Society of Gene Therapy* **27**, 623-635, doi:10.1016/j.ymthe.2019.01.002 (2019).

41 Wang, B., Li, J. & Xiao, X. Adeno-associated virus vector carrying human minidystrophin genes effectively ameliorates muscular dystrophy in mdx mouse model. *Proceedings of the National Academy of Sciences of the United States of America* **97**, 13714-13719, doi:10.1073/pnas.240335297 (2000).

42 Wang, Z. *et al.* Sustained AAV-mediated dystrophin expression in a canine model of Duchenne muscular dystrophy with a brief course of immunosuppression. *Molecular therapy : the journal of the American Society of Gene Therapy* **15**, 1160-1166, doi:10.1038/sj.mt.6300161 (2007).

43 Wang, Z. *et al.* Successful regional delivery and long-term expression of a dystrophin gene in canine muscular dystrophy: a preclinical model for human therapies. *Molecular therapy : the journal of the American Society of Gene Therapy* **20**, 1501-1507, doi:10.1038/mt.2012.111 (2012).

44 Zhang, Y. & Duan, D. Novel mini-dystrophin gene dual adeno-associated virus vectors restore neuronal nitric oxide synthase expression at the sarcolemma. *Human gene therapy* **23**, 98-103, doi:10.1089/hum.2011.131 (2012).

45 Gloss, D., Moxley, R. T., 3rd, Ashwal, S. & Oskoui, M. Practice guideline update summary: Corticosteroid treatment of Duchenne muscular dystrophy: Report of the Guideline Development Subcommittee of the American Academy of Neurology. *Neurology* **86**, 465-472, doi:10.1212/wnl.0000000000002337 (2016).

46 Griggs, R. C. *et al.* Efficacy and safety of deflazacort vs prednisone and placebo for Duchenne muscular dystrophy. *Neurology* **87**, 2123-2131, doi:10.1212/wnl.0000000000003217 (2016).

47 Schara, U., Mortier & Mortier, W. Long-Term Steroid Therapy in Duchenne Muscular Dystrophy-Positive Results versus Side Effects. *J Clin Neuromuscul Dis* **2**, 179-183, doi:10.1097/00131402-200106000-00002 (2001).

48 Aartsma-Rus, A. *et al.* Theoretic applicability of antisense-mediated exon skipping for Duchenne muscular dystrophy mutations. *Human mutation* **30**, 293-299, doi:10.1002/humu.20918 (2009).

49 Casimersen (Amondys 45) for Duchenne muscular dystrophy. *Med Lett Drugs Ther* **63**, e104-e105 (2021).

50 Cirak, S. *et al.* Exon skipping and dystrophin restoration in patients with Duchenne muscular dystrophy after systemic phosphorodiamidate morpholino oligomer treatment: an open-label, phase 2, dose-escalation study. *Lancet* **378**, 595-605, doi:10.1016/s0140-6736(11)60756-3 (2011).

51 Clemens, P. R. *et al.* Safety, Tolerability, and Efficacy of Viltolarsen in Boys With Duchenne Muscular Dystrophy Amenable to Exon 53 Skipping: A Phase 2 Randomized Clinical Trial. *JAMA Neurol* **77**, 982-991, doi:10.1001/jamaneurol.2020.1264 (2020).

52 Frank, D. E. *et al.* Increased dystrophin production with golodirsen in patients with Duchenne muscular dystrophy. *Neurology* **94**, e2270-e2282, doi:10.1212/wnl.0000000000009233 (2020).

53 Mendell, J. R. *et al.* Eteplirsen for the treatment of Duchenne muscular dystrophy. *Ann Neurol* **74**, 637-647, doi:10.1002/ana.23982 (2013).

54 Muntoni, F. *et al.* Golodirsen Induces Exon Skipping Leading to Sarcolemmal Dystrophin Expression in Duchenne Muscular Dystrophy Patients With Mutations Amenable to Exon 53 Skipping (S22.001). *Neurology* **90**, S22.001 (2018).

55 Servais, L. *et al.* Long-Term Safety and Efficacy Data of Golodirsen in Ambulatory Patients with Duchenne Muscular Dystrophy Amenable to Exon 53 Skipping: A First-in-human, Multicenter, Two-Part, Open-Label, Phase 1/2 Trial. *Nucleic Acid Ther* **32**, 29-39, doi:10.1089/nat.2021.0043 (2022).

56 van Putten, M. *et al.* Low dystrophin levels increase survival and improve muscle pathology and function in dystrophin/utrophin double-knockout mice. *Faseb j* **27**, 2484-2495, doi:10.1096/fj.12-224170 (2013).

57 Sharp, P. S., Bye-a-Jee, H. & Wells, D. J. Physiological characterization of muscle strength with variable levels of dystrophin restoration in mdx mice following local antisense therapy. *Molecular therapy : the journal of the American Society of Gene Therapy* **19**, 165-171, doi:10.1038/mt.2010.213 (2011).

58 van Putten, M. *et al.* The effects of low levels of dystrophin on mouse muscle function and pathology. *PLoS One* **7**, e31937, doi:10.1371/journal.pone.0031937 (2012).

59 Duan, D. Micro-Dystrophin Gene Therapy Goes Systemic in Duchenne Muscular Dystrophy Patients. *Human gene therapy* **29**, 733-736, doi:10.1089/hum.2018.012 (2018).

60 Ates, I., Rathbone, T., Stuart, C., Bridges, P. H. & Cottle, R. N. Delivery Approaches for Therapeutic Genome Editing and Challenges. *Genes (Basel)* **11**, doi:10.3390/genes11101113 (2020).

61 Li, H. L. *et al.* Precise correction of the dystrophin gene in duchenne muscular dystrophy patient induced pluripotent stem cells by TALEN and CRISPR-Cas9. *Stem Cell Reports* **4**, 143-154, doi:10.1016/j.stemcr.2014.10.013 (2015).

62 Ousterout, D. G. *et al.* Correction of dystrophin expression in cells from Duchenne muscular dystrophy patients through genomic excision of exon 51 by zinc finger nucleases. *Molecular therapy : the journal of the American Society of Gene Therapy* **23**, 523-532, doi:10.1038/mt.2014.234 (2015).

63 Cong, L. *et al.* Multiplex genome engineering using CRISPR/Cas systems. *Science (New York, N.Y.)* **339**, 819-823, doi:10.1126/science.1231143 (2013).

64 Jinek, M. *et al.* A programmable dual-RNA-guided DNA endonuclease in adaptive bacterial immunity. *Science (New York, N.Y.)* **337**, 816-821, doi:10.1126/science.1225829 (2012).

65 Mali, P. *et al.* RNA-guided human genome engineering via Cas9. *Science (New York, N.Y.)* **339**, 823-826, doi:10.1126/science.1232033 (2013).

66 Lieber, M. R. The mechanism of double-strand DNA break repair by the nonhomologous DNA end-joining pathway. *Annual review of biochemistry* **79**, 181-211, doi:10.1146/annurev.biochem.052308.093131 (2010).

67 Maggio, I., Liu, J., Janssen, J. M., Chen, X. & Gonçalves, M. A. Adenoviral vectors encoding CRISPR/Cas9 multiplexes rescue dystrophin synthesis in unselected populations of DMD muscle cells. *Sci Rep* **6**, 37051, doi:10.1038/srep37051 (2016).

68 Young, C. S. *et al.* A Single CRISPR-Cas9 Deletion Strategy that Targets the Majority of DMD Patients Restores Dystrophin Function in hiPSC-Derived Muscle Cells. *Cell Stem Cell* **18**, 533-540, doi:10.1016/j.stem.2016.01.021 (2016).

69 Zhang, Y. *et al.* CRISPR-Cpf1 correction of muscular dystrophy mutations in human cardiomyocytes and mice. *Sci Adv* **3**, e1602814, doi:10.1126/sciadv.1602814 (2017).

70 Emami, M. R. *et al.* Polyrotaxane Nanocarriers Can Deliver CRISPR/Cas9 Plasmid to Dystrophic Muscle Cells to Successfully Edit the DMD Gene. *Advanced Therapeutics* **2**, 1900061, doi:https://doi.org/10.1002/adtp.201900061 (2019).

71 Tabebordbar, M. *et al.* In vivo gene editing in dystrophic mouse muscle and muscle stem cells. *Science (New York, N.Y.)* **351**, 407-411, doi:10.1126/science.aad5177 (2016).

72 Zhu, P. *et al.* CRISPR/Cas9-Mediated Genome Editing Corrects Dystrophin Mutation in Skeletal Muscle Stem Cells in a Mouse Model of Muscle Dystrophy. *Mol Ther Nucleic Acids* **7**, 31-41, doi:10.1016/j.omtn.2017.02.007 (2017).

73 Bengtsson, N. E. *et al.* Muscle-specific CRISPR/Cas9 dystrophin gene editing ameliorates pathophysiology in a mouse model for Duchenne muscular dystrophy. *Nature communications* **8**, 14454, doi:10.1038/ncomms14454 (2017).

74 Long, C. *et al.* Postnatal genome editing partially restores dystrophin expression in a mouse model of muscular dystrophy. *Science (New York, N.Y.)* **351**, 400-403, doi:10.1126/science.aad5725 (2016).

75 Nelson, C. E. *et al.* In vivo genome editing improves muscle function in a mouse model of Duchenne muscular dystrophy. *Science (New York, N.Y.)* **351**, 403-407, doi:10.1126/science.aad5143 (2016).

76 Xu, L. *et al.* CRISPR-mediated Genome Editing Restores Dystrophin Expression and Function in mdx Mice. *Molecular therapy : the journal of the American Society of Gene Therapy* **24**, 564-569, doi:10.1038/mt.2015.192 (2016).

77 Young, C. S., Mokhonova, E., Quinonez, M., Pyle, A. D. & Spencer, M. J. Creation of a Novel Humanized Dystrophic Mouse Model of Duchenne Muscular Dystrophy and Application of a CRISPR/Cas9 Gene Editing Therapy. *J Neuromuscul Dis* **4**, 139-145, doi:10.3233/JND-170218 (2017).

78 Amoasii, L. *et al.* Gene editing restores dystrophin expression in a canine model of Duchenne muscular dystrophy. *Science (New York, N.Y.)* **362**, 86-91, doi:10.1126/science.aau1549 (2018).

79 Hakim, C. H. *et al.* Cas9-specific immune responses compromise local and systemic AAV CRISPR therapy in multiple dystrophic canine models. *Nature communications* **12**, 6769, doi:10.1038/s41467-021-26830-7 (2021).

80 Moretti, A. *et al.* Somatic gene editing ameliorates skeletal and cardiac muscle failure in pig and human models of Duchenne muscular dystrophy. *Nat Med* **26**, 207-214, doi:10.1038/s41591-019-0738-2 (2020).

81 Meng, H., Leong, W., Leong, K. W., Chen, C. & Zhao, Y. Walking the line: The fate of nanomaterials at biological barriers. *Biomaterials* **174**, 41-53, doi:10.1016/j.biomaterials.2018.04.056 (2018).

82 Anselmo, A. C. & Mitragotri, S. Nanoparticles in the clinic: An update. *Bioeng Transl Med* **4**, e10143, doi:10.1002/btm2.10143 (2019).

83 Mitchell, M. J. *et al.* Engineering precision nanoparticles for drug delivery. *Nat Rev Drug Discov* **20**, 101-124, doi:10.1038/s41573-020-0090-8 (2021).

84 Ventola, C. L. Progress in Nanomedicine: Approved and Investigational Nanodrugs. *P t* **42**, 742-755 (2017).

85 Chen, Z. *et al.* Targeted Delivery of CRISPR/Cas9-Mediated Cancer Gene Therapy via Liposome-Templated Hydrogel Nanoparticles. *Advanced functional materials* **27**, doi:10.1002/adfm.201703036 (2017).

86 Finn, J. D. *et al.* A Single Administration of CRISPR/Cas9 Lipid Nanoparticles Achieves Robust and Persistent In Vivo Genome Editing. *Cell reports* **22**, 2227-2235, doi:10.1016/j.celrep.2018.02.014 (2018).

87 Jiang, C. *et al.* A non-viral CRISPR/Cas9 delivery system for therapeutically targeting HBV DNA and pcsk9 in vivo. *Cell research* **27**, 440-443, doi:10.1038/cr.2017.16 (2017).

88 Kenjo, E. *et al.* Low immunogenicity of LNP allows repeated administrations of CRISPR-Cas9 mRNA into skeletal muscle in mice. *Nature communications* **12**, 7101, doi:10.1038/s41467-021-26714-w (2021).

89 Miller, J. B. *et al.* Non-Viral CRISPR/Cas Gene Editing In Vitro and In Vivo Enabled by Synthetic Nanoparticle Co-Delivery of Cas9 mRNA and sgRNA. *Angewandte Chemie (International ed. in English)* **56**, 1059-1063, doi:10.1002/anie.201610209 (2017).

90 Qiu, M. *et al.* Lipid nanoparticle-mediated codelivery of Cas9 mRNA and single-guide RNA achieves liver-specific in vivo genome editing of Angptl3. *Proceedings of the National Academy of Sciences of the United States of America* **118**, doi:10.1073/pnas.2020401118 (2021).

91 Wang, M. *et al.* Efficient delivery of genome-editing proteins using bioreducible lipid nanoparticles. *Proceedings of the National Academy of Sciences of the United States of America* **113**, 2868-2873, doi:10.1073/pnas.1520244113 (2016).

92 Yin, H. *et al.* Therapeutic genome editing by combined viral and non-viral delivery of CRISPR system components in vivo. *Nature biotechnology* **34**, 328-333, doi:10.1038/nbt.3471 (2016).

93 Yin, H. *et al.* Structure-guided chemical modification of guide RNA enables potent non-viral in vivo genome editing. *Nature biotechnology* **35**, 1179-1187, doi:10.1038/nbt.4005 (2017).

94 Zuris, J. A. *et al.* Cationic lipid-mediated delivery of proteins enables efficient protein-based genome editing in vitro and in vivo. *Nature biotechnology* **33**, 73-80, doi:10.1038/nbt.3081 (2015).

95 Sun, W. *et al.* Self-assembled DNA nanoclews for the efficient delivery of CRISPR-Cas9 for genome editing. *Angewandte Chemie (International ed. in English)* **54**, 12029-12033, doi:10.1002/anie.201506030 (2015).

96 Ha, J. S. *et al.* Poly-sgRNA/siRNA ribonucleoprotein nanoparticles for targeted gene disruption. *Journal of controlled release : official journal of the Controlled Release Society* **250**, 27-35, doi:10.1016/j.jconrel.2017.02.007 (2017).

97 Liu, Y. *et al.* Systemic delivery of CRISPR/Cas9 with PEG-PLGA nanoparticles for chronic myeloid leukemia targeted therapy. *Biomater Sci* **6**, 1592-1603, doi:10.1039/c8bm00263k (2018).

98 Timin, A. S. *et al.* Efficient gene editing via non-viral delivery of CRISPR-Cas9 system using polymeric and hybrid microcarriers. *Nanomedicine : nanotechnology, biology, and medicine* **14**, 97-108, doi:10.1016/j.nano.2017.09.001 (2018).

99 Noureddine, A. *et al.* Engineering of monosized lipid-coated mesoporous silica nanoparticles for CRISPR delivery. *Acta Biomater* **114**, 358-368, doi:10.1016/j.actbio.2020.07.027 (2020).

100 Lee, B. *et al.* Nanoparticle delivery of CRISPR into the brain rescues a mouse model of fragile X syndrome from exaggerated repetitive behaviours. *Nature biomedical engineering* **2**, 497-507, doi:10.1038/s41551-018-0252-8 (2018).

101 Lee, K. *et al.* Nanoparticle delivery of Cas9 ribonucleoprotein and donor DNA in vivo induces homology-directed DNA repair. *Nature biomedical engineering* **1**, 889-901, doi:10.1038/s41551-017-0137-2 (2017).

102 Lee, K. *et al.* Synthetically modified guide RNA and donor DNA are a versatile platform for CRISPR-Cas9 engineering. *eLife* **6**, doi:10.7554/eLife.25312 (2017).

103 Mout, R. *et al.* Direct Cytosolic Delivery of CRISPR/Cas9-Ribonucleoprotein for Efficient Gene Editing. *ACS nano* **11**, 2452-2458, doi:10.1021/acsnano.6b07600 (2017).

104 Lin, Y. *et al.* Exosome-Liposome Hybrid Nanoparticles Deliver CRISPR/Cas9 System in MSCs. *Adv Sci (Weinh)* **5**, 1700611, doi:10.1002/advs.201700611 (2018).

105 Wang, J., Chen, R. & Lu, F. M. [Exosome-mediated CRISPR/Cas9 system targets to cut the intercellular transmission function of hepatitis B virus genome]. *Zhonghua Gan Zang Bing Za Zhi* **27**, 610-614, doi:10.3760/cma.j.issn.1007-3418.2019.08.005 (2019).

106 Alsaiari, S. K. *et al.* Endosomal Escape and Delivery of CRISPR/Cas9 Genome Editing Machinery Enabled by Nanoscale Zeolitic Imidazolate Framework. *Journal of the American Chemical Society* **140**, 143-146, doi:10.1021/jacs.7b11754 (2018).

107 Zheng, Q., Li, W., Mao, L. & Wang, M. Nanoscale metal-organic frameworks for the intracellular delivery of CRISPR/Cas9 genome editing machinery. *Biomater Sci* **9**, 7024-7033, doi:10.1039/d1bm00790d (2021).

108 Wei, T., Cheng, Q., Min, Y. L., Olson, E. N. & Siegwart, D. J. Systemic nanoparticle delivery of CRISPR-Cas9 ribonucleoproteins for effective tissue specific genome editing. *Nature communications* **11**, 3232, doi:10.1038/s41467-020-17029-3 (2020).

109 Mingozzi, F. *et al.* AAV-1-mediated gene transfer to skeletal muscle in humans results in dose-dependent activation of capsid-specific T cells. *Blood* **114**, 2077-2086, doi:10.1182/blood-2008-07-167510 (2009).

110 Nathwani, A. C. *et al.* Adenovirus-associated virus vector-mediated gene transfer in hemophilia B. *N Engl J Med* **365**, 2357-2365, doi:10.1056/NEJMoa1108046 (2011).

111 Srivastava, A. In vivo tissue-tropism of adeno-associated viral vectors. *Curr Opin Virol* **21**, 75-80, doi:10.1016/j.coviro.2016.08.003 (2016).

112 Zincarelli, C., Soltys, S., Rengo, G. & Rabinowitz, J. E. Analysis of AAV serotypes 1-9 mediated gene expression and tropism in mice after systemic injection. *Molecular therapy : the journal of the American Society of Gene Therapy* **16**, 1073-1080, doi:10.1038/mt.2008.76 (2008).

113 Amoasii, L. *et al.* Single-cut genome editing restores dystrophin expression in a new mouse model of muscular dystrophy. *Sci Transl Med* **9**, doi:10.1126/scitranslmed.aan8081 (2017).

114 El Refaey, M. *et al.* In Vivo Genome Editing Restores Dystrophin Expression and Cardiac Function in Dystrophic Mice. *Circ Res* **121**, 923-929, doi:10.1161/circresaha.117.310996 (2017).

115 Min, Y. L. *et al.* CRISPR-Cas9 corrects Duchenne muscular dystrophy exon 44 deletion mutations in mice and human cells. *Sci Adv* **5**, eaav4324, doi:10.1126/sciadv.aav4324 (2019).

116 Nelson, C. E. *et al.* Long-term evaluation of AAV-CRISPR genome editing for Duchenne muscular dystrophy. *Nat Med* **25**, 427-432, doi:10.1038/s41591-019-0344-3 (2019).

117 Kwon, J. B. *et al.* In Vivo Gene Editing of Muscle Stem Cells with Adeno-Associated Viral Vectors in a Mouse Model of Duchenne Muscular Dystrophy. *Molecular therapy. Methods & clinical development* **19**, 320-329, doi:10.1016/j.omtm.2020.09.016 (2020).

118 Nance, M. E. *et al.* AAV9 Edits Muscle Stem Cells in Normal and Dystrophic Adult Mice. *Molecular therapy : the journal of the American Society of Gene Therapy* **27**, 1568-1585, doi:10.1016/j.ymthe.2019.06.012 (2019).

119 Bengtsson, N. E., Tasfaout, H., Hauschka, S. D. & Chamberlain, J. S. Dystrophin Gene-Editing Stability Is Dependent on Dystrophin Levels in Skeletal but Not Cardiac Muscles. *Molecular therapy : the journal of the American Society of Gene Therapy* **29**, 1070-1085, doi:10.1016/j.ymthe.2020.11.003 (2021).

120 Charlesworth, C. T. *et al.* Identification of preexisting adaptive immunity to Cas9 proteins in humans. *Nat Med* **25**, 249-254, doi:10.1038/s41591-018-0326-x (2019).

121 Louis Jeune, V., Joergensen, J. A., Hajjar, R. J. & Weber, T. Pre-existing anti-adeno-associated virus antibodies as a challenge in AAV gene therapy. *Human gene therapy methods* **24**, 59-67, doi:10.1089/hgtb.2012.243 (2013).

122 Simhadri, V. L. *et al.* Prevalence of Pre-existing Antibodies to CRISPR-Associated Nuclease Cas9 in the USA Population. *Molecular therapy. Methods & clinical development* **10**, 105-112, doi:10.1016/j.omtm.2018.06.006 (2018).

123 Wagner, D. L. *et al.* High prevalence of Streptococcus pyogenes Cas9-reactive T cells within the adult human population. *Nat Med* **25**, 242-248, doi:10.1038/s41591-018-0204-6 (2019).

124 Li, A. *et al.* AAV-CRISPR Gene Editing Is Negated by Pre-existing Immunity to Cas9. *Molecular therapy : the journal of the American Society of Gene Therapy* **28**, 1432-1441, doi:10.1016/j.ymthe.2020.04.017 (2020).

125 Mingozzi, F. & High, K. A. Immune responses to AAV vectors: overcoming barriers to successful gene therapy. *Blood* **122**, 23-36, doi:10.1182/blood-2013-01-306647 (2013).

126 Perrin, G. Q., Herzog, R. W. & Markusic, D. M. Update on clinical gene therapy for hemophilia. *Blood* **133**, 407-414, doi:10.1182/blood-2018-07-820720 (2019).

127 Penaud-Budloo, M. *et al.* Adeno-associated virus vector genomes persist as episomal chromatin in primate muscle. *Journal of virology* **82**, 7875-7885, doi:10.1128/JVI.00649-08 (2008).

128 Zhang, F., Song, G. & Tian, Y. Anti-CRISPRs: The natural inhibitors for CRISPR-Cas systems. *Animal Model Exp Med* **2**, 69-75, doi:10.1002/ame2.12069 (2019).

129 Li, A. *et al.* A Self-Deleting AAV-CRISPR System for In Vivo Genome Editing. *Molecular therapy. Methods & clinical development* **12**, 111-122, doi:10.1016/j.omtm.2018.11.009 (2019).

130 Merienne, N. *et al.* The Self-Inactivating KamiCas9 System for the Editing of CNS Disease Genes. *Cell reports* **20**, 2980-2991, doi:10.1016/j.celrep.2017.08.075 (2017).

131 Zhu, J., Huang, X. & Yang, Y. The TLR9-MyD88 pathway is critical for adaptive immune responses to adeno-associated virus gene therapy vectors in mice. *J Clin Invest* **119**, 2388-2398, doi:10.1172/jci37607 (2009).

132 Chan, Y. K. *et al.* Engineering adeno-associated viral vectors to evade innate immune and inflammatory responses. *Sci Transl Med* **13**, doi:10.1126/scitranslmed.abd3438 (2021).

133 Faust, S. M. *et al.* CpG-depleted adeno-associated virus vectors evade immune detection. *J Clin Invest* **123**, 2994-3001, doi:10.1172/jci68205 (2013).

134 Kornegay, J. N. *et al.* Widespread muscle expression of an AAV9 human mini-dystrophin vector after intravenous injection in neonatal dystrophin-deficient dogs. *Molecular therapy : the journal of the American Society of Gene Therapy* **18**, 1501-1508, doi:10.1038/mt.2010.94 (2010).

135 Dobrowsky, T., Gianni, D., Pieracci, J. & Suh, J. AAV manufacturing for clinical use: Insights on current challenges from the upstream process perspective. *Current Opinion in Biomedical Engineering* **20**, 100353, doi:https://doi.org/10.1016/j.cobme.2021.100353 (2021).

136 Barrangou, R. & Doudna, J. A. Applications of CRISPR technologies in research and beyond. *Nature biotechnology* **34**, 933-941, doi:10.1038/nbt.3659 (2016).

137 Doudna, J. A. & Charpentier, E. Genome editing. The new frontier of genome engineering with CRISPR-Cas9. *Science (New York, N.Y.)* **346**, 1258096, doi:10.1126/science.1258096 (2014).

138 Moser, H. Duchenne muscular dystrophy: pathogenetic aspects and genetic prevention. *Human genetics* **66**, 17-40 (1984).

139 Monaco, A. P., Bertelson, C. J., Liechti-Gallati, S., Moser, H. & Kunkel, L. M. An explanation for the phenotypic differences between patients bearing partial deletions of the DMD locus. *Genomics* **2**, 90-95 (1988).

140 Lau, C. H. & Suh, Y. In vivo genome editing in animals using AAV-CRISPR system: applications to translational research of human disease. *F1000Res* **6**, 2153, doi:10.12688/f1000research.11243.1 (2017).

141 Boutin, S. *et al.* Prevalence of serum IgG and neutralizing factors against adeno-associated virus (AAV) types 1, 2, 5, 6, 8, and 9 in the healthy population: implications for gene therapy using AAV vectors. *Human gene therapy* **21**, 704-712, doi:10.1089/hum.2009.182 (2010).

142 Le Guiner, C. *et al.* Long-term microdystrophin gene therapy is effective in a canine model of Duchenne muscular dystrophy. *Nature communications* **8**, 16105, doi:10.1038/ncomms16105 (2017).

143 Charlesworth, C. T. *et al.* Identification of Pre-Existing Adaptive Immunity to Cas9 Proteins in Humans. 243345, doi:10.1101/243345 %J bioRxiv (2018).

144 Grieger, J. C. & Samulski, R. J. Packaging capacity of adeno-associated virus serotypes: impact of larger genomes on infectivity and postentry steps. *Journal of virology* **79**, 9933-9944, doi:10.1128/JVI.79.15.9933-9944.2005 (2005).

145 Givens, B. E., Naguib, Y. W., Geary, S. M., Devor, E. J. & Salem, A. K. Nanoparticle-Based Delivery of CRISPR/Cas9 Genome-Editing Therapeutics. *The AAPS journal* **20**, 108, doi:10.1208/s12248-018-0267-9 (2018).

146 Jativa, S. D. *et al.* Enhanced Delivery of Plasmid DNA to Skeletal Muscle Cells using a DLC8-Binding Peptide and ASSLNIA-Modified PAMAM Dendrimer. *Mol Pharm* **16**, 2376-2384, doi:10.1021/acs.molpharmaceut.8b01313 (2019).

147 Afzal, E. *et al.* Nanolipodendrosome-loaded glatiramer acetate and myogenic differentiation 1 as augmentation therapeutic strategy approaches in muscular dystrophy. *Int J Nanomedicine* **8**, 2943-2960, doi:10.2147/ijn.S43219 (2013).

148 Bassi, E. *et al.* Persistent dystrophin protein restoration 90 days after a course of intraperitoneally administered naked 2'OMePS AON and ZM2 NP-AON complexes in mdx mice. *J Biomed Biotechnol* **2012**, 897076, doi:10.1155/2012/897076 (2012).

149 Bibee, K. P. *et al.* Rapamycin nanoparticles target defective autophagy in muscular dystrophy to enhance both strength and cardiac function. *Faseb j* **28**, 2047-2061, doi:10.1096/fj.13-237388 (2014).

150 Brown, P. K., Qureshi, A. T., Moll, A. N., Hayes, D. J. & Monroe, W. T. Silver nanoscale antisense drug delivery system for photoactivated gene silencing. *ACS nano* **7**, 2948-2959, doi:10.1021/nn304868y (2013).

151 Chiper, M., Tounsi, N., Kole, R., Kichler, A. & Zuber, G. Self-aggregating 1.8kDa polyethylenimines with dissolution switch at endosomal acidic pH are delivery carriers for plasmid DNA, mRNA, siRNA and exon-skipping oligonucleotides. *Journal of controlled release : official journal of the Controlled Release Society* **246**, 60-70, doi:10.1016/j.jconrel.2016.12.005 (2017).

152 Costanzo, M. *et al.* Uptake and intracellular fate of biocompatible nanocarriers in cycling and noncycling cells. *Nanomedicine (Lond)* **14**, 301-316, doi:10.2217/nnm-2018-0148 (2019).

153 Falzarano, M. S. *et al.* Biodistribution and molecular studies on orally administered nanoparticle-AON complexes encapsulated with alginate aiming at inducing dystrophin rescue in mdx mice. *Biomed Res Int* **2013**, 527418, doi:10.1155/2013/527418 (2013).

154 Kim, Y. *et al.* Polymersome delivery of siRNA and antisense oligonucleotides. *Journal of controlled release : official journal of the Controlled Release Society* **134**, 132-140, doi:10.1016/j.jconrel.2008.10.020 (2009).

155 Kinouchi, N. *et al.* Atelocollagen-mediated local and systemic applications of myostatin-targeting siRNA increase skeletal muscle mass. *Gene Ther* **15**, 1126-1130, doi:10.1038/gt.2008.24 (2008).

156 Negishi, Y. *et al.* Bubble liposomes and ultrasound exposure improve localized morpholino oligomer delivery into the skeletal muscles of dystrophic mdx mice. *Mol Pharm* **11**, 1053-1061, doi:10.1021/mp4004755 (2014).

157 Ochiya, T. *et al.* New delivery system for plasmid DNA in vivo using atelocollagen as a carrier material: the Minipellet. *Nat Med* **5**, 707-710, doi:10.1038/9560 (1999).

158 Rimessi, P. *et al.* Cationic PMMA nanoparticles bind and deliver antisense oligoribonucleotides allowing restoration of dystrophin expression in the mdx mouse. *Molecular therapy : the journal of the American Society of Gene Therapy* **17**, 820-827, doi:10.1038/mt.2009.8 (2009).

159 Wang, M. *et al.* Pluronic-PEI copolymers enhance exon-skipping of 2'-O-methyl phosphorothioate oligonucleotide in cell culture and dystrophic mdx mice. *Gene Ther* **21**, 52-59, doi:10.1038/gt.2013.57 (2014).

160 Williams, J. H., Schray, R. C., Sirsi, S. R. & Lutz, G. J. Nanopolymers improve delivery of exon skipping oligonucleotides and concomitant dystrophin expression in skeletal muscle of mdx mice. *BMC Biotechnol* **8**, 35, doi:10.1186/1472-6750-8-35 (2008).

161 Williams, J. H., Sirsi, S. R., Latta, D. R. & Lutz, G. J. Induction of dystrophin expression by exon skipping in mdx mice following intramuscular injection of antisense oligonucleotides complexed with PEG-PEI copolymers. *Molecular therapy : the journal of the American Society of Gene Therapy* **14**, 88-96, doi:10.1016/j.ymthe.2005.11.025 (2006).

162 Wenz, G., Han, B. H. & Muller, A. Cyclodextrin rotaxanes and polyrotaxanes. *Chemical reviews* **106**, 782-817, doi:10.1021/cr970027+ (2006).

163 Ji, Y. *et al.* Development of self-assembled multi-arm polyrotaxanes nanocarriers for systemic plasmid delivery in vivo. *Biomaterials* **192**, 416-428, doi:10.1016/j.biomaterials.2018.11.027 (2019).

164 Maddalo, D. *et al.* In vivo engineering of oncogenic chromosomal rearrangements with the CRISPR/Cas9 system. *Nature* **516**, 423-427, doi:10.1038/nature13902 (2014).

165 Zugates, G. T., Anderson, D. G., Little, S. R., Lawhorn, I. E. & Langer, R. Synthesis of poly(beta-amino ester)s with thiol-reactive side chains for DNA

delivery. *Journal of the American Chemical Society* **128**, 12726-12734, doi:10.1021/ja061570n (2006).

166 Yamashita, A. *et al.* Synthesis of a biocleavable polyrotaxane-plasmid DNA (pDNA) polyplex and its use for the rapid nonviral delivery of pDNA to cell nuclei. *Nature protocols* **1**, 2861-2869, doi:10.1038/nprot.2006.438 (2006).

167 Ooya, T. *et al.* Biocleavable polyrotaxane-plasmid DNA polyplex for enhanced gene delivery. *Journal of the American Chemical Society* **128**, 3852-3853, doi:10.1021/ja055868+ (2006).

168 Ronn, L. C. *et al.* Identification of a neuritogenic ligand of the neural cell adhesion molecule using a combinatorial library of synthetic peptides. *Nature biotechnology* **17**, 1000-1005, doi:10.1038/13697 (1999).

169 Yin, H. *et al.* Pip5 transduction peptides direct high efficiency oligonucleotide-mediated dystrophin exon skipping in heart and phenotypic correction in mdx mice. *Molecular therapy : the journal of the American Society of Gene Therapy* **19**, 1295-1303, doi:10.1038/mt.2011.79 (2011).

170 Waldner, C., Roose, M. & Ryffel, G. U. Red fluorescent Xenopus laevis: a new tool for grafting analysis. *BMC developmental biology* **9**, 37, doi:10.1186/1471-213x-9-37 (2009).

171 Nomoto, T. *et al.* Three-layered polyplex micelle as a multifunctional nanocarrier platform for light-induced systemic gene transfer. *Nature communications* **5**, 3545, doi:10.1038/ncomms4545 (2014).

172 Benjaminsen, R. V., Mattebjerg, M. A., Henriksen, J. R., Moghimi, S. M. & Andresen, T. L. The possible "proton sponge " effect of polyethylenimine (PEI) does not include change in lysosomal pH. *Molecular therapy : the journal of the American Society of Gene Therapy* **21**, 149-157, doi:10.1038/mt.2012.185 (2013).

173 Wojnilowicz, M., Glab, A., Bertucci, A., Caruso, F. & Cavalieri, F. Super-resolution Imaging of Proton Sponge-Triggered Rupture of Endosomes and Cytosolic Release of Small Interfering RNA. *ACS nano* **13**, 187-202, doi:10.1021/acsnano.8b05151 (2019).

174 Xu, M. *et al.* PEG-Detachable Polymeric Micelles Self-Assembled from Amphiphilic Copolymers for Tumor-Acidity-Triggered Drug Delivery and Controlled Release. *ACS applied materials & interfaces*, doi:10.1021/acsami.8b13059 (2019).

175 Ji, L. L., Fu, R. & Mitchell, E. W. Glutathione and antioxidant enzymes in skeletal muscle: effects of fiber type and exercise intensity. *Journal of applied physiology (Bethesda, Md. : 1985)* **73**, 1854-1859, doi:10.1152/jappl.1992.73.5.1854 (1992).

176 Montero, D., Tachibana, C., Rahr Winther, J. & Appenzeller-Herzog, C. Intracellular glutathione pools are heterogeneously concentrated. *Redox biology* **1**, 508-513, doi:10.1016/j.redox.2013.10.005 (2013).

177 Sen, C. K., Marin, E., Kretzschmar, M. & Hanninen, O. Skeletal muscle and liver glutathione homeostasis in response to training, exercise, and immobilization. *Journal of applied physiology (Bethesda, Md. : 1985)* **73**, 1265-1272, doi:10.1152/jappl.1992.73.4.1265 (1992).

178 Sen, C. K., Rahkila, P. & Hanninen, O. Glutathione metabolism in skeletal muscle derived cells of the L6 line. *Acta physiologica Scandinavica* **148**, 21-26, doi:10.1111/j.1748-1716.1993.tb09527.x (1993).

179 Capecchi, M. R. High efficiency transformation by direct microinjection of DNA into cultured mammalian cells. *Cell* **22**, 479-488 (1980).

180 Capkovic, K. L., Stevenson, S., Johnson, M. C., Thelen, J. J. & Cornelison, D. D. Neural cell adhesion molecule (NCAM) marks adult myogenic cells committed to differentiation. *Experimental cell research* **314**, 1553-1565, doi:10.1016/j.yexcr.2008.01.021 (2008).

181 Fidzianska, A. & Kaminska, A. Neural cell adhesion molecule (N-CAM) as a marker of muscle tissue alternations. Review of the literature and own observations. *Folia neuropathologica* **33**, 125-128 (1995).

182 Snijders, T. *et al.* Satellite cells in human skeletal muscle plasticity. *Frontiers in physiology* **6**, 283, doi:10.3389/fphys.2015.00283 (2015).

183 Moore, S. E., Thompson, J., Kirkness, V., Dickson, J. G. & Walsh, F. S. Skeletal muscle neural cell adhesion molecule (N-CAM): changes in protein and mRNA species during myogenesis of muscle cell lines. *The Journal of cell biology* **105**, 1377-1386 (1987).

184 Kulkarni, J. A. *et al.* Design of lipid nanoparticles for in vitro and in vivo delivery of plasmid DNA. *Nanomedicine : nanotechnology, biology, and medicine* **13**, 1377-1387, doi:10.1016/j.nano.2016.12.014 (2017).

185 Li, L. M. *et al.* ScreenFect A: an efficient and low toxic liposome for gene delivery to mesenchymal stem cells. *Int J Pharm* **488**, 1-11, doi:10.1016/j.ijpharm.2015.04.050 (2015).

186 Ellis, B. L. *et al.* A survey of ex vivo/in vitro transduction efficiency of mammalian primary cells and cell lines with Nine natural adeno-associated virus (AAV1-9) and one engineered adeno-associated virus serotype. *Virology journal* **10**, 74, doi:10.1186/1743-422x-10-74 (2013).

187 Kuzmin, D. A. *et al.* The clinical landscape for AAV gene therapies. *Nat Rev Drug Discov* **20**, 173-174, doi:10.1038/d41573-021-00017-7 (2021).

188 Mendell, J. R. *et al.* Current Clinical Applications of In Vivo Gene Therapy with AAVs. *Molecular therapy : the journal of the American Society of Gene Therapy* **29**, 464-488, doi:10.1016/j.ymthe.2020.12.007 (2021).

189 Xu, L., Lau, Y. S., Gao, Y., Li, H. & Han, R. Life-Long AAV-Mediated CRISPR Genome Editing in Dystrophic Heart Improves Cardiomyopathy without Causing Serious Lesions in mdx Mice. *Molecular therapy : the journal of the American Society of Gene Therapy* **27**, 1407-1414, doi:10.1016/j.ymthe.2019.05.001 (2019).

190 Hakim, C. H. *et al.* AAV CRISPR editing rescues cardiac and muscle function for 18 months in dystrophic mice. *JCI Insight* **3**, doi:10.1172/jci.insight.124297 (2018).

191 Ronzitti, G., Gross, D. A. & Mingozzi, F. Human Immune Responses to Adeno-Associated Virus (AAV) Vectors. *Front Immunol* **11**, 670, doi:10.3389/fimmu.2020.00670 (2020).

192 Ruffing, M., Heid, H. & Kleinschmidt, J. A. Mutations in the carboxy terminus of adeno-associated virus 2 capsid proteins affect viral infectivity: lack of an RGD integrin-binding motif. *J Gen Virol* **75 (Pt 12)**, 3385-3392, doi:10.1099/0022-1317-75-12-3385 (1994).

193 Wu, P. *et al.* Mutational analysis of the adeno-associated virus type 2 (AAV2) capsid gene and construction of AAV2 vectors with altered tropism. *J Virol* **74**, 8635-8647, doi:10.1128/jvi.74.18.8635-8647.2000 (2000).

194 Bryant, D. H. *et al.* Deep diversification of an AAV capsid protein by machine learning. *Nature biotechnology* **39**, 691-696, doi:10.1038/s41587-020-00793-4 (2021).

195 Marques, A. D. *et al.* Applying machine learning to predict viral assembly for adeno-associated virus capsid libraries. *Molecular therapy. Methods & clinical development* **20**, 276-286, doi:10.1016/j.omtm.2020.11.017 (2021).

196 Maheshri, N., Koerber, J. T., Kaspar, B. K. & Schaffer, D. V. Directed evolution of adeno-associated virus yields enhanced gene delivery vectors. *Nature biotechnology* **24**, 198-204, doi:10.1038/nbt1182 (2006).

197 Müller, O. J. *et al.* Random peptide libraries displayed on adeno-associated virus to select for targeted gene therapy vectors. *Nature biotechnology* **21**, 1040-1046, doi:10.1038/nbt856 (2003).

198 Perabo, L. *et al.* In vitro selection of viral vectors with modified tropism: the adeno-associated virus display. *Molecular therapy : the journal of the American Society of Gene Therapy* **8**, 151-157, doi:10.1016/s1525-0016(03)00123-0 (2003).

199 Perabo, L. *et al.* Combinatorial engineering of a gene therapy vector: directed evolution of adeno-associated virus. *J Gene Med* **8**, 155-162, doi:10.1002/jgm.849 (2006).

200 Lee, E. J., Guenther, C. M. & Suh, J. Adeno-Associated Virus (AAV) Vectors: Rational Design Strategies for Capsid Engineering. *Curr Opin Biomed Eng* **7**, 58-63, doi:10.1016/j.cobme.2018.09.004 (2018).

201 Pulicherla, N. *et al.* Engineering liver-detargeted AAV9 vectors for cardiac and musculoskeletal gene transfer. *Molecular therapy : the journal of the American Society of Gene Therapy* **19**, 1070-1078, doi:10.1038/mt.2011.22 (2011).

202 Govindasamy, L. *et al.* Structural insights into adeno-associated virus serotype 5. *J Virol* **87**, 11187-11199, doi:10.1128/jvi.00867-13 (2013).

203 Xie, Q. *et al.* The atomic structure of adeno-associated virus (AAV-2), a vector for human gene therapy. *Proceedings of the National Academy of Sciences of the United States of America* **99**, 10405-10410, doi:10.1073/pnas.162250899 (2002).

204 Li, C. & Samulski, R. J. Engineering adeno-associated virus vectors for gene therapy. *Nat Rev Genet* **21**, 255-272, doi:10.1038/s41576-019-0205-4 (2020).

205 Koerber, J. T., Jang, J. H. & Schaffer, D. V. DNA shuffling of adeno-associated virus yields functionally diverse viral progeny. *Molecular therapy : the journal of the American Society of Gene Therapy* **16**, 1703-1709, doi:10.1038/mt.2008.167 (2008).

206 Li, W. *et al.* Engineering and selection of shuffled AAV genomes: a new strategy for producing targeted biological nanoparticles. *Molecular therapy : the journal of the American Society of Gene Therapy* **16**, 1252-1260, doi:10.1038/mt.2008.100 (2008).

207 Körbelin, J. *et al.* Pulmonary Targeting of Adeno-associated Viral Vectors by Next-generation Sequencing-guided Screening of Random Capsid Displayed Peptide Libraries. *Molecular therapy : the journal of the American Society of Gene Therapy* **24**, 1050-1061, doi:10.1038/mt.2016.62 (2016).

208 Varadi, K. *et al.* Novel random peptide libraries displayed on AAV serotype 9 for selection of endothelial cell-directed gene transfer vectors. *Gene Ther* **19**, 800-809, doi:10.1038/gt.2011.143 (2012).

209 Davidsson, M. *et al.* A systematic capsid evolution approach performed in vivo for the design of AAV vectors with tailored properties and tropism. *Proceedings of the National Academy of Sciences of the United States of America* **116**, 27053-27062, doi:10.1073/pnas.1910061116 (2019).

210 Goertsen, D. *et al.* AAV capsid variants with brain-wide transgene expression and decreased liver targeting after intravenous delivery in mouse and marmoset. *Nat Neurosci* **25**, 106-115, doi:10.1038/s41593-021-00969-4 (2022).

211 Hanlon, K. S. *et al.* Selection of an Efficient AAV Vector for Robust CNS Transgene Expression. *Molecular therapy. Methods & clinical development* **15**, 320-332, doi:10.1016/j.omtm.2019.10.007 (2019).

212 Nonnenmacher, M. *et al.* Rapid evolution of blood-brain-barrier-penetrating AAV capsids by RNA-driven biopanning. *Molecular therapy. Methods & clinical development* **20**, 366-378, doi:10.1016/j.omtm.2020.12.006 (2021).

213 Börner, K. *et al.* Pre-arrayed Pan-AAV Peptide Display Libraries for Rapid Single-Round Screening. *Molecular therapy : the journal of the American Society of Gene Therapy* **28**, 1016-1032, doi:10.1016/j.ymthe.2020.02.009 (2020).

214 Tabebordbar, M. *et al.* Directed evolution of a family of AAV capsid variants enabling potent muscle-directed gene delivery across species. *Cell* **184**, 4919-4938.e4922, doi:10.1016/j.cell.2021.08.028 (2021).

215 Weinmann, J. *et al.* Identification of a myotropic AAV by massively parallel in vivo evaluation of barcoded capsid variants. *Nature communications* **11**, 5432, doi:10.1038/s41467-020-19230-w (2020).

216 Ying, Y. *et al.* Heart-targeted adeno-associated viral vectors selected by in vivo biopanning of a random viral display peptide library. *Gene Ther* **17**, 980-990, doi:10.1038/gt.2010.44 (2010).

217 Maurer, A. C. *et al.* The Assembly-Activating Protein Promotes Stability and Interactions between AAV's Viral Proteins to Nucleate Capsid Assembly. *Cell reports* **23**, 1817-1830, doi:10.1016/j.celrep.2018.04.026 (2018).

218 Gromova, A., Tierney, M. T. & Sacco, A. FACS-based Satellite Cell Isolation From Mouse Hind Limb Muscles. *Bio Protoc* **5**, doi:10.21769/bioprotoc.1558 (2015).

219 DiMattia, M. A. *et al.* Structural insight into the unique properties of adeno-associated virus serotype 9. *J Virol* **86**, 6947-6958, doi:10.1128/jvi.07232-11 (2012).

220 Nonnenmacher, M., van Bakel, H., Hajjar, R. J. & Weber, T. High capsid-genome correlation facilitates creation of AAV libraries for directed evolution. *Molecular therapy : the journal of the American Society of Gene Therapy* **23**, 675-682, doi:10.1038/mt.2015.3 (2015).

221 Bachman, J. F. *et al.* Prepubertal skeletal muscle growth requires Pax7-expressing satellite cell-derived myonuclear contribution. *Development* **145**, doi:10.1242/dev.167197 (2018).

222 Berry, G. E. & Asokan, A. Cellular transduction mechanisms of adeno-associated viral vectors. *Curr Opin Virol* **21**, 54-60, doi:10.1016/j.coviro.2016.08.001 (2016).

223 Deverman, B. E. *et al.* Cre-dependent selection yields AAV variants for widespread gene transfer to the adult brain. *Nature biotechnology* **34**, 204-209, doi:10.1038/nbt.3440 (2016).

224 Ravindra Kumar, S. *et al.* Multiplexed Cre-dependent selection yields systemic AAVs for targeting distinct brain cell types. *Nature methods* **17**, 541-550, doi:10.1038/s41592-020-0799-7 (2020).

225 Huang, S. J. *et al.* Cell Type-Specific TRAnscription-Dependent Directed Evolution (TRADE) Identifies Novel AAV Capsids Capable of Enhanced Neuronal Transduction In Mice And Non-Human Primates. *Molecular Therapy* **27**, 24-25 (2019).

226 Roca, X., Sachidanandam, R. & Krainer, A. R. Intrinsic differences between authentic and cryptic 5' splice sites. *Nucleic Acids Res* **31**, 6321-6333, doi:10.1093/nar/gkg830 (2003).

227 Ruoslahti, E. RGD and other recognition sequences for integrins. *Annu Rev Cell Dev Biol* **12**, 697-715, doi:10.1146/annurev.cellbio.12.1.697 (1996).

228 Herrmann, A. K. *et al.* A Robust and All-Inclusive Pipeline for Shuffling of Adeno-Associated Viruses. *ACS Synth Biol* **8**, 194-206, doi:10.1021/acssynbio.8b00373 (2019).

229 Morales, L., Gambhir, Y., Bennett, J. & Stedman, H. H. Broader Implications of Progressive Liver Dysfunction and Lethal Sepsis in Two Boys following Systemic High-Dose AAV. *Molecular therapy : the journal of the American Society of Gene Therapy* **28**, 1753-1755, doi:10.1016/j.ymthe.2020.07.009 (2020).

230 Adachi, K., Enoki, T., Kawano, Y., Veraz, M. & Nakai, H. Drawing a high-resolution functional map of adeno-associated virus capsid by massively parallel sequencing. *Nature communications* **5**, 3075, doi:10.1038/ncomms4075 (2014).

231 de Alencastro, G. *et al.* Tracking Adeno-Associated Virus Capsid Evolution by High-Throughput Sequencing. *Human gene therapy* **31**, 553-564, doi:10.1089/hum.2019.339 (2020).

232 Körbelin, J. *et al.* A brain microvasculature endothelial cell-specific viral vector with the potential to treat neurovascular and neurological diseases. *EMBO Mol Med* **8**, 609-625, doi:10.15252/emmm.201506078 (2016).

233 Körbelin, J. & Trepel, M. How to Successfully Screen Random Adeno-Associated Virus Display Peptide Libraries In Vivo. *Human gene therapy methods* **28**, 109-123, doi:10.1089/hgtb.2016.177 (2017).

234 Marsic, D., Méndez-Gómez, H. R. & Zolotukhin, S. High-accuracy biodistribution analysis of adeno-associated virus variants by double barcode sequencing. *Molecular therapy. Methods & clinical development* **2**, 15041, doi:10.1038/mtm.2015.41 (2015).

235 Paulk, N. K. *et al.* Bioengineered AAV Capsids with Combined High Human Liver Transduction In Vivo and Unique Humoral Seroreactivity. *Molecular therapy : the journal of the American Society of Gene Therapy* **26**, 289-303, doi:10.1016/j.ymthe.2017.09.021 (2018).

236 Westhaus, A. *et al.* High-Throughput In Vitro, Ex Vivo, and In Vivo Screen of Adeno-Associated Virus Vectors Based on Physical and Functional Transduction. *Human gene therapy* **31**, 575-589, doi:10.1089/hum.2019.264 (2020).

237 Yang, L. *et al.* A myocardium tropic adeno-associated virus (AAV) evolved by DNA shuffling and in vivo selection. *Proceedings of the National Academy of Sciences of the United States of America* **106**, 3946-3951, doi:10.1073/pnas.0813207106 (2009).

238 High-dose AAV gene therapy deaths. *Nature biotechnology* **38**, 910-910, doi:10.1038/s41587-020-0642-9 (2020).

239 Day, J. W. *et al.* Onasemnogene abeparvovec gene therapy for symptomatic infantile-onset spinal muscular atrophy in patients with two copies of SMN2 (STR1VE): an open-label, single-arm, multicentre, phase 3 trial. *Lancet Neurol* **20**, 284-293, doi:10.1016/s1474-4422(21)00001-6 (2021).

240 Day, J. W. *et al.* Clinical Trial and Postmarketing Safety of Onasemnogene Abeparvovec Therapy. *Drug Saf* **44**, 1109-1119, doi:10.1007/s40264-021-01107-6 (2021).

241 Guillou, J. *et al.* Fatal Thrombotic Microangiopathy Case following Adeno-Associated Viral SMN Gene Therapy. *Blood Adv*, doi:10.1182/bloodadvances.2021006419 (2022).

242 Biosciences, S. Solid Biosciences Announces FDA Lifts Clinical Hold on IGNITE DMD Clinical Trial. (2020).

243 D'Amico, A. *et al.* Hepatobiliary disease in XLMTM: a common comorbidity with potential impact on treatment strategies. *Orphanet J Rare Dis* **16**, 425, doi:10.1186/s13023-021-02055-1 (2021).

244 Pfizer. Pfizer's New Phase 1b Results of Gene Therapy in Ambulatory Boys with Duchenne Muscular Dystrophy (DMD) Support Advancement into Pivotal Phase 3 Study. (2020).

245 Shieh, P. B. *et al.* Re: "Moving Forward After Two Deaths in a Gene Therapy Trial of Myotubular Myopathy" by Wilson and Flotte. *Human gene therapy* **31**, 787, doi:10.1089/hum.2020.217 (2020).

246 Rajavel, K. *et al.* Co-Prevalence of Pre-Existing Immunity to Different Serotypes of Adeno-Associated Virus (AAV) in Adults with Hemophilia. *Blood* **134**, 3349-3349, doi:10.1182/blood-2019-123666 (2019).

247 Mendell, J. R. *et al.* Testing preexisting antibodies prior to AAV gene transfer therapy: rationale, lessons and future considerations. *Molecular therapy. Methods & clinical development* **25**, 74-83, doi:10.1016/j.omtm.2022.02.011 (2022).

248 Patton, K. S. *et al.* Monitoring cell-mediated immune responses in AAV gene therapy clinical trials using a validated IFN-γ ELISpot method. *Molecular therapy. Methods & clinical development* **22**, 183-195, doi:10.1016/j.omtm.2021.05.012 (2021).

249 Smith, J. G., Liu, X., Kaufhold, R. M., Clair, J. & Caulfield, M. J. Development and validation of a gamma interferon ELISPOT assay for quantitation of cellular immune responses to varicella-zoster virus. *Clin Diagn Lab Immunol* **8**, 871-879, doi:10.1128/cdli.8.5.871-879.2001 (2001).

250 Ferla, R. *et al.* Non-clinical Safety and Efficacy of an AAV2/8 Vector Administered Intravenously for Treatment of Mucopolysaccharidosis Type VI. *Molecular therapy. Methods & clinical development* **6**, 143-158, doi:10.1016/j.omtm.2017.07.004 (2017).

251 Majowicz, A. *et al.* Successful Repeated Hepatic Gene Delivery in Mice and Non-human Primates Achieved by Sequential Administration of AAV5(ch) and AAV1. *Molecular therapy : the journal of the American Society of Gene Therapy* **25**, 1831-1842, doi:10.1016/j.ymthe.2017.05.003 (2017).

252 Butler, A., Hoffman, P., Smibert, P., Papalexi, E. & Satija, R. Integrating single-cell transcriptomic data across different conditions, technologies, and species. *Nature biotechnology* **36**, 411-420, doi:10.1038/nbt.4096 (2018).

253 Davies, D. H. *et al.* Profiling the humoral immune response to infection by using proteome microarrays: high-throughput vaccine and diagnostic antigen discovery. *Proceedings of the National Academy of Sciences of the United States of America* **102**, 547-552, doi:10.1073/pnas.0408782102 (2005).

254 Davies, D. H. *et al.* Proteome-wide analysis of the serological response to vaccinia and smallpox. *Proteomics* **7**, 1678-1686, doi:10.1002/pmic.200600926 (2007).

255 Vigil, A., Davies, D. H. & Felgner, P. L. Defining the humoral immune response to infectious agents using high-density protein microarrays. *Future Microbiol* **5**, 241-251, doi:10.2217/fmb.09.127 (2010).

256 Herzog, R. W. *et al.* Long-term correction of canine hemophilia B by gene transfer of blood coagulation factor IX mediated by adeno-associated viral vector. *Nat Med* **5**, 56-63, doi:10.1038/4743 (1999).

257 Kotterman, M. A. *et al.* Antibody neutralization poses a barrier to intravitreal adeno-associated viral vector gene delivery to non-human primates. *Gene Ther* **22**, 116-126, doi:10.1038/gt.2014.115 (2015).

258 Verdera, H. C., Kuranda, K. & Mingozzi, F. AAV Vector Immunogenicity in Humans: A Long Journey to Successful Gene Transfer. *Molecular therapy : the journal of the American Society of Gene Therapy* **28**, 723-746, doi:10.1016/j.ymthe.2019.12.010 (2020).

259 Zhang, Y. C. *et al.* Immunity to adeno-associated virus serotype 2 delivered transgenes imparted by genetic predisposition to autoimmunity. *Gene Ther* **11**, 233-240, doi:10.1038/sj.gt.3302144 (2004).

260 Weeratna, R. D., Wu, T., Efler, S. M., Zhang, L. & Davis, H. L. Designing gene therapy vectors: avoiding immune responses by using tissue-specific promoters. *Gene Ther* **8**, 1872-1878, doi:10.1038/sj.gt.3301602 (2001).

261 Binks, M. (American Society of Gene & Cell Therapy (ASGCT), 2021).

262 Morris, C. (American Society of Gene & Cell Therapy (ASGCT), 2021).

263 Hamilton, B. A. & Wright, J. F. Challenges Posed by Immune Responses to AAV Vectors: Addressing Root Causes. *Front Immunol* **12**, 675897, doi:10.3389/fimmu.2021.675897 (2021).

264 Zaiss, A. K. *et al.* Complement is an essential component of the immune response to adeno-associated virus vectors. *Journal of virology* **82**, 2727-2740, doi:10.1128/JVI.01990-07 (2008).

265 Martino, A. T. *et al.* The genome of self-complementary adeno-associated viral vectors increases Toll-like receptor 9-dependent innate immune responses in the liver. *Blood* **117**, 6459-6468, doi:10.1182/blood-2010-10-314518 (2011).

266 Sasai, M., Linehan, M. M. & Iwasaki, A. Bifurcation of Toll-like receptor 9 signaling by adaptor protein 3. *Science (New York, N.Y.)* **329**, 1530-1534, doi:10.1126/science.1187029 (2010).

267 Rogers, G. L. *et al.* Plasmacytoid and conventional dendritic cells cooperate in crosspriming AAV capsid-specific CD8(+) T cells. *Blood* **129**, 3184-3195, doi:10.1182/blood-2016-11-751040 (2017).

268 Wright, J. F. Quantification of CpG Motifs in rAAV Genomes: Avoiding the Toll. *Molecular therapy : the journal of the American Society of Gene Therapy* **28**, 1756-1758, doi:10.1016/j.ymthe.2020.07.006 (2020).

269 Guillerey, C. *et al.* Pivotal role of plasmacytoid dendritic cells in inflammation and NK-cell responses after TLR9 triggering in mice. *Blood* **120**, 90-99, doi:10.1182/blood-2012-02-410936 (2012).

270 Krieg, A. M., Efler, S. M., Wittpoth, M., Al Adhami, M. J. & Davis, H. L. Induction of systemic TH1-like innate immunity in normal volunteers following subcutaneous but not intravenous administration of CPG 7909, a synthetic B-class CpG oligodeoxynucleotide TLR9 agonist. *J Immunother* **27**, 460-471, doi:10.1097/00002371-200411000-00006 (2004).

271 Krogmann, A. O. *et al.* Proinflammatory Stimulation of Toll-Like Receptor 9 with High Dose CpG ODN 1826 Impairs Endothelial Regeneration and Promotes Atherosclerosis in Mice. *PLoS One* **11**, e0146326, doi:10.1371/journal.pone.0146326 (2016).

272 Kwissa, M., Nakaya, H. I., Oluoch, H. & Pulendran, B. Distinct TLR adjuvants differentially stimulate systemic and local innate immune responses in nonhuman primates. *Blood* **119**, 2044-2055, doi:10.1182/blood-2011-10-388579 (2012).

273 Mathes, A. L. *et al.* CpGB DNA activates dermal macrophages and specifically recruits inflammatory monocytes into the skin. *Exp Dermatol* **24**, 133-139, doi:10.1111/exd.12603 (2015).

274 Båve, U. *et al.* Fc gamma RIIa is expressed on natural IFN-alpha-producing cells (plasmacytoid dendritic cells) and is required for the IFN-alpha production induced by apoptotic cells combined with lupus IgG. *J Immunol* **171**, 3296-3302, doi:10.4049/jimmunol.171.6.3296 (2003).

275 Wang, J. P., Asher, D. R., Chan, M., Kurt-Jones, E. A. & Finberg, R. W. Cutting Edge: Antibody-mediated TLR7-dependent recognition of viral RNA. *J Immunol* **178**, 3363-3367, doi:10.4049/jimmunol.178.6.3363 (2007).

276 Fitzpatrick, Z. *et al.* Influence of Pre-existing Anti-capsid Neutralizing and Binding Antibodies on AAV Vector Transduction. *Molecular therapy. Methods & clinical development* **9**, 119-129, doi:10.1016/j.omtm.2018.02.003 (2018).

277 Hösel, M. *et al.* Toll-like receptor 2-mediated innate immune response in human nonparenchymal liver cells toward adeno-associated viral vectors. *Hepatology* **55**, 287-297, doi:10.1002/hep.24625 (2012).

278 Alonso, A., Bayón, Y., Renedo, M. & Crespo, M. S. Stimulation of Fc gamma R receptors induces monocyte chemoattractant protein-1 in the human monocytic cell line THP-1 by a mechanism involving I kappa B-alpha degradation and formation of p50/p65 NF-kappa B/Rel complexes. *Int Immunol* **12**, 547-554, doi:10.1093/intimm/12.4.547 (2000).

279 Song, W. C. Crosstalk between complement and toll-like receptors. *Toxicol Pathol* **40**, 174-182, doi:10.1177/0192623311428478 (2012).

280 Thieblemont, N. *et al.* Triggering of complement receptors CR1 (CD35) and CR3 (CD11b/CD18) induces nuclear translocation of NF-kappa B (p50/p65) in human monocytes and enhances viral replication in HIV-infected monocytic cells. *J Immunol* **155**, 4861-4867 (1995).

281 Sun, S. C. The non-canonical NF-κB pathway in immunity and inflammation. *Nat Rev Immunol* **17**, 545-558, doi:10.1038/nri.2017.52 (2017).

282 Parameswaran, N. & Patial, S. Tumor necrosis factor-α signaling in macrophages. *Crit Rev Eukaryot Gene Expr* **20**, 87-103, doi:10.1615/critreveukargeneexpr.v20.i2.10 (2010).

283 Dorrington, M. G. & Fraser, I. D. C. NF-κB Signaling in Macrophages: Dynamics, Crosstalk, and Signal Integration. *Front Immunol* **10**, 705, doi:10.3389/fimmu.2019.00705 (2019).

284 Butterfield, J. S. S. *et al.* TLR9-Activating CpG-B ODN but Not TLR7 Agonists Triggers Antibody Formation to Factor IX in Muscle Gene Transfer. *Human gene therapy methods* **30**, 81-92, doi:10.1089/hgtb.2019.013 (2019).

285 Jegerlehner, A. *et al.* TLR9 signaling in B cells determines class switch recombination to IgG2a. *J Immunol* **178**, 2415-2420, doi:10.4049/jimmunol.178.4.2415 (2007).

286 Kadowaki, N. *et al.* Subsets of human dendritic cell precursors express different toll-like receptors and respond to different microbial antigens. *J Exp Med* **194**, 863-869, doi:10.1084/jem.194.6.863 (2001).

287 Jabbar, A. *et al.* Advances and Perspectives in the Application of CRISPR-Cas9 in Livestock. *Mol Biotechnol* **63**, 757-767, doi:10.1007/s12033-021-00347-2 (2021).

288 Liu, Q. *et al.* Application of CRISPR/Cas9 in Crop Quality Improvement. *Int J Mol Sci* **22**, doi:10.3390/ijms22084206 (2021).

289 Gootenberg, J. S. *et al.* Nucleic acid detection with CRISPR-Cas13a/C2c2. *Science (New York, N.Y.)* **356**, 438-442, doi:10.1126/science.aam9321 (2017).

290 Satomura, A. *et al.* Precise genome-wide base editing by the CRISPR Nickase system in yeast. *Sci Rep* **7**, 2095, doi:10.1038/s41598-017-02013-7 (2017).

291 Zetsche, B. *et al.* Cpf1 is a single RNA-guided endonuclease of a class 2 CRISPR-Cas system. *Cell* **163**, 759-771, doi:10.1016/j.cell.2015.09.038 (2015).

292 Gillmore, J. D. *et al.* CRISPR-Cas9 In Vivo Gene Editing for Transthyretin Amyloidosis. *N Engl J Med* **385**, 493-502, doi:10.1056/NEJMoa2107454 (2021).

293 Kaiser, J. CRISPR helps a blind woman see, but doesn't help all patients. *Gene-editing treatment shows its promise—and limits—in first trial* (2021).

294 Kaiser, J. CRISPR injected into the blood treats a genetic disease for first time. *Novel treatment using messenger RNA sharply cuts production of mutant liver protein, although it's too early to show patients with rare condition benefit* (2021).

295 Chicoine, L. G. *et al.* Plasmapheresis eliminates the negative impact of AAV antibodies on microdystrophin gene expression following vascular delivery. *Molecular therapy : the journal of the American Society of Gene Therapy* **22**, 338-347, doi:10.1038/mt.2013.244 (2014).

296 Corti, M. *et al.* Evaluation of Readministration of a Recombinant Adeno-Associated Virus Vector Expressing Acid Alpha-Glucosidase in Pompe Disease:

Preclinical to Clinical Planning. *Hum Gene Ther Clin Dev* **26**, 185-193, doi:10.1089/humc.2015.068 (2015).

297 Halbert, C. L., Standaert, T. A., Wilson, C. B. & Miller, A. D. Successful readministration of adeno-associated virus vectors to the mouse lung requires transient immunosuppression during the initial exposure. *J Virol* **72**, 9795-9805, doi:10.1128/jvi.72.12.9795-9805.1998 (1998).

298 Manning, W. C., Zhou, S., Bland, M. P., Escobedo, J. A. & Dwarki, V. Transient immunosuppression allows transgene expression following readministration of adeno-associated viral vectors. *Human gene therapy* **9**, 477-485, doi:10.1089/hum.1998.9.4-477 (1998).

299 Ros-Gañán, I. *et al.* Optimising the IgG-degrading enzyme treatment regimen for enhanced adeno-associated virus transduction in the presence of neutralising antibodies. *Clin Transl Immunology* **11**, e1375, doi:10.1002/cti2.1375 (2022).

300 Arnett, A. L. *et al.* Adeno-associated viral (AAV) vectors do not efficiently target muscle satellite cells. *Molecular therapy. Methods & clinical development* **1**, doi:10.1038/mtm.2014.38 (2014).

301 Bucher, K., Rodríguez-Bocanegra, E., Dauletbekov, D. & Fischer, M. D. Immune responses to retinal gene therapy using adeno-associated viral vectors - Implications for treatment success and safety. *Prog Retin Eye Res* **83**, 100915, doi:10.1016/j.preteyeres.2020.100915 (2021).